Search for Scalar Quarks in e^+e^- collisions at LEP II

Dissertation

zur Erlangung des akademischen Grades

doctor rerum naturalium

(Dr. rer. nat.)

im Fach Physik

eingereicht an der

Mathematisch-Naturwissenschaftlichen Fakultät I
der Humboldt-Universität zu Berlin

von

Diplom-Physiker Serge Sushkov,
geboren am 24. Marz 1974 in Katav-Ivanovsk, Russland

Präsident der Humboldt-Universität zu Berlin
Prof. Dr. Jürgen Mlynek

Dekan der Mathematisch-Naturwissenschaftlichen Fakultät I
Prof. Dr. Michael Linscheid

Gutachter:	1.	Prof. Dr. T. Hebbeker
	2.	Prof. Dr. H. Kolanoski
	3.	Prof. Dr. T. Lohse

eingereicht am:	16.03.2003
Tag der mündlichen Prüfung:	22.09.2003

Abstract

Diese Dissertation beschäftigt sich mit der Suche nach dem skalaren Top Quark $\tilde{t}_1$ und dem skalaren Bottom Quark $\tilde{b}_1$ innerhalb des *Minimal Supersymmetric Standard Model (MSSM)* unter der Annahme der R-Paritätserhaltung. Suchen nach den folgenden Zerfallsmoden des Stop-Quark wurden durchgeführt: $\tilde{t}_1 \to c\tilde{\chi}^0_1$, $\tilde{t}_1 \to bl\tilde{\nu}$ (wobei l mit gleichen Wahrscheinlichkeiten entweder e, μ oder τ ist) und $\tilde{t}_1 \to b\tau\tilde{\nu}$ (nur das Tau-Lepton wird berücksichtigt). Zusätzlich wurde der Dreikörperzerfall $\tilde{t}_1 \to bW\tilde{\chi}^0_1$ im erlaubten Massenbereich $M_{\tilde{t}_1} > M_b + M_W + M_{\tilde{\chi}^0_1} \geq$ 86 GeV gesucht. Für das Sbottom-Quark wurde der Zerfall $\tilde{b}_1 \to b\tilde{\chi}^0_1$ studiert. Jede dieser Zerfallsmoden wurde voneinander unabhängig unter der Annahme eines 100 %igen Verzweigungsverhältnisses untersucht.

Für diese Suche wurden Daten aus e^+e^--Kollisionen bei Schwerpunktsenergien im Bereich von 202−208 GeV benutzt. Die Daten wurden im Jahr 2000 von dem L3 Detektor am Large Electron Positron Collider (*LEP*) am CERN aufgenommen. Ferner wurden die Resultate der Datenanalyse aus dem Jahr 2000 mit Resultaten der Squark-Suche kombiniert, die die L3 Kollaboration in vorhergehenden Jahren bei Schwerpunktsenergien von 161 bis 202 GeV durchgeführt hat.

Die untersuchten Squark Zerfallskanäle bestimmen die Topologie der für uns interessanten Ereignisse: 2 Jets (oder b-Jets) + fehlende Energie (+ 2 Leptonen für die Stop-Dreikörperzerfälle). Die $\tilde{t}_1 \to bW\tilde{\chi}^0_1$ Zerfallstopologie hängt signifikant von den weiteren Zerfällen des W-Bosons ab und kann bis zu 6 Jets im Endzustand haben. Die Annahme der R-Paritätserhaltung impliziert die Stabilität des *leichtesten supersymmetrischen Teilchens* (des LSP), das das leichteste Neutralino $\tilde{\chi}^0_1$ ist. Das LSP wechselwirkt nur schwach und entweicht deswegen unentdeckt. Ein besonderes Merkmal der Signal-Ereignisse ist somit eine erhebliche Menge fehlender Energie E_{miss}. Die *sichtbare Energie* $E_{vis} = E_{tot} - E_{miss}$ ist in etwa proportional zu der Massendifferenz zwischen dem Squark und dem LSP, $\Delta M = M_{\tilde{t}_1} - M_{LSP}$. Weil die Standardmodell-Untergrundzusammensetzung vom Anteil der sichtbaren Energie abhängt, hängt die Analyse auch vom Wert von ΔM ab.

Abhängig von der Menge fehlender Energie kann der Standardmodell-Untergrund in drei Kategorien eingeteilt werden:

- die *zwei-Fermion*-Prozesse sind $e^+e^- \to e^+e^-$, $e^+e^- \to \mu^+\mu^-$, $e^+e^- \to \tau^+\tau^-$ and $e^+e^- \to q\,\bar{q}$;

- die *vier-Fermion*-Kategorie besteht aus $e^+e^- \to W^+W^-$, $e^+e^- \to W^\pm e^\mp \nu$, $e^+e^- \to Z^0Z^0$ und $e^+e^- \to Z^0e^+e^-$ Prozessen;

- die *zwei-Photon*-Untergrundprozesse sind $e^+e^- \rightarrow e^+e^-e^+e^-$, $e^+e^- \rightarrow e^+e^-\mu^+\mu^-$, $e^+e^- \rightarrow e^+e^-\tau^+\tau^-$ and $e^+e^- \rightarrow e^+e^-q\ \bar{q}$.

Der letzte Prozess, $e^+e^- \rightarrow e^+e^-q\ \bar{q}$, trägt den grössten Anteil zu den SM-Untergrundprozessen bei (wegen sehr hohem und stark schwankendem E_{miss} und dem grössten Wirkungsquerschnitt).

Im ersten Schritt der Analyse wurden Events mit der gewünschten Topologie (2 Jets und hohes E_{miss}) *vorselektiert*. Die Selektion von Stop- und Sbottom-Ereignissen wurde durch die Minimierung der mit 95% *Confidence Level (C.L.)* erwarteten oberen Grenze des Squark-Wirkungsquerschnitts – berechnet aus MC-Vorhersagen – optimiert, wobei der kleine theoretisch vorhergesagte Produktionswirkungsquerschnitt des Squarks berücksichtigt wurde. In allen für den jeweiligen Squark Zerfallskanal optimierten Selektionen stimmt die Anzahl von Daten Events mit der erwarteten Anzahl von Standardmodellprozessen überein:

- für den $\tilde{t}_1 \rightarrow c\tilde{\chi}^0_1$ Zerfall wurden 29 Daten-Events beobachtet, wobei 26.5 ± 2.7 Events von den SM-Prozessen erwartet wurden;

- für den Dreikörperzerfall $\tilde{t}_1 \rightarrow bl\tilde{\nu}$ wurden 4 Daten-Events selektiert bei einer Standardmodell-Erwartung von 4.0 ± 1.0 Events;

- für den Zerfall $\tilde{t}_1 \rightarrow b\tau\tilde{\nu}$ sind die Daten- und SM-Eventzahlen 5 bzw. 3.9 ± 1.0;

- in der Selektion für $\tilde{t}_1 \rightarrow bW\tilde{\chi}^0_1$ wurden 184 Daten Events beobachtet und 181.6 ± 3.0 Events wurden vom Standardmodell vorhergesagt;

- für den Bottom Squark Zerfall $\tilde{b}_1 \rightarrow b\tilde{\chi}^0_1$ entsprachen die beobachteten 6 Events der SM-Erwartung von 7.7 ± 1.3 Events.

Es wurden keine MSSM-Skalar-Quarks in den Daten des Experiments beobachtet und das Resultat der Suche ist negativ.

Die *modellunabhängige* 95 % C.L. obere Grenze für den Squark-Produktionswirkungsquerschnitt wurde aus der gemessenen Anzahl von Daten-Events und der aus dem Standardmodell erwarteten Eventanzahl berechnet. Für die Berechnung der oberen Grenzen der Produktionswirkungsquerschnitte wurden die Resultate der Squark-Suchen aus den L3-Daten bei Schwerpunktsenergien von $\sqrt{s} = 202 - 208$ GeV mit den Resultaten aus vorherigen Suchen der L3-Kollaboration bei 161 GeV $< \sqrt{s} <$ 202 GeV kombiniert. Eine neue Methode wurde entwickelt, um die *kombinierten* Grenzen zu berechnen. Die Methode berücksichtigt die statistische Unabhängigkeit jeder Messung und die Abhängigkeit des Squark-Produktionswirkungsquerschnittes von der Schwerpunktsenergie. In der Berechnung wurde den systematischen Unsicherheiten in der Standardmodell-Untergrundabschätzung und der Signal-Selektionseffizienz Rechnung getragen.

Für die hier betrachteten Squark-Zerfälle $\tilde{t}_1 \rightarrow c\tilde{\chi}^0_1$, $\tilde{t}_1 \rightarrow bl\tilde{\nu}$, $\tilde{t}_1 \rightarrow b\tau\tilde{\nu}$ und $\tilde{b}_1 \rightarrow b\tilde{\chi}^0_1$ werden typisch folgende oberen Grenzen mit 95% C.L. für den Squark Produktionswirkungsquerschnitt erhalten:

$$\sigma^{95\%}_{\tilde{t}_1} < 0.05 - 0.2\ pb;$$

$$\sigma_{\tilde{b}_1}^{95\%} < 0.05 - 0.1 \; pb.$$

Bei den Suchen nach dem Stop-Dreikörperzerfall $\tilde{t}_1 \rightarrow bW\tilde{\chi}_1^0$ wurden die Produktionswirkungsquerschnitte über 0.7 − 1.0 pb mit 95 % C.L. ausgeschlossen.

Innerhalb des Minimal Supersymmetrischen Standard Modells mit R-Paritätserhaltung wurden die unabhängigen Wirkungsquerschnittsgrenzen für den Ausschluss von MSSM Parametern benutzt, insbesondere für die Stop- und Sbottom-Massen.

Die Squark-Massen wurden für jeden betrachteten Zerfallskanal in Hinsicht zwei möglichen Szenarien ausgeschlossen: für den maximalen und den (näherungsweise) minimalen theoretischen Wirkungsquerschnitt. Der erste Fall korrespondiert zur maximalen Mischung zwischen den links- und rechtshändigen Squark-Eigenzuständen, $\cos\theta_{LR} = 1$; der zweite Fall ist definiert durch den Wert von $\cos\theta_{LR}$, bei dem die Squarks vom Z^0 Boson entkoppeln. Abhängig vom Wert ΔM wurden die Squark Massen mit 95 % C.L. bis zu den folgenden Werten ausgeschlossen:

$$\tilde{t}_1 \rightarrow c\tilde{\chi}_1^0 \; : \qquad M_{\tilde{t}_1}^{\sigma_{min}} < 90 - 93 \text{ GeV}, \quad M_{\tilde{t}_1}^{\sigma_{max}} < 95 - 96 \text{ GeV};$$

$$\tilde{t}_1 \rightarrow bl\tilde{\nu} \; : \qquad M_{\tilde{t}_1}^{\sigma_{min}} < 87 - 89 \text{ GeV}, \quad M_{\tilde{t}_1}^{\sigma_{max}} < 90 - 91 \text{ GeV};$$

$$\tilde{t}_1 \rightarrow b\tau\tilde{\nu} \; : \qquad M_{\tilde{t}_1}^{\sigma_{min}} < 83 - 88 \text{ GeV}, \quad M_{\tilde{t}_1}^{\sigma_{max}} < 88 - 91 \text{ GeV};$$

$$\tilde{b}_1 \rightarrow b\tilde{\chi}_1^0 \; : \qquad M_{\tilde{b}_1}^{\sigma_{min}} < 76 - 83 \text{ GeV}, \quad M_{\tilde{b}_1}^{\sigma_{max}} < 94 - 97 \text{ GeV}.$$

In beiden Fällen werden die *experimentell beobachteten* 95% C.L. Massen Ausschlussgrenzen mit den aus Monte Carlo Simulationen ohne SUSY Teilchen *erwarteten* verglichen. Die experimentallen Ausschlussgrenzen Sind verträglich mit den erwarteten.

Die mit 95 % C.L. erhaltene obere Grenze für den Stop-Produktionquerschnitt ist im Zerfall $\tilde{t}_1 \rightarrow bW\tilde{\chi}_1^0$ grösser als die zugehörige theoretische Vorhersage. Der Ausschluss mit 95 % C.L. auf Massen war mit dem zur Verfügung stehenden Datensatz aus diesen Grund nicht möglich.

Unter der Annahme, dass die Zerfallstopologie der *skalaren Quarks der ersten zwei Generationen* ähnlich dem Zweikörperzerfall des Stop ist, wurden die Resultate der Suche nach dem Zerfall $\tilde{t}_1 \rightarrow c\tilde{\chi}_1^0$ auch für die Berechnung der Massenausschlussgrenzen für die Squarks der ersten beiden Familien benutzt. Zwei Möglichkeiten wurden hier in Erwägung gezogen: die Massenentartung zwischen vier ($\tilde{u}$, $\tilde{d}$, $\tilde{c}$, $\tilde{s}$) und fünf ($\tilde{b}$ zusätzlich) Squarks. Die Ausschlussgrenzen mit 95% C.L. auf die massenentarteten skalaren Quarks in den Fällen der “nur-rechts” oder “links-und-rechts” Eigenzustände sind die folgenden:

$$\tilde{q} = \tilde{u}\;\tilde{d}\;\tilde{c}\;\tilde{s} : \qquad M_{\tilde{q_R}} < 95 - 96 \text{ GeV}, \quad M_{\tilde{q_{LR}}} < \; 99 - 100 \text{ GeV};$$

$$\tilde{q} = \tilde{u}\;\tilde{d}\;\tilde{c}\;\tilde{s}\;\tilde{b} : \qquad M_{\tilde{q_R}} < 96 - 97 \text{ GeV}, \quad M_{\tilde{q_{LR}}} < \; 99 - 101 \text{ GeV}.$$

Mit der Annahme der Gaugino-Vereinigung an der GUT-Skala im MSSM wurden die Grenzen für die vierfach massenentarteten Squarks erneut in der $m_{\tilde{g}}$-$m_{\tilde{q}}$-Ebene interpretiert. Ferner wurde das absolute Limit auf den MSSM-Parameter M_2, der für

$\tan\beta = 4$ aus anderen L3-SUSY-Suchen (für Chargino, Neutralino und skalare Leptonen) ermittelt worden ist, in ein Gluino-Massenlimit übersetzt. Die mit 95% C.L. erhaltenen Ausschlussgrenzen in der $m_{\tilde{\mathrm{g}}}$-$m_{\tilde{\mathrm{q}}}$-Massenebene sind

$$M_{\tilde{\mathrm{g}}} > 267 - 314 \text{ GeV},$$

$$M_{\tilde{\mathrm{q}}} > 99 - 100 \text{ GeV}.$$

Abstract

This thesis is devoted to searches for the scalar top quark $\tilde{t}_1$ and the scalar bottom quark $\tilde{b}_1$ within the framework of the Minimal Supersymmetric Standard Model (*MSSM*) with the assumption of R-parity conservation. Searches for the following decay modes of the stop quark have been performed: $\tilde{t}_1 \to c\tilde{\chi}^0_1$, $\tilde{t}_1 \to bl\tilde{\nu}$ (where l is either e, μ or τ with equal probabilities) and $\tilde{t}_1 \to b\tau\tilde{\nu}$ (where only the tau lepton is considered). In addition, a three body decay $\tilde{t}_1 \to bW\tilde{\chi}^0_1$ has been searched for in the allowed mass region of $M_{\tilde{t}_1} > M_b + M_W + M_{\tilde{\chi}^0_1} \geq$ 86 GeV. For the sbottom quark the decay $\tilde{b}_1 \to b\tilde{\chi}^0_1$ was considered. Each of these decay modes was considered independently assuming a branching ratio of 100%.

For this search, the experimental data of e^+e^- collisions at center-of-mass energies in the range of $202 - 208$ GeV have been used. These data were collected in the year 2000 by the L3 detector at the Large Electron Positron Collider (*LEP*) at CERN. The results of the year 2000 data analysis were also combined with results of the squark searches performed by the L3 Collaboration in previous years at center-of-mass energies from 161 up to 202 GeV.

The analyzed squark decay channels determine the topology of the events of our interest: 2 jets (or b-jets) + missing energy (+ 2 leptons for stop three body decays). The $\tilde{t}_1 \to bW\tilde{\chi}^0_1$ decay topology depends significantly on the further decay of the W boson and can have up to 6 jets in the final state. The assumed conservation of R-parity implies stability of the *lightest supersymmetric particle* (the LSP), which is the lightest neutralino $\tilde{\chi}^0_1$. The LSP interacts only weakly and thus escapes undetected. This leads to a large missing energy E_{miss} as a feature of the signal events. The *visible energy* $E_{vis} = E_{tot} - E_{miss}$ is roughly proportional to the difference between the masses of the squark and the LSP, $\Delta M = M_{\tilde{t}_1} - M_{LSP}$, and since the Standard Model background composition depends on the visible energy fraction, the whole analysis depends also on the value of ΔM.

Depending on the magnitude of E_{vis}, the Standard Model background can be grouped into three categories:

- the *two-fermion* processes are $e^+e^- \to e^+e^-$, $e^+e^- \to \mu^+\mu^-$, $e^+e^- \to \tau^+\tau^-$ and $e^+e^- \to q\,\bar{q}$;
- the four-fermion category is composed of $e^+e^- \to W^+W^-$, $e^+e^- \to W^\pm e^\mp \nu$, $e^+e^- \to Z^0Z^0$ and $e^+e^- \to Z^0e^+e^-$ processes;
- the two-photon background processes are $e^+e^- \to e^+e^-e^+e^-$, $e^+e^- \to e^+e^-\mu^+\mu^-$, $e^+e^- \to e^+e^-\tau^+\tau^-$ and $e^+e^- \to e^+e^-q\,\bar{q}$.

The last process, $e^+e^- \rightarrow e^+e^- q\,\bar{q}$, constitutes the largest fraction of all SM background processes (due to very high and highly fluctuating E_{miss} and the highest cross section).

At the very first step of the analysis, only the events of interesting topology (with 2 jets and high E_{miss}) were *preselected*. Then, taking into account the small value of the theoretically predicted production cross section of the scalar quarks, the selection of stop and sbottom events was optimized by minimization of the 95% *confidence level expected upper limit* on the squark cross section using calculated Monte Carlo events. In all selections optimized for each particular squark decay channel, the number of selected data events statistically agrees with the number of events expected from the Standard Model processes:

- for $\tilde{t}_1 \rightarrow c\tilde{\chi}^0_1$ decay, 29 data evens were observed, while 26.5 ± 2.7 were expected from the SM processes;
- for the three body decay $\tilde{t}_1 \rightarrow bl\tilde{\nu}$, 4 data events were selected and the expectation from the Standard Model is 4.0 ± 1.0 events;
- for the decay $\tilde{t}_1 \rightarrow b\tau\tilde{\nu}$ the data and SM event numbers are 5 and 3.9 ± 1.0, respectively;
- in the selection for $\tilde{t}_1 \rightarrow bW\tilde{\chi}^0_1$, 184 data events were observed and 181.6 ± 3.0 were expected from the Standard Model;
- for the bottom squark decay $\tilde{b}_1 \rightarrow b\tilde{\chi}^0_1$ the observed 6 events correspond to the SM expectation of 7.7 ± 1.3.

Thus, the MSSM scalar quarks were not observed in the experimental data and the search results are negative.

The *model independent* 95 % C.L. upper limits on the squark production cross section have been derived from the numbers of the observed data events and numbers of events expected from the Standard Model. For calculation of the upper cross section limits, the results of the squark searches performed in the L3 data of $\sqrt{s} = 202 - 208$ GeV were combined with results of searches performed by the L3 Collaboration previously in the data of $\sqrt{s}$ from 161 up to 202 GeV. A new method has been developed for calculating such *combined* limits. This method takes into account the statistical independence of each measurement and the dependency of the squark production cross section on the center-of-mass energy. In this calculation, the systematic uncertainties in the Standard Model background estimation and in the signal selection efficiency have been also accounted for.

For the considered squark decays $\tilde{t}_1 \rightarrow c\tilde{\chi}^0_1$, $\tilde{t}_1 \rightarrow bl\tilde{\nu}$, $\tilde{t}_1 \rightarrow b\tau\tilde{\nu}$ and $\tilde{b}_1 \rightarrow b\tilde{\chi}^0_1$, the typical obtained 95% C.L. upper limits on the squark production cross section are:

$$\sigma^{95\%}_{\tilde{t}_1} < 0.05 - 0.2\ pb;$$

$$\sigma^{95\%}_{\tilde{b}_1} < 0.05 - 0.1\ pb.$$

In the searches for the stop three body decay $\tilde{t}_1 \to bW\tilde{\chi}^0_1$, the cross sections above $0.7 - 1.0$ pb have been excluded at 95 % C.L.

Within the framework of MSSM with conserved R-parity, the experimental model independent cross section limits have been used for exclusion of the MSSM model parameters, in particular, exclusion of the stop and the sbottom masses. For each considered decay channel, the squark masses have been excluded in two possible scenarios: for the maximal and for the (approximately) minimal theoretical cross section. The first case corresponds to the maximal mixing between the left and right squark eigenstates, $\cos\theta_{LR} = 1$; the second case is defined by the $\cos\theta_{LR}$ value, where squarks decouple from the Z^0 boson. Depending on the ΔM value, the squark masses have been excluded at 95 % C.L. up to the following values:

$$
\begin{array}{llll}
\tilde{t}_1 \to c\tilde{\chi}^0_1 \ : & M^{\sigma_{min}}_{\tilde{t}_1} < 90 - 93 \text{ GeV}, & M^{\sigma_{max}}_{\tilde{t}_1} < 95 - 96 \text{ GeV}; \\
\tilde{t}_1 \to bl\tilde{\nu} \ : & M^{\sigma_{min}}_{\tilde{t}_1} < 87 - 89 \text{ GeV}, & M^{\sigma_{max}}_{\tilde{t}_1} < 90 - 91 \text{ GeV}; \\
\tilde{t}_1 \to b\tau\tilde{\nu} \ : & M^{\sigma_{min}}_{\tilde{t}_1} < 83 - 88 \text{ GeV}, & M^{\sigma_{max}}_{\tilde{t}_1} < 88 - 91 \text{ GeV}; \\
\tilde{b}_1 \to b\tilde{\chi}^0_1 \ : & M^{\sigma_{min}}_{\tilde{b}_1} < 76 - 83 \text{ GeV}, & M^{\sigma_{max}}_{\tilde{b}_1} < 94 - 97 \text{ GeV}.
\end{array}
$$

For both cases, the *experimentally observed* 95% C.L. mass exclusions are compared to the *expected* ones, which have been obtained from the Monte-Carlo assuming no SUSY particles. The observed exclusions of the squark masses are at the same level as the expected ones.

The obtained 95 % C.L. upper limits on the stop production cross section in the decay $\tilde{t}_1 \to bW\tilde{\chi}^0_1$ are bigger than the corresponding theoretical predictions, so, the exclusion of masses at 95 % C.L. was not possible with the available data sample.

Assuming the topology of decays of the *scalar quarks of the first two generations* to be similar to the two body decay of the stop, the results of the searches for the decay $\tilde{t}_1 \to c\tilde{\chi}^0_1$ have been also used for calculation of the mass exclusion limits for the squarks of the first two families. Two possibilities were considered here: the mass degeneracy between four ($\tilde{u}$, $\tilde{d}$, $\tilde{c}$, $\tilde{s}$) and five ($\tilde{b}$ in addition) squarks. The 95% C.L. exclusion limits on the mass degenerate scalar quarks for the cases of the "right-only" or "left-and-right" eigenstates are the following:

$$
\begin{array}{lll}
\tilde{q} = \tilde{u}\ \tilde{d}\ \tilde{c}\ \tilde{s} : & M_{\tilde{q_R}} < 95 - 96 \text{ GeV}, & M_{\tilde{q_{LR}}} < \ 99 - 100 \text{ GeV}; \\
\tilde{q} = \tilde{u}\ \tilde{d}\ \tilde{c}\ \tilde{s}\ \tilde{b} : & M_{\tilde{q_R}} < 96 - 97 \text{ GeV}, & M_{\tilde{q_{LR}}} < \ 99 - 101 \text{ GeV}.
\end{array}
$$

Using the MSSM assumption about gaugino unification at the GUT scale, the limits on the four mass degenerate squarks have been reinterpreted on the $m_{\tilde{g}}$, $m_{\tilde{q}}$ plane. Moreover, the absolute limit on the MSSM parameter M_2, obtained for $\tan\beta = 4$ from other L3 SUSY searches (for chargino, neutralino and scalar leptons), has been translated into a gluino mass limit. The obtained 95% C.L. exclusions in the $m_{\tilde{g}}$, $m_{\tilde{q}}$ mass plane are

$$M_{\tilde{g}} > 267 - 314 \text{ GeV},$$

$$M_{\tilde{q}} > 99 - 100 \text{ GeV}.$$

Contents

Chapter 1

Introduction

The first ideas of matter composition of some very small "bricks" appeared many centuries ago. In modern Particle Physics, such "basic bricks", which have no further substructure, are called *elementary particles*. Particle Physics investigates their properties and interactions between them.

The theoretical framework of modern Particle Physics is called *Standard Model* (SM). It classifies the elementary particles into two categories: the *fundamental fermions* and the *gauge bosons*. The fermions are grouped into three families of *quarks* and *leptons* and are the basic constituents of matter. There are four types of interactions between the elementary particles: strong, electromagnetic, weak and gravitational. They have different nature and properties and are mediated by *gauge bosons*. The gravitation is too weak in the microscopic world and is not considered in the Standard Model. The formalism of the other three interactions is based on the principle of local gauge invariance of the Lagrangian under certain symmetry transformations.

The electromagnetic interactions are described by the theory of Quantum Electrodynamics (QED), which is based on a $U(1)_{em}$ gauge symmetry group. The electromagnetic interactions affect particles with electrical charge and are mediated by a massless gauge boson, the *photon* γ. The weak interactions affect both quarks and leptons and are mediated by massive vector gauge bosons $W^{\pm}$ and Z^0. Within the Theory of Glashow-Weinberg-Salam, which is based on a $U(1)_Y \times SU(2)_L$ gauge symmetry group, the weak interactions are unified with the electromagnetic ones. The strong interactions are realized by the exchange of massless gluons g and affect quarks and hadron particles composed of them. This force is described by Quantum Chromodynamics (QCD), based on the gauge group $SU(3)_C$. The non-zero mass values of elementary particles in the Standard Model Theory are provided by the so-called *Higgs mechanism of Spontaneous Symmetry Breaking*, which introduces also the *scalar Higgs boson* particle. The theories of the electroweak and the strong interactions together with the Higgs mechanism constitute the Standard Model. This theory is described in **Chapter 2** of this thesis.

The appearance of the Standard Model was a real break-through in Particle Physics. Many experimental confirmations of this theory, especially the discovery of the $W^{\pm}$ and Z^0 bosons in 1983 and the discovery of the top quark in 1995, have made the Standard Model the fundamental theory of elementary particles. But despite of it's numerous experimental confirmations, this theory seems to be not perfect and fully understood.

There are many strong conceptual indications for physics beyond the Standard Model: the *"hierarchy"* and the *"fine tuning"* problems in attempts to extrapolate the SM to the very big energy scales ($\sim 10^{14} - 10^{16}$ GeV), the problem of unification of gauge couplings and interactions at very high energies (the *Grand Unification Theory*, GUT), the desired incorporation of quantum gravity into the theory and others. To solve these problems, several theoretical extensions were proposed, intended both to include the Standard Model itself and to explain it's problematic points. All these questions are considered in **Chapter 3**.

Supersymmetry (SUSY) is one of the most elegant solutions for building a theory beyond the Standard Model. SUSY contains the Standard Model itself and introduces a higher level symmetry between fermions and bosons. New fermions appear as supersymmetric partners for the "ordinary" SM bosons, and new SUSY boson partners are related to the SM fermions. Within Supersymmetry, the "hierarchy" and the "fine tuning" problems are solved due to cancellations of the mass divergences of the scalar fields, the three couplings unify at the GUT scale and there is a way to incorporate quantum gravity. The simplest Supersymmetric model is a generalization of the SM theory with a minimal number of introduced SUSY partners. This theory is called *Minimal Supersymmetric extension of the Standard Model* (the MSSM). It has many parameters, undetermined by the moment. For practical investigations, certain assumptions about them were added and such a scenario of the MSSM is called *the Constrained MSSM* (the CMSSM). After the electroweak symmetry breaking in SUSY, the interaction eigenstates of supersymmetric particles mix and produce the physical eigenstates. For sfermions (scalar partners of SM fermions), this mixing is proportional to the masses of the appropriate SM fermions. Thus, the scalar top $\tilde{t}_1$ and the scalar bottom $\tilde{b}_1$ can be among the lightest SUSY particles within the CMSSM framework. The Supersymmetry Theory and the CMSSM scenario are considered in more details in **Chapter 4**.

The Large Electron-Positron Collider (LEP) at CERN has achieved center-of-mass energies up to 208 GeV. It provided experimental data suitable for new phenomena searches within several theoretical models of modern Particle Physics. Searches for the $\tilde{t}_1$ and the $\tilde{b}_1$ quarks constitute the subject of this thesis. **Chapter 5** describes the phenomenology of scalar quark production in e^+e^- collisions at LEP II. The following decays have been searched for in this analysis: $\tilde{t}_1 \to c\tilde{\chi}^0_1$, $\tilde{t}_1 \to b\ell\tilde{\nu}$ ($\ell = e, \mu, \tau$ with equal branchings), $\tilde{t}_1 \to b\tau\tilde{\nu}$ (dominant decay to τ) and $\tilde{b}_1 \to b\tilde{\chi}^0_1$. The assumed conservation of the *R-parity* quantum number affects the topology of the squark events. It leads to the existence of a stable lightest SUSY particle (LSP), which is the weakly interacting lightest neutralino $\tilde{\chi}^0_1$. This in turn implies the missing energy in the squark decay events, which can be significant depending on the LSP mass. So, the topology of the signal events is two jets + missing energy (+ two leptons for three body stop decays).

In this analysis, the experimental data collected with the L3 Detector in the year 2000 has been used. The overview of the LEP Accelerator and details of the L3 Experimental Setup, as well as the simulation and reconstruction software are described in **Chapter 6**.

Chapter 7 presents the description of features of the simulated squark signal and the Standard Model background processes, the strategy of the search analysis and its procedures.

After the search algorithm is developed and optimized, the search for squarks in the experimental data can be performed. This is described in **Chapter 8**.

Since no evidence for the searched squark signal has been found, the experimental upper limits on the scalar quark production cross section have been derived. Within the CMSSM framework, the cross section limits are interpreted as exclusion limits on masses of the scalar top and the scalar bottom quarks. **Chapter 9** is devoted to the calculation of these limits.

In addition to the considered stop decays, the three body decay $\tilde{t}_1 \rightarrow bW\tilde{\chi}_1^0$ has been analyzed. Because of the phenomenological features of this decay, its analysis slightly differs from the other ones and is described separately in **Chapter 10**.

Chapter 11 compares the results obtained here to the corresponding search results of the other LEP Experiments (ALEPH, DELPHI and OPAL) and to the squark searches at the Tevatron. Future prospects for SUSY quark searches at the LHC and a Linear e^+e^- Collider are also reviewed there.

Chapter 2

The Standard Model of Particle Physics

2.1 Particles, Interactions and Symmetries

Particle Physics describes elementary particles (the basic constituents of matter, which do not have any substructure), their properties and interactions between them.

In Particle Physics, the microscopic objects (the elementary particles, atoms, molecules, etc.) have at the same time the properties of both material substances (particles in the classical sense) and field waves, representing a particle evolution in space and time. From the other side, a particle-like object can be considered as a quantum of the corresponding field; these quanta can be created in vacuum (from the field energy) and destroyed. This concept is the basis of *Quantum Field Theory* [1,2], which describes both particles and fields (both relativistic and non-relativistic) by wave functions $\Psi(x_\mu)$, where $x_\mu = (\vec{x}; t)$ are the space-time coordinates. Interactions between particles and fields are described by a *Lagrangian*, which is constructed from the wave functions:

$$L = E_{kin}\{\Psi(x_\mu)\} - E_{pot}\{\Psi(x_\mu)\}, \tag{2.1}$$

where E_{kin} and E_{pot} are the kinetic and potential field energies correspondingly. Evolution of fields in space-time is given by the *equations of motion*, which are derived using the *Hamiltonian variational principle*:

$$\delta S = 0 \quad \Rightarrow \quad \partial_\mu \frac{\delta L}{\delta(\partial_\mu \Psi)} - \frac{\delta L}{\delta \Psi} = 0, \tag{2.2}$$

where ∂_μ is the partial derivative $\partial/\partial x_\mu$ and the *action* S is defined as

$$S = \int d^4x L(x). \tag{2.3}$$

The interactions between elementary particles are mediated by the interaction field quanta, which in turn represent another kind of elementary particles. In this sense, all the elementary particles are grouped into two types: the basic constituents of matter, called the *fundamental fermions* and the interaction carrier particles, called the *intermediate* *vector bosons*. The fermions have a spin quantum number equal to 1/2 and obey the Fermi-Dirac statistics, while the vector bosons have a spin value of 1 and are described by the Bose-Einstein statistics.

All known interaction forces between the elementary particles, called the *fundamental forces*, are classified into four types: the *electromagnetic* (e.m.), *weak*, *strong* and *gravitational*. Each interaction field has its distinct characteristics, such as type of space-time transformations, a particular set of conservation rules that are obeyed by the interaction and a characteristic coupling constant, whose value determines the magnitude of the corresponding force (and, consequently, the cross sections, decay rates, etc.). The strengths of the fundamental forces (determined by the values of the corresponding coupling constants) are compared in Table 2.1. Note that the gravitational interaction becomes important only at very high mass scales (in astrophysics) and is negligible at the microscopic level, so, it is not accounted for in theory of Particle Physics.

Fundamental Interaction	Strength (arbitrary units)	Range	Acts on particles
strong	1	10^{-15} m	quarks
electromagnetic	$\simeq \frac{1}{137}$	infinite	electrically charged
weak	10^{-5}	10^{-17} m	all
gravitational	$\sim 10^{-39}$	infinite	all

***Table 2.1:** The basic characteristics of the fundamental forces*

The elementary particles have a set of characteristic quantities, called *quantum numbers*, whose values define the particle properties (electrical charge, spin, etc.) and types and properties of the interactions, in which certain particles are involved (lepton and baryon quantum numbers, flavour, etc.). These characteristics and properties serve for classification of the elementary particles.

The symmetries of interactions under various phase or space-time transformations (i.e. such transformations of the wave functions, which leave the Lagrangian *invariant*) are also used for classification of interactions and particles and play an important role in building of the particle theory in general. Such symmetries can be *discrete* (like time inversion or charge conjugation) and *continuous* (like rotation in space, etc.). From the other point of view, the *internal* symmetries (corresponding to phase transformations) can be *global* and *local* (also called *gauge*). Global transformations do not depend on the space-time point coordinates, while local transformations do depend. *Noether's theorem* states a relation between symmetries and conservation laws. The existence of a global symmetry leads to the existence of associated charge and current, which both are conserved. For example, symmetry under space translation leads to momentum conservation and symmetry under time translation is connected to the conservation of energy.

Symmetry is represented mathematically by a corresponding *symmetry group*, a set of irreducible symmetry operators and associated group *generator(s)*, connected with the particle quantum numbers. For example, the electrical charge Q is connected with the $U(1)_{em}$ group generator; the weak isospin operators $T_i = \sigma_i/2$ ($i = 1, 2, 3$; σ_i are the Pauli matrices) are the generators of the symmetry group $SU(2)_L$; and the hypercharge $Y = Q - T_3$ is a generator of the group $U(1)_Y$. Global symmetries describe free particles and correspond to scalar type of the wave functions, while gauge (local) symmetries describe the particle interactions and correspond to wave functions of vector type. Thus, Particle Physics considering the particle interactions is a *gauge field theory.*

The known fundamental fermion fields in Particle Physics are classified according to their quantum numbers as shown in Table 2.2.

Group	H	Family			T_3	Y	Q
		1	2	3			
Leptons $L = 1 \quad B = 0$	-1	$\begin{pmatrix}\nu_e \\ e\end{pmatrix}_L$	$\begin{pmatrix}\nu_\mu \\ \mu\end{pmatrix}_L$	$\begin{pmatrix}\nu_\tau \\ \tau\end{pmatrix}_L$	$1/2$ $-1/2$	$-1/2$ $-1/2$	0 -1
	+1	e_R	μ_R	τ_R	0	-1	-1
Quarks $B = 1/3 \quad L = 0$	-1	$\begin{pmatrix}u \\ d^w\end{pmatrix}_L$	$\begin{pmatrix}c \\ s^w\end{pmatrix}_L$	$\begin{pmatrix}t \\ b^w\end{pmatrix}_L$	$1/2$ $-1/2$	$1/6$ $1/6$	$2/3$ $-1/3$
	+1	u_R d_R	c_R s_R	t_R b_R	0 0	$2/3$ $-1/3$	$2/3$ $-1/3$

Table 2.2: *Classification of the fundamental fermion fields. The presented quantum numbers are: L - the lepton number, B - the baryon number, H - the helicity, T_3 - the third component of the weak isospin, Q - the electrical charge and Y - the hypercharge.*

The fermions are subdivided into two main groups: quarks, which do participate in the strong interactions, and leptons, which do not. Each group has left- and right-handed components distinguished by the *chirality* quantum number, -1 and $+1$, respectively. [1] From another point of view, the fermions are grouped into three families, which are identical in every property, except of the mass. Within each family, the quarks are subdivided into two distinct states, called *up* (u, c and t quarks) and *down* (d, s and b), while leptons are distinguished as neutrinos and e, μ and τ-leptons. The left-handed

---

[1] Note that the existence of only one, left-handed component of neutrino in the Standard Model (as listed in Table 2.2) follows from the assumption that neutrino is strictly massless. However, recent solar and atmospheric neutrino experiments have proved the effect of *neutrino oscillations* from one to another flavour state [1,3]. This implies the *existence of finite non-zero* mass for neutrino [4] (although of a very small value, being within the current limits from accelerator measurements, e.g. $m_{\nu_e} < 3$ eV). In the Standard Model it can be provided by introducing into the theory additional right-haded neutrino component ν_R. But since the neutrino mass does not directly affect the theoretical framework of our analysis, we may *for simplicity* consider it in this thesis as massless and having only the left component.

fermions transform under the weak isospin symmetry group $SU(2)_L$ as doublets

$$f_L = \begin{pmatrix} \nu_i \\ \ell_i \end{pmatrix}, \quad \begin{pmatrix} u_i \\ d_i^w \end{pmatrix}, \tag{2.4}$$

where $i = 1, 2, 3$ is a family index, while the right-handed fermions $f_R = \ell_R^i,\ u_R^i,\ d_R^i$ transform as singlets. The weak eigenstates of the left-handed down-type quarks d_i^w, ($i = 1, 2, 3$ for d^w, s^w and b^w), presented in Table 2.2, correspond to the field wave functions, used in Particle Physics theory, but the real particles, existing in nature and observed (perhaps, indirectly) experimentally, are represented by the mass eigenstates, which are related to the weak ones through the *Cabibbo-Kabayashi-Maskawa* mixing matrix [5]:

$$(d_L^i)^{mass} = \sum_{j=1}^{3} V_{ij}^{CKM} (d_L^j)^{weak}. \tag{2.5}$$

The real fermion particles and their basic properties are listed in Table 2.3. The quark mass values should be considered as approximate because quarks can not be observed directly due to the feature of their confinement. The quark masses can only be estimated by properties of hadron particles composed of them.

Family	Leptons		Quarks	
	particle	mass	particle	mass
1	ν_e	< 3 eV	u	$1.5 - 4.5$ MeV
	e	0.511 MeV	d	$5 - 8.5$ MeV
2	ν_μ	< 0.19 MeV	c	$1.0 - 1.4$ GeV
	μ	105.7 MeV	s	$80 - 155$ MeV
3	ν_τ	< 18.2 MeV	t	174.3 ± 5.1 GeV
	τ	1.777 GeV	b	$4.0 - 4.5$ GeV

Table 2.3: *The fundamental fermions and their masses [4].*

For each fermion particle there is also the corresponding *anti-particle*, which is identical with it in all properties (mass, family, flavour, etc.), but has opposite signs of internal quantum numbers (electrical charge, etc.).

Note also, that atoms are composed of fermions of the first family because they are the lightest and stable (u and d quarks form a nucleon and electrons with nucleon form an atom), while the fermions of the second and third families exist only at high energies (either in star cores and cosmic rays, or are produced in modern accelerator experiments); they are very short-lived and eventually decay to the fermions of the first family.

Each of the three fundamental interactions, considered in Particle Physics (omitting the gravitational one), is described by a gauge quantum field theory, based on a particular gauge symmetry group and its mathematical representations. Theory of *Quantum*

Electrodynamics (QED) is based on the $U(1)_{e.m.}$ gauge group and describes the electromagnetic interactions [2, 6]. *Quantum Chromodynamics* (QCD) corresponds to the strong interactions and is built on the $SU(3)_c$ gauge group [2, 6]. The weak interactions are described by the theory based on the gauge symmetry group $U(1)_Y \times SU(2)_L$ and since the electromagnetic group $U(1)_{e.m.}$ enters here as a subgroup, the electromagnetic and weak interactions are considered as unified on this basis and the theory is called *the Electroweak Theory*, known also as the *Glashow-Weinberg-Salam Standard Model of Electroweak interactions* by names of its authors [7].

The formalism of each of these theories is based on the construction of the gauge-invariant Lagrangian from the particles' and fields' wave functions using the symmetry group generators and in this sense it is common for all of them: for QED, for QCD and for the Electroweak Theory. Let us briefly overview the major building blocks of these theories.

2.2 Quantum Electrodynamics

QED postulates the $U(1)_{e.m.}$ local gauge symmetry as a basic characteristic feature of the electromagnetic interactions. It means that a corresponding gauge phase transformation of the fermion particle wave function $\Psi(x)$

$$\Psi(x) \rightarrow \Psi'(x) = e^{i\theta(x)}\Psi(x) \tag{2.6}$$

must not affect the evolution (equation of motion) of the particle, or, in other words, the fermion Lagrangian must remain invariant under this transformation. Considering the Lagrangian of a *free fermion* (i.e. the fermion having no interactions)

$$L_{free} = \bar{\Psi}(i\gamma^\mu \partial_\mu - m)\Psi, \tag{2.7}$$

where m is the fermion mass and γ^μ are the *Dirac matrices* [1], we realize, that it is *not* invariant under (2.6). To fulfill the requirement of gauge invariance, we have to modify the Lagrangian (2.7) by introducing a vector gauge field $A_\mu(x)$ with the following gauge transformation property:

$$A_\mu(x) \rightarrow A'_\mu(x) = A_\mu(x) + \frac{1}{e}\partial_\mu \theta(x), \tag{2.8}$$

where e is the electrical charge (in units of charge of the positron particle), the parameter connected with the generator of the symmetry group $U(1)_{e.m.}$. Then, replacing the partial derivative ∂_μ by a derivative of the so-called *"covariant form"*

$$D_\mu = \partial_\mu - ieA_\mu(x), \tag{2.9}$$

we obtain the Lagrangian

$$L_{invar.} = \bar{\Psi}(i\gamma^\mu D_\mu - m)\Psi, \tag{2.10}$$

which becomes invariant under the $U(1)_{e.m.}$ transformation (2.6) and corresponds to a fermion, that interacts with the quantum of the electromagnetic field, the *photon* γ.

Adding the kinetic term of the electromagnetic field $-\frac{1}{4}F_{\mu\nu}F^{\mu\nu}$, where $F_{\mu\nu}$ is the strength tensor of the electromagnetic field

$$F_{\mu\nu} = \partial_\mu A_\nu(x) - \partial_\nu A_\mu(x), \tag{2.11}$$

we obtain the complete Lagrangian of the QED Theory:

$$\begin{array}{rcl} L_{QED} & = & \bar{\Psi}(i\gamma^\mu D_\mu - m)\Psi - \frac{1}{4}F_{\mu\nu}F^{\mu\nu} = \\ \text{free fermions} & = & \bar{\Psi}(i\gamma^\mu \partial_\mu - m)\Psi + \\ \text{interaction term} & + & \bar{\Psi}e\gamma^\mu A_\mu \Psi - \\ \text{kinetic energy of e.m. field} & - & \frac{1}{4}F_{\mu\nu}F^{\mu\nu} \ . \end{array} \tag{2.12}$$

From this very brief overview of the QED formalism we see, that the principle of gauge invariance under the $U(1)_{e.m.}$ symmetry group transformations has a great consequence for the theory, because it leads to the appearance of a gauge vector field $A_\mu(x)$, associated with the quantum of the electromagnetic field, the photon, which is responsible for the electromagnetic interactions of fermions.

Note also that the experimentally proved massless of the photon is important for the gauge invariance in the theory (if the photon would have a non-zero mass, then the mass term of type $m^2 A_\mu A^\mu$ breaks the gauge invariance of the QED Lagrangian).

2.3 Quantum Chromodynamics

The theory of strong interactions is based on the more complex gauge symmetry group $SU(3)_c$, where the index c denotes the *color charge* and 3 corresponds to three possible color states of quarks: *red*, *green* and *blue*. But because the principle of the theory construction remains the same - the requirement of gauge invariance under the symmetry transformations, the formalism of QCD has a form very similar to Quantum Electrodynamics.

Since the symmetry group of type $SU(n)$ has $n^2 - 1$ generators, the $SU(3)_c$ has eight generators λ_a $(a = 1, ..., 8)$, called the *Gell-Mann matrices*, and the same number of vector gauge bosons g_a, called *gluons*, which are associated to these group generators. The strong interactions between quarks are mediated by the exchange of gluons, which carry the charges of color.

Experimental observations suggest that quarks do not exist as free, separate particles. The nature of the strong forces is such that quarks are bound into composite particles, consisting of three quarks - *baryons*, or of quark-antiquark pairs - *mesons*. This feature is known as *confinement* of quarks and it was one of the reasons to use the $SU(3)_c$ group as a basis for QCD. Within the framework of Quantum Chromodynamics quarks are triplets of the $SU(3)_c$ gauge group

$$q = \begin{pmatrix} q_1 \\ q_2 \\ q_3 \end{pmatrix}, \tag{2.13}$$

while mesons and baryons are color singlets

$$M = \sum_i \bar{q}_i q^i, \tag{2.14}$$

$$B = \sum_{ijk} \varepsilon^{ijk} q_i q_j q_k, \tag{2.15}$$

where the indices $i, j, k = 1, 2, 3$ run over the three color states of quarks and ε^{ijk} is the completely antisymmetric *Levi-Civita* tensor.

The transformation corresponding to the color symmetry of the $SU(3)_c$ gauge group is

$$q(x) \to q\,'(x) = e^{i\frac{\lambda_a}{2}\theta^a(x)} q(x) \tag{2.16}$$

and the requirement of gauge invariance of the QCD Lagrangian under (2.16) leads to the introduction of gauge gluon fields G^a_μ of strong interaction with transformation rule

$$G^a_\mu \to G'^a_\mu = G^a_\mu + \frac{1}{g_3}\partial_\mu \theta^a(x) + f^{abc}\theta^b(x) G^c_\mu, \tag{2.17}$$

where g_3 is the strong coupling constant (frequently denoted also as g_3) and f^{abc} $(a = 1, ..., 8)$ are the structure constants of the $SU(3)_c$ group. The covariant derivative has the following form:

$$D_\mu = \partial_\mu + i g_3 \frac{\lambda_a}{2} G^a_\mu. \tag{2.18}$$

Then the gauge invariant Lagrangian of QCD appears (in the form similar to the L_{QED}):

$$L_{QCD} = \sum_i \bar{q}_i (i\gamma^\mu D_\mu - m_i) q_i - \frac{1}{4} F^a_{\mu\nu} F^{\mu\nu}_a, \tag{2.19}$$

where $F^a_{\mu\nu}$ is the gluon field strength tensor

$$F^a_{\mu\nu} = \partial_\mu G^a_\nu - \partial_\nu G^a_\mu + g_3 f^{abc} G^b_\mu G^c_\nu. \tag{2.20}$$

Despite of the formal similarity of the QED and QCD Lagrangians, there is an important difference: the gluon kinetic term $-1/4 F^a_{\mu\nu} F^{\mu\nu}_a$ contains three- and four-gluon terms, which correspond to the self-interaction gluon vertices. This is not the case for the gauge boson of QED: photons do not carry electrical charge and do not interact (couple) to each other.

2.4 The Electroweak Theory

The formalism of the Electroweak Theory is similarly built on requirement of the gauge invariance of Lagrangian under the $U(1)_Y \times SU(2)_L$ symmetry group transformations. The structure of the EW Theory is defined by the properties of this symmetry group.

Four vector gauge boson fields appear here. One of them, B_μ, is associated with generator of the $U(1)_Y$ group, the hypercharge Y. Three others, W^i_μ $(i = 1, 2, 3)$, are related to the $SU(2)_L$ generators, the weak isospin T_i $(i = 1, 2, 3)$. The $SU(2)_L$ subgroup of the EW gauge group implies symmetry of the Lagrangian under the following transformations:

$$f_L \to f'_L = e^{i\,\vec{T}\vec{\theta}(x)} f_L, \tag{2.21}$$

$$f_R \to f_R, \tag{2.22}$$

where the left-handed fermion component transforms as doublet (2.4); the transformations corresponding to the $U(1)_Y$ EW subgroup are (here fermions transform as singlets)

$$f \to f' = e^{iY\alpha(x)} f. \tag{2.23}$$

The transformation rules for the vector gauge bosons B_μ and $\vec{W}_\mu$ correspond to the structure of the EW subgroups, to which they belong: B_μ transforms under $U(1)_Y$ and $\vec{W}_\mu$ under $SU(2)_L$ as

$$B_\mu \to B'_\mu = B_\mu - \frac{1}{g_1}\partial_\mu \alpha(x), \tag{2.24}$$

$$W^i_\mu \to W'^i_\mu = W^i_\mu - \frac{1}{g_2}\partial_\mu \theta^i(x) + \varepsilon^{ijk}\theta^j(x) W^k_\mu, \tag{2.25}$$

where g_1 and g_2 are the correspondent gauge coupling constants.

The covariant derivative takes the form

$$D_\mu = \partial_\mu - ig_1 Y B_\mu - ig_2 \vec{T}\vec{W}_\mu \tag{2.26}$$

and the kinetic (self-interaction) terms for the e.m. and weak gauge fields are correspondingly

$$-\frac{1}{4}B_{\mu\nu}B^{\mu\nu} \tag{2.27}$$

and

$$-\frac{1}{4}\vec{W}_{\mu\nu}\vec{W}^{\mu\nu}, \tag{2.28}$$

where

$$B_{\mu\nu} = \partial_\mu B_\nu - \partial_\nu B_\mu, \tag{2.29}$$

$$\vec{W}_{\mu\nu} = \partial_\mu \vec{W}_\nu - \partial_\nu \vec{W}_\mu + g_2 \vec{W}_\mu \times \vec{W}_\nu. \tag{2.30}$$

Then the $U(1)_Y \times SU(2)_L$ gauge invariant Lagrangian of the Electroweak Theory appears in the following form:

$$L_{EW} = \sum_f \bar{f} i\gamma^\mu D_\mu f - \frac{1}{4}B_{\mu\nu}B^{\mu\nu} - \frac{1}{4}\vec{W}_{\mu\nu}\vec{W}^{\mu\nu}. \tag{2.31}$$

The vector gauge bosons (B_μ and $\vec{W}_\mu$) until here correspond to the interaction eigenstates, which after rotation to the physical basis become the photon field A_μ and two charged $W^\pm_\mu$ and one neutral Z^0 electroweak bosons. The relation between the interaction and the physical eigenstates reads as

$$W^\pm_\mu = W^1_\mu \pm iW^2_\mu \tag{2.32}$$

and

$$\begin{pmatrix} Z_\mu \\ A_\mu \end{pmatrix} = \begin{pmatrix} \cos\theta_w & -\sin\theta_w \\ \sin\theta_w & \cos\theta_w \end{pmatrix} \begin{pmatrix} W^3_\mu \\ B_\mu \end{pmatrix}, \tag{2.33}$$

where θ_w is a characteristic mixing angle of the neutral weak boson sector called *the Weinberg angle* and defined through the gauge coupling constants g_1 and g_2 as

$$\cos\theta_w = \frac{g_1}{\sqrt{g_1^2 + g_2^2}}. \tag{2.34}$$

After the transformation of the vector gauge bosons to the physical basis, the Lagrangian (2.31) can be rewritten in the form where the electroweak interactions between fermions are given by separate terms:

$$\begin{array}{rcl} L_{EW} & = & \\ \text{free fermions} & = & \sum\limits_f \bar{f} i\gamma^\mu \partial_\mu f - \\ \text{e.m. interactions} & - & \sum\limits_f \bar{f} e Q_f \gamma^\mu A_\mu f - \\ \text{weak neutral-current int.} & - & \sum\limits_f \bar{f} \frac{g_2}{2\cos\theta_w} \gamma^\mu (g_V - g_A \gamma^5) Z_\mu f - \\ \text{weak charge-current int.} & - & \sum\limits_f \bar{f}_L \frac{g_2}{\sqrt{2}} \gamma^\mu (\sigma_+ W_\mu^+ + \sigma_- W_\mu^-) f_L \ , \end{array} \tag{2.35}$$

where Q_f is the electrical charge of particular fermion f (in units of the positron charge); $g_V = T_f^3 - 2Q_f \sin^2\theta_w$ and $g_A = T_f^3$ are the coupling constants corresponding to the parts of the weak neutral-current interactions, which transform as vector and axial vector, respectively; the matrices $\sigma_\pm = 1/2(\sigma_1 \pm i\sigma_2)$ realize the transformations between up- and down-type fermions which occur in the weak charged-current interactions.

2.5 The Standard Model

Now, after consideration of each of the interactions separately - the electromagnetic, electroweak and strong, we can briefly summarize their basic components as shown in Table 2.4.

Fundamental Interaction	Symmetry Group	Group Generators	Gauge Couplings	Gauge Fields
Electroweak	$U(1)_Y$	Y	g_1	B_μ
	$SU(2)_L$	T^i $(i = 1, 2, 3)$	g_2	W_μ^i $(i = 1, 2, 3)$
Strong	$SU(3)_c$	λ_a $(a = 1, ..., 8)$	g_3	G_μ^a $(a = 1, ..., 8)$

Table 2.4: *Summary of gauge symmetry properties of the electromagnetic, weak and strong interactions.*

The neutral leptons (neutrinos) undergo only the weak interactions since they have neither electrical nor strong (color) charges. The charged leptons are involved in both electromagnetic and weak interactions. But quarks do participate in all interactions, in electroweak and strong. Thus, we need to consider all interactions together and for this purpose we combine the $SU(3)_c$ gauge group of QCD with the $U(1)_Y \times SU(2)_L$ symmetry group of the Electroweak Theory into one gauge group $U(1)_Y \times SU(2)_L \times SU(3)_c$ and require the corresponding gauge invariance of Lagrangian of such combined theory.

The group generators, the associated gauge boson fields and the gauge coupling constants remain the same as in the separate QCD and EW theories and the fermion and gauge boson fields transformation rules and the covariant derivative also appear as corresponding combinations:

$$f(x) = f'(x) = V(x)f(x), \tag{2.36}$$

where

$$V(x) = exp\{\frac{i}{2}(Y\alpha(x) + \vec{\sigma}\vec{\beta}(x) + \lambda_a\theta^a(x))\}, \tag{2.37}$$

$$B_\mu \to B'_\mu = VB_\mu V^{-1} + \frac{i}{g_1}(\partial_\mu V)V^{-1}, \tag{2.38}$$

$$\vec{W}_\mu \to \vec{W}'_\mu = V\vec{W}_\mu V^{-1} + \frac{i}{g_2}(\partial_\mu V)V^{-1}, \tag{2.39}$$

$$G^a_\mu \to G'_\mu = VG^a_\mu V^{-1} + \frac{i}{g_3}(\partial_\mu V)V^{-1} \tag{2.40}$$

and covariant derivative

$$D_\mu = \partial_\mu - ig_1 Y B_\mu - ig_2\vec{T}\vec{W}_\mu + ig_3\frac{\lambda_a}{2}G^a_\mu. \tag{2.41}$$

The gauge invariant Lagrangian gets the form similar to the QCD and EW Lagrangians with presence of both the QCD and the EW kinetic terms:

$$L_{SM} = \sum_f \bar{f}i\gamma^\mu D_\mu f - \frac{1}{4}B_{\mu\nu}B^{\mu\nu} - \frac{1}{4}\vec{W}_{\mu\nu}\vec{W}^{\mu\nu} - \frac{1}{4}F^a_{\mu\nu}F^{\mu\nu}_a. \tag{2.42}$$

The constructed in such way theory based on the combination of the QCD and EW gauge symmetry groups $U(1)_Y \times SU(2)_L \times SU(3)_c$, together with described above classification of the fermions and the introduced vector gauge boson fields / particles by requirement of the gauge invariance is called *Standard Model of Elementary Particles and Fundamental Interactions* (SM in short) [1,7].

It should be noted here that initially the term "Standard Model" has appeared as a title of the Glashow-Weinberg-Salam model of the electroweak interactions and in early literature authors may call by the Standard Model the EW Theory. Keeping in mind that this is just a subject of convention, in this thesis I call with the Standard Model term a theory of combined gauge symmetry group $U(1)_Y \times SU(2)_L \times SU(3)_c$.

One very important point in this combined group is the fact that junction of the EW and the QCD symmetry groups into one *does not mean unification of the strong and electroweak interactions* similarly to unification of the electromagnetic and weak interactions in combined EW group $U(1)_Y \times SU(2)_L$, because the EW unification is caused by the mixing of the electromagnetic and weak field components B_μ and W^3_μ in building of the physical gauge boson fields A_μ and Z^0_μ.

2.6 EW Symmetry Breaking and Higgs Mechanism

The SM Lagrangian, as well as the QCD and the EW Lagrangians, have been considered with absence of fermion and boson mass terms of type $m_f \bar{f} f$, $m_B B_\mu B^\mu$ ($m_A A_\mu A^\mu$), $m_W W_\mu^{i(\pm)} W^\mu_{i(\pm)}$, etc, which would break the gauge invariance of these Lagrangians. Thus, to preserve the invariance of the Standard Model, one should assume massless elementary particles, which is obviously not the case in nature according to our experimental knowledge: only photon and gluons are massless (about the neutrino mass see footnote at page 6).

The simplest possibility to introduce particle masses in the theory in a way which allows to keep at the same time its gauge invariance, is the so-called *Higgs mechanism of Spontaneous (EW) Symmetry Breaking* (SSB for shortness) [1,2,8]. The term "Spontaneous Symmetry Breaking" denotes the situation, when system with interactions (and, correspondingly, the Lagrangian) possess a symmetry, but its vacuum state (minimum of its potential) does not. The *Goldstone Theorem* proves, that in the case of SSB additional scalar boson particles (called *Goldstone bosons*) must exist and their interactions with vector gauge bosons provide them with masses. In the case of the gauge (SM) theory, we need to introduce for this purpose a scalar boson field, called *Higgs field*. The simplest possibility for the Higgs field is a complex scalar $SU(2)_L$ doublet

$$\Phi = \begin{pmatrix} \phi^+ \\ \phi_0 \end{pmatrix} \tag{2.43}$$

with four real components ϕ_k ($k = 1, ..., 4$)

$$\phi^+ = \phi_1 \pm i\phi_2, \tag{2.44}$$

$$\phi_0 = \phi_3 \pm i\phi_4 \tag{2.45}$$

and with hypercharge $Y(\Phi) = 1$. The renormalizable form of the potential for this field is

$$V(\Phi) = \lambda(\Phi^\dagger\Phi)^2 - \mu^2\Phi^\dagger\Phi, \tag{2.46}$$

where $\lambda > 0$ and μ^2 are the model parameters. The shape of the minimum of the potential $V(\Phi)$, corresponding to the vacuum state, depends on the sign of μ^2:

- in the case $\mu^2 < 0$, the vacuum $< 0 \,|\Phi|\, 0 >= 0$ is symmetric under $U(1)_Y \times SU(2)_L$ and there is no SSB, as shown in Figure 2.1, a);
- if $\mu^2 > 0$, then the vacuum is

$$< 0 \,|\Phi|\, 0 >= \begin{pmatrix} 0 \\ \frac{v}{\sqrt{2}} \end{pmatrix}, \tag{2.47}$$

  where the parameter $v = \mu/\sqrt{\lambda}$ is called the *vacuum expectation value* (v.e.v.) and is given by $v = (\sqrt{2}G_F)^{-1/2} \simeq 246$ GeV (G_F is the Fermi constant, $G_F \simeq 1.16 \times 10^{-5}\ GeV^{-2}$). The value of $arg(\Phi)$ is no fixed, so there can be an infinite number of particular vacuum states as shown in Figure 2.1, b). Once for $arg(\Phi)$ a particular value is chosen, the symmetry becomes spontaneously broken.

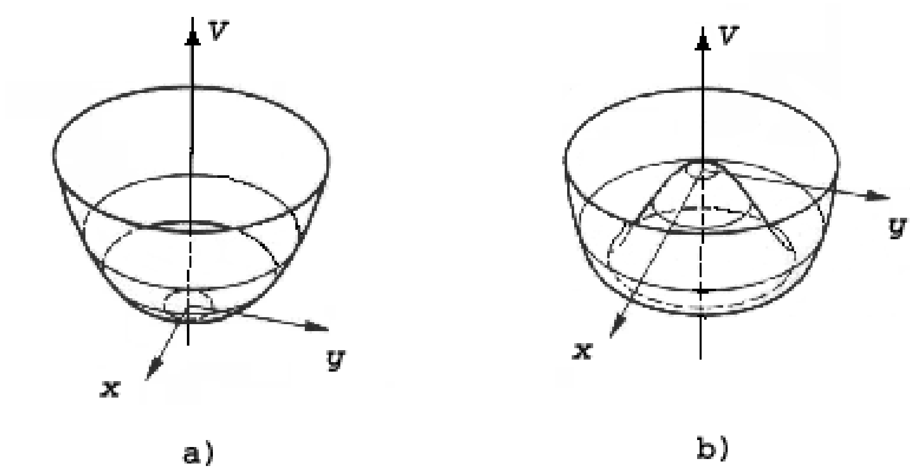

Figure 2.1: *The shape of the minimum of the Higgs potential* $V(\Phi)$*: a) for* $\mu^2 < 0$ *and b) for* $\mu^2 > 0$.

Now the corresponding Lagrangian of the SM, which contains particle masses and keeps the gauge invariance, takes the form

$$L_{SM} = L_{ferm} + L_{gauge} + L_{SSB} + L_{YW}, \tag{2.48}$$

where the components are: L_{ferm} - fermion part (including fermion interactions), L_{gauge} - gauge self-interaction part, L_{SSB} - symmetry breaking and L_{YW} - so-called *Yukawa Lagrangian*,

$$L_{ferm} = \sum_f \bar{f} i \gamma^\mu D_\mu f, \tag{2.49}$$

$$L_{gauge} = -\frac{1}{4} B_{\mu\nu} B^{\mu\nu} - \frac{1}{4} \vec{W}_{\mu\nu} \vec{W}^{\mu\nu} - \frac{1}{4} F^a_{\mu\nu} F^{\mu\nu}_a, \tag{2.50}$$

$$L_{SSB} = (D_\mu \Phi)^\dagger (D^\mu \Phi) - V(\Phi), \tag{2.51}$$

$$L_{YW} = \lambda_e \bar{\ell}_L \Phi e_R + \lambda_u \bar{q}_L \tilde{\Phi} u_R + \lambda_d \bar{q}_L \Phi d_R + (2^{nd}\ and\ 3^{rd} families) + h.c., \tag{2.52}$$

where ℓ_L and q_L are the left-handed lepton and quark $SU(2)_L$ doublets given by (2.4) and ℓ_R and q_R are the right-handed singlets and $\tilde{\Phi} = i\sigma_2 \Phi^*$. The L_{SSB} component corresponds to Higgs interactions with the gauge vector fields $W^\pm$ and Z^0, while L_{YW} contains Higgs interactions with fermion fields.

After a particular vacuum state has been fixed by choosing $arg(\Phi)$ and the symmetry has been broken, the physical spectrum of particles is built according to the Goldstone approach by "small quantum phase excitations" around this vacuum, which cost no energy. The $\Phi(x)$ field can be rewritten in the form

$$\Phi(x) = exp\{\frac{i\vec{\sigma}\vec{\xi}(x)}{\upsilon}\}\left(\begin{array}{c} 0 \\ \frac{\upsilon+H(x)}{\sqrt{2}} \end{array}\right), \tag{2.53}$$

where $\vec{\xi}(x)$ and $H(x)$ are these “small excitation” fields. The first one, $\vec{\xi}(x)$, corresponds to the ϕ_1, ϕ_2 and ϕ_3 components of the introduced Higgs field $\Phi(x)$ and is unphysical, because it can be eliminated by gauge transformations. The second one, $H(x)$, is associated with the forth component ϕ_4 of $\Phi(x)$ and corresponds to the physical Higgs particle.

Now the fermion and gauge boson mass terms appear in the L_{SSB} and L_{YW} components of the SM Lagrangian:

$$(D_\mu\Phi)^\dagger(D^\mu\Phi) = m_W^2 W_\mu^+ W_-^\mu + \frac{1}{2}m_Z^2 Z_\mu Z^\mu + ... \tag{2.54}$$

$$V(\Phi) = \frac{1}{2}m_H^2 H^2 + ... \tag{2.55}$$

$$L_{YW} = m_e\bar{e}_L e_R + m_u\bar{u}_L U_R + m_d\bar{d}_L d_R + ... \tag{2.56}$$

with the particle mass values

$$m_W = \frac{\upsilon}{2}g_2, \tag{2.57}$$

$$m_Z = \frac{\upsilon}{2}\sqrt{g_1^2 + g_2^2}, \tag{2.58}$$

$$m_f = \frac{\upsilon}{\sqrt{2}}\lambda_f \quad (f = e, u, d, ...), \tag{2.59}$$

$$m_H = \mu\sqrt{2}, \tag{2.60}$$

$$m_g = m_\gamma = 0 \tag{2.61}$$

and

$$m_W/m_Z = \cos\theta_w. \tag{2.62}$$

Note, that the parameters λ and μ are undetermined in the theory and so, the Higgs boson mass m_H must be determined experimentally.

It is also important to mention, that the Higgs mechanism of Spontaneous EW Symmetry Breaking is one of the best theoretical models of masses origin, and usually it is considered as a part of the Standard Model framework.

Now, the basic properties (including mass) of the vector gauge boson particles of the Standard Model can be summarized as shown in Table 2.5.

Interaction	Boson	Q	Mass
E.m.	γ	0	0
Weak	$W^{\pm}$	± 1	80.4 GeV
	Z^0	0	91.2 GeV
Strong	g	0	0

Table 2.5: *Basic properties of the Standard Model vector gauge boson particles [4].*

2.7 Experimental Confirmations of the SM

The Standard Model is not only the most complete theory of Particle Physics available at the moment, but also is the most successfully tested in many experiments.

Not only the existence of the gauge vector bosons $W^{\pm}$ and Z^0 has been predicted by the theory, but their masses have been at a good level of accuracy calculated and then confirmed experimentally, first, indirectly, through measurement of the fine structure constant α, the Fermi constant G_F and the Weinberg angle θ_w [9], and, finally, through their direct observation in CERN experiments in 1983 [1, 10]. Existence of the gauge bosons of strong interactions, the gluons, was demonstrated experimentally at DESY in 1979 [11].

Another important part of the SM, the fermion family content, has been built on the information from several experiments, which discovered heavy elementary and composite resonance particles. The τ-lepton has been discovered at SLAC [12]. The c-quark has been discovered in a SPEAR experiment at SLAC and independently at Brookhaven Laboratory in 1974 by detection of the J/Ψ meson, composed of $c\bar{c}$ pair [13]. The more heavy b-quark has been found at Fermilab in 1977 by observation of the Υ-mesons ($b\bar{b}$ resonance) and this was the discovery of the *third family of quarks* [14]. Finally, the heaviest quark, the top, has been discovered at Fermilab in 1994 [15] and so, the whole fermion family has obtained complete experimental confirmation.

The only key particle in the Standard Model, which is still to be discovered experimentally, is the Higgs scalar boson. One of the difficulties here is the fact, that its mass is not predicted theoretically. Another point is, that its mass can be larger than accessible at the current e^+e^- experiments ($\sqrt{s} < 209$ GeV at LEP) or the cross section of Higgs production at a $p\bar{p}$ collider (at Fermilab), where the available energy is higher (up to 1.8 TeV), can be very small. Therefore, due to very high rates of background processes, very large luminosities may be needed for the Higgs discovery. Nevertheless, the theory gives an upper bound on the possible Higgs mass ($m_H \leq 1$ TeV) and current experiments have set the experimental lower limit of 114.4 GeV (LEP, [16]). So, the Higgs discovery is a one of the main goals of the modern and future accelerator experiments (at Tevatron, Fermilab and LHC, CERN).

Chapter 3

Theory Developments Beyond the Standard Model

3.1 Problems of the Standard Model

Although the Standard Model is successfully confirmed in many experiments, there are numerous questions, which can not be answered by the SM, and various conceptual indications that it is not the "ultimate theory of everything".

All these questions and indications arise both from various purely theoretical aspects and from several kinds of experimental evidences, and they can be related to several topics: understanding of existing symmetries and parameters, extrapolation of the theory to the very big energy scales, unification of interactions and gravity incorporation, astrophysics and cosmology, etc.

First, the fermion classification and interactions via the gauge vector bosons are well described by the gauge symmetry group $U(1)_Y \times SU(2)_L \times SU(3)_c$, but the origin of this group is not completely understood. Another question is: is there a symmetry between the three fermion families and if so, why is it broken ? Are there more symmetries between particles in nature ?

The origin of the fermion and boson masses is well described theoretically by the Higgs mechanism of the EW symmetry breaking. However, the negative results of all modern experimental searches for the Higgs particle allow one to hesitate, is there an alternative mechanism of the mass origin. Moreover, the deeper understanding of the particles mass spectrum (why it is exactly so and why it is so wide: from 0.5 MeV up to 175 GeV ?) would be very desirable.

Next, the Standard Model depends on nineteen arbitrary parameters: the three gauge couplings g_1, g_2 and g_3 of the $U(1)_Y \times SU(2)_L \times SU(3)_c$ group; the nine quark and charged-lepton mass values; the two parameters μ^2 and λ, which determine the mass and self-interactions of the scalar Higgs boson; the three angles and one phase that specify the quark mixing matrix and an additional phase θ_{QCD} that characterizes the QCD vacuum state. In a satisfactory theory these parameters should not appear as absolutely free, and there should be a way to understand their values and to establish relations between them.

Another important topic is the problem of gravitational interactions. The ultimate theory should incorporate this fourth interaction, especially when the theory starts to consider the very big energy scales (of the order of the Planck energy $E_p = \sqrt{\hbar c^5/G_N} \simeq 10^{19}$ GeV; here G_N is the Newton constant, $G_N \simeq 10^{-38}\ GeV^{-2}$), where gravity becomes important and can not be neglected, since the strength of the gravitational interactions grows quadratically with energy. However, building a consistent *quantum* theory of gravity remains a hard problem, because it results not in a renormalizable theory.

An important question is also why the electromagnetic and the weak interactions are unified in the Standard Model, but the strong one is not unified with the electroweak. Could it happen that they unify at very high energy scales (of the order of the Planck energy) ?

These two last topics are the starting point for the so-called *Grand Unification Theory* (GUT) approach [17], where the three gauge coupling constants are thought to unify at a large energy scale and thereby provide the basis for understanding of the common origin of all interactions (perhaps three, but hopefully the gravity can appear also on this basis). In the Standard Model the dependence of the gauge couplings on the energy scale appears due to radiative corrections and is accounted for by the *Renormalization Group Equations* (RGEs). The calculations show that the three gauge couplings approach each other at the energy scale $E_{GUT} \sim 10^{14} - 10^{16}$ GeV. However, the unification of them does not really occur with the particle content of the Standard Model alone. This makes it possible to assume that the Standard Model is an effective theory which is valid up to some energy scale cut-off Λ, beyond which a more general theory appears, and in this sense the SM is a low-energy approximation of a more general theory. One may feel tempted to associate Λ with the Planck or GUT scale values and to incorporate the SM into a more general theory just by extrapolating it up to the GUT/Planck scale. However, this attempt causes the so-called *"hierarchy"* (or *"naturalness"*) problem [18], i.e. the Higgs mass parameter tends to grow significantly due to the radiative corrections from self-interactions, fermion and W-boson loops:

$$\Delta m_H^2 \sim O(\frac{\lambda}{4\pi})^2 \int\limits_0^\Lambda \frac{d^4k}{k^2} \sim O(\frac{\lambda}{4\pi})^2 \Lambda^2, \tag{3.1}$$

where λ is the fermion (boson) trilinear coupling to the Higgs field. Indeed, if we assume $\Lambda \simeq E_{GUT}$ (or $\Lambda \simeq E_P$), then the quantum corrections (3.1) become much larger than the physical value of the Higgs boson mass itself ($m_H \sim 10^2$ GeV). This, in turn, makes $W^\pm$ and Z^0 bosons also very heavy at the order of the GUT/Planck scales. To keep m_H (i.e. the radiative corrections) small with rise of the energy scale requires an unnatural re-adjustment of the model parameters when going to the high scales, known as *"fine tuning"* procedure. This is a rather unsatisfactory situation and obviously a more elegant solution would be some theoretical principle allowing the Higgs mass corrections to remain of the order of its physical scale.

There are several more questions to the Standard Model, coming from the neutrino experiments, top quark physics, non-accelerator experiments, cosmology, etc.

For example, the neutrino oscillations and the possibility for the ν to have a very small but non-zero mass leads to the introduction of at least seven more parameters in the theory: three neutrino masses, three mixing angles and a CP-violating phase. Cosmological inflation implies at least one new mass scale of order 10^{16} GeV; the cosmological baryon asymmetry also introduces additional parameters.

3.2 Main Scenarios Beyond the Standard Model

All these questions and problems have made it necessary to consider the development of a framework *beyond the Standard Model* (these theories are denoted as BSM [19, 3]). Several alternative BSM models have been built so far based on the ideas of solving one or another particular difficulty of the Standard Model.

Attempts to extrapolate the SM to very big energy scales, to introduce the unification of interactions and at the same time to avoid the "hierarchy" problem have lead to several GUT theories [17], based on the idea of existence of one gauge symmetry group G of higher symmetry order, corresponding to all interactions unified together at high E scale, which breaks down to the SM symmetry group at scale $m_U \gg m_Z$:

$$G_{GUT} \overset{m_U}{\longmapsto} G_{SM} \equiv U(1)_Y \times SU(2)_L \times SU(3)_c \overset{m_Z}{\longmapsto} U(1)_{e.m.} \times SU(3)_c \tag{3.2}$$

There are several possibilities within the GUT approach, which are based on various kinds of the higher order gauge group: $SU(5)$, $SO(10)$, etc.

Another BSM scenario is a theory called *Technicolor* (TC) [20], which is based on the assumption that the energy cut-off parameter Λ is not of the order of the GUT/Planck scale, but is located somewhere slightly above the Fermi scale $G_F^{-1/2} \simeq 300$ GeV. Then the electroweak symmetry breaking scenario can be considered in an alternative way: the SM Higgs scalar field can be replaced by some fermion condensate, introduced by a new strong interaction near the Fermi scale. The Technicolor Theory adds a gauge symmetry group $SU(N)_{TC}$ to the SM symmetry groups with corresponding coupling constant g_{TC} and an additional generation of fermion particles, called *technifermions*. This alternative to the Higgs mechanism approach has the advantage that the "hierarchy" problem is solved simply by avoiding the Higgs particle. But it also has the disadvantage that fermion masses and mixings are not reproduced. Several further model scenarios within TC are being developed in order to account for the fermion spectrum and so, the TC Theory is not yet built in a fully consistent way and is still under investigations.

Completely different kind of BSM concept is *String Theory*, or the *Theory of Extra Dimensions* [1]. It is based on the idea of representing particles by string-like extended objects (with size of order of 10^{-35} m) instead of considering them as point-like. The matter particles (the fermions) are being considered as closed strings (loops), while the interaction particles (the gauge bosons) as open ones, corresponding to the finite nature of the interactions instead of the point-like. This allows to avoid divergences in the construction of a quantum theory of gravity and so, to incorporate the gravitational interactions into Quantum Particle Physics. The requirement of renormalizability of the theory leads to the introduction of additional dimensions (at least 6 more) to the usual space-time, but this does not cause serious problems because they are considered as "curled up" or, compacted within size

$$\ell_P = \frac{\hbar}{cE_P} \sim 10^{-35}m. \tag{3.3}$$

Note also, that the gravitational interactions are considered as corresponding to strings in these additional ("transverse" to the usual space-time) dimensions and therefore, not present in the Standard Model. The String Theory is a rapidly developing approach and several scenarios are being considered.

For completeness we should also mention another model - the *Leptoquark Theory* [21], which proposes to consider the SM fermions as not really elementary particles, but as composed of even smaller ones (similarly to the composedness of mesons and baryons in terms of quarks).

But among all of the possible theories beyond the Standard Model the most elegant, well developed and self-consistent one is a theory called *Supersymmetry* (SUSY in short) [1, 22, 23]. It introduces a new additional symmetry between fermions and bosons, i.e. introduces an additional scalar partner particle to each of the SM fermions and an additional fermion partner to each of the SM gauge bosons. Moreover, many of the considered above BSM concepts can be also included in the SUSY framework (e.g. unification at the GUT scale, gravity and strings, etc.) Therefore, Supersymmetry is not an alternative theory to the above models, but is a more general one.

However, none of the theories beyond the Standard Model have been experimentally confirmed at the moment. All of them are currently under intense theoretical development and are being actively searched for in the modern experiments. Experimental searches for the Supersymmetry partners of the SM quarks form the subject of this thesis.

Chapter 4

Supersymmetry

4.1 Basic Concepts and Advantages of SUSY

In 1928, P.A.M. Dirac had incorporated the symmetries of the Lorenz group into quantum mechanics and as a natural consequence of this he had found that for each known particle there should be a partner particle, which is known now as antiparticle. In a similar manner, the Theory of Supersymmetry introduces a new symmetry in Particle Physics called *supersymmetry*, which links fermions and bosons by placing them into one representation of supersymmetric algebra called *supermultiplet*. The symmetry transformations between fermions and bosons are realized via so-called spin-1/2 operators S_α (where α is a spinorial index). These operators are of fermionic character and together with the Poincare group they constitute the Supersymmetry algebra [24]. And similarly to the particle-antiparticle symmetry, incorporation of the boson-fermion symmetry into the Particle Physics again leads to the prediction of existence of partner particles (called *SUSY partners* or *sparticles*) for all known Standard Model particles.

The beauty of the idea of a symmetry between fermions and bosons is not the only motivation for SUSY. Another SUSY benefit is that introducing of supersymmetric algebra in the theory provides an elegant solution for the main theoretical difficulties of the Standard Model: the “hierarchy” problem in extrapolation to the high energy scales, the unification of interactions at the GUT/Planck scale and the incorporation of gravitational interactions into Particle Physics.

Indeed, the introduction of SUSY partners to each of the SM particles means, that for each loop of the quantum corrections to the Higgs boson mass (Figure 4.1) a corresponding loop of the SUSY partner particle is added. Then, since the fermion and boson loops have opposite signs, each sparticle loop will compensate the correction from the corresponding SM particle and the quadratic divergences in (3.1) become canceled [25]:

$$\Delta m_H^2 = (\frac{\lambda_b}{4\pi})^2(\Lambda^2 + m_b^2) - (\frac{\lambda_f}{4\pi})^2(\Lambda^2 + m_f^2) = O(\frac{\lambda}{4\pi})^2 \| m_b^2 - m_f^2 \|, \tag{4.1}$$

where m_f and m_b are the fermion and boson masses and $\lambda_f = \lambda_b = \lambda$ is the universal fermion and boson coupling to the scalar Higgs field.

Next, introduction of new SUSY particles in the theory affects the evolution of the gauge couplings with the energy scale. If we assume that masses of scalar partners to

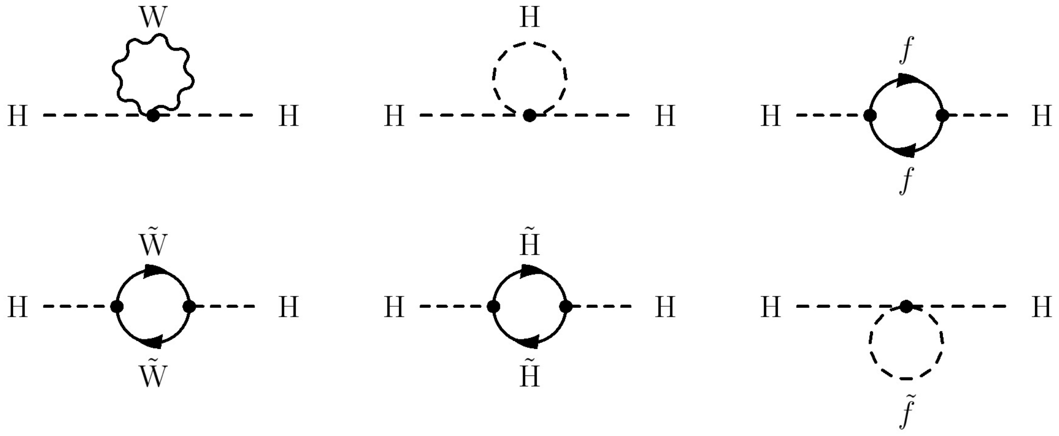

Figure 4.1: *One-loop quantum corrections to m_H^2 within the Standard Model only (upper row) and in Supersymmetry (upper and lower rows together). The SUSY loops (lower row) compensate corresponding corrections of the Standard Model.*

the SM fermions are of the order of 10^2 GeV and modify the Renormalization Group Equations (RGE) accordingly, then the running gauge couplings can really meet in a single point at a scale of $\sim 10^{16}$ GeV [26] as shown in Figure 4.2. Thus, SUSY makes a significant step toward the Grand Unification Theory framework.

Finally, being realized locally, SUSY naturally accommodates Einstein's General Theory of Relativity [27] and postulates gravity as an interaction mediated by gauge bosons called *gravitons*. Thus, the concept of SUSY can be a step towards a theory of all interactions.

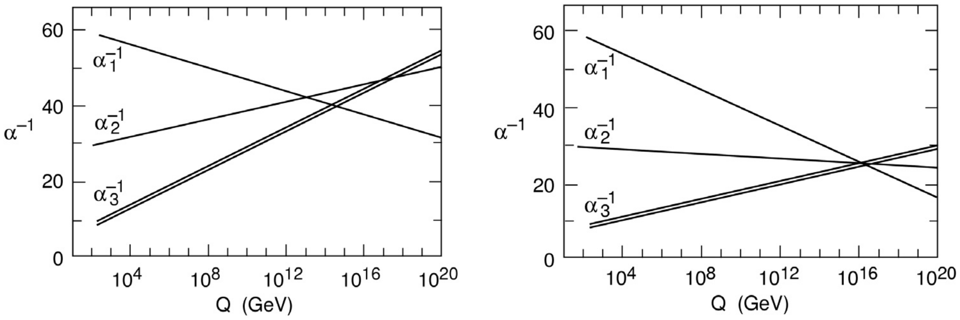

Figure 4.2: *Evolution of the $U(1)_Y \times SU(2)_L \times SU(3)_c$ gauge coupling constants $\alpha_1 = \sqrt{\frac{5}{3}\frac{g_1^2}{4\pi}}$, $\alpha_2 = \frac{g_2^2}{4\pi}$, $\alpha_3 = \frac{g_3^2}{4\pi}$ with energy scale Q calculated by the Renormalization Group Equations a) for the SM particle content; b) for the SUSY particle content (unification in one point at $\sim 10^{16}$ GeV) [23]. The double line for α_3 denotes the current experimental uncertainty on this coupling, while the errors for α_1 and α_2 are too small to be visible.*

4.2 The MSSM and Supermultiplets

Supersymmetry groups particles into representations of the supersymmetric algebra called *supermultiplets*, each containing both fermions and bosons, which serve as superpartners of each other. Fermion and boson partners, which inhabit the same supermultiplet, have equal masses, $m_b = m_f$. Furthermore, the supersymmetry generators act independently of any internal symmetry, implying that particles in the same supermultiplet have identical electric charges, weak isospin and color. Numbers of bosonic and fermionic degrees of freedom in a supermultiplet are also equal, $n_b = n_f$.

The simplest supersymmetric theory called *Minimal Supersymmetric Standard Model* (MSSM in short) is built directly on the basis of the SM particle content and is the simplest extension of the Standard Model with introduced SUSY partners to the SM particles [28, 29, 30]. In principle, there is no strong theoretical restriction, which would forbid introduction of more complicated superfields and a richer set of particles [31], so the MSSM can be considered as the most simple case of a SUSY Theory.

The MSSM is built on the two simplest possible kinds of supermultiplets, satisfying the requirements described above:

- *the chiral supermultiplet*, containing a single spin-1/2 Weyl fermion and a complex scalar field;
- *the gauge supermultiplet*, consisting of a massless spin-1 vector gauge boson and its superpartner, a massless spin-1/2 Weyl fermion, called *gaugino* (or *Majorana particle*) and having the same gauge transformation properties for the left- and right-handed components.

In the MSSM, each of the known fundamental particles must reside either in a chiral or in a gauge supermultiplet and have a superpartner with spin differing by half a unit.

The SM fermions can only be placed in chiral supermultiplets together with their supersymmetric partners - scalar quarks (*squarks*) and scalar leptons (*sleptons*). The left- and right-handed states of quarks and leptons are separate two-component Weyl fermions with different SM gauge transformation properties. Therefore each must have its own complex scalar partner, $\tilde{f}_L$ and $\tilde{f}_R$.

The Higgs boson must reside in a chiral supermultiplet because it has spin 0. It turns out, that one Higgs supermultiplet is not enough. One reason for this is the structure of supersymmetric theories, where only a $Y = +1/2$ Higgs chiral supermultiplet can have the Yukawa couplings necessary to give masses to up-type quarks; and only a $Y = -1/2$ Higgs can have the Yukawa coupling necessary to give masses to down-type quarks and to the charged leptons. Thus, there are two $SU(2)_L$-doublet complex scalar fields H_u and H_d. The doublet H_u has two components H_u^+ and H_u^0, while the H_d consists of H_d^0 and H_d^- components.

The chiral supermultiplets of the MSSM are classified according to their transformation properties under the SM gauge group $U(1)_Y \times SU(2)_L \times SU(3)_c$; this is summarized in Table 4.1. The standard convention is that all chiral supermultiplets are defined in terms of left-handed Weyl spinors, so that the *conjugates* of the right-handed quarks and leptons and their superpartners are used.

Names		spin 0	spin 1/2	$SU(3)_c$ multiplets	$SU(2)_L$ multiplets	$U(1)_Y$ hypercharge
squarks / quarks (× 3 families)	Q	$(\tilde{u}_L \;\; \tilde{d}_L)$	$(u_L \;\; d_L)$	3	2	1/6
	$\overline{U}$	$\tilde{u}^*_R$	$u^\dagger_R$	$\bar{3}$	1	-2/3
	$\overline{D}$	$\tilde{d}^*_R$	$d^\dagger_R$	$\bar{3}$	1	1/3
sleptons / leptons (× 3 families)	L	$(\tilde{\nu}_L \;\; \tilde{e}_L)$	$(\nu_L \;\; e_L)$	1	2	-1/2
	$\overline{E}$	$\tilde{e}^*_R$	$e^\dagger_R$	1	1	1
Higgs / higgsinos	H_u	$(H^+_u \;\; H^0_u)$	$(\tilde{H}^+_u \;\; \tilde{H}^0_u)$	1	2	+1/2
	H_d	$(H^0_d \;\; H^-_d)$	$(\tilde{H}^0_d \;\; \tilde{H}^-_d)$	1	2	-1/2

Table 4.1: *The chiral supermultiplets of the Minimal Supersymmetric Standard Model. Symbols for the supermultiplets as a whole are indicated in the second column. The bar on $\overline{U}$, $\overline{D}$ and $\overline{E}$ fields is part of the name and does not denote any kind of conjugation. [30, 32, 33]*

The vector bosons of the Standard Model must reside in gauge supermultiplets. Their fermionic superpartners are usually referred to as *gauginos*. The gauge bosons W^i_μ and B_μ have associated spin-1/2 superpartners $\tilde{W}^i_\mu$ and $\tilde{B}_\mu$ respectively, which are called *winos* and *bino*. After the EW symmetry breaking, the W^3_μ and B_μ gauge eigenstates mix to give the mass eigenstates Z^0 and γ. The similar gaugino mixtures of $\tilde{W}^3_\mu$ and $\tilde{B}_\mu$ are *zino* $\tilde{Z}^0$ and *photino* $\tilde{\gamma}$. The superpartner of the gluon, which mediates the $SU(3)_c$ color gauge interactions of QCD, is a spin-1/2 color-octet particle called *gluino* $\tilde{g}$. The gauge supermultiplets are summarized in Table 4.2.

Names	spin 1/2	spin 1	$SU(3)_c$ multiplets	$SU(2)_L$ multiplets	$U(1)_Y$ hypercharge
gluino / gluon	$\tilde{g}$	g	8	1	0
winos / W-bosons	$\tilde{W}^i$	W^i	1	3	0
bino / B-boson	$\tilde{B}$	B	1	1	0

Table 4.2: *The gauge supermultiplets of the Minimal Supersymmetric Standard Model. [30, 32] (The gauge boson of gravitational interactions, the graviton G, and its supersymmetric partner, the gravitino $\tilde{G}$, are omitted here.)*

4.3 The MSSM Lagrangian

Having specified the superfields of the theory, the next step is to construct the Lagrangian with requirement of SM gauge and SUSY invariance. Omitting for shortness the intermediate formulae, we present here the SUSY Lagrangian expressed in terms of the superfield components [29, 26, 33]:

$$L_{SUSY} = L_{kin.} + L_{gauge} + L_{quartic} + L_{superpot.} \tag{4.2}$$

where $L_{kin.}$, L_{gauge} and $L_{quartic}$ are:

$$\begin{aligned} \mathrm{L}_{kin.} &= \sum_i (D_\mu S_i)^\dagger (D^\mu S_i) + \sum_i \bar{\Psi}_i \tfrac{i}{2}\gamma^\mu D_\mu \Psi_i \\ &+ \sum_A \bar{\lambda}_A \tfrac{i}{2}\gamma^\mu D_\mu \lambda_A - \tfrac{1}{4}\sum_A F^A_{\mu\nu} F^{\mu\nu}_A, \end{aligned} \tag{4.3}$$

$$L_{gauge} = -\sqrt{2}\sum_{i,A}\Big[S_i^\dagger g_\alpha t_{\alpha A} \bar{\Psi}_i \frac{1-\gamma_5}{2}\lambda_A + h.c.\Big], \tag{4.4}$$

$$L_{quartic} = -\frac{1}{2}\sum_A \Big[\sum_i S_i^\dagger g_\alpha t_{\alpha A} S_i\Big]^2 \tag{4.5}$$

(and $L_{superpot.}$ is described below).

Here S_i denotes the scalar component (and Ψ_i - the fermionic one) of the i^{th} chiral supermultiplet, $F^A_{\mu\nu}$ is the Yang-Mills gauge field and λ_A is the gaugino superpartner of the corresponding SM gauge boson. The sum $\sum\limits_i$ runs over all fermion fields Ψ_i of the Standard Model, over their scalar partners S_i and also over the two Higgs doublets and their fermionic partners. The sum $\sum\limits_A$ runs over the $SU(3)_c$, $SU(2)_L$ and $U(1)_Y$ gauge fields and over their fermionic partners, the gauginos. The covariant derivatives D_μ are the gauge covariant derivatives appropriate to the particular symmetry group representation to which the field belongs.

The $L_{kin.}$ part of the SUSY Lagrangian contains the gauge invariant kinetic energies for the components of the chiral and gauge superfields, which determine how all the particles interact with gauge bosons. The Standard Model Lagrangian is also contained here. The L_{gauge} term describes the interactions of gauginos with matter and with the Higgs multiplets, which are also determined by the gauge couplings. Here $t_{\alpha A}$ is the matrix representation of the group generators and g_α are the corresponding SM gauge coupling constants. (Thus, the interaction strengths in SUSY are fixed in terms of the SM gauge couplings). The $L_{quartic}$ part contains the terms with quartic couplings of the scalar matter fields.

The only part of the SUSY Lagrangian, which is not strictly defined by the structure of the supermultiplets and by the SM gauge and SUSY invariance, is $L_{superpot.}$, depending on an analytic function W of the chiral superfields $\hat{S} = Q, \overline{U}, \overline{D}, L, \overline{E}, H_u, H_d$. This function is called *superpotential* and describes the Yukawa interactions between the Higgs fields and the fermions (and their superpartners) [34]. It must be at most cubic in the superfields since higher orders would yield non-renormalizable interactions in the

Lagrangian. The $U(1)_Y \times SU(2)_L \times SU(3)_c$ invariant superpotential has the following form (for the first generation of fermions and their scalar partners):

$$\begin{aligned} \mathrm{W} &= \varepsilon_{ij}\mu H_u^i H_d^j + \varepsilon_{ij}\Big[\lambda_L H_d^i \bar{L}^j \bar{E} + \lambda_D H_d^i Q^j \bar{D} + \lambda_U H_u^j Q^i \bar{U}\Big] \\ &+ \varepsilon_{ij}\Big[\lambda_1 L^i L^j \bar{E} + \lambda_2 L^i Q^j \bar{D}\Big] + \lambda_3 \bar{U}\bar{D}\bar{D}, \end{aligned} \tag{4.6}$$

where i,j are $SU(2)_L$ doublet indices and $\varepsilon_{ij} = -\varepsilon_{ji}$ (with $\varepsilon_{12} = 1$) contracts the $SU(2)_L$ doublet fields and $\lambda_{1,2,3}$ are coefficients. With this superpotential the corresponding part of the SUSY Lagrangian reads:

$$L_{superpot.} = -\sum_i \Big\|\frac{\partial W}{\partial \hat{S}_i}\Big\|^2_{\hat{S}_i = S_i} - \frac{1}{2}\sum_{i,j}\Big\{\bar{\psi}_i\Big(\frac{1-\gamma_5}{2}\Big)\Big(\frac{\partial^2 W}{\partial \hat{S}_i \partial \hat{S}_j}\Big)_{\hat{S}_\ell = S_\ell}\psi_j + h.c.\Big\}. \tag{4.7}$$

The term $\mu H_u^i H_d^j$ in the superpotential (4.6) gives masses to the Higgs bosons when applying $\partial W/\partial \hat{S}$ in $L_{superpot.}$, and μ is called the *higgsino mass parameter*. The terms of the superpotential proportional to λ_L, λ_D and λ_U give the usual Yukawa interactions of fermions with the Higgs fields. These coefficients are determined in terms of the fermion masses and the vacuum expectation values (v.e.v.) of the neutral members of the scalar components of the Higgs doublets:

$$\begin{aligned} \upsilon_1 &\equiv < H_d^0 > \\ \upsilon_2 &\equiv < H_u^0 > . \end{aligned} \tag{4.8}$$

The ratio

$$\tan\beta = \upsilon_2/\upsilon_1 \tag{4.9}$$

is an additional free parameter with respect to the Standard Model Theory.

4.4 R-parity

The terms of the superpotential (4.6) proportional to λ_1, λ_2 do contribute to lepton number violating interactions and those proportional to λ_3 do allow the baryon number violating processes. For instance, this would allow the proton to decay at tree level through the exchange of the scalar partner of the d quark. But it does not happen in nature. To avoid these undesirable lepton and baryon number violations in a natural way, a special symmetry called *R-parity* has been introduced [30,35]. It defines a multiplicative quantum number

$$R = (-1)^{2s+3(B-L)} \tag{4.10}$$

where s, B and L are the spin, baryon and lepton quantum numbers respectively, and postulates its *conservation* in particle interactions. All the Standard Model particles have R-parity value +1 and the SUSY partner particles have it equal to −1. Thus, the lepton and baryon number violation processes are not possible.

The requirement of R-parity conservation has very important phenomenological consequences:

- SUSY particles can only be pair produced in collisions of SM particles;
- a SUSY particle decays to SM particle(s) and supersymmetric one(s);
- at the end of the SUSY particle decay chain the *lightest supersymmetric particle* called *the LSP* is produced and remains stable (i.e. can disappear only in pair-annihilations with its antiparticle).

The experimental limits on the existence of exotic isotopes [36] imply that the LSP must be a neutral and only weakly interacting particle. That's why, a generic signature for (R-parity conserving) SUSY processes in high energy particle collisions is *missing energy* from the LSP particles, which escape undetected. In the MSSM framework, the LSP can be either the lightest neutralino particle $\tilde{\chi}_1^0$ (which is a mixed state of neutral gauginos and higgsinos and will be discussed in the next sections) or the sneutrino $\tilde{\nu}$. However, the possibility of the sneutrino to be the LSP has been ruled out by the LEP I limits on the invisible Z width [37].

The R-parity conservation and the consequent existence of the only weakly interacting and stable LSP have a very important implication for cosmology, since the LSP particle is an excellent candidate for the non-baryonic *Cold Dark Matter* (CDM).

For completeness, we should mention, that the possible scenario of Supersymmetry with *R-parity violation* (RPV-SUSY) is also considered as alternative model development, where there is no stable LSP and the lightest SUSY particle decays further into the ordinary SM particles. The phenomenology of such a model is significantly different from Supersymmetry with R-parity conservation and missing energy is not a signature for production of SUSY particles. The problem of the baryon and lepton number violation terms in the superpotential (4.6) requires another kind of solution in this case, for example, either assuming the coefficients $\lambda_{1,2,3}$ to be small enough to satisfy the experimental observations, or, setting λ_1 and λ_2 or only λ_3 exactly equal to zero for explicit suppression of the proton decay, and so on.

The analysis presented in this thesis is based on the MSSM framework *with R-parity conservation* and the LSP particle is assumed to be the lightest neutralino $\tilde{\chi}_1^0$.

4.5 The Breaking of Supersymmetry

Up to this point, Supersymmetry was considered as an *unbroken* symmetry, which is obviously not the case, because otherwise the SUSY partner particles would have the same masses as the ordinary SM particles, and thus, the spartners should have been observed quite some time ago.

However, the intention to keep the radiative corrections to the Higgs mass in the order of the Electroweak scale ($\sim 10^2$ GeV) when going to the high energy scales requires to assume that the mass splitting of the superpartner particles after the Supersymmetry breaking should not be much larger than the EW scale [38,39,40]. Therefore, it is usually assumed that the SUSY breaking occurs in a "hidden" sector at some high energy scale and this sector interacts with the "visible" one (i.e. with the ordinary SM particles and their superpartners with masses of the EW order) only via the exchange of superheavy particles.

There are two main possibilities here concerning the type of such interaction. The first one is the *gravity-mediated Supersymmetry breaking*, called *SUGRA* [41, 42], where the hidden sector communicates with the visible MSSM sector by means of the gravitational interactions, mediated by *graviton* G and it's supersymmetric partner *gravitino* $\tilde{G}$ (in this case the Goldstone particle which appears in the symmetry breaking mechanism is absorbed by the gravitino and thus, gravitino plays the role similar to the scalar Higgs in the SM Electroweak Symmetry breaking). The SUSY breaking occurs in this scenario at an energy order of $10^{10} - 10^{11}$ GeV and the gravitino mass is of the order of the EW scale.

The second alternative scenario is the *gauge-mediated Supersymmetry breaking* (*GMSB*) [31], where such communication is realized via the ordinary $U(1)_Y \times SU(2)_L \times SU(3)_c$ gauge interactions and the SUSY breaking scale is much lower, typically of the order of $10^4 - 10^6$ GeV. The gravitino in this case has a mass in the eV-KeV range and therefore is the best candidate to be the LSP. However, the GMSB phenomenology is very different from the gravity-mediated SUSY breaking model, which is assumed in the analysis of this thesis.

The mechanism of Supersymmetry breaking is implemented by introducing of explicit "soft" SUSY breaking terms in the Lagrangian [43]. The dimension of such terms must be not bigger than 3, which means that the possible soft SUSY breaking operators are:

- mass terms for the scalar members of the chiral supermultiplets and for the vector members of the gauge supermultiplets,
- bi-linear mixing terms (so-called B-terms) and
- trilinear scalar mixing terms (called A-terms).

The usual strategy is to add to the Lagrangian all of the mass and mixing terms which are allowed by the gauge symmetries and by the requirement of R-parity conservation. Then the complete "soft" SUSY breaking Lagrangian (for the first generation family) is given by [26, 43]:

$$\begin{aligned} \mathrm{L}_{soft} = \; & - \mathrm{m}_1^2 \|H_d\|^2 - m_2^2 \|H_u\|^2 + B\mu\varepsilon_{ij}(H_d^i H_u^j + h.c.) \\ & - \mathrm{M}_Q^2 \bar{Q}^i Q^j - M_U^2 \bar{U} U - M_D^2 \bar{D} D - M_L^2 \bar{L}^i L^j - M_E^2 \bar{E} E \\ & - \frac{1}{2} \left[M_1 \overline{\tilde{B}^0} \tilde{B}^0 + M_2 \overline{\tilde{W}^a} \tilde{W}^a + M_3 \bar{\tilde{g}} \tilde{g} \right] \\ - \frac{g_2 \varepsilon_{ij}}{\sqrt{2} M_W} & \left[\frac{m_d}{\cos\beta} A_d H_d^i Q^j \tilde{d}_R^* + \frac{m_u}{\sin\beta} A_u H_u^j Q^i \tilde{u}_R^* + \frac{m_e}{\cos\beta} A_e H_d^i L^j \tilde{e}_R^* + h.c. \right], \end{aligned} \tag{4.11}$$

where i, j are the $SU(2)_L$ doublet indices and the scalar and gaugino masses and bi- and trilinear mixing terms are arbitrary. The difference of the scalar and gaugino masses from the SM fermion and gauge boson masses means the desired breaking of the mass degeneracy between the SM particles and their SUSY partners, i.e. the SUSY breaking. The A-terms affect primarily the particles of the third generation, while the B-term mixes the scalar components of the two Higgs doublets.

All these terms are called "soft" because they do not introduce quadratic divergences. In the most general case, all of the mass and interaction terms in (4.11) are matrices involving all three generations.

The origin of all these terms in (4.11) is left unspecified and so, L_{soft} contains in total 124 arbitrary SUSY model parameters [44], whereas the Lagrangian of unbroken SUSY (4.2) contains only $\tan\beta$ as a new theory parameter in addition to the Standard Model (plus coefficients $\lambda_{1,2,3}$).

4.6 The EW Symmetry Breaking in SUSY

Another important topic is the ability of Supersymmetry to provide the Electroweak symmetry breaking mechanism, which was considered within the Standard Model Theory in section 2.6.

The scalar Higgs potential can be derived from the superpotential W (4.6) and from L_{soft} (4.11). After performing the $SU(2)_L$ gauge transformations in order to eliminate the non-physical components of the Higgs field, the Higgs potential appears in the form:

$$\begin{aligned} \mathrm{V}_H &= \Big(\|\mu\|^2 + m_1^2\Big)\|H_d\|^2 + \Big(\|\mu\|^2 + m_2^2\Big)\|H_u\|^2 - \mu B \varepsilon_{ij}\Big(H_d^i H_u^j + h.c.\Big) \\ &+ \frac{g_1^2 + g_2^2}{8} \Big(\|H_d\|^2 + \|H_u\|^2\Big)^2 + \frac{g_2^2}{2} \|H_d^* H_u\|^2. \end{aligned} \tag{4.12}$$

Using the Renormalization Group Equations, m_1^2 and m_2^2 are evolved from the GUT scale down to the EW scale, which gives large Yukawa coupling contributions. This can result in negative values for one or both mass-square terms, therefore leading to the spontaneous breaking of the Higgs potential symmetry.

After the Supersymmetry breaking, five physical Higgs particles appear: two neutral CP-even, h and H (with $m_h < m_H$), one neutral CP-odd, denoted A, and a pair of charged Higgs particles $H^\pm$. Their masses at tree level are given by:

$$m_A^2 = \frac{2\|\mu B\|}{\sin 2\beta}, \tag{4.13}$$

$$m_{H^\pm}^2 = m_A^2 + m_W^2, \tag{4.14}$$

$$m_{h,H}^2 = \frac{1}{2}\Big[m_A^2 + m_Z^2 \mp \sqrt{(m_A^2 + m_Z^2)^2 - 4m_A^2 m_Z^2 \cos^2 2\beta}\,\Big]. \tag{4.15}$$

It follows from Equation (4.15) that the mass of the lightest neutral Higgs h should be smaller than $m_Z\|cos2\beta\|$. However, taking into account radiative corrections to the Higgs masses, which can be large, the upper bound on m_h can be moved up to 130 GeV [45].

The EW gauge bosons $W^\pm$ and Z^0 obtain masses, which are fixed by the common vacuum expectation value parameter $\upsilon^2 = \upsilon_1^2 + \upsilon_2^2$:

$$m_W = \frac{\upsilon}{\sqrt{2}} g_2, \tag{4.16}$$

$$m_Z = \frac{\upsilon}{\sqrt{2}}\sqrt{g_1^2 + g_2^2}. \tag{4.17}$$

The up-type quarks get their masses entirely from υ_2, while the down-type ones and the charged leptons obtain them from υ_1, as a consequence of the hypercharge quantum numbers of H_u and H_d, given in Table 4.1. Then for the corresponding Yukawa couplings we obtain the following relations:

$$\lambda_U = \frac{g_2 m_u}{\sqrt{2} m_W \sin\beta}, \tag{4.18}$$

$$\lambda_D = \frac{g_2 m_d}{\sqrt{2} m_W \cos\beta}, \tag{4.19}$$

$$\lambda_L = \frac{g_2 m_\ell}{\sqrt{2} m_W \cos\beta}. \tag{4.20}$$

Thus, the Electroweak symmetry breaking can be generated radiatively [46] within the framework of Supersymmetry, whereas in the Standard Model it is put in "by hands". This fact serves as one more important advantage of the SUSY model.

4.7 The Constrained MSSM

So, the most general case of the Minimal Supersymmetric Standard Model with minimal field content as described earlier and with R-parity conservation contains in total 124 model parameters. A further deeper understanding of the SUSY breaking mechanism and evolution with energy up to the GUT scales may relate many of these parameters and so, restrict the total number of arbitrary ones. Several experimental facts and theoretical principles give hints for the reduction of the set of free parameters.

For instance, the observed behavior of the gauge couplings with energy and their unification at the GUT scale suggests the unification at the GUT scale of the gaugino masses:

$$M_1 = M_2 = M_3 \equiv m_{1/2} \qquad (GUT). \tag{4.21}$$

Having this at the GUT scale as initial condition and using the RGEs for evolution down to the low energies, one finds (at one-loop level) their relation at the EW scale [47]:

$$\frac{3M_1}{5g_1^2} = \frac{M_2}{g_2^2} = \frac{M_3}{g_3^2}, \quad M_2 \approx 0.82\ m_{1/2} \qquad (EW). \tag{4.22}$$

Furthermore, in order to avoid lepton number violation, the slepton mass matrices $\tilde{M}_L$ and $\tilde{M}_{\overline{E}}$ should be flavour diagonal. Next, constraints on the Flavour Changing Neutral Current (FCNC) processes suggest that the squark mass matrices and the trilinear couplings should be also flavour diagonal [48]. The GUT approach lets to assume the mass unification of squarks and sleptons at the GUT scale, similarly to the mass unification of the gauginos:

$$M_Q = M_D = M_U = M_L = M_E \equiv m_0 \qquad (GUT), \tag{4.23}$$

$$A_d = A_u = A_e \equiv A_0 \qquad (GUT), \tag{4.24}$$

The MSSM Theory with this set of assumptions and corresponding reduction of the number of arbitrary parameters is called *constrained MSSM* (CMSSM) [46, 49]. It has only 6 free parameters in addition to the Standard Model, which are:

- M_2 - the $SU(2)_L$ gaugino mass at EW scale,
- m_0 - the universal scalar mass at GUT scale,
- A_0 - the universal trilinear coupling at GUT scale,
- $\tan\beta$ - the ratio of the vacuum expectation values of the two Higgs fields at EW scale,
- μ - the higgsino mass parameter at EW scale,
- M_A - the CP-odd Higgs boson mass.

When these 6 parameters are fixed at certain values, the entire sparticle spectrum at the Electroweak scale is derived using the Renormalization Group Equations.

The CMSSM is the most attractive SUSY scenario for experimental searches in the High Energy Physics. The CMSSM model (with gravity mediated SUSY breaking and R-parity conservation) is the theoretical framework of this thesis.

There is even more constrained version of CMSSM, where it is assumed that the soft-SUSY breaking Higgs masses are also equal to the masses of other scalars:

$$m_1 = m_2 \equiv m_0 \qquad (GUT). \tag{4.25}$$

and furthermore, the acquirement of the EW symmetry breaking in SUSY with the measured value of Z^0 gauge boson mass can restrict the dependence on the μ parameter to a dependence on only its sign (thus, reducing the set of the free parameters from 6 down to 4 plus a two-fold ambiguity corresponding to the $sign(\mu)$). This version of the CMSSM is called *mSUGRA* [38, 50]. In addition to the Standard Model it contains the following four arbitrary parameters:

- $m_{1/2}$ - the $SU(2)_L$ gaugino mass at GUT scale,
- m_0 - the universal scalar mass at GUT scale,
- A_0 - the universal trilinear coupling at GUT scale,
- $\tan\beta$ - the ratio of the vacuum expectation values of the two Higgs fields at EW scale,
- $sign(\mu)$ - sign of the higgsino mass parameter at EW scale.

4.8 The Mixing and CMSSM Particle Content

After the Electroweak symmetry breaking in SUSY, the interaction eigenstates of sparticles with the same quantum numbers mix and produce the physical states.

The Sfermion Mixing

In general, the left $\tilde{f}_L$ and right $\tilde{f}_R$ field components of sfermions mix into the mass eigenstates. With completely arbitrary soft SUSY terms, the physical states are obtained by diagonalization of 6×6 mass matrices, one for up-type squarks, one for down-type ones and one for the charged sleptons. They can be decomposed into 2×2 matrices, when ignoring the intergenerational mixing, which is a reasonable assumption to avoid oversized FCNC. These 2×2 mass matrices for the scalar quarks and charged scalar leptons are given by [51]:

$$M_f^2 = \begin{pmatrix} m_{\tilde{f}_L}^2 & a_f m_f \\ a_f m_f & m_{\tilde{f}_R}^2 \end{pmatrix} \tag{4.26}$$

with

$$m_{\tilde{f}_L}^2 = M_{\tilde{F}}^2 + m_Z^2 \cos 2\beta (T_f^3 - Q_f \sin^2\theta_W) + m_f^2, \tag{4.27}$$

$$m_{\tilde{f}_R}^2 = M_{\tilde{F}'}^2 + Q_f m_Z^2 \cos 2\beta \sin^2\theta_W + m_f^2, \tag{4.28}$$

$$a_f = A_f - \mu (\tan\beta)^{-2T_f^3}, \tag{4.29}$$

where $F \equiv Q, L$ for squarks and sleptons, respectively; F' denotes U in the case of up-type squarks, D in the case of down-type ones and L in the case of the charged sleptons; T_f^3 is the third component of the weak isospin; m_f is the mass of the Standard Model fermion, corresponding to a given sparticle and $M_{\tilde{F}}$ and $M_{\tilde{F}'}$ are the soft SUSY masses at the EW scale, which are derived from the GUT scale values using the Renormalization Group Equations (there are three contributions here: from the gaugino and Yukawa couplings and from the trilinear terms, and it can be shown [52, 53], that $M_{\tilde{F}}$ and $M_{\tilde{F}'}$ are much lower for the third generation compared to the first and second families).

The relation between the weak and the mass eigenstates of the sfermions is expressed through the mixing angle θ_{LR} as:

$$\begin{pmatrix} \tilde{f}_1 \\ \tilde{f}_2 \end{pmatrix} = \begin{pmatrix} \cos\theta_{LR} & \sin\theta_{LR} \\ -\sin\theta_{LR} & \cos\theta_{LR} \end{pmatrix} \begin{pmatrix} \tilde{f}_L \\ \tilde{f}_R \end{pmatrix}, \tag{4.30}$$

where

$$\cos\theta_{LR} = \frac{-a_f m_f}{\sqrt{(m_{\tilde{f}_L}^2 - m_{\tilde{f}_1}^2)^2 + a_f^2 m_f^2}}, \tag{4.31}$$

$$\sin\theta_{LR} = \frac{m_{\tilde{f}_L}^2 - m_{\tilde{f}_1}^2}{\sqrt{(m_{\tilde{f}_L}^2 - m_{\tilde{f}_1}^2)^2 + a_f^2 m_f^2}}. \tag{4.32}$$

Then the masses of the two physical eigenstates of the sfermions are given by:

$$m_{\tilde{f}_{1,2}}^2 = \frac{1}{2}\big(m_{\tilde{f}_L}^2 + m_{\tilde{f}_R}^2 \mp \sqrt{(m_{\tilde{f}_L}^2 - m_{\tilde{f}_R}^2)^2 + 4a_f^2 m_f^2}\big), \tag{4.33}$$

with the general convention that $\tilde{f}_1$ denotes the lighter of the two sfermion mass eigenstates, $m_{\tilde{f}_1} \leq m_{\tilde{f}_{L,R}} \leq m_{\tilde{f}_2}$.

As it is seen from (4.33), the size of mixing between $\tilde{f}_L$ and $\tilde{f}_R$ is proportional to the corresponding SM fermion mass and so, can be approximately neglected for the first two generations, which means that the mass eigenstates can be regarded as the interaction ones. However, since the SM top quark is significantly heavier compared to all other SM quarks, the situation for the scalar top is completely different: the mixing between $\tilde{t}_L$ and $\tilde{t}_R$ is big and the resulting mass eigenstates have a significant mass splitting, which makes the lighter scalar top eigenstate $\tilde{t}_1$ being the lightest of all the physical scalar quarks. For the sbottom quark the magnitude of the mixing depends on the $\tan\beta$ value, which enters into the a_f parameter: strong mixing occurs at large $\tan\beta$ (> 10) and this case is preferred in many GUT scenarios (for instance, solution of $\lambda_b(GUT) = \lambda_\tau(GUT)$ equation, which is a condition for b and τ Yukawa coupling unification, gives $\tan\beta \sim 35$ [54]). So, the lighter sbottom quark $\tilde{b}_1$ is considered (in the framework of the SUSY scenario of this thesis) as the second lightest scalar quark mass eigenstate.

The Gaugino Mixing

The interaction eigenstates of gauginos also mix with each other and produce physical eigenstates of SUSY particles.

Mixing of charged winos $\tilde{W}^\pm$ and higgsinos $\tilde{H}^\pm$ gives two physical states called *charginos* $\tilde{\chi}_1^\pm$ and $\tilde{\chi}_2^\pm$ (with convention $m_{\tilde{\chi}_1^\pm} \leq m_{\tilde{\chi}_2^\pm}$). Their mass values are given by [55]:

$$m^2_{\tilde{\chi}^\pm_{1,2}} = \frac{1}{2}(M_2^2 + \mu^2 + 2m_W^2) \mp \frac{1}{2}\sqrt{(M_2^2 + \mu^2 + 2m_W^2)^2 - 4(\mu M_2 - m_W^2 \sin 2\beta)^2}. \quad (4.34)$$

In case $M_2 \ll \|\mu\|$, the lighter chargino is mainly the wino and the heavier chargino is mainly higgsino-like. The situation reverses if $M_2 \gg \|\mu\|$.

The neutral wino, bino and neutral higgsinos combine to produce four *neutralinos*, $\tilde{\chi}^0_{1,2,3,4}$ with the convention $m_{\tilde{\chi}_1^0} \leq m_{\tilde{\chi}_2^0} \leq m_{\tilde{\chi}_3^0} \leq m_{\tilde{\chi}_4^0}$. These eigenstates are characterized by a 4×4 mass mixing matrix [56], which in the $(\tilde{B}, \tilde{W}^3, \tilde{H}_d^0, \tilde{H}_u^0)$ basis takes the following form:

$$\begin{pmatrix} M_1 & 0 & -m_Z\cos\beta\sin\theta_W & m_Z\sin\beta\sin\theta_W \\ 0 & M_2 & m_Z\cos\beta\cos\theta_W & -m_Z\sin\beta\cos\theta_W \\ -m_Z\cos\beta\sin\theta_W & m_Z\cos\beta\sin\theta_W & 0 & \mu \\ m_Z\sin\beta\sin\theta_W & -m_Z\sin\beta\cos\theta_W & \mu & 0 \end{pmatrix} \quad (4.35)$$

If $M_2 \ll \|\mu\|$, the lightest neutralino $\tilde{\chi}_1^0$ is mainly the photino, the next lightest one $\tilde{\chi}_2^0$ is mainly the zino and the two heaviest neutralinos $\tilde{\chi}_{3,4}^0$ are mainly the higgsinos. For $M_2 \gg \|\mu\|$, the two lightest neutralinos are mainly the higgsinos, $\tilde{\chi}_3^0$ is mainly the photino and $\tilde{\chi}_4^0$ is mainly zino.

The gluino $\tilde{g}$, which is the only color octet gaugino, remains unmixed after the Electroweak symmetry breaking. In the MSSM with gaugino unification at the GUT scale, the gluino mass can be related to M_3 and M_2 in the following way:

$$m_{\tilde{g}} = M_3 = \frac{g_3^2}{g_2^2}M_2 \approx 2.6\ m_{1/2}, \quad (4.36)$$

however, the QCD corrections to this relation can be important [57].

Note also, that eigenstates of the superpartner of the graviton, the gravitino $\tilde{G}$, also do not mix, but the detailed consideration of the theory of gravity is outside the scope of this thesis.

The CMSSM Particle Content

After specification of the MSSM model scenario and eigenstate mixing after the Electroweak symmetry breaking, the physical particle content of the CMSSM can be summarized as shown in Table 4.3.

"Ordinary" Particles		Supersymmetric Partners			
		Interaction Eigenstates		Mass Eigenstates	
$\ell = e, \mu, \tau$	Ch. Leptons	$\tilde{\ell}_{L,R}$	Sleptons	$\tilde{\ell}_{1,2}$	
ν_ℓ	Neutrinos	$\tilde{\nu}_\ell$	Sneutrinos	$\tilde{\nu}_\ell$	
$q = u, d, c, s, t, b$	Quarks	$\tilde{q}_{L,R}$	Squarks	$\tilde{q}_{1,2}$	
g	Gluon	$\tilde{g}$	Gluino	$\tilde{g}$	
$\mathrm{W}^\pm$	W−*bosons*	$\tilde{W}^\pm$	*Winos*	$\tilde{\chi}^\pm_{1,2}$	Charginos
$\mathrm{H}^\pm$	*Ch.Higgses*	$\tilde{H}^\pm$	*Higgsinos*		
γ	*photon*	$\tilde{\gamma}$	*Photino*	$\tilde{\chi}^0_{1,2,3,4}$	Neutralinos
Z^0	$Z - boson$	$\tilde{Z}^0$	*Zino*		
h, H, A	*Neut.Higgses*	$\tilde{H}_{1,2}$	*Higgsinos*		
G	Graviton	$\tilde{G}$	Gravitino	$\tilde{G}$	

Table 4.3: *The CMSSM particle content after the EW symmetry breaking.*

Chapter 5

Scalar Quarks in e^+e^- Collisions

5.1 Stop and Sbottom Production at LEP II

Due to the assumed conservation of R-parity, sparticles can only be pair produced in interactions of the Standard Model particles. The general scheme for sfermion pair production in e^+e^- collisions is the Z/γ exchange, as shown in Figure 5.1 (for selectrons, there is also an additional t-channel contribution). The tree level cross section for a production of a scalar quark pair is given by [58, 59]:

$$\sigma_{ee\to\tilde{q}_1\tilde{q}_1} = \frac{\pi\alpha^2}{s}\left(1-\frac{4m^2_{\tilde{q}_1}}{s}\right)^{3/2}\left[e_q^2 + a^2 T_{ZZ} - a e_q T_{Z\gamma}\right], \tag{5.1}$$

$$T_{ZZ} = \frac{1+v_e^2}{256\sin^4\theta_W\cos^4\theta_W}\,\frac{s^2}{(s-m_Z^2)^2+m_Z^2\Gamma_Z^2}, \tag{5.2}$$

$$T_{Z\gamma} = \frac{v_e}{8\sin^2\theta_W\cos^2\theta_W}\,\frac{s(s-m_Z^2)}{(s-m_Z^2)^2+m_Z^2\Gamma_Z^2}, \tag{5.3}$$

where $\sqrt{s}$ is the center-of-mass energy, α is the fine structure constant, e_q is the charge of the squarks ($e_t = 2/3$, $e_b = -1/3$), $a = 4(I_3\cos^2\theta_{LR} - e_q\sin^2\theta_W)$ is the $Z\tilde{q}\bar{\tilde{q}}$ coupling

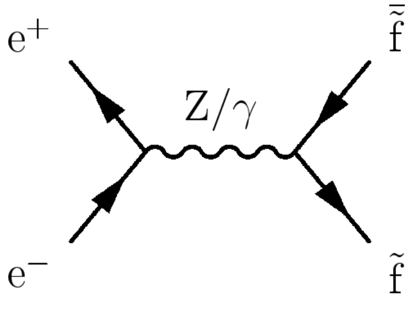

Figure 5.1: *The general scheme for sfermion pair production at LEP. (For selectrons, there is also an additional contribution from t-channel exchange).*

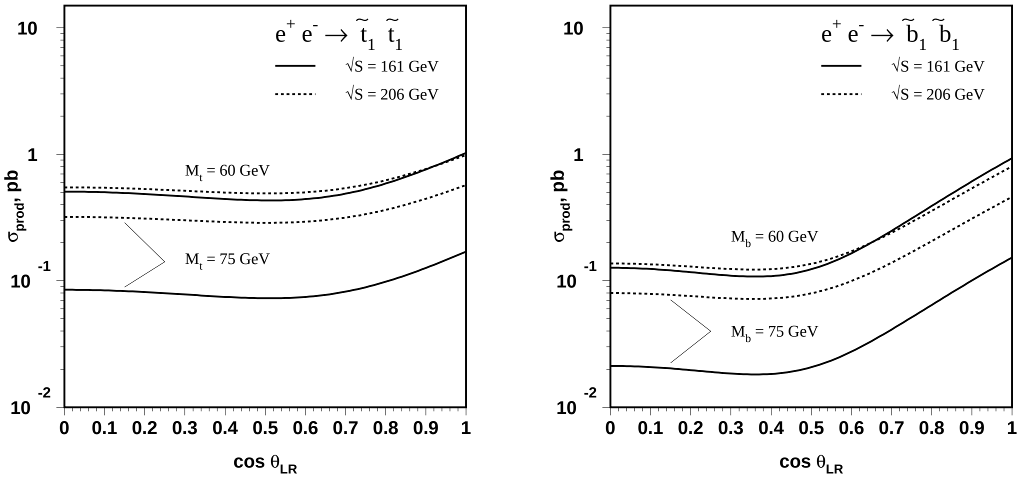

Figure 5.2: *The dependency of the stop and sbottom production cross section on the mixing angle θ_{LR} for fixed $\sqrt{s}$ and fixed squark masses.*

and $v_e = 4\sin^2\theta_W - 1$. The first and the second terms in Equation 5.1 correspond to the cases of sfermion production via purely γ or purely Z exchange, while the third term describes the $\gamma - Z$ interference, which explains the characteristic minimum in dependence of the sfermion production cross section on the mixing angle θ_{LR}. The cross section is maximal at $\cos\theta_{LR} = 1$, which corresponds to the case of no mixing, $\tilde{f}_1 \equiv \tilde{f}_L$, and it comes to the minimum at

$$\cos^2\theta_{LR}\Big|_{\sigma=min} = \frac{e_q \sin^2\theta_W}{I_3}\Big[1 + (1 - \frac{s}{m_Z^2})F(\sin^2\theta_W)\Big], \qquad (5.4)$$

where $F(\sin^2\theta_W) = \cos^2\theta_W(L_e+R_e)/(L_e^2+R_e^2)$ with $L_e = \sin^2\theta_W - 1/2$ and $R_e = \sin^2\theta_W$ [60, 61].

The considered *tree level* cross sections are suitable for scalar fermions in general, which can be either squarks or sleptons (except selectrons having additional t-channel contribution). On the other side, in the case of the scalar quarks, there is an additional contribution from QCD radiative corrections (due to gluons), which enhances the production cross section of squarks [62, 63]. On the other side, the SUSY-QCD corrections are found to be of the order of a few percent (below 2 %, [64]).

The dependency of the scalar top and the scalar bottom production cross section on the mixing angle θ_{LR}, on the scalar quark mass and on the center-of-mass energy is illustrated in Figures 5.2 and 5.3. As it is seen, in general the production cross section decreases with the squark mass at fixed values of center-of-mass energy and the mixing angle. But it increases with center-of-mass energy at fixed values of the squark mass and the mixing angle (when the squark mass is close to the kinematic limit). The dependency on the mixing angle has a flat shape at $\cos\theta_{LR} < 0.5$ and has its minimum near the point, where the scalar quarks decouple from the Z boson (at $\cos\theta_{LR} = 0.57$ for the stop and $\cos\theta_{LR} = 0.39$ for the sbottom), above $\cos\theta_{LR} = 0.5 - 0.7$ the cross section increases

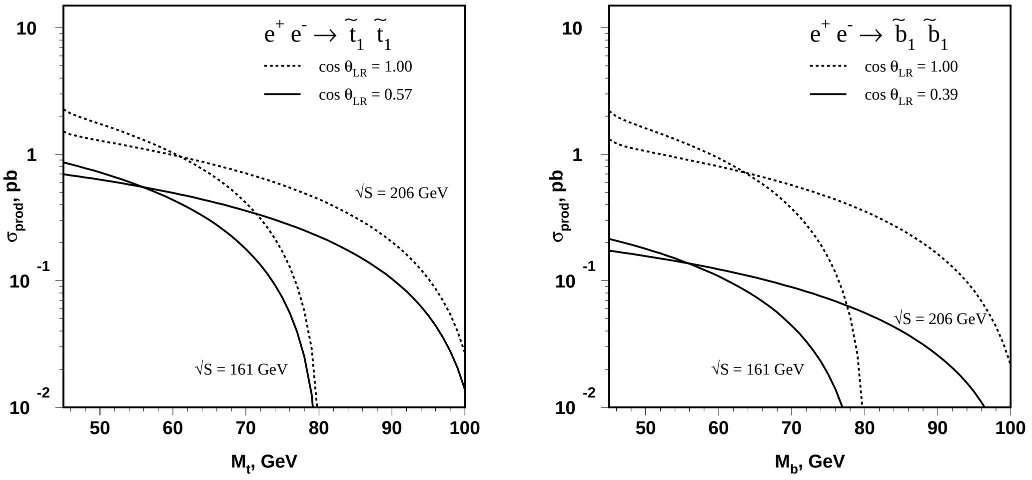

Figure 5.3: *The dependency of the stop and sbottom production cross section on the squark masses for fixed* $\sqrt{s}$ *and mixing angle* θ_{LR} *(two values are used:* $\cos\theta_{LR} = 1$ *corresponding to no mixing and* $\cos\theta_{LR} = 0.57$ *for stop and* $\cos\theta_{LR} = 0.39$ *for sbottom, corresponding to the decoupling from the Z boson.)*

and reaches its maximum at $\cos\theta_{LR} = 1$. The dependency on the mixing angle is bigger for the scalar bottom quark pair production compared to the scalar top pairs, because of the dependency on the corresponding Standard Model quark mass ($m_t \gg m_b$). Also, the dependency on the mixing angle is much smaller near the kinematic limit at fixed center-of-mass energy.

The produced pairs of scalar top or scalar bottom quarks have the angular distribution, which is typical for scalar particles:

$$\frac{d\sigma}{d\cos\vartheta} = \frac{3}{4}\sigma\sin^2\vartheta, \tag{5.5}$$

where ϑ is the scattering angle.

5.2 Decays of Stop and Sbottom Quarks

Within the assumed CMSSM framework with conserved R-parity, the scalar fermions predominantly decay to the Standard Model fermion of the same flavour plus neutralino, $\tilde{f} \to f\tilde{\chi}_i^{0(*)}$, and to the SM fermion of the other flavour plus chargino, $\tilde{f} \to f'\tilde{\chi}_i^{\pm(*)}$.

The lightest scalar bottom quark $\tilde{b}_1$ decays at LEP II energies according to this scheme:

(a) $\tilde{b}_1 \to b\tilde{\chi}_1^0$

(b) $\tilde{b}_1 \to b\tilde{\chi}_2^0$

(c) $\tilde{b}_1 \to c\tilde{\chi}_1^-$.

The decay (b) to the next-to-lightest neutralino, $\tilde{\chi}_2^0$, would have a large phase-space suppression due to the lower limits of the $\tilde{\chi}_2^0$ mass, about 65-90 GeV [65]. That's why we do not consider this decay. For the majority of the MSSM scenarios, the cross section of chargino pair production is higher than the cross sections of the stop or the sbottom pair production in e^+e^- collisions at LEP II energies. Therefore the charginos would be discovered first from the direct pair production and not from the decays of the scalar quarks. The experimental 95 % C.L. limit on the lightest chargino mass obtained by L3 [65], $m_{\tilde{\chi}_1^\pm} \geq 93$ GeV is very close to the kinematic limit and thus, excludes decay (c) from our consideration. So, only the sbottom decay (a) is searched for in this analysis.

The situation with the lightest scalar top decays at LEP II is less trivial, because the Standard Model top quark is too heavy for pair production at LEP II and the decay $\tilde{t}_1 \to t\tilde{\chi}_1^0$ is prohibited. Thus, the following stop decay modes are left for consideration:

(e) $\tilde{t}_1 \to b\tilde{\chi}_1^+$

(f) $\tilde{t}_1 \to c\tilde{\chi}_1^0$

(g) $\tilde{t}_1 \to b\ell\tilde{\nu}$

(h) $\tilde{t}_1 \to b\tilde{\ell}\nu$

(k) $\tilde{t}_1 \to bW\tilde{\chi}_1^0$.

Decay (e) has practically 100 % branching ratio, when kinematically allowed. However, we exclude this decay from our consideration due to the above mentioned experimental limits on the chargino mass.

Decay (f) is the one of our special interest because it corresponds to the case when $\tilde{t}_1$ is the lightest *visible* SUSY particle and therefore is potentially the first one to be discovered at LEP II. This decay is a flavour changing weak process. In the case of absence of any flavour changing effects in the squark sector, this decay proceeds through a loop as shown in Figure 5.4, otherwise it occurs at tree-level through the stop-scharm mixing. The estimated decay time for this process $\tau \sim 10^{-14} - 10^{-15}$ s is much longer than the strong interaction time scale $\sim 10^{-23}$ s, therefore the scalar top quark hadronizes into colorless states before it decays. This proceeds in the following way: the produced in e^+e^- interaction stop quark first radiates off gluons and this phase can be treated perturbatively; then there is a nonperturbative phase, when the stop hadronizes into a "meson" $\tilde{t}_1\bar{q}$ or a "baryon" $\tilde{t}_1qq$; and only afterwards the stop decays [63]. This mechanism is illustrated in Figure 5.5, which is suitable to hadronisation of both the scalar top and the scalar bottom quarks. (More exactly, for the sbottom quark, the hadronisation scenario depends on the gaugino-higgsino content of the neutralino and the sbottom lifetime can be comparable to the hadronisation time, but since this affects only the track multiplicity, but does not change the event topology, we follow the "hadronisation before decay" scenario also for the sbottom quark).

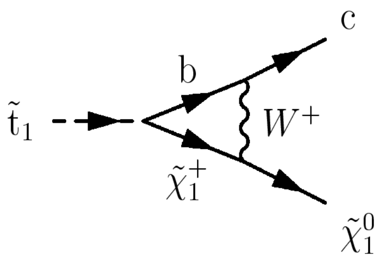

Figure 5.4: *The Feynman diagram for the flavour changing decay* $\tilde{t}_1 \longrightarrow c\tilde{\chi}_1^0$.

The three-body decays (g) and (h) proceed in two steps via virtual chargino exchange: $\tilde{t}_1 \longrightarrow b\tilde{\chi}_1^+$ and then $\tilde{\chi}_1^+ \longrightarrow \ell\tilde{\nu}/\tilde{\ell}\nu$. The Feynman graph for the $\tilde{t}_1 \longrightarrow bl\tilde{\nu}$ case is presented in Figure 5.6 (and the diagram is very similar for the $\tilde{t}_1 \longrightarrow b\tilde{\ell}\nu$ case). The estimated stop quark lifetime $\tau \sim 10^{-17}$ s is also longer than the typical hadronisation time implying that hadronisation again will take place before the scalar top quark decay [58]. When kinematically allowed, these three-body decays can dominate, thus they are considered in parallel to the two-body stop decay (f) and also, both of the stop quarks produced in e^+e^- collisions decay in the same way (no mixed cases, when one stop decays through (e) and another one through (g) or (h) are considered). The produced slepton/sneutrino in turn decay via $\tilde{\ell}^{\pm} \longrightarrow \ell^{\pm}\tilde{\chi}_1^0, \ell^{\pm}\tilde{\chi}_2^0, \tilde{\nu}\tilde{\chi}_1^{\pm}$ and $\tilde{\nu} \longrightarrow \nu\tilde{\chi}_1^0, \nu\tilde{\chi}_2^0, \ell^{\pm}\tilde{\chi}_1^{\mp}$, however, decays involving a chargino are precluded (because chargino would be discovered first) and decays to the next-to-lightest neutralino $\tilde{\chi}_2^0$ also have a large phase-space suppression from the lower limits on the $\tilde{\chi}_2^0$ mass [65]. Thus, we assume that $\tilde{\nu} \longrightarrow \nu\tilde{\chi}_1^0$ and $\tilde{\ell} \longrightarrow \ell\tilde{\chi}_1^0$ occur with 100 % branching ratio and therefore, both of (g) and (h) decays have the same particles in the final state: b, ℓ, ν and $\tilde{\chi}_1^0$. So, we consider for simplicity only one of these decays, namely, $\tilde{t}_1 \longrightarrow b\ell\tilde{\nu}$, but keep in mind that the process (h) may occur very similarly. Taking into account that the third generation sfermions are expected to be lighter than sfermions

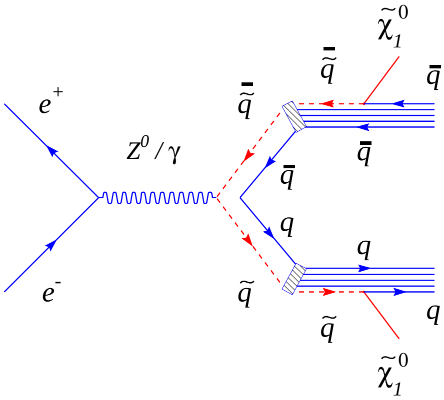

Figure 5.5: *The mechanism of hadronisation and decay of the scalar top and the scalar bottom quarks: a squark decays after the hadronization.*

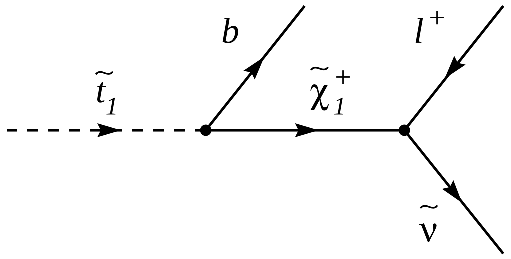

Figure 5.6: *The Feynman diagram for the* $\tilde{t}_1 \rightarrow bl\tilde{\nu}$ *decay.*

of the first two generations, the lepton/slepton in the final state can be predominantly tau/stau. On the other side, if there is no sizable mass splitting between three generation of sneutrinos, $\tilde{\nu}_e$, $\tilde{\nu}_\mu$ and $\tilde{\nu}_\tau$, or between three generations of sleptons, $\tilde{e}$, $\tilde{\mu}$ and $\tilde{\tau}$, then the lepton/slepton flavour in decays (g) and (h) is determined by the chargino composition. For the wino-like chargino, decays to all three lepton/slepton flavours occur with equal probabilities. If the chargino is mainly the higgsino, the decay to tau/stau becomes dominant. Thus, we consider the two above scenarios separately: either lepton is e, μ or τ with equal branching ratios, or the separate case of the lepton being with 100 % branching τ (and similarly for the slepton case).

When kinematically allowed, decay (k) also dominates over the two-body stop decay, but it is possible only in the small parameter corner of the stop and neutralino masses, $M_{\tilde{t}_1} > M_b + M_W + M_{\tilde{\chi}_1^0} \geq 86$ GeV, that's why it is considered *as additional* and as *complementary to the* $\tilde{t}_1 \rightarrow c\tilde{\chi}_1^0$ decay and it is described separately in Chapter 10.

To summarize, in our search analysis we consider the following decay channels of the scalar top and the scalar bottom quarks: $\tilde{t}_1 \rightarrow c\tilde{\chi}_1^0$, $\tilde{t}_1 \rightarrow bl\tilde{\nu}$, $\tilde{t}_1 \rightarrow b\tau\tilde{\nu}$, $\tilde{b}_1 \rightarrow b\tilde{\chi}_1^0$ and $\tilde{t}_1 \rightarrow bW\tilde{\chi}_1^0$; each channel is analyzed separately with assumed 100% branching ratio.

5.3 The Squark Monte Carlo Generator

For the Monte Carlo generation of the scalar top and the scalar bottom production and their decays, an event generator developed for the OPAL Collaboration [66] was modified by the L3 Collaboration MC Group.

In the first step of the $e^+e^- \rightarrow \tilde{t}_1\bar{\tilde{t}}_1$ event simulation the ISR photon(s) is (are) emitted and the reduced center-of-mass energy is calculated. Then, perturbative gluon emission off the squarks is performed. Since the squark is a scalar particle, the spectrum of gluons differs from that emitted off a Standard Model quark. In particular, the squark fragmentation function is harder than that of a fermion of the same mass. However, at

LEP energies, using JETSET [67] with default emission probabilities (which assumes the radiating particle is a fermion) can be regarded as an adequate description of the process [68].

As discussed in the previous section, the stop (sbottom) quark forms a "meson" $\tilde{t}_1\bar{q}$ ($\tilde{b}_1\bar{q}$) or a "baryon" $\tilde{t}_1 qq$ ($\tilde{b}_1 qq$) before it decays. In the MC the hadronisation is performed according to the Lund Model as implemented in JETSET. The choice on the flavour of the spectator quark(s) is made using the Lund prediction and is mainly restricted to u, d and s quarks [67]. An invariant mass of 500 MeV is assigned to the spectator system. The energy sharing among the produced hadrons is described according to the Peterson fragmentation function [69] with the parameter $\varepsilon_{\tilde{q}}$ propagated from ε_b of the b-quark:

$$\varepsilon_{\tilde{q}} = \varepsilon_b \frac{m_b^2}{m_{\tilde{q}}^2}, \tag{5.6}$$

where $\varepsilon_b = 0.0035$ [70] and $m_b = 5$ GeV.

After hadronisation the stop (sbottom) hadrons decay and produce c or b quarks (depending on the decay mode specified), which in turn undergo fragmentation.

The stop leptonic three-body decay mode is implemented in the MC according to the following scheme: first, the decay products are distributed according to phase space, i.e. assuming that there is no dynamics involved. However, this is not actually true and the weak structure of the decay matrix element has to be taken into account [58]. The matrix element depends on many SUSY parameters. In the approximation of $m_b \to 0$ and $m_{\tilde{t}_1} << m_{\tilde{\chi}_1^+} << m_{\tilde{\chi}_2^+}$, the decay distribution has the form [58]:

$$\frac{d\Gamma}{dz_b dz_\ell} \propto \left[(1 - z_b)(1 - z_\ell) - \frac{m_{\tilde{\nu}}^2}{m_{\tilde{t}_1}^2}\right], \tag{5.7}$$

where $z_b = 2p_{\tilde{t}_1} p_b / m_{\tilde{t}_1}^2$ and $z_\ell = 2p_{\tilde{t}_1} p_\ell / m_{\tilde{t}_1}^2$ are the scaled energies of the b-quark and lepton. This structure of the decay distribution is implemented in the Monte Carlo.

Chapter 6

The L3 Experiment at LEP

6.1 The LEP Collider

The Large Electron Positron Collider (LEP) is the biggest collider built by physicists so far to accelerate e^+e^- beams. It provided the highest center-of-mass energy for e^+e^- collisions - up to $\sqrt{s} = 208$ GeV. The Collider has the form of a ring with a circumference of 26.7 km and was built by the European Organization for Nuclear Research (CERN) at the border of France and Switzerland near Geneva (Figure 6.1).

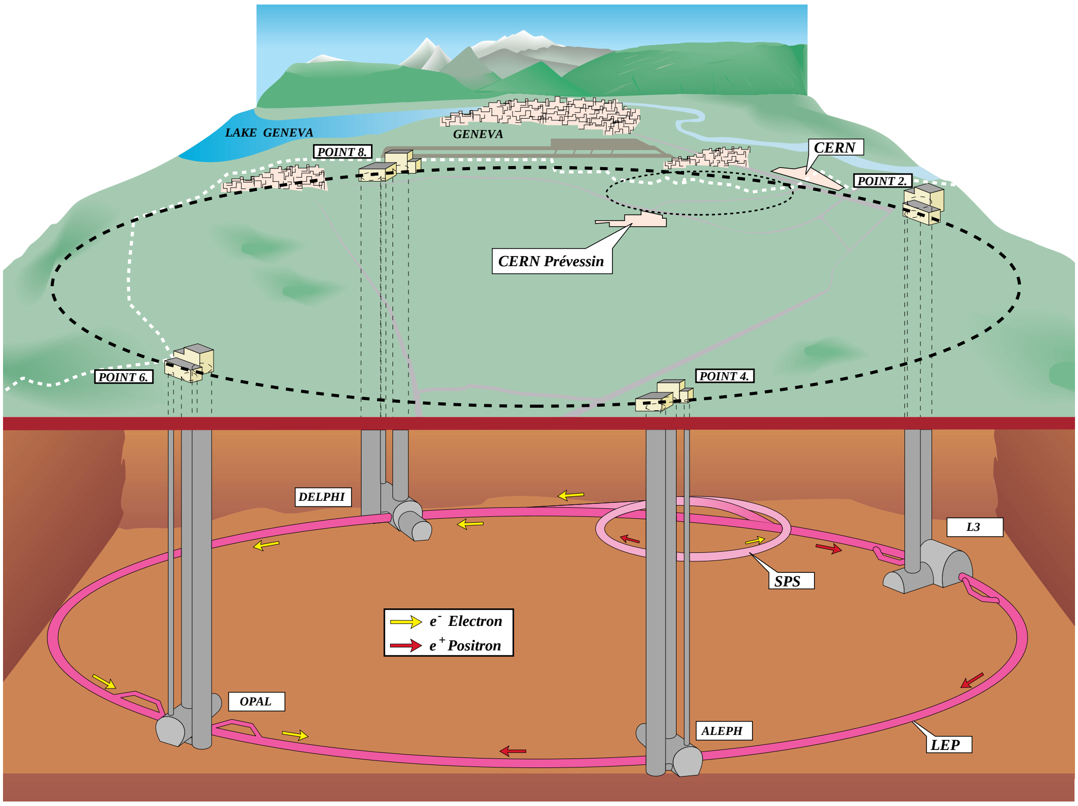

Figure 6.1: *The LEP Collider and the Detectors.*

Electron and positron beams are accelerated in the LEP ring in opposite directions and collide at four interaction areas equipped with four separate particle detectors, ALEPH, DELPHI, L3 and OPAL [70]. Each detector is a quite complicated experimental setup, which triggers, identifies and measures energy, momentum and directions of particles and jets produced in the collisions of e^+e^- beams. The detectors make complete and independent measurements of similar physics processes, serving as complementary but stand-alone experiments.

The LEP operation has started in 1989 and finished in the fall of the year 2000. During these years there were two phases of the LEP operation: the first phase (called LEP I) in the years 1989-1995, and the second phase (LEP II) afterwards. The center-of-mass energy of e^+e^- collisions at LEP I was close to the Z boson mass (about 91.2 GeV). The primary goal of this phase of operation were tests of the Standard Model and precise measurements of the model parameters. Searches for the Higgs boson and new phenomena were also performed. The second phase of LEP operation has started in the fall of 1995. During the LEP II period the center-of-mass energy was continuously increased from 130 GeV in 1995 up to 208 GeV at the end of the operations in the year 2000. These years the main goals were the searches for the Higgs boson and for new phenomena, in particular, searches for SUSY particles, as well as more tests and measurements within the Standard Model with ZZ and W^+W^- pair production.

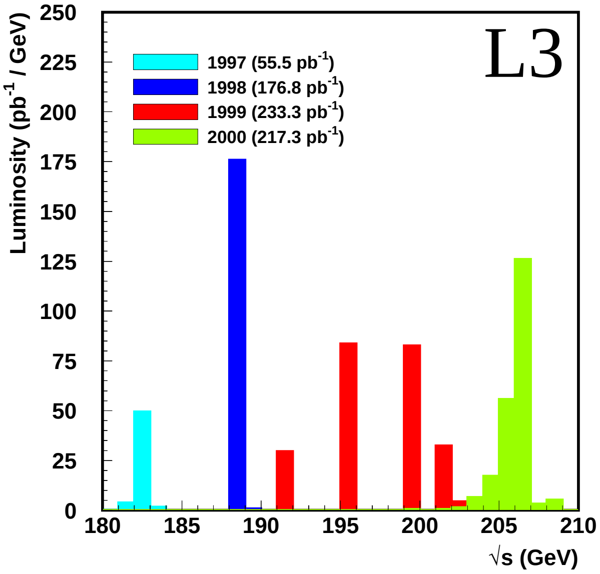

Figure 6.2: *The integrated luminosities collected by the L3 detector from 1997 to 2000.*

Figure 6.2 shows the typical integrated luminosities collected by each of the four LEP experiments at different $\sqrt{s}$ during the last four years of LEP operation. In the year 2000 each of the four LEP experiments collected data at center-of-mass energies from 202 and 208 GeV with an integrated luminosity over 200 pb^{-1}.

Since the increase of the center-of-mass energy of e^+e^- beams leads to increase of the radiation losses, further increase of the energy becomes more expensive and less efficient.

Therefore, in the year 2000 the operation of the LEP Collider has been stopped and now the LEP tunnel is being prepared for the LHC experiments.

6.2 The L3 Detector at LEP

The L3 detector [71] is a general purpose particle detector designed and built to trigger, identify and measure energies, momenta and directions of electrons, photons, muons and hadrons, produced in e^+e^- collisions. Figure 6.3 shows a 3-dimensional view of the detector setup.

To measure the momenta of charged particles with the help of a magnetic field, the detector is surrounded by a solenoidal magnet, providing a uniform 0.5 Tesla field along the beam axis.

The following right handed coordinate system is used in the experiment: the origin is in the geometric center of the detector; the positive z axis coincides with the direction of the electron beam; the y axis points vertically upward and the x axis goes toward the center of the LEP ring. The distance between a point in the x-y plane and the geometric center of the detector is the radius **r**. The azimuthal angle ϕ is an angle between the

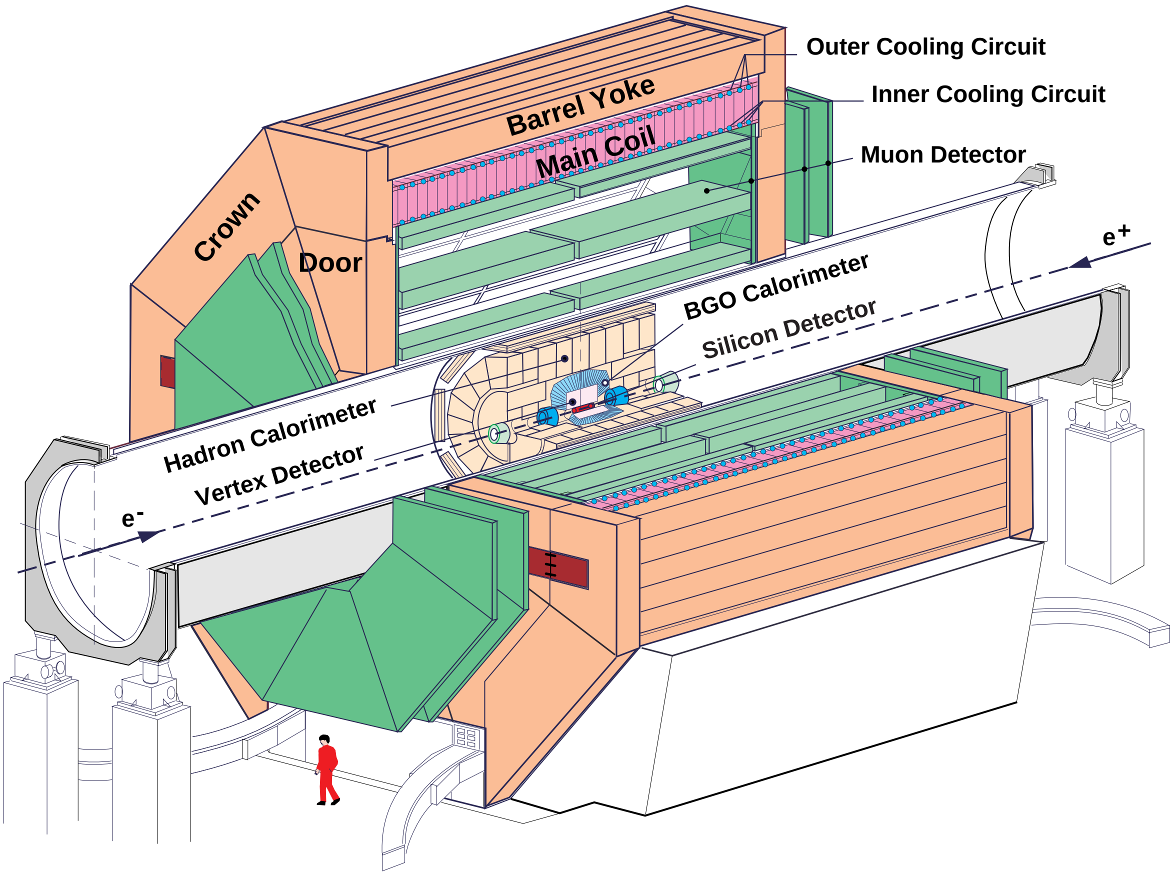

,

__Figure 6.3:__ The 3D view of the L3 detector at LEP.

radius vector $\vec{r}$ and the positive x axis. The polar angle θ is an angle between the direction of a particle and the electron beam direction.

The major components of the L3 detector are characteristic for all general purpose detectors, used in modern High-Energy Physics: the central tracking system surrounding the interaction point; then the electromagnetic and hadron calorimeters and finally the muon spectrometer (their hierarchy is illustrated in Figures 6.3 and 6.4).

The particular L3 detector components are the following:

1. The Central Tracking System
    - The Silicon Microvertex Detector (SMD)
    - The Time Expansion Chamber (TEC)
    - The Z Chamber
    - The Forward Tracking Chamber (FTC)
2. The Calorimetry System
    - The Electromagnetic Calorimeter (BGO ECAL)
    - The Hadron Calorimeter (HCAL)

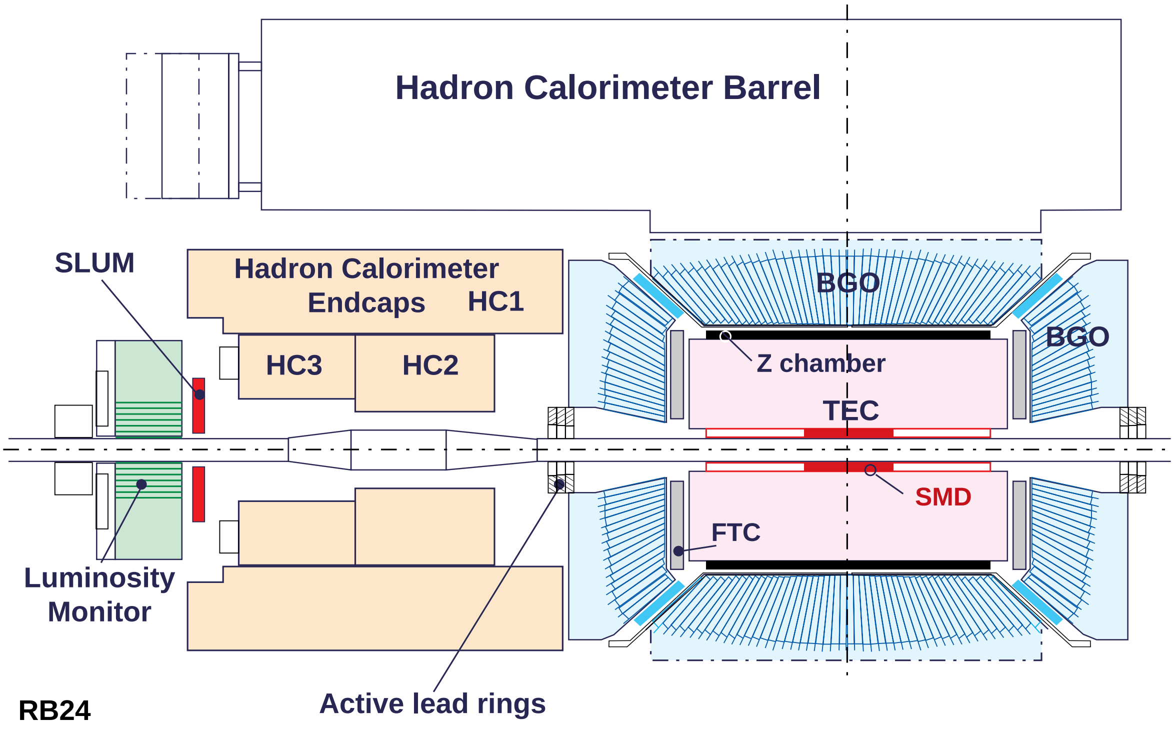

__Figure 6.4:__ Schematic view of the tracking and the calorimeter systems of the L3 detector.

3. The Muon Spectrometer (MUCH)

4. The Magnet System

5. Additional Detectors

    - The Scintillator Counters
    - The Active Lead Rings (ALR)
    - The Luminosity Monitor

In the following sections all these subdetectors are briefly reviewed.

6.2.1 The Central Tracking System

The Central Tracking System consists of the vertex and tracking parts, serving correspondingly for a determination of the origin points of the tracks close to the interaction area and for a measurement of the further traces of particles for the later reconstruction of their tracks.

4.2.1.1 The Silicon Microvertex Detector

The Silicon Microvertex Detector (SMD) is the innermost L3 subdetector, directly surrounding the beam pipe of the collider, which has a radius of 5.3 cm [72]. The main goal of the SMD detector is to locate the particle traces in the area close to the interaction point. After combining with further tracking information, this allows to improve significantly the momentum resolution of the tracks and to identify possible secondary vertices, arising from the decays of particles like hadrons containing a b quark.

The SMD detector consists of two similar cylindrical layers around the beam pipe with radii of about 6 cm and 8 cm, respectively. The length of the SMD along the z-axis is 30 cm which yields a polar angle coverage of $22^\circ \leq \theta \leq 158^\circ$. Both layers consist of 12 modules (ladders), subdivided into two independent halves at $\theta = 0^\circ$. The half-ladders consist of 2 double-sided silicon sensors, which are 70 mm long, 40 mm wide and made from 300 μm thick n-type silicon of high purity. The junction side of the sensors consists of 25 μm wide strips with a readout pitch of 50 μm. They run parallel to the beam axis and so, provide the determination of the $r\phi$ coordinate. On the other side the implantation strips are arranged perpendicular to the junction side strips with a pitch of 50 μm. The readout pitch is 200 μm for $0.53 \leq\mid \cos\theta \mid\leq 0.93$ and 150 μm for $\mid \cos\theta \mid\leq 0.53$. These strips are used for the r-z measurement. A resolution of 7.5 μm in rϕ and 14.3 μm in z is obtained [73]. The structure of the SMD ladders and their arrangement in the $r\phi$-plane are shown in Figure 6.5.

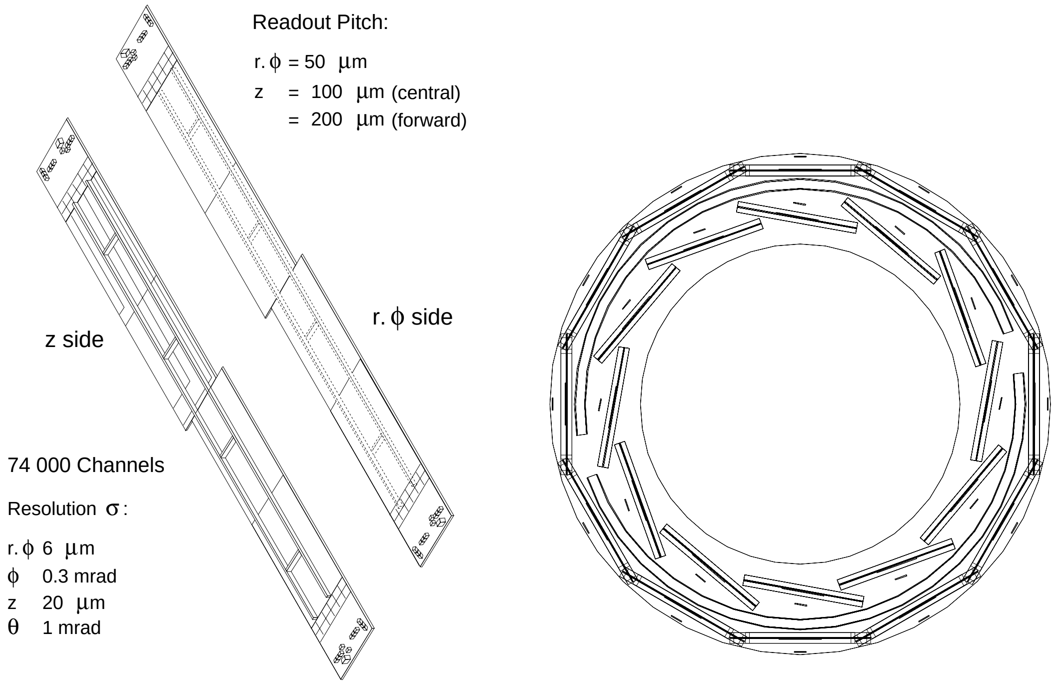

Figure 6.5: *The Silicon Microvertex Detector: the ladder structure (left) and ladder arrangement in the $r\phi$-plane (right).*

4.2.1.2 The Time Expansion Chamber

The Time Expansion Chamber (Figures 6.4 and 6.6) plays the role of the main central tracking detector and serves for the reconstruction of the $r\phi$ and z coordinates of the tracks of charged particles and their momentum. The detector consists of two concentric cylindrical drift chambers with a common gas volume and common end plates. It operates in the time expansion mode. The drift chambers are subdivided into sectors. The anode and cathode wires run in z direction. The inner drift chamber consists of 12 sectors with 8 anode wires each. The outer drift chamber is subdivided into 24 sectors with 54 anode wires each. The inner and the outer radius of the TEC equals 9.15 cm and 45.6 cm, respectively. The length is 126 cm. The anode planes are surrounded by grid planes which divide the drift regions in areas of different field strength. The small field strength between the cathode and the grid plane leads to a small drift velocity which results in a very good spatial resolution. In the region of the high field strength gas amplification occurs and the electron avalanche is detected by the anodes. In order to resolve the left right ambiguity additional wires in the grid plane are read out. The gas mixture consists of 80 % CO_2 and 20 % isobutane. The drift velocity is 6 μm/ns. In rϕ a resolution of (50-60) μm is obtained. Some anode wires are read out on both sides. These signals are used to obtain a rough z coordinate (resolution some cm) by means of the charge division principle.

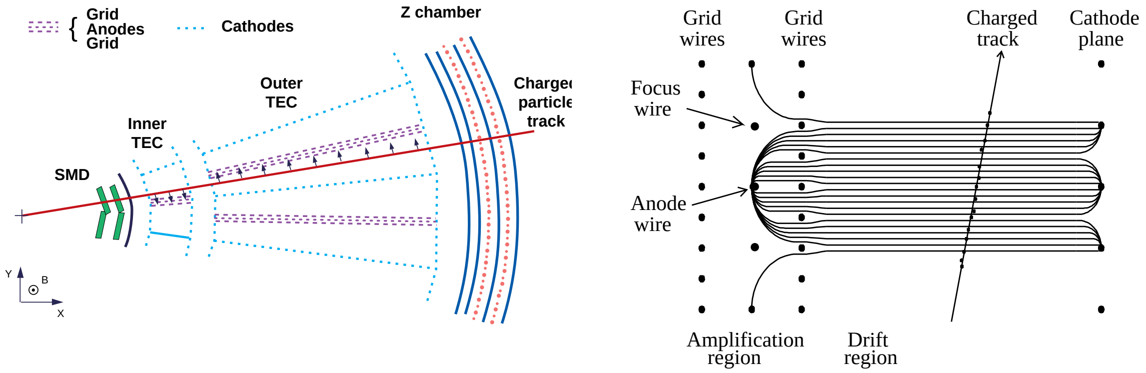

Figure 6.6: *The Central Tracker: $r\phi$ view of the SMD, TEC and the Z Chambers (left) and the drift field in the TEC (right).*

4.2.1.3 The Z Chamber

Particles with a polar angle between 42° and 138° will pass the *Z chamber*. This detector supplements the measurements of TEC and SMD with a z coordinate at $r = 50\ cm$. It consists of two multiwire proportional chambers with cathode readout. The anode wires are aligned in z direction. The two chambers contain two cathode layers each. The cathode layers are made of 240 strips with a pitch of 4.45 mm. The strips of two of the layers are arranged perpendicular to the z direction (z layer) and the strips of the other two layers run under a stereo angle of ±69°. The gas mixture consists of 80 % Argon, 16 % CO_2 and 4 % isobutane. A charged particle traversing the chamber ionizes the gas. The resulting electron avalanche around the anode wire induces image charges on the cathode layers. The relative amount of the signal measured on the individual cathode strips is used for the coordinate determination. The ϕ component of the stereo layer allows the matching of the cluster with a TEC track. The z layers are used for the measurement of the z coordinate. The resolution varies depending on the polar angle. At $\cos\theta = 0$ the resolution is about 200 μm whereas at $|\cos\theta| = 0.74$ the resolution is 1000 μm. The special design of the readout electronics can be used to tag the interacting bunchlet when LEP is operating in the Bunch Train Mode [74].

4.2.1.4 The Forward Tracking Chamber

Complementary to the Z Chamber, the Forward Tracking Chamber is an additional tracking detector just outside the TEC (Figure 6.4). It consists of drift chambers and is used to measure the position and direction of the tracks on the forward edge of the tracker system and provides a spatial resolution of better than 200 μm and an angular resolution better than 10 $mrad$.

6.2.2 The Calorimetry System

In modern particle physics experiments the particles produced in beam collisions, especially, hadrons and jets, have a very high energy. Therefore, they may penetrate very deep in the material around. Moreover, the level of their penetration into the detector material fluctuates. So, it is possible to measure the energy of hadrons or jets only if they are totally absorbed in the detector and do not carry the fluctuating portion of their energy outside. By these reasons, to measure energies of hadrons and jets, one has to use thick detectors consisting of dense material - the calorimeters.

Since the electromagnetic and strong interactions of particles with matter are quite different, the particles participating only in electromagnetic processes produce showers, which develop very differently from those produced by hadrons. The first ones are much shorter and narrower. That's why, the calorimetry system consists usually of two complementary parts: the electromagnetic calorimeter inside, and the hadron calorimeter outside the first one. In this way, all electromagnetic showers are absorbed in the electromagnetic calorimeter, and the hadron ones in the hadron detector. And only weakly interacting particles, but no showers go outside.

4.2.2.1 The Electromagnetic Calorimeter

The electromagnetic calorimeter (BGO) is a uniform-type calorimeter and allows the very precise measurement of electrons and photons with energies between 100 MeV and 100 GeV [75]. It consists of bismuth germanate ($Bi_4Ge_3O_{12}$) crystals pointing to the interaction region, Figure 6.7. The crystals have a front face of 2×2 cm^2, a rear face of 3×3 cm^2 and a length of 24 cm, corresponding to the radiation length of $\sim 21\ X_0$. In the central part of the detector (barrel) there are 7680 crystals. They cover the polar angle $42° \leq \theta \leq 138°$. In the forward-backward region (endcap) of the detector there are 1527 BGO crystals which cover the angles $11.6° \leq \theta \leq 38°$ and $142° \leq \theta \leq 168.4°$. The scintillation light of the BGO crystals is collected by two photodiodes which are mounted at the rear face of the crystals. The energy resolution is 5 % at 100 MeV and

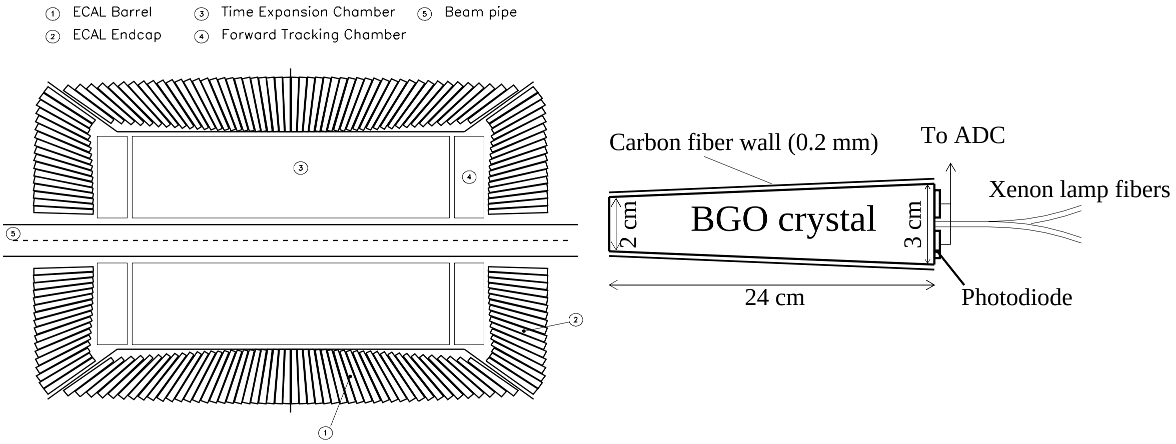

Figure 6.7: *The arrangement of the BGO crystals in the ECAL and schematic view of the crystal signal readout.*

less than 2 % at energies larger than 1 GeV [76].

The gaps between the barrel and the endcap BGO crystals are filled with lead-scintillating fiber calorimeters, called SPACAL or EGAP (Figure 6.4, [77]). They consists of 24 modules (bricks) containing a lead structure filled with scintillating fibers. The scintillation light is collected by phototriodes glued on the rear site of the bricks. The energy resolution of the SPACAL is 15 % at 45 GeV.

4.2.2.2 The Hadron Calorimeter

The energy of hadrons is measured in the hadron calorimeter (Figure 6.8). As in the case of the BGO, it also consists of a barrel and two endcap parts. The barrel calorimeter allows the energy measurement within $35° \leq \theta \leq 145°$ whereas the endcap calorimeters cover the angles $5.5° \leq \theta \leq 35°$ and $145° \leq \theta \leq 174.5°$ in the forward-backward region of the detector.

The central part of the hadron calorimeter contains 9 rings with 16 modules. These modules consist of uranium absorber plates with a width of 5.5 mm interspersed with proportional wire chambers. There are in total 7968 chambers in the barrel part. The two endcaps are each built up of one outer and two inner rings. Each of these rings contains 12 modules.

The material, which a particle arising from the interaction point has to traverse, depends on the polar angle and varies between 6 and 7 nuclear absorption lengths. A muon filter mounted on the outside wall of HCAL, serves also as an additional absorption length suppressing the flow of secondary particles from the hadron calorimeter into the muon chambers.

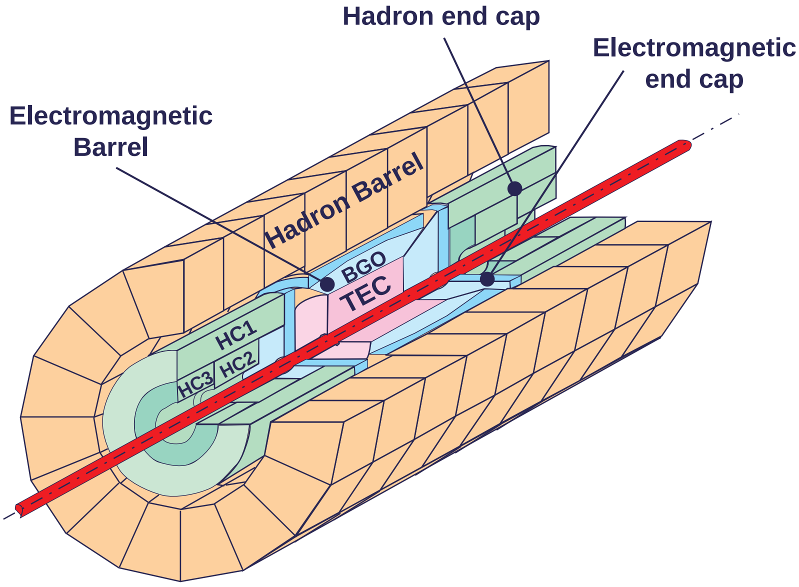

Figure 6.8: *The Hadron Calorimeter of the L3 detector.*

6.2.3 The Muon Spectrometer

The muon detector is the outermost and the largest part in the L3 experiment (Figure 6.9). It envelopes all other detector components. It was designed to measure muon momenta with very high precision. The barrel part of the detector covers the polar angle range from 44° to 136°. It consists of two halves with a gap at z=0. Each of the halves is subdivided into octants. As illustrated in Figure 6.10 (left) each octant consists of five precision drift chambers (P-chambers) which are arranged in three layers. The outer and inner chambers contain 16 wires each whereas the middle chambers are equipped with 24 wires. In order to determine the z-coordinate of a muon track, there is a set of Z-chambers mounted on the top and the bottom of the inner and the outer layer. The momentum resolution for muons measured in all 3 layers is $\sigma_{\mathrm{p}}/\mathrm{p} \approx 2.5\%$ at 45 GeV.

The barrel part of the muon detector is complemented by a forward backward spectrometer covering the polar angles $24° \leq \theta \leq 44°$ and $136° \leq \theta \leq 156°$. Three rings consisting of 16 drift chambers are attached to the magnet doors as shown in Figure 6.10. They are triggered by Resistive Plate Counters (RPCs). The magnet doors are wrapped up with coils producing a toroidal magnetic field of 1.2 T. The resolution depends on the polar angle or, more precisely, on whether the inner and middle layers of the barrel detector were also hit by the muon. The momentum resolution varies from 6% at $\theta = 43°$ to 35% at $\theta = 28°$ [78].

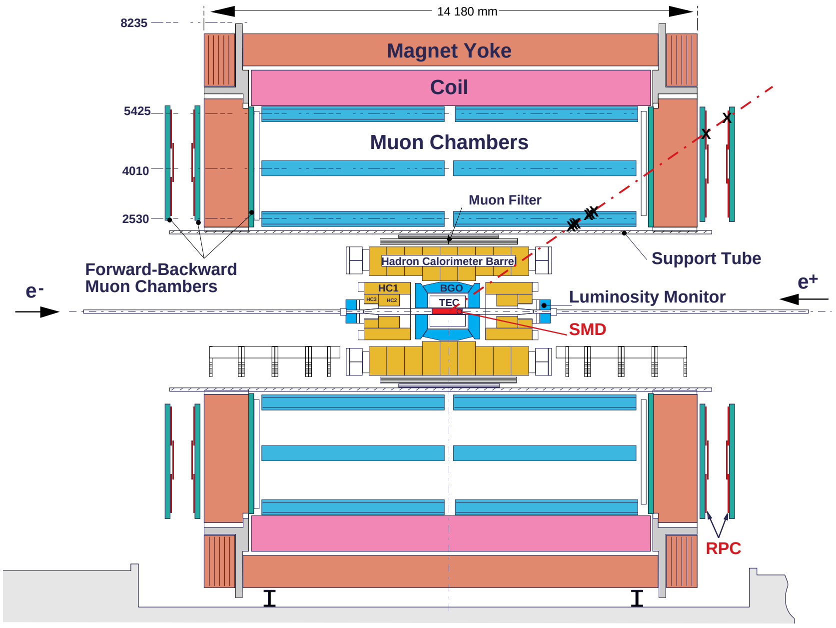

Figure 6.9: *The outer part of the L3 Detector: the Muon Spectrometer and the Magnet.*

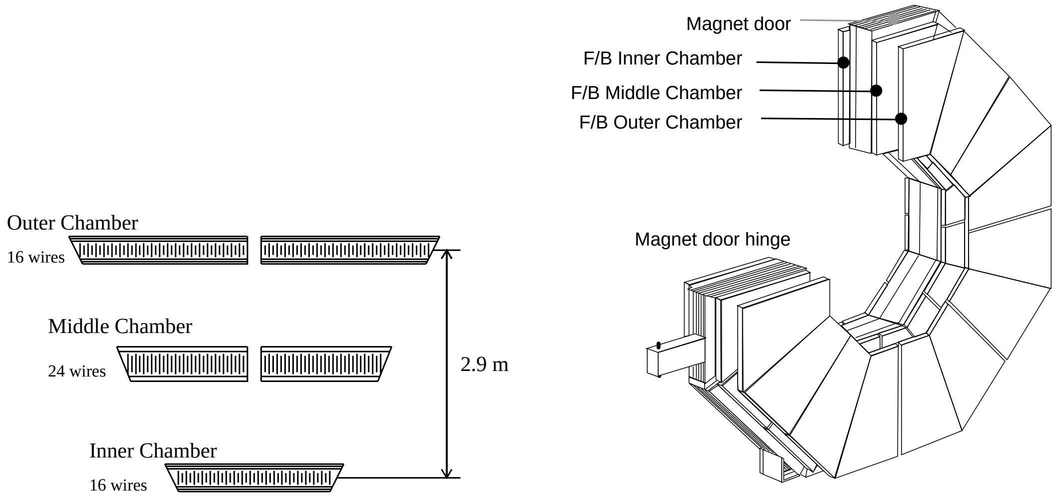

Figure 6.10: *Left: the structure of a muon octant in the barrel. Right: The forward-backward muon chambers.*

6.2.4 The Magnet System

The Magnet System surrounds the whole L3 Detector except the End-Cap (Forward/Backward) Muon Chambers (Figure 6.9). The magnet has an octagonal shaped solenoidal coil with inner radius of 5.93 m and total length of 11.90 m. The coil is surrounded by the iron yoke with an outer radius of 7.90 m. The magnet system provides a uniform 0.5 Tesla solenoidal field parallel to the beam axis, which allows bending of the charged particles tracks and measurement of their momenta in the central tracking system and in the barrel muon chambers.

6.2.5 Additional Detectors

Beside the main components of the L3 detector, the tracker, the calorimeters and the muon spectrometer, there are several smaller detector systems, which serve for auxiliary purposes.

4.2.5.1 The Scintillator Counters

The scintillator counters system consists of 30 single plastic scintillator plates of size 10 mm thick × 290 cm long × 167(187) mm width, which are located between the electromagnetic and the hadron calorimeter. The counters are read out by photomultipliers and the signal is processed by Time-to-Digital Converters (TDCs), which provide the precise time information on the signal with a resolution of 0.46 ns. This allows easily to discriminate cosmic muons from particles produced in the beam collisions. Another purpose of the Scintillator Counters is to trigger hadron events using the scintillator hit multiplicity.

4.2.5.2 The Active Lead Rings

The Active Lead Rings (ALR) are additional detectors, placed in the forward region at distances ±104 *cm* from the interaction point, covering the polar angle ranges of $4^\circ < \theta < 9^\circ$ and $171^\circ < \theta < 176^\circ$ for negative z (Figure 6.4). The ALR detector is used for tagging particles in the forward region and for the improvement of the hermeticy of the whole L3 detector. These detectors consist of $18.5mm$ $(3.3X_0)$ thick lead sheets, needed to initiate particle interactions with matter, followed by plastic scintillators, registering the particle showers.

4.2.5.3 The Luminosity Monitor

A precise knowledge of the luminosity is very important for most of the measurements made at LEP. This is achieved by measuring low angle Bhabha scattering and comparing the measured rate with a precise theoretical calculation [79]. The L3 luminosity monitor consists of two electromagnetic calorimeters complemented with two silicon trackers (SLUM). These two sets are located at $z = \pm 2.7$ m (Figure 6.4) and cover the polar angles $24.93 \text{ mrad} \leq \theta \leq 69.94 \text{ mrad}$.

6.2.6 The Trigger and Data Acquisition System

An efficient trigger system is needed to separate interesting physics events from those events which just contain energy deposits caused by beam-gas, beam-wall interactions, synchrotron radiation or detector noise. All subdetectors are prepared for data taking by the beam crossing signal ($\approx 1.7\ \mu$s before the electron and positron bunches are expected to collide).

The number of events written to tape is reduced in 3 steps. The first step (level-1 Trigger) takes coarse information from the subdetectors into account. These are track information from the TEC (TEC trigger), energy deposits in the calorimeters (energy trigger), scintillator hits (scintillator trigger), energy deposits in the luminosity monitor (luminosity trigger) and tracks in the muon chamber (muon trigger). If one of these triggers has fired, the event is passed to the level-2 trigger, where more time is available to make a first cross check between the individual triggers. This removes already a large fraction of the background events mentioned above. If an event was accepted by more than one trigger, the event is not rejected. At the trigger level-3 the full information of an event is available. The correlation between the individual subdetector information is exploited and tighter requirements on the individual decisions can be made. Events with multiple positive decisions on trigger level-1 or with a luminosity trigger are not rejected. All events passing the trigger level-3 decision are written to tape.

6.3 Detector Simulation and Event Reconstruction

Understanding of the observed experimental results can be achieved only when they are compared to the corresponding theoretical model. In particular, to understand the data, measured and recorded with the L3 detector, people need to compare it with what one can expect from already known physics processes, happening in e$^+$e$^-$ collisions at given center-of-mass energies, like Z or W production. Such expectations should be estimated as precisely as possible taking into account the characteristics and parameters of the particular experimental setup. So, we need *to simulate* by Monte Carlo programs the response, which the L3 detectors will give us from the known processes. From the other side, when looking for a new physics, we need theoretical predictions for them also to be compared with experiment. That's why Monte Carlo simulation is of the same importance for the physics analysis as the L3 experimental data itself.

6.3.1 The Monte Carlo Event Generation

At this level, we consider physics events themselves - the particle production and decay rates and their kinematics. No interaction with detector material is considered here.

First of all, we need to define, which physics events are the most important and expected in e$^+$e$^-$ collisions at a given center-of-mass energy. For example, $e^+e^- \to e^+e^-$, $e^+e^- \to q\,\bar{q}$, $e^+e^- \to W^+W^-$ and $e^+e^- \to Z^0Z^0$ processes are important for studies of two-jet events. So, we need to generate banks of events of these processes as they occur in e$^+$e$^-$ collisions.

At this level, several Monte Carlo generators exist and can be used for different processes. Among several alternative possibilities, the most precise and well-tuned generators have been chosen for each particular process. The generators used in the L3 collaboration and processes, simulated by them, are shown in table 6.1.

M. C. Generator	Physics Processes
BHWIDE [80]	$e^+e^- \to e^+e^-$
KORALZ [81]	$e^+e^- \to \mu^+\mu^-$ and $e^+e^- \to \tau^+\tau^-$
KORALW [82]	$e^+e^- \to W^+W^-$
PHOJET [83]	$e^+e^- \to e^+e^-q\,\bar{q}$
EXCALIBUR [84]	$e^+e^- \to f\bar{f}f'\bar{f}'$ and $e^+e^- \to W^\pm e^\mp \nu$
DIAG36 [85]	$e^+e^- \to e^+e^-e^+e^-$, $e^+e^- \to e^+e^-\mu^+\mu^-$ and $e^+e^- \to e^+e^-\tau^+\tau^-$
PYTHIA [67]	$e^+e^- \to q\,\bar{q}$, $e^+e^- \to Z^0Z^0$ and $e^+e^- \to Z^0e^+e^-$
SUSYGEN [86]	supersymmetry processes

Table 6.1: *The Monte Carlo generators used in the L3 Collaboration.*

For some processes, special event generators have been developed within the LEP working groups. For example, for the generation of stop and sbottom quarks and their decays, a PYTHIA-based GSQUARK generator has been developed for the L3 experiment in collaboration with the OPAL group. On the other side, the experimental data also was used for tuning of the simulation parameters for those processes, which are difficult to simulate precisely, like, for example, the $e^+e^- \to e^+e^-q\,\bar{q}$ process [87,88], where two electrons usually escape at very low angles in the beam pipe, taking an unknown fraction of the total visible energy.

6.3.2 Simulation of the Detector Response

After the physics events are generated, the next step is to calculate, what response the L3 detector and its subsystems will give to each of these events, i.e. which signals these events will produce.

For the simulation of the tracking of particles through the detector material, the general purpose simulation program GEANT3 [89] is used. Based on these program tools, the exact geometry and material parameters of each L3 subdetector are described for the simulation at very detailed level, with accuracy of 0.1 mm. The magnetic field inside the L3 detector is also taken into account using a special grid mapping of the magnetic field in space. Each generated physics event is then simulated in the detector in the following way: the results of process generation, i.e. the produced particles with their momenta are the inputs for the detector response program; then, tracking of each particle in the detector is simulated according to its interaction with atoms and nuclei of the detector materials, like decays, ionization losses, multiple scattering, photoproduction, δ-rays and so on. This simulation uses the cross sections of particular particle interactions with particular target materials at given energies. For the complicated hadronic shower interactions, the GHEISHA [90] simulation package is used. The shower development and individual particle tracking is done down to very low energies of the particles (down to 100 KeV for $e^{\pm}$ and γ, 1 MeV for muons and charged hadrons and down to 10 KeV for neutrons). After that, the particles are considered as stopped in the material due to the kinetic energy losses in the multiple scattering. The results of the test beam studies of the L3 subdetectors, like linearity, compensation and resolution of the e.m. and hadron calorimeters and resolution of the tracker and muon chambers, are also taken into account for tuning the program parameters for a most accurate simulation. The ADC and TDC conversions are also considered in the simulation, providing the results in the same form, as the output of the L3 readout electronics. During the detector operation some imperfections may occur, like electronics noise or darkening of the BGO crystals due to the high radiation or dead wires in the muon chambers. These circumstances are also taken into account as worsening of the corresponding signals, to make the simulation corresponding to the real life. The program developed in this way and used for the simulation of the L3 detector response, is called SIL3. [71].

6.3.3 The Event Reconstruction

The event reconstruction procedure produces the physically meaningful observables, like particle tracks, energy depositions and jet clusters in the calorimeter, identified leptons and missing energy and momentum, from the detector signals of raw format. This procedure is implemented both on the events, generated and simulated by means of Monte Carlo, and on the events from the real e^+e^- collisions data. The reconstruction of known Monte Carlo events helps to understand how precisely the reconstruction is done, and, from the other side, allows to understand, what physics event corresponds to the reconstructed signal from the real e^+e^- beam event. The program of event reconstruction for L3 is called REL3 [71].

Chapter 7

Methodology of the Squark Search

As it was mentioned in the previous chapter, the general idea of experimental data analysis is the comparison of what we measure with what is explained and expected from the existing theoretical model. Thus, the general procedure of analysis deals with three types of event samples: the *experimental data*, the *simulated signal* events and the *simulated background* events.

One important principle here is the requirement that our search method should be absolutely independent of the experimental data. We should develop the method of searches according to our theoretical knowledge and expectations and only then apply it to the experimental data and conclude, what we measure. Therefore the analysis algorithm described in this chapter deals only with simulated signal and background events. Afterwards the search itself is performed on the collected experimental data. This is described in the next chapter.

First, we consider only the $\tilde{t}_1 \to c\tilde{\chi}_1^0$, $\tilde{t}_1 \to bl\tilde{\nu}$, $\tilde{t}_1 \to b\tau\tilde{\nu}$ and $\tilde{b}_1 \to b\tilde{\chi}_1^0$ squark decay channels. Analyzes for these decays are very similar to each other and we call them *main considered squark decay channels*. The *additional* analysis for the three body stop decay $\tilde{t}_1 \to bW\tilde{\chi}_1^0$ differs slightly from the above channels and we describe it in a separate chapter.

7.1 Simulated Squark Signal Samples

The production of the scalar top and scalar bottom quarks in e$^+$e$^-$ collisions at LEP and their decays were discussed in detail in chapter 5. Here we describe the search for the dominating squark production and decay modes, which are listed below with their expected event topology:

$$\begin{array}{llll}
e^+e^- \to \tilde{t}_1\tilde{t}_1 \ , & \tilde{t}_1 \to c\tilde{\chi}_1^0 : & \text{2 jets} & + E_{miss} \\
e^+e^- \to \tilde{b}_1\tilde{b}_1 \ , & \tilde{b}_1 \to b\tilde{\chi}_1^0 : & \text{2 b-jets} & + E_{miss} \\
e^+e^- \to \tilde{t}_1\tilde{t}_1 \ , & \tilde{t}_1 \to bl\tilde{\nu} : & \text{2 b-jets + 2 leptons} & + E_{miss} \\
e^+e^- \to \tilde{t}_1\tilde{t}_1 \ , & \tilde{t}_1 \to b\tau\tilde{\nu} : & \text{2 b-jets + 2 } \tau\text{-leptons} & + E_{miss}
\end{array}$$

The Feynman graphs for these stop and sbottom decays are shown in Figure 7.1.

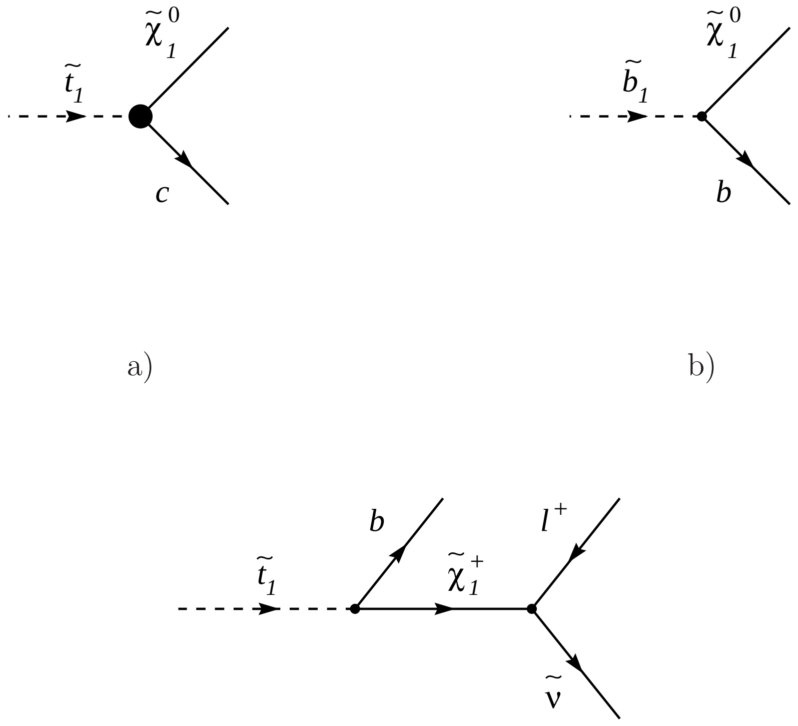

a) b)

c)

Figure 7.1: *Feynman graphs for the considered two body decays of the lightest scalar top, $\tilde{t}_1 \to c\tilde{\chi}_1^0$ (a), the lightest scalar bottom, $\tilde{b}_1 \to b\tilde{\chi}_1^0$ (b), and for stop leptonic decays $\tilde{t}_1 \to bl\tilde{\nu}$ (c) with ℓ being either e, μ, τ or purely τ. The full circle in graph (a) denotes the loop of the flavour changing current (see Chapter 5 for more details).*

The corresponding signal events have the following topological features:

- the significant missing energy E_{miss} is a common feature, because it follows from the R-parity conservation and stability of the LSP, which is assumed to be the lightest neutralino $\tilde{\chi}_1^0$ (in the leptonic stop decay channels the sneutrino decays further into the SM neutrino and the LSP, $\tilde{\nu} \to \nu\tilde{\chi}_1^0$);
- the three-body decays have leptons in the final state; since the τ leptons decay within the detector into one or more charged particles, in contrast to electrons and muons, the decay $\tilde{t}_1 \to b\tau\tilde{\nu}$ is analyzed separately from the decay $\tilde{t}_1 \to b\ell\tilde{\nu}$;
- for each channel we expect two high multiplicity acoplanar jets; the b-jets can be distinguished from other quark jets by means of identifying secondary vertices, also known as *B-tagging*;

- one important feature is the strong dependence of the signal kinematics on the fraction of the visible energy E_{vis} in the event, which is roughly proportional to the mass difference between the squark and the escaping LSP (or $\tilde{\nu}$)

  $$\Delta M = M_{squark} - M_{\tilde{\chi}_1^0(\tilde{\nu})} \sim E_{vis}$$

  (*hereafter, for generalization purposes, when we will speak about the mass difference between squark and the LSP, we will always keep in mind that the LSP is the neutralino* $\tilde{\chi}_1^0$*, and for the leptonic stop decay channels we understand this mass difference as* $M_{squark} - M_{\tilde{\nu}}$*, because the decay* $\tilde{\nu} \rightarrow \nu\tilde{\chi}_1^0$ *is invisible*). When the masses of the squark and the LSP are close to each other, the missing energy E_{miss} is very big in the event and correspondingly, the track multiplicity, their momenta and energy depositions are low. When the mass difference is higher, the track multiplicity, their momenta and energy depositions increase, which gives a completely different event shape, and, consequently, a different kind of background than in the first case.

The squark signal events were produced with the PYTHIA-based Monte Carlo generator GSQUARK [66] for e^+e^- collisions at a center-of-mass energy of 206 GeV. Since both the squark and the LSP masses are unknown, and due to the mentioned dependency of the signal topology on their mass difference, the Monte Carlo signal samples with various M_{squark} and M_{LSP} ($M_{\tilde{\nu}}$ for leptonic stop decays) were generated with mass steps of a few GeV in order to cover all regions of the mass plane. Since the stop and sbottom masses have already been excluded by LEP I up to 45 GeV, we simulate for our analysis MC samples with $M_{\tilde{t}_1}$ and $M_{\tilde{b}_1}$ varying from 45 GeV up to the kinematic limit (E_{beam}) with steps of about 5-10 GeV. The $\tilde{\chi}_1^0$ neutralino mass was scanned from 1 to $M_{\tilde{t}_1} - 3$ GeV for the $\tilde{t}_1 \rightarrow c\tilde{\chi}_1^0$ decay and from 1 to $M_{\tilde{b}_1} - 7$ GeV for the $\tilde{b}_1 \rightarrow b\tilde{\chi}_1^0$ channel. Since the sneutrino mass has also been excluded by LEP I up to 43 GeV, we simulate MC samples with $M_{\tilde{\nu}}$ varying from 43 up to $M_{\tilde{t}_1} - 8$ GeV for the three-body stop decays.

In total, about 180 signal samples were produced, each containing at least 1000 events.

7.2 The Standard Model Background Processes

Depending on the signal topology and kinematics, different Standard Model processes may constitute important or negligible background. In particular, for the considered squark signal channels, we can classify the SM backgrounds by the following criteria: number and type of reconstructed jets in the event; presence or absence of a lepton pair (suitable for the leptonic stop decays); fraction of missing and visible energy (the ΔM dependence) and, of course, the type of physics of the considered process.

Based on the type of physics reaction, we group all Standard Model processes, which may serve as a background, into three categories: two-fermion, four-fermion and two-photon processes.

The first group, **two-fermion** production, consists of the following processes: $e^+e^- \rightarrow e^+e^-$, $e^+e^- \rightarrow \mu^+\mu^-$, $e^+e^- \rightarrow \tau^+\tau^-$ and $e^+e^- \rightarrow q\ \bar{q}$. These processes occur through

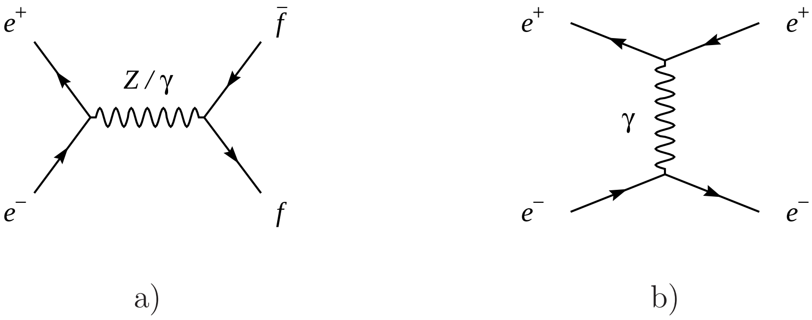

Figure 7.2: *Two-fermion production at LEP.*

the exchange of a virtual Z or γ as shown in Figure 7.2 a). The cross sections for these processes decrease proportional to $1/s$ with increasing center-of-mass energy. There is also an additional t-channel contribution for $\mathrm{e}^+\mathrm{e}^-$ production presented in Figure 7.2 b). At $\sqrt{s} = 206$ GeV the cross section of $\mathrm{e}^+\mathrm{e}^-$ production is one of the highest among all considered backgrounds and is about 1.3 *nb*. For the $\mu^+\mu^-$ and $\tau^+\tau^-$ production the cross sections are very close and approximately equal to 7 *pb*, while for the $q\bar{q}$-production it amounts to about 80 *pb*. The lepton pairs in these processes are coplanar (except leptons from the decaying tau-leptons). The $\mathrm{e}^+\mathrm{e}^-$, $\mu^+\mu^-$ and $q\bar{q}$ events usually have small or no missing energy E_{miss}, except in the cases of a hard photon from initial-state radiation, which escapes undetected in the beam pipe and therefore contributes to E_{miss}. In general, the leptonic pairs serve as a background for the leptonic stop decays $\tilde{t}_1 \rightarrow bl\tilde{\nu}$ and $\tilde{t}_1 \rightarrow b\tau\tilde{\nu}$, while $q\bar{q}$ and $\tau^+\tau^-$ correspond to the two body squark decays.

The second, **four-fermion** group of backgrounds consists of the processes: $e^+e^- \rightarrow W^+W^-$, $e^+e^- \rightarrow W^\pm e^\mp \nu$, $e^+e^- \rightarrow Z^0Z^0$ and $e^+e^- \rightarrow Z^0e^+e^-$. The W^+W^- pairs are produced through the virtual Z^0 or γ exchange in the s-channel and ν exchange in the t-channel (Figures 7.3 a,b). The Z^0Z^0 production occurs through only weak t-channel diagram (as shown in Figure 7.4 a). The single W ($We\nu$) and single Z^0 (Zee) production diagrams are shown in Figures 7.3, c) and 7.4, b), respectively.

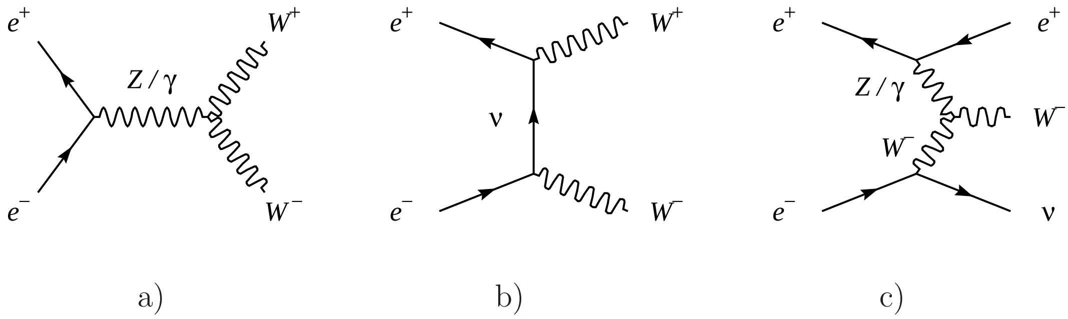

Figure 7.3: *The W pair (a,b) and single W (c) production at LEP.*

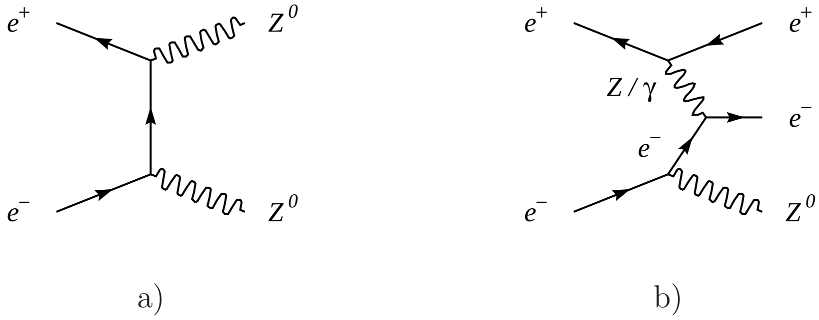

__Figure 7.4:__ The pair (a) and single (b) Z^0 production at LEP.

The $W^{\pm}$ and Z^0 pair production cross sections saturate after the center-of-mass energy reaches a value of about twice the mass $W^{\pm}$ or Z^0, respectively. For single $W^{\pm}$ and single Z^0 production the cross sections continue to increase with higher $\sqrt{s}$. The W^+W^-, $We\nu$, Z^0Z^0 and Zee processes are significant background sources for all the squark channels. Depending on the decays of the W, either $W^{\pm} \rightarrow q\bar{q}$ or $W^{\pm} \rightarrow l\nu$, the W^+W^- pairs show a topology of either four-jets, two-jets + lepton(s) or purely leptons with some missing energy due to the neutrinos. Therefore the significance of this background differs from event to event. The Z^0Z^0 and $Z^0e^+e^-$ processes may also have both jets and leptons in the final state as well as E_{miss}. The considerable missing energy present in $We\nu$ events is to a large extent due to the $e^{\pm}$ usually escaping in the beam pipe.

The third category of background events are **two-photon interactions**, $e^+e^- \rightarrow e^+e^-f\bar{f}$, which also have four fermions in the final state, like the four-fermion group. But this background differs from it by the production mechanism (Figure 7.5). The two-photon interactions have the biggest cross section compared to all other processes at LEP, which is practically independent of $\sqrt{s}$. Therefore this background is very important. The main contribution here comes from the $e^+e^- \rightarrow e^+e^-q\ \bar{q}$ channel with a cross section of about 16.3 nb at $\sqrt{s} = 206$ GeV, while the remaining channels are much less important: the cross sections for $e^+e^- \rightarrow e^+e^-e^+e^-$ and $e^+e^- \rightarrow e^+e^-\mu^+\mu^-$ processes

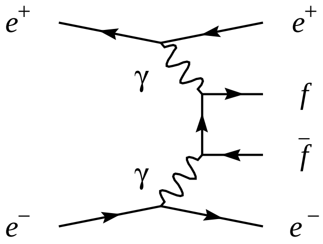

__Figure 7.5:__ The two gamma fermion production at LEP.

are about 0.7 *nb* and the cross section for $e^+e^- \to e^+e^-\tau^+\tau^-$ is about 0.4 *nb*. Since the e^+e^- pair in the final state is usually scattered at very small angles and escapes in the beam pipe, the missing energy E_{miss} is in general quite large. Therefore this background contributes mainly to the region of very low mass difference between the squark and the LSP. Moreover, the uncertainty in the simulation of this process and in the estimation of its cross section are much higher than for other processes. This makes the two-photon processes the most difficult kind of background and requires much higher Monte Carlo statistics for it.

The cross section values, Monte Carlo generators and numbers of generated events for all considered Standard Model background processes are given in Table 7.1. Figure 7.6 shows the cross section dependence on the center-of-mass energy.

To eliminate the influence of the Monte Carlo statistics, the amount of the MC simulated events for each process must exceed at least several times (better, more than 10 times) the number of events of the corresponding process in the experimental data.

In order to correspond to the statistics of the experimental data, the Monte Carlo simulated events of the Standard Model background processes are then weighted according to their cross section σ and the integrated luminosity L_{int} of the experimental data in the following way:

$$N_W = \omega\ N_{M.C.}, \qquad \omega = \frac{L_{int}\ \sigma}{N_{M.C.}}, \tag{7.1}$$

where N_{MC} and N_W are numbers of simulated and re-weighted events and ω is a weight.

Background Group	SM Process	Monte Carlo Generator		σ, pb (at $\sqrt{s} = 206$ GeV)	Number of events, ~
Two fermion	e^+e^-	BHWIDE	[80]	1 300	1 200 000
	$\mu^+\mu^-$	KORALZ	[81]	7	15 000
	$\tau^+\tau^-$	KORALZ	[81]	7	15 000
	$q\bar{q}$	PYTHIA	[67]	80	200 000
Four fermion	W^+W^-	KORALW	[82]	20	150 000
	$We\nu$	EXCALIBUR	[84]	1	10 000
	Z^0Z^0	PYTHIA	[67]	1	10 000
	$Z^0e^+e^-$	PYTHIA	[67]	4	20 000
Two photon	$e^+e^-e^+e^-$	DIAG36	[85]	700	1 800 000
	$e^+e^-\mu^+\mu^-$	DIAG36	[85]	700	1 500 000
	$e^+e^-\tau^+\tau^-$	DIAG36	[85]	400	1 200 000
	$e^+e^-q\,\bar{q}$	PHOJET	[83]	16 300	22 000 000

Table 7.1: *The Monte Carlo generators, cross sections and statistics for the SM background processes.*

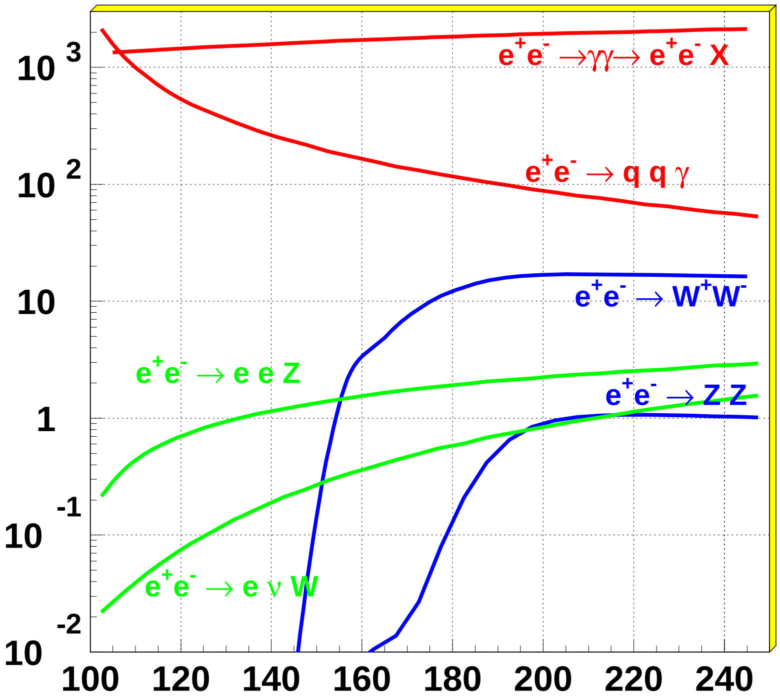

Figure 7.6: *The cross sections of the two-photon, two-fermion and four-fermion Standard Model processes (σ in pb vs. $\sqrt{s}$ in GeV) [70, 71].*

The Monte Carlo signal events are weighted in the same way according to the theoretical prediction on their cross section, but since it is not known exactly, this weighting is just conventional and in the analysis only the signal selection efficiency is used, which does not depend on the value of the cross section.

7.3 The Analysis Tools

The basic idea of our search analysis is the separation of signal events from the known backgrounds by using various properties and features of the events. This can be realized by means of numerical restrictions (cuts) on certain variables describing the event topology, like the total transverse momentum p_T, energy deposition in electromagnetic and hadron calorimeters, etc. To perform this, and, in general, to analyze the event properties numerically, the set of variables, describing the event topology, should be defined and calculated for every event, both for the experimental data and for the Monte Carlo. This procedure includes also particle identification, reconstruction of hadron jets and calculation of their parameters, etc.

7.3.1 Particle Identification

Detectors of different types are used for particle identification. Depending on the detector properties as e.g. radiation and interaction length, the spatial resolution, etc., the

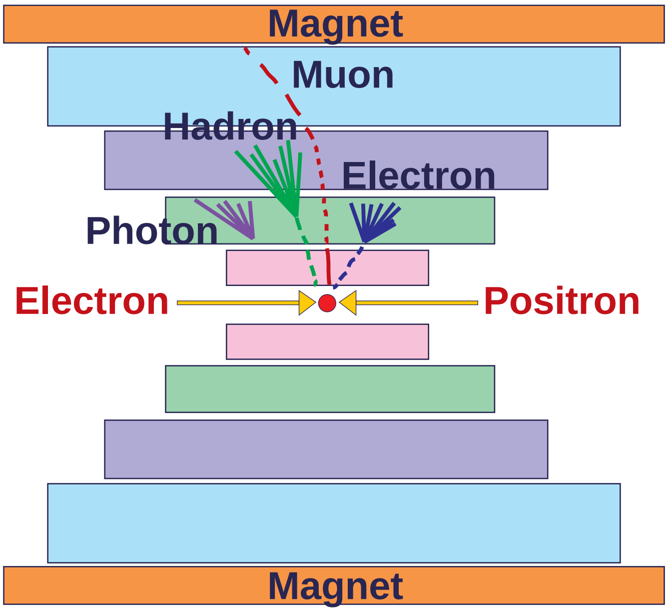

Figure 7.7: *Principles of particle identification in the L3 detector.*

detector response can be used to identify the particle. The following L3 subdetectors allow to perform the identification of particles: Central Tracker, Electromagnetic and Hadronic Calorimeters and Muon Spectrometer. This identification is described in more details below and is summarized in Figure 7.7 and in Table 7.2.

Electron Identification

Identification of electrons is based on two features of their penetration through detectors and interaction mechanisms: tracks in the Central Tracker system and specific

Identified Particle	Central Tracker	ECAL	HCAL	Muon Chambers
γ	—	e.m. shower	—	—
$e^{\pm}$	track	e.m. shower	—	—
μ	track	MIP only	MIP only	track
charged hadron	track	MIP / shower	had. shower	—

Table 7.2: *Basic principles of identification of particles penetrating a particular detector of the L3 setup.*

electromagnetic showers in ECAL. The initially produced electrons are expected to be fully stopped in ECAL and only small tails of electromagnetic showers may reach HCAL due to statistical fluctuations.

Because the electron is a charged particle, it ionizes the gas. The produced ions drift in an electric field and induce signals in the TEC wires called *hits*. Using the set of hits along the particle way with direction from the interaction point, the track is reconstructed. Since usually in e^+e^- collision events a lot of charged particles are produced and since they produce numerous hits in the Central Tracker, possible noise or bias hits should be eliminated from the reconstruction procedure to avoid fake track reconstruction. This is done by requiring some minimal quality of the track to be accepted:

- the momentum of the track must be greater than 0.2 GeV;
- the transverse momentum must be greater than 50 MeV;
- the track must consist of at least 10 TEC hits;
- the distance of closest approach to the primary vertex, DCA, must be not more than 10 mm;
- the difference between the first and last wire numbers should be at least 15.

In the Electromagnetic Calorimeter, electrons and photons cause specific shower, developing via electromagnetic interactions. Compared to the shower of hadrons, the electromagnetic showers is much narrower and shorter and is practically confined in the ECAL (Figure 7.8). This defines two major requirements for showers in the ECAL to be identified as electromagnetic: the transverse size and the length.

The major deposition of the energy in the electromagnetic shower is usually contained within one crystal of the BGO ECAL, which is called the *hottest* cell and is considered to be the shower center. In the transverse plane the shower is mainly contained in 3×3 crystals around the central cell. To distinguish the electromagnetic shower from the hadronic one, the following cut on the lateral energy profile is used:

$$\frac{E_{corr.9}}{E_{corr.25}} > 0.93, \tag{7.2}$$

where $E_{corr.9}$ and $E_{corr.25}$ are corrected energy depositions in 3×3 and 5×5 matrices of crystals around the hottest one with energy E_1:

$$E_{corr.9} = \frac{E_9}{a_1 E_1/E_9 + a_2} \qquad E_{corr.25} = \frac{E_25}{b_1 E_1/E_25 + b_2}. \tag{7.3}$$

The calibration coefficients a_1, a_2, b_1 and b_2 depend on the ECAL region and are used in order to take into account the acceptance and hermeticy of the ECAL detector. The E_9/E_{25} ratio is close to one for electromagnetic showers and much smaller for hadronic ones.

This ratio is also compared to a reference distribution obtained from the test beam data and a χ^2_{EM} is calculated as a measure of the hypothesis that the shower has electromagnetic origin.

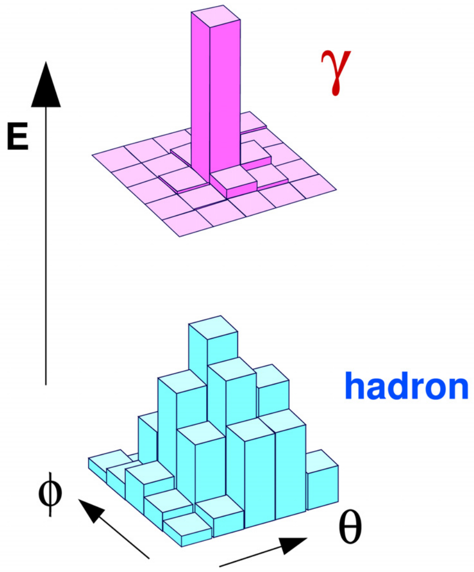

Figure 7.8: *Schematic view of the energy depositions of the electromagnetic (top) and hadron (bottom) showers in calorimeter cells (crystals of BGO ECAL).*

Another quantity for the separation of the electromagnetic and hadronic showers is E_{HCAL}/E_{ECAL}, where E_{ECAL} is the energy in the BGO crystals of the cluster and E_{HCAL} is the energy deposition in HCAL just behind the ECAL cluster. For the electromagnetic showers this ratio must not exceed 0.2.

Finally, $E_{corr.9}$ is taken as electron (photon) energy and its direction is calculated according the center-of-gravity weighting method from the energy depositions in the crystals belonging to the cluster and the e^+e^- interaction point. An electron is considered isolated if the total energy deposited in the cone of 10° around its direction is less than 2 GeV.

Photon Identification

Both electrons and photons interact electromagnetically when penetrating the ECAL, which means that both of them produce similar electromagnetic showers. The electron-photon separation is based on the fact that photons do not produce tracks in the Central Tracker System.

Since usually many tracks and calorimeter clusters may be produced in e^+e^- collisions, the matching between the direction of the electromagnetic shower and the track in TEC is important. This matching is based on the difference between azimuthal angles ϕ of the weighted shower center and the impact point of the track into the BGO calorimeter. The track is matched, if $|\Delta\phi| < 50\ mrad$. Taking into account, that the precision in polar angle in TEC is $\Delta\theta = 0.1\ mrad$ and is worse than the precision in azimuthal angle $\Delta\phi = 0.3\ mrad$, the match requirement on the θ angle is much softer, e.g. $|\Delta\theta| < 50 - 200\ mrad$.

Muon Identification

Muons have a specific type of interactions with matter: they do not decay in the detector and interact only as a minimum ionizing particle (MIP) without producing a shower in the calorimeters. Except for tracks in the Central Tacker System, muons usually penetrate the calorimeters without significant interaction and produce tracks in the Muon Chambers. Low energy muons with momentum below 1.5 GeV do not have enough energy to reach the Muon Detector. Therefore only those tracks in MUCH, which have a momentum above this threshold are considered as muon candidates. Good muons have a track in the Muon Spectrometer and a track in the TEC detector. Both tracks are matched if the azimuthal angle difference $|\Delta\phi|$ is not greater than 100 $mrad$. Depending on the availability of the z-coordinate information from TEC, SMD or Z-Chamber, the difference in polar angle $|\Delta\theta|$ is required to be below $50 - 200\ mrad$.

If the track in the Muon Spectrometer is not matched to any track in the Central Tracker, then it is still considered as a muon candidate if it is confirmed by a hit in the scintillation counters within a 30° azimuthal sector around the track direction and within $5ns$ after the event has started. Otherwise it is suspected to be a cosmic muon, that is not produced in the e^+e^- beam collision.

To reject a cosmic or punch-through muon, the DCA in the planes perpendicular and parallel to the beam direction should be less than 200 mm and 300 mm, respectively. There is also an additional requirement on the DCA significance: $DCA_{xy}/\sigma_{DCA_{xy}} < 4$ and $DCA_z/\sigma_{DCA_z} < 5$.

The muon is considered isolated if the energy deposition in the calorimeter between the cones of 5° and 10° around the track is less than 2 GeV.

Identification of Charged Hadrons

When hadrons (except $\pi^0 \to \gamma\gamma$) cross the detector, their identification is completely different from those of leptons and photons. The strong interactions in which hadrons are involved lead to much higher particle multiplicities. Hadrons produce much broader and longer showers in calorimeters (Figure 7.8). Usually the hadron shower originates in the ECAL, but it develops mainly in the more dense and large HCAL. Sometimes, shower tails may leak into the Muon Chambers. This depends on the initial hadron energy and is a subject of statistical fluctuations.

The special case is a *jet*, which is a set of many hadrons originated in the process of a quark hadronisation. Hadrons in a jet are going at small angles to each other and this results in the high multiplicity tracks and hadronic showers.

Identification of Tau Lepton

The branching ratio of tau decays to electron and neutrino or muon and neutrino is about 17 %. In these cases the τ is identified as an electron or a muon.

Since the tau-lepton is much more massive than electron and muon, it can decay also to hadrons (mainly K and π mesons), which decay in turn. However, the branching ratio of decays to 5 or more charged particles is already negligible (< 0.5 %). Therefore, showers from hadronic decays of the tau-lepton have smaller multiplicity and are narrower compared to jets.

The following criteria have been developed for the τ identification: number of tracks in the Central Tracker not more than 3; number of calorimetric clusters inside the jet not more than 8; ratio of energy in a cone between 10° and 20° around the jet direction and the jet (10° cone) energy, E_{10-20}/E_{jet}, less than one.

7.3.2 Jet Clustering

After the hadronisation, the signature of quarks are high multiplicity jets. To induce the quark properties from the jets, one needs special methods, e.g. clustering algorithms. There are several jet clustering algorithms developed for experimental High Energy Physics. In the L3 experiment, the iterative DURHAM algorithm [91] is widely used. It starts with calorimeter clusters as “pseudo-particles”. To avoid noisy crystals of ECAL and cells of HCAL, only those having energy depositions above 100 MeV are taken into account. Then, for each pair of such ”pseudo-particles” i and j with energies E_i and E_j and open angle α_{ij}, the quantity

$$y_{ij} = \frac{2\ min(E_i^2, E_j^2)\ (1 - \cos\alpha_{ij})}{E_{vis}^2} \tag{7.4}$$

is calculated, where E_{vis} is the total visible energy in the event. The pair with the smallest value of y_{ij} is then merged into a new ”pseudo-particle” by four-momentum addition. Then the list of ”pseudo-particles” is regenerated and the combinatorial procedure repeats until every such y_{ij} becomes greater than some pre-defined cutoff value y_{cut} or only a pre-defined number of jets survives. Finally, the obtained list of ”pseudo-particles” becomes a list of jets found in the event.

Thus, y_{cut} is the free parameter of the jet clustering algorithm. Depending on its value, the tracks and calorimeter clusters of the same event can be grouped into 2, 3, or n jets. For example, value of y_{cut} corresponding to the change of the number of found jets in a particular event from 4 to 3 is denoted y_{34}.

7.3.3 B-tagging

B-tagging is an algorithm that calculates the probability that the event contains hadrons with b-quarks, based on the decay length (life time) information. This information is very important in a study of processes with b-quarks for distinguishing b-jets from other types of jets.

The typical lifetime of hadrons containing b-quark is about 1.5 ps, corresponding to a decay length of several millimeters. Due to the high resolution of the Vertex Detector and the Time Expansion Chamber, this decay length can be observed experimentally.

Many other hadrons, consisting of u, d and c quarks, have either much shorter lifetime and decay practically at the interaction point, or much longer lifetime, like $\pi^{\pm}$, protons, etc. The charmed hadrons, containing c-quark(s) have decay length of about 1 mm and serve as a main source for fake b-quark identification.

Except from the decay length there are some more characteristics which help to distinguish b-quarks from others quarks: the charged particle multiplicity, the reconstructed mass at the decay point, the jet shapes and prompt leptons from the semileptonic decays of B-mesons. All this information is also used in the B-tagging calculation. The detailed description of the technique of B-tagging employed in the L3 experiment is given in [92]. Here only the main ideas are described.

The information on the decay lengths of particles inside a jet is evaluated by checking the compatibility that all tracks in a jet originate from the primary interaction point. This is achieved by calculating the crossing point of every track in the jet with the jet axis. The distance between this crossing point and the primary vertex is denoted as a decay length L with a resolution σ_L. This quantity is signed with the following convention: it is positive, if the crossing point lies on the way of the supposed flight of the particles inside the jet from the interaction point in jet direction; if the crossing point lies on the opposite side of the interaction point with respect to the jet direction, then it is negative. If one plots the significance of the decay length L/σ_L, then one expects a symmetric distribution with respect to zero for quarks decaying very close to the interaction point. For b-quarks, the distribution is asymmetric, enhanced in the positive side, because the b-quarks have a finite decay length (Figure 7.9). The negative side of this distribution is fitted with a suitable function. The resolution function $R(s)$, obtained from this fit, is then used for the positive side of the distribution to calculate the probability $P(s)$, that a track with a significance larger than s originates in the primary interaction point, according to the formula:

$$P(s) = \frac{\int\limits_{s}^{\infty} R(s')ds'}{\int\limits_{0}^{\infty} R(s')ds'}. \tag{7.5}$$

The individual track probabilities are weighted according to the decay length resolution and track momenta and are finally combined into a weighted probability P_w as described in detail in [93]. Jets with b-quarks correspond to low values of this quantity. Finally, the B-tagging discriminant variable is defined in as follows:

$$D_{Btag} = -\log P_w. \tag{7.6}$$

For further improvement of the B-tagging performance a neural network is used, which uses in addition to the decay length information also the information about possible secondary vertices, track multiplicity, reconstructed invariant masses, momenta and jet shape variables. The distributions of the final B-tagging discriminant together with tagging efficiencies and purity are illustrated in Figure 7.10.

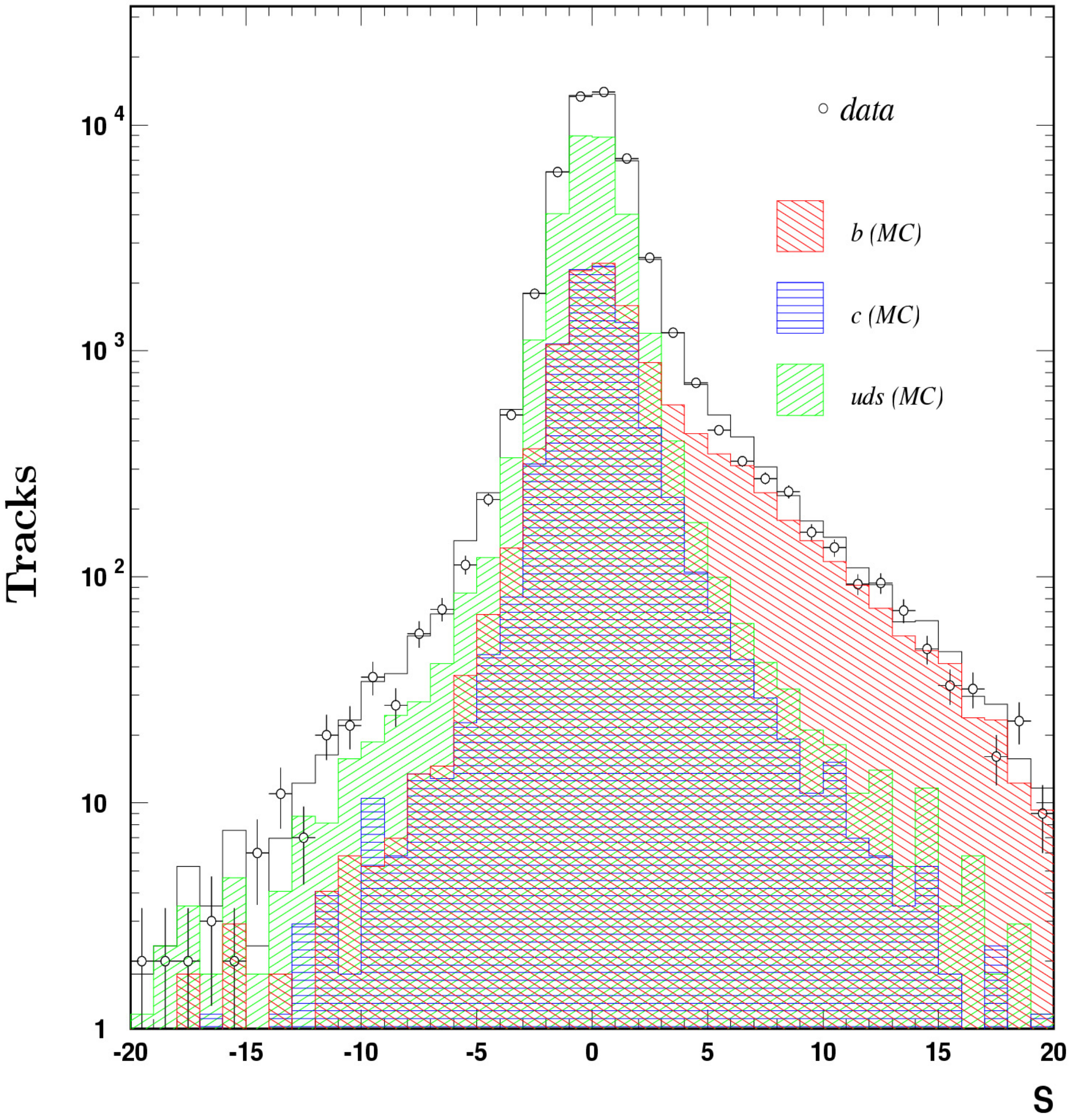

Figure 7.9: *The decay length significance distribution for jets with b, c and uds quarks [70, 71].*

7.3.4 The Kinematical Variables

As it was already mentioned above, to analyze the properties and the topology of various events, one needs to define and calculate for each event a set of quantities, called in general *kinematical variables*. Besides from the number of identified photons, electrons, muons, taus and jets and their energies and momenta, the major kinematical variables, commonly used in the L3 experiment, are the following:

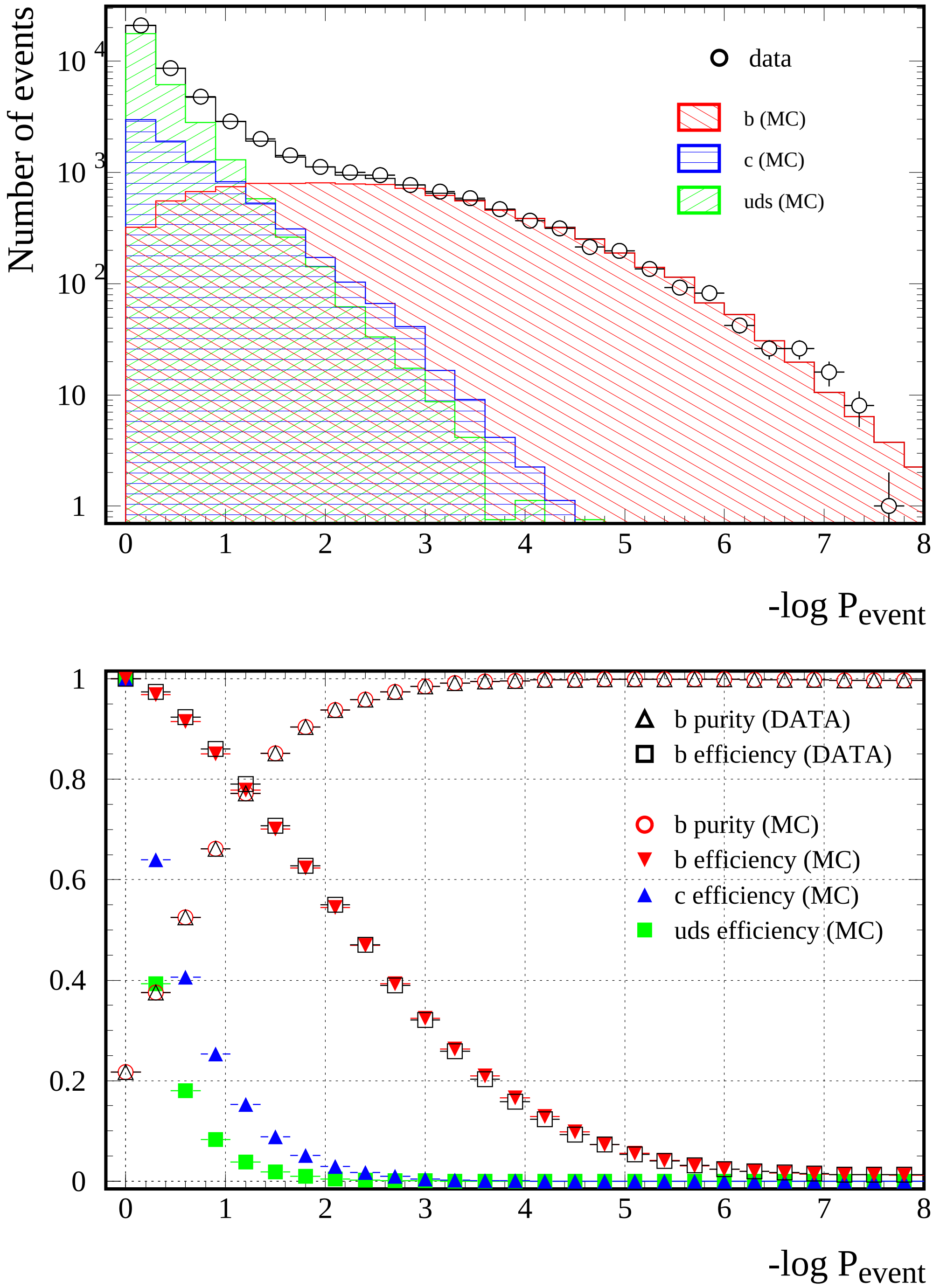

Figure 7.10: *The B-tagging discriminant distribution (a) and tagging efficiency and purity as a function of the cut on* D_{Btag} *(example for L3 data from 1998 year) and comparison with Monte Carlo simulation [70, 71].*

DCA_{min}	Minimum distance of closest approach (DCA) of all tracks in the $r - \phi$ plane.
N_{trk}	Total number of tracks in the Central Tracker System.
N_{clus}	Number of calorimeter clusters, i.e. those having energy depositions above 100 MeV.
N_{gtrk}/N_{trk}	Fraction of "good" tracks in the total number of tracks. The "good" tracks are chosen by additional criteria: number of hits $N_{hits} \geq 15$ and transverse momentum $p_T \geq 100$ MeV.
N_{scint}	Number of hits in the Scintillator Counters in the 5 ns time interval from the bunch crossing.
E_{vis}	Total visible energy in the event, which is equal to the sum of energies, measured in the Central Tracking System, in the calorimeters and in the Muon Chambers.
E_{miss}	Total missing energy in the event, which is calculated as the difference between the center-of-mass energy and the measured visible energy.
p_T	Total transverse momentum in the event ($p_T = p \ \sin\theta$).
(sin) θ_{miss}	(Sinus of) the polar angle of the missing momentum.
E_{vis}^{30}	Energy deposition in cones of 30° half opening angle around the beam directions.
E_{vis}^{30}/E_{vis}	Fraction of visible energy, deposited in 30° cones around the beam directions. Characteristic quantity for the two-photon background events.
$E_{\perp}^{25}$	Energy deposition in $r - \phi$ sector of 25° half opening angle around the direction of the total missing momentum.
E_l, θ_l, ϕ_l	Energy, polar and azimuthal angle of identified (most energetic) isolated lepton.
E_{LUMI}	Total energy deposited in the Luminosity Monitor Detector.
E_{ALR}	Total energy deposited in the Active Lead Rings.
E_{TEC}	The sum of energies associated with charged tracks reconstructed in the TEC detector.
E_{SPACAL}	Energy deposited in the SPACAL calorimeters.
Collinearity	The space angle between two jets (or between two most energetic leptons).

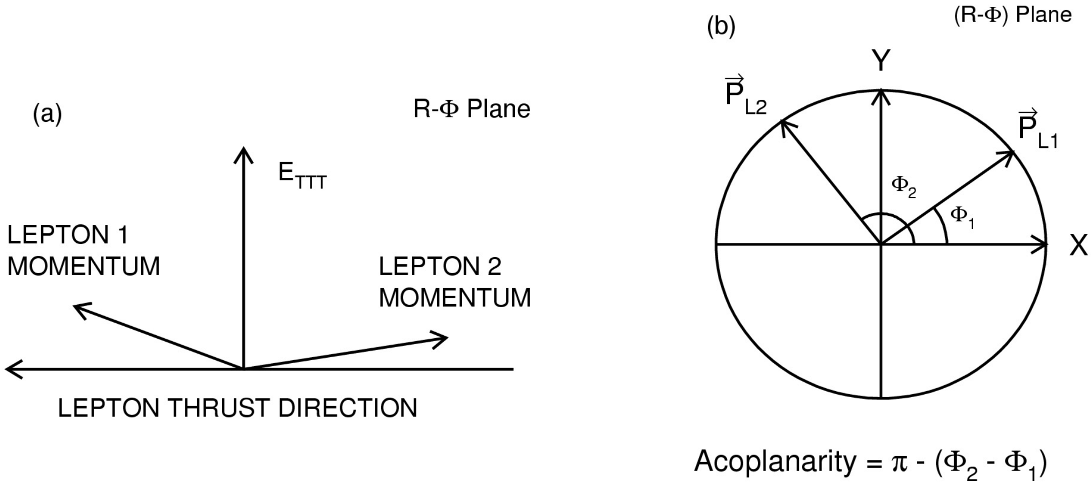

Figure 7.11: *Illustration of the calculation of the E_{TTT} variable (a) and acoplanarity (b) (the acoplanarity is defined as $\pi - (\phi_1 - \phi_2)$, while the coplanarity is $\phi_1 - \phi_2$; the similar convention is for the terms collinearity and acollinearity).*

D_{Btag}	The B-tagging discriminant variable.
$y_\perp$	Jet width, which is defined as the ratio of the sum of the jet's particles momenta transverse to the jet direction, and the jet energy, $\sum p_\perp \ / \ E_{jet}$ (this variable is suitable for distinguishing between broad and narrow jets).
$Thrust$	The event thrust is defined by the following formula (Figure 7.11 a): $Thrust = max \ \frac{\sum \lvert E_{clus}\vec{n}_{clus}\vec{n}_{thrust}\rvert + \sum \lvert \vec{P}_{trk}\vec{n}_{thrust}\rvert + \sum \lvert \vec{P}_{much}\vec{n}_{thrust}\rvert}{\sum E_{clus} + \sum P_{trk} + \sum P_{much}},$ where the thrust axis $\vec{n}_{thrust}$ is the direction which maximizes this expression and the thrust value is the value of the expression at the maximum.
E_{TTT}	Absolute value of the projection of the total momentum of the two most energetic leptons onto the direction, perpendicular to the trust computed in the $r - \phi$ plane. If two leptons form an angle less than 90°, then E_{TTT} is defined as the total transverse momentum of these two leptons (Figure 7.11 a).
E_{TTJ}	Variable, similar to E_{TTL}, but computed for two jets in the analysis of two-jet topology events.
Coplanarity	The angle between two jets (or two most energetic leptons for two-lepton event topology) in the $r - \phi$ plane (Figure 7.11 b).

7.4 The Analysis Procedures

In general, searches for new physics phenomena imply looking for an excess in the number of selected data events over the number of expected Standard Model events in the specific final states of the considered signal and in the region where the signal can explain the excess. In order to locate such an excess, if present, the analysis is carried out in several selection steps of Monte-Carlo signal and background events. Usually one applies cuts on kinematical variables such that as many as possible signal events are passed, but as many as possible background events are rejected.

The corresponding procedure of *tuning the selection* with the usage of only Monte Carlo signal and background samples are described in detail in this section. After the optimal selection for the particular signal processes has been found, it is applied to the data sample in order to find out if we really observe an excess in the experimental data with respect to the Standard Model expectation. This phase of analysis is referred to as *the search* itself and will be described in the next chapter.

7.4.1 Preselection of the Event Samples

In the very first analysis stage the goal is to get rid of events which have obviously irrelevant topological or kinematical features. This procedure is called *preselection.* In order to avoid losses of signal at this preliminary stage of the analysis, preselection cuts are chosen soft enough from the point of view of signal selection, but rejecting everything which is far from similar to the considered signal. Nevertheless, since the fraction of events having topological or kinematical features different enough form the signal is high, the background rejection at this step is also high.

The preselection has also the aim to get rid of events with unreliable or faulty information from the L3 subdetectors, e.g. events, containing fake tracks due to too high background level in TEC, or many calorimetric clusters due to possible radiation damages of some ECAL crystals or due to noise in the HCAL or in the read-out electronics.

Also, at the preselection level we cut out the beam-gas, beam-wall and the cosmic muon events.

In our analysis, the preselection was realized by means of the following requirements on the events. Only events passing these requirements were considered for a more detailed study.

- $N_{trk} \geq 5$
  Lower cut on total number of tracks rejects events with low multiplicity in TEC (mainly Bhabha, dimuon, $\tau^+\tau^-$ two-fermion and $e^+e^-e^+e^-$, $e^+e^-\mu^+\mu^-$, $e^+e^-\tau^+\tau^-$ two-photon backgrounds).

- $10 \leq N_{clus} \leq 40$
  Like the cut on N_{trk}, a lower cut on the multiplicity of calorimeter clusters rejects leptonic two-fermion and leptonic two-photon backgrounds. An upper cut removes $q\bar{q}$ and $e^+e^-q\ \bar{q}$ events.

- $E_{vis} > 5\ GeV$
  This cut removes events with very low visible energy, which are beam-gas and beam-wall events and radiative two-fermion processes.

- $p_T > 2\ GeV$
  Like the lower cut on E_{vis}, this requirement also removes radiative two-fermion as well as beam-gas and beam-wall events.

- $\sin\theta_{miss} > 0.2$
  Removes low-angle events, which are mainly Bhabha and $e^+e^-q\ \bar{q}$ events, as well as other two-photon events.

- $E^{30}_{vis}/E_{vis} < 0.25$
  Similar to the cut on θ_{miss}, this upper cut on the fraction of visible energy deposited in 30° around the beam direction, removes low-angle events and is very powerful for the suppression of $e^+e^-q\ \bar{q}$ events.

- $E_{LUMI} < 5\ GeV$
  Upper cut on the energy deposited in the Luminosity detector rejects low angle (mainly two-photon) events.

- $E_{LUMI} + E_{ALR} < 10\ GeV$
  This cut is additional to the previous one and also rejects low-angle two-photon events.

- $E_{vis}/\sqrt{s} < 0.8$
  The upper cut on the visible energy requires the significant missing energy and removes well-balanced hadron events like $q\bar{q}$ and four-fermion processes.

- $N_{gtrk}/N_{trk} \geq 0.5$
  This cut on the fraction of good track in the total number of tracks is a cut on track quality and rejects fake tracks.

- $E_{TEC}/E_{vis} < 0.8$
  Upper cut on the fraction of visible energy associated with the TEC detector removes events with too high multiplicity in TEC, which are beam background events. This cut also rejects events with fake tracks.

- $E_{SPACAL}/E_{vis} < 0.3$
  Upper cut on the fraction of visible energy deposited in the SPACAL calorimeters rejects events with jet(s), going into the gap between the central and forward (backward) parts of the calorimeter detectors, where the resolution is degraded. This cut also removes possible noise in the SPACAL detector and read-out electronics.

Although this level of the analysis should be independent of the experimental data, we apply the same preselection cuts to both Monte Carlo and data events, because later we will perform the search on the preselected sample of data, containing only the events of topology of our interest, two jets plus missing energy. In addition, we also want to control the *overall* consistency between the set of the considered Standard Model processes and the experimental data, which should exist because the cross section and fraction of events for the SUSY signal is negligible compared to all other (SM) processes in the data and MC samples and a possible discrepancy between data and SM Monte Carlo *at this level of analysis* would indicate non-proper simulation of some of the SM processes or of the detector response. Therefore the preselection cuts are applied at this level also to the data, but here it is safe and does not cause any dependency of our search algorithm on the data.

Event numbers for SM Background processes and the corresponding number of data events are listed in Table 7.3. Just for comparison, an estimation for the corresponding event numbers before the preselection are calculated according to the cross sections and the integrated luminosity of the collected experimental data $L_{int} = 217.3\, pb^{-1}$ (Equation (7.1)). The number of preselected data events is 3856. The total number of events, expected for this topology from the Standard Model, is 4189.1 ± 22.9. Such discrepancy

Considered Standard Model Processes and Experimental Data	Approximate estimate $N_w^{raw} = \sigma \times L_{int}$	Number of preselected events
$e^+e^- \to e^+e^-$	$\sim 277\ 000$	0
$e^+e^- \to \mu^+\mu^-$	$\sim 1\ 500$	0
$e^+e^- \to \tau^+\tau^-$	$\sim 1\ 500$	16.8 ± 1.3
$e^+e^- \to q\ \bar{q}$	$\sim 17\ 000$	464.2 ± 5.9
$e^+e^- \to W^+W^-$	$\sim 4\ 000$	609.9 ± 3.9
$e^+e^- \to W^\pm e^\mp \nu$	~ 200	58.2 ± 0.3
$e^+e^- \to Z^0 Z^0$	~ 200	41.8 ± 1.1
$e^+e^- \to Z^0 e^+e^-$	~ 800	10.4 ± 0.6
$e^+e^- \to e^+e^-e^+e^-$	$\sim 150\ 000$	0
$e^+e^- \to e^+e^-\mu^+\mu^-$	$\sim 150\ 000$	0
$e^+e^- \to e^+e^-\tau^+\tau^-$	$\sim 85\ 000$	31.2 ± 1.6
$e^+e^- \to e^+e^-q\ \bar{q}$	$\sim 3\ 500\ 000$	2956.6 ± 21.6
Sum of *considered* SM Backgrounds	$\sim 4\ 200\ 000$	4189.1 ± 22.9
Data $\sqrt{s} = 202 - 208\ GeV$	$\sim 9\ 500\ 000$	3856

Table 7.3: *Number of events in the SM and Data samples, which passed the preselection cuts and estimate for the corresponding number of events before the preselection according to the cross sections and integrated luminosity. (Number of raw data events is bigger than estimate for the sum of considered SM backgrounds because only SM processes with two-jets and E_{miss} topology are taken into account as interesting for our signal topology.) The quoted errors are due to MC statistics only.*

is due to the high uncertainty in the simulation of $e^+e^- \to q\ \bar{q}$ events, which constitute at this level of analysis the biggest fraction of background. In addition to the comparison between the total numbers of preselected events, the consistency between the data and the SM Monte Carlo samples is even better visible in comparison of various distributions of kinematical variables. In Figures 7.12 and 7.13 the preselected data points are well reproduced by the Monte Carlo prediction, which means that the preselected MC sample is rather well describing the data events being analyzed.

As seen from Figures 7.12-7.13, the major discrepancy between the preselected data and the Monte Carlo events is located in the very low E_{vis} region, which corresponds to the $e^+e^-q\ \bar{q}$ two-photon background. The $e^+e^-q\ \bar{q}$ Monte Carlo is the biggest source of the overall background uncertainty due to uncertainties in its simulation. Another problem at this region of visible energy is that the detector performance and the electronics noise have much bigger contributions to the total measurement uncertainty, than in the medium and high regions of E_{vis}, where the detector resolution is much better. Because of the importance of the $e^+e^-q\ \bar{q}$ process, special studies were performed in the L3 Collaboration to provide the most realistic simulation of these events. In these studies, several Monte Carlo generators were compared to each other and to the experimental data, measured by the L3 detector [88]. The PHOJET generator showed the best agreement and was tuned according to this research.

The main background contributions are $e^+e^-q\ \bar{q}$, W^+W^- and $q\bar{q}$ processes, which represent all three types of the SM backgrounds, two-photon, two- and four-fermion, corresponding to the very low, medium and high regions of E_{vis}, as seen in Figure 7.12. All other SM processes, which are not negligible in the raw MC and data samples, are totally or almost completely eliminated after the preselection, which means that this procedure reduces dramatically (by a factor $\sim 10^3$) the total number of background events. At the same time, the signal efficiency is kept at a rather good level at this stage of analysis, varying from $57 - 74$ % depending on the ΔM region. The worst case corresponds to the very low ΔM values of the signal simulation, where, again, the major fraction of $e^+e^-q\ \bar{q}$ events is located. To keep the signal efficiency as high as possible at this preliminary stage, only soft cuts against the $e^+e^-q\ \bar{q}$ process are applied. This background is dominating with 2956.6 ± 21.6 events, corresponding to about 70 % of the total background statistics.

The number of signal events still amounts only to a tiny fraction of the total event sample, which means that a further, more precise analysis is necessary. As it is visible in Figures 7.12-7.13, the best conditions for separating signal from background are expected at low and medium E_{vis}, small *collinearity* and E^{30}_{vis}/E_{vis} and high E_{TTJ}/p_T and D_{Btag} regions. At the same time, different backgrounds will be important in particular regions of the ΔM. Therefore a dedicated analysis should be preformed individually for different ΔM ranges.

7.4.2 Procedure of the Selection Optimization

After the preselection stage we are left with about 1 % of the total amount of data and Monte Carlo events, but the number of possible signal events still amounts to only a tiny fraction of this sample. The goal now is to accurately tune the selection, i.e. to find

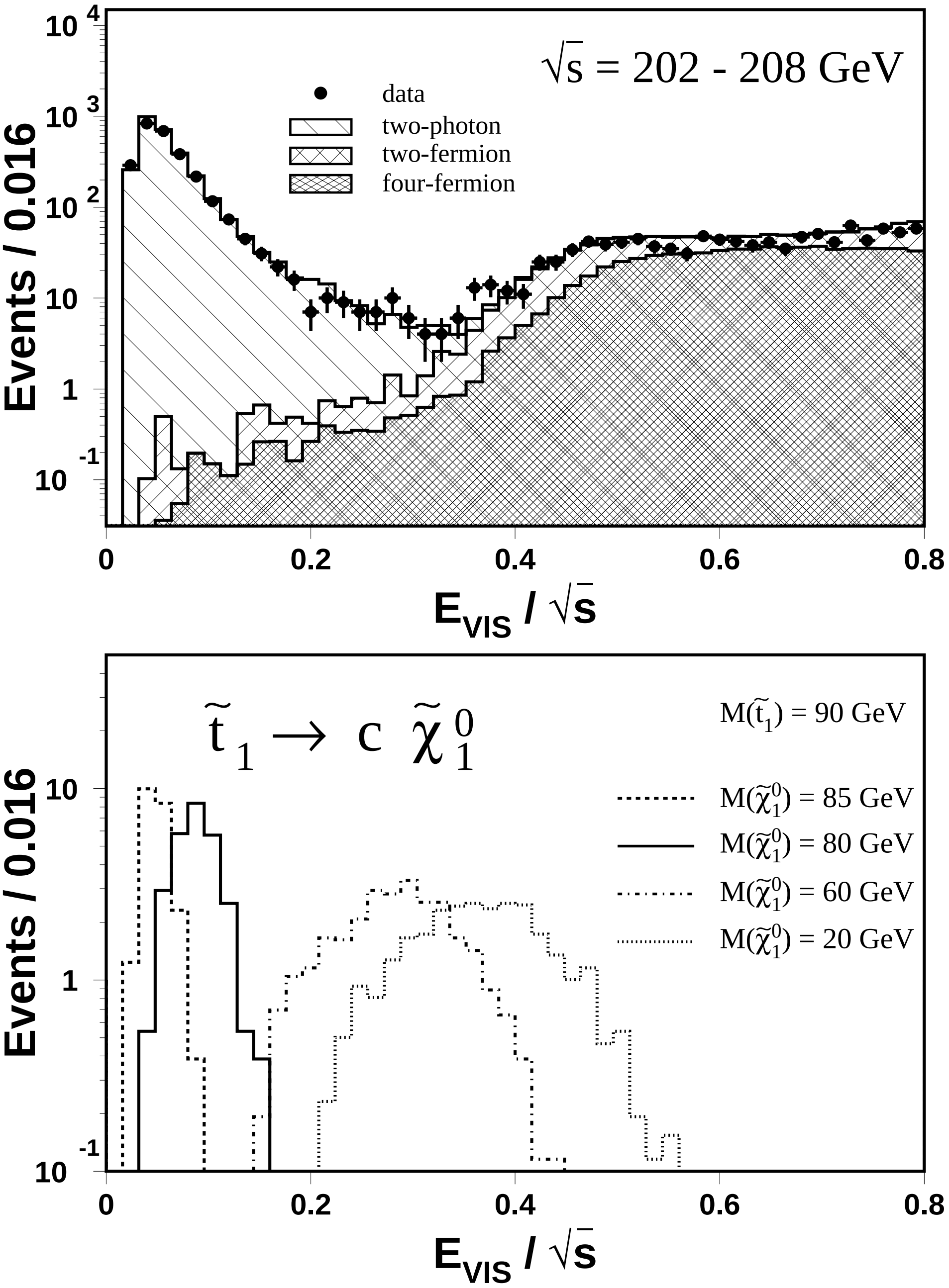

Figure 7.12: *Distribution of E_{vis} after applying the preselection cuts for Data and SM Background Processes (top) and for simulated $\tilde{t}_1 \rightarrow c\tilde{\chi}^0_1$ signal events for various mass differences ΔM between the squark and the LSP. In the upper plot, the SM Backgrounds are summed up. The signal cross sections have typical values expected in the CMSSM.*

a set of most sensitive kinematical variables and to define optimal cut values. These cut values should be optimal in a sense to further reduce background and to increase the

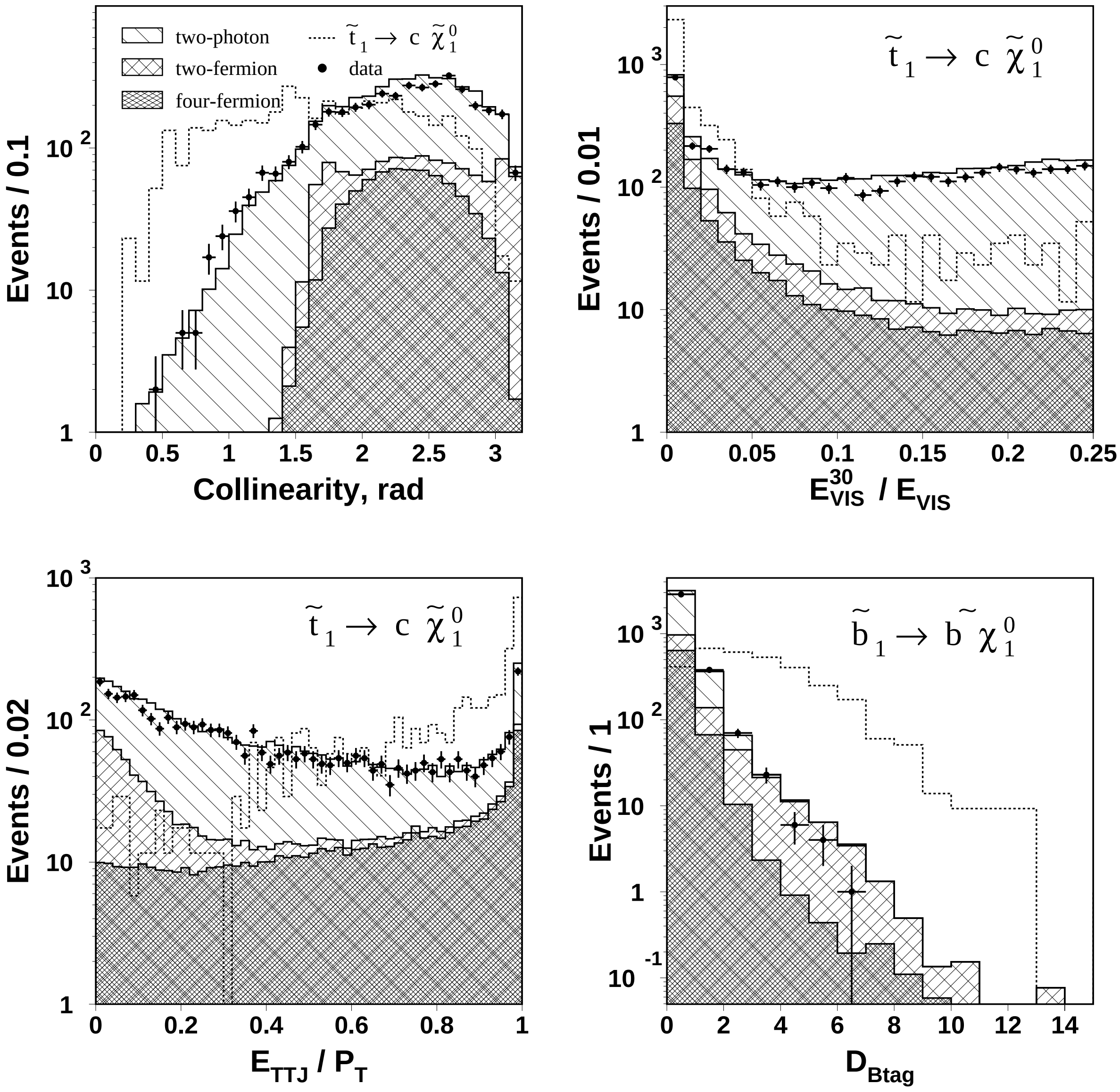

Figure 7.13: *Distributions of collinearity, E_{vis}^{30}/E_{vis}, E_{TTJ}/p_T and D_{Btag} variables after applying the preselection cuts. The SM Backgrounds are summed up, while signal curves are superimposed. The signal cross sections have typical values expected in the CMSSM (scaled by factor 150 for better comparison with background plots). Presented signals correspond to the medium ΔM range (20-40 GeV).*

sensitivity to the signal.

Now we should take into account the unique features of each of the four particular squark decays, $\tilde{t}_1 \rightarrow c\tilde{\chi}_1^0$, $\tilde{t}_1 \rightarrow bl\tilde{\nu}$, $\tilde{t}_1 \rightarrow b\tau\tilde{\nu}$ and $\tilde{b}_1 \rightarrow b\tilde{\chi}_1^0$, Since there are slight differences in topologies of these decays (presence or absence of leptons and b-quarks), the set of the most sensitive variables will be different. The selection optimization will be done for each channel separately, although the selection procedures will be similar.

Since, as it was shown above, the kinematics of the squark signal and corresponding background composition is very dependent on $\Delta M = M_{squark} - M_{LSP}$, the selection optimization should be performed individually for different ΔM ranges. We choose the following ranges: very low ($\Delta M < 10\ GeV$), low ($10 \leq \Delta M \leq 20\ GeV$), medium ($20 < \Delta M \leq 40\ GeV$) and high ($\Delta M > 40\ GeV$). This means, that within the same squark decay channel we choose the same set of cuts on the kinematical variables, but then we perform four independent optimizations for four ΔM ranges. So, we do 16 independent optimizations in total: 4 ΔM ranges for each of the 4 squark decay channels.

The signal kinematics are also dependent on the center-of-mass energy $\sqrt{s}$, at which the scalar quarks are produced. This implies we should simulate signals for different $\sqrt{s}$ and perform different selection optimizations for each $\sqrt{s}$. On the other hand, since we do not know both the squark mass and the LSP mass (or the sneutrino mass), we can not do a direct mass reconstruction and use some mass-dependent cuts. Therefore we assume, that the production cross section of the squarks and event topology are smoothly and not too much changing in the considered range of $\sqrt{s} = 202 - 208\ GeV$ and do the optimization and perform searches in this center-of-mass energy range in a whole. To be on the safe side, we avoid the usage of absolute energy or momentum variables and use only those that are normalized to $\sqrt{s}$ (like $E_{vis}/\sqrt{s}$) or are ratios (E^{30}_{vis}/E_{vis} or E_{TTJ}/p_T). This also has the advantage of dealing with the highest available integrated luminosity in any particular selection, which is a benefit for such small signals.

Choice of the Selection Variables

Among many kinematical variables describing all events, the most important ones corresponding to the main topological features of the signal events should be chosen. As it was mentioned before, the studied scalar quarks are characterized by two jets plus significant missing energy. In the $\tilde{t}_1 \rightarrow bl\tilde{\nu}$ and $\tilde{t}_1 \rightarrow b\tau\tilde{\nu}$ channels, high energetic leptons become an additional feature. For channels with b-quarks the B-tagging variable is also of high importance. Similarly, depending on the other topological and kinematical features of the signal, we choose other sensitive kinematical variables of the above mentioned set.

To choose such a set of variables, distributions of many of them were considered and possible differences between shapes of the signal and the Standard Model background processes were analyzed. From the analysis of these distributions, upper or lower (or both) cuts on the corresponding variables were proposed. The exact numerical values of the cuts are found by the optimization procedure.

The choice of only a few most important variables is necessary because during the selection optimization we optimize all these cuts *simultaneously* and take into account possible correlations between them, which becomes difficult if we use too many variables together. Sometimes, even a combination of two variables into one includes the correlation between them and gives better performance, than using them separately.

Since the four investigated squark channels have a similar topology, the following cuts on the kinematical variables were chosen for optimization as common for all four signal channels (see list of variables and Figures in section 5.3.4):

- Both upper and lower cut on the visible energy, normalized to the center-of-mass energy, $E_{vis}/\sqrt{s}$. The upper cut suppresses four-fermion (W^+W^- and Z^0Z^0) backgrounds and is important for the signal at low ΔM, while the lower cut works against two-photon (mainly $e^+e^-q\ \bar{q}$) background and is very powerful for signal of medium or high ΔM. Tuning of the upper cut takes into account also the requirement of significant missing energy in the event.

- An upper cut on the fraction of visible energy in a 30° cone around the beam directions, E^{30}_{vis}/E_{vis}. Tuning of this cut helps to find a better separation of the signal from the $e^+e^-q\ \bar{q}$ background, especially in the very low region of E_{vis}.

- A lower cut on the total transverse momentum (or, equivalently, missing p_T), normalized to the center-of-mass energy, $p_T/\sqrt{s}$. This cut rejects low-p_T events, which are mainly $e^+e^-q\ \bar{q}$, $q\bar{q}$, $We\nu$ and Zee backgrounds.

- An upper cut on the absolute value of the cosine of the polar angle of missing momentum, $|\cos\theta_{miss}|$, is useful against low-angle events, mainly $e^+e^-q\ \bar{q}$ and radiative $q\bar{q}$. (This is similar to the lower cut on $\sin\theta_{miss}$.)

- An upper cut on the absolute value of the cosine of the polar angle of the event thrust direction, $|\cos\theta_{thrust}|$, rejects events with a high fraction of low-angle momenta particles. This cut supplements the cuts on $p_T/\sqrt{s}$ and $|\cos\theta_{miss}|$.

- An upper cut on the *coplanarity* rejects events where two jets are close to a back-to-back topology, which is characteristic for W^+W^- and Z^0Z^0 events. A lower cut on the *collinearity* is also possible for the studied signal topology, but is less efficient compared to the cut on the *coplanarity* and to the other cuts. Therefore finally it was not included in the optimization procedure.

- A lower cut on the ratio of the E_{TTJ} to the transverse momentum, E_{TTJ}/p_T, has been found to be better than a cut on E_{TTJ}. It is related to a rejection of back-to-back events, in particular, W^+W^- background.

In order to take into account the topological difference between squark decays in each particular channel (with or without leptons, with c or b-quarks, etc.), the following additional cuts are used for the selection of only the relevant signal channels:

- A lower cut on the product of widths of the two jets, $y^1_\perp \times y^2_\perp$, is similar to, but more effective than a lower cut on the minimal width of two jets, $y^{min}_\perp$. This cut is relevant to distinguish between taus and mis-reconstructed jets and real (high multiplicity) hadronic jets. It rejects events with both jets being narrow compared to events with only one tau or two hadronic jets. Of course, for leptonic squark decays $\tilde{t}_1 \to bl\tilde{\nu}$ and $\tilde{t}_1 \to b\tau\tilde{\nu}$ this cut is allowed to be soft.

- A lower cut on the B-tagging discriminant D_{Btag} is important for the selection of events with b-quarks in jets. Obviously, this cut is not used for the $\tilde{t}_1 \to c\tilde{\chi}^0_1$ channel.

- Also, for the leptonic squark decays, $\tilde{t}_1 \to bl\tilde{\nu}$ and $\tilde{t}_1 \to b\tau\tilde{\nu}$, a cut on the energy of the most energetic lepton, normalized to the center-of-mass energy, $E^{max}_{lept}/\sqrt{s}$, is very useful. An upper cut helps to reject high-energetic leptons from $W^{\pm}$ and Z^0 decays in the medium and high regions of E_{vis}, while a lower cut can be useful as a requirement of the presence of at least one energetic lepton, especially in the low E_{vis} region.

Since for the scalar top decay $\tilde{t}_1 \to bl\tilde{\nu}$ the lepton can be either an electron, muon or tau, the kinematics and correspondingly the cuts can be slightly different depending on the particular flavour of the produced lepton. To take this difference into account, we perform separate optimizations for each type of (the most energetic) lepton in the samples of the Monte Carlo events and find three sets of optimal cut values for these three cases. Later, when dealing with the experimental data, we choose appropriate cuts in each event depending on the flavour of the most energetic lepton.

The Optimization Algorithm

Now the goal is to develop an algorithm that can find the optimal numerical cut values on the chosen set of the most sensitive variables, thus providing maximal background suppression, but preserving the signal efficiency as high as possible at the same time. From the mathematical point of view, it implies the minimization of a function, that depends on the kinematical variables. I.e. finding a global minimum of a surface in N_{cuts}-dimensional space, where the coordinates of this space are the cut variables.

An important point here is that the theoretical prediction for the signal cross section is very small (in the order of 0.1 pb), which means that the possibly selected signal is of the order of a few events in the collected experimental data sample. Therefore in the optimization algorithm we must deal with small numbers of the selected signal and surviving background events that are distributed according to Poisson statistics. Because the signal is small, we choose a function of the cut values that corresponds to a 95 % *confidence level (C.L.) upper limit on the expected production cross section* of the scalar quarks, averaged over a large number of Monte Carlo trials (assuming there is no signal). It is defined in the following way:

$$\xi(N_{BG};\ \varepsilon) = \sum_{n=0}^{\infty} P(N_{BG};\ n)\ \frac{N_S^{95}(n)}{\varepsilon\ L_{int}}\ , \tag{7.7}$$

$$P(\mu;\ n) = e^{-\mu}\ \frac{\mu^n}{n!}\ , \tag{7.8}$$

where N_{BG} is the number of surviving Standard Model background events, ε is the efficiency of the signal selection, L_{int} is the integrated luminosity of the experimental data (which plays the role of a normalization constant), $P(N_{BG};\ n)$ is the Poisson probability of observing n events with an expected mean value of N_{BG} events and N_S^{95} is the 95 % C.L. upper limit on the number of selected signal events, when n events are observed and N_{BG} are expected from the background. The function (7.7), which has to be minimized, is called *sensitivity function*, because it reflects the sensitivity of the selection on the cross section of the signal: the smaller the value of this function is, the better sensitivity to the signal we achieve. Values of N_S^{95} for given n and N_{BG} can be calculated numerically according to the following *Bayesian approach* formula (see [94] and [95] for details):

$$1 - C.L. = \frac{\sum\limits_{k=0}^{n} P(N_{BG} + N_S^{CL}(n);\ k)}{\sum\limits_{k=0}^{n} P(N_{BG};\ k)}\ , \tag{7.9}$$

with the confidence level required to be $C.L. = 0.95$.

When ε and N_{BG} are estimated using Monte Carlo events, the sensitivity $\xi(N_{BG};\ \varepsilon)$ can be considered as a measure for the "best signal-over-background" separation. The minimization of (7.7) is performed by means of the MINUIT package [96] from the CERNLIB program library. The dependence of $\xi(N_{BG};\ \varepsilon)$ on the cut variables is established through the dependence of the number of selected background events N_{BG} and signal selection efficiency ε on the selection variables $\{X_i\},\ i = 1, N_{cuts}$, which are simultaneously varied by MINUIT to find a global minimum of this function. During the optimization process the dependence of $\xi(N_{BG};\ \varepsilon)$ on the cut variables $\{X_i\}$ is analyzed and the correlations between the cut variables in the multidimensional space are automatically taken into account. In such a minimization in a multidimensional space, the more variables are used the more difficult it is to find the *global* minimum, because many *local* minima exist and special care should be taken to find the lowest of them, which is the overall minimum. To realize this, the global minimization is done through a big number of minimization attempts with variation of the main parameters of the optimization program: the starting point of the optimization (since from different starting points in this N_{cuts}-dimensional space the surface descends to different local minima) and the optimization step size (since a large step size is useful if the minimum is far away from the starting point, but a small one is more suitable for narrow minima of the surface). After all these minimization attempts have been performed, the best of them (with lowest minimum and having no minimization errors, i.e. successfully converged), is chosen as a global minimum and the corresponding values of the variables $\{X_i^{opt}\},\ i = 1, N_{cuts}$ are taken as the optimal cut values, which thus provide the best (the smallest) 95 % C.L. expected upper limit on the squark production cross section.

The optimization process in the N_{cuts}-dimensional space can be visualized and verified by projecting all cut variables on some axis, for example, "time" or "optimisation steps", and by representing the path to the minimum as change of ε, N_{BG} and $\xi(N_{BG};\ \varepsilon)$ with the step number j in the following way. Let us denote the initial cut values as $\{X_i^{start}\},\ i = 1, N_{cuts}$ and those, corresponding to the (global) minimum as $\{X_i^{opt}\}$. Then at some optimization step number j (where $j = 1$ corresponds to the start of the optimization and $j = N_{steps}$ to the optimal point), the change of the cut values can be represented as:

$$X_i^j = X_i^{start} + (X_i^{opt} - X_i^{start})\frac{j}{N_{steps}} \tag{7.10}$$

We should note, that during a real optimization process, all cuts are varied not proportional to each other, but according to the dependence of the sensitivity function

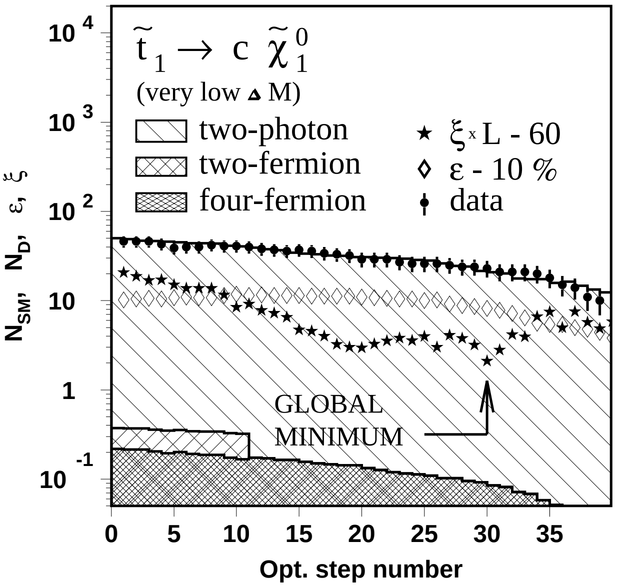

Figure 7.14: *Illustration of the optimization process according to the representation of the cut change by Equation (7.10). (See comments in the text).*

$\xi(N_{BG};\ \varepsilon)$ on the particular cut, i.e. according to its derivatives, because a real surface in this multidimensional space is not a plane. The Equation (7.10) corresponds to a *projection* of the real optimisation process to one dimension in order to make this process visible, i.e. it corresponds to a *direct line* through the real surface in N_{cuts}-dimensional space from the start point to the optimal one.

The illustration plot, corresponding to the optimization for the $\tilde{t}_1 \rightarrow c\tilde{\chi}^0_1$ channel at very low ΔM range is presented in Figure 7.14. (The signal selection efficiency curve is shifted by 10% below "by hands" just for better visualization on the picture. Similarly, the sensitivity function $\xi(N_{BG};\ \varepsilon)$, denoted as "sf" on the plot, is scaled "by hands" by the factor L_{int} and shifted by 60 units below, purely for better visualization in superposition on the plot of numbers of the background and data events. The data is included for illustration of its consistency with the Monte Carlo background and has not any influence on the optimization results.) It is seen, that tightening of the selection cuts leads not only to a background reduction, but also to losses of the signal efficiency, so the really optimal point is difficult to find just from the ratio between signal and background.

Results of the Optimization

As it was described in section 7.1, since masses of both the squark and the LSP are unknown to us, the signal samples were simulated for various mass combinations. Because the decay kinematics are mainly defined not by the squark and LSP masses, but rather by their difference, $\Delta M = M_{squark} - M_{LSP}$, there is no need to perform an optimization for every combination of squark and LSP masses, but it is enough to do it for various ΔM values at some fixed squark mass. So, samples with $M_{squark} = 90\ GeV$ and with several mass values for the LSP (or the sneutrino), corresponding to various ranges of ΔM, were used for the optimization.

As it was already mentioned, the total ΔM range was subdivided into four typical subranges: very low $\Delta M < 10\ GeV$, low $10 \leq \Delta M \leq 20\ GeV$, medium $20 < \Delta M \leq 40\ GeV$ and high $\Delta M > 40\ GeV$. For particular optimisations, the signal Monte Carlo samples with $M_{squark} = 90$ GeV and the ΔM values listed in Table 7.4 have been used.

Squark decay $M_{sq} = 90$ GeV	very low ΔM (M_{LSP}) GeV	low ΔM (M_{LSP}) GeV	medium ΔM (M_{LSP}) GeV	high ΔM (M_{LSP}) GeV
$\tilde{t}_1 \to c\tilde{\chi}_1^0$	5 (85)	10 (80)	30 (60)	70 (20)
$\tilde{t}_1 \to bl\tilde{\nu}$	8 (82)	20 (70)	40 (50)	47 (43)
$\tilde{t}_1 \to b\tau\tilde{\nu}$	8 (82)	20 (70)	40 (50)	47 (43)
$\tilde{b}_1 \to b\tilde{\chi}_1^0$	7 (83)	10 (80)	30 (60)	70 (20)

Table 7.4: *The ΔM and M_{LSP} values of the generated squark signal used for particular optimisations.*

In order to achieve results that are statistically independent on the particular Monte Carlo samples used, the total SM background and signal MC samples were subdivided into two parts, one of which was used for the optimization program. After the program has performed the minimization of the sensitivity function (7.7), the cut values (for a given ΔM of a given squark channel) are frozen and recorded as results. Then the second half of the Monte Carlo samples was used for the independent estimation of the signal selection efficiency and numbers of background events, which were taken as a real result of optimized selection. The data sample was not subdivided into the halves because it is used for measuring the number of events only after the optimization is done.

The optimal cut values, obtained and recorded after the procedure of the minimization of the sensitivity function (7.7) for the four analyzed squark decay channels and four ΔM regions are listed in Tables 7.5-7.8.

For the leptonic squark decays $\tilde{t}_1 \to bl\tilde{\nu}$ and $\tilde{t}_1 \to b\tau\tilde{\nu}$, separate optimizations were performed for events with the most energetic lepton being e, μ or τ. After the cuts for these channels have been optimized, on the second (test) MC sample for every particular event such cuts (either from "e", "μ" or "τ" optimizations) were used, which provide a better value of the sensitivity function for this event.

Except of the Figure 7.14, which is related more to the process of the optimization, the obtained *optimal values* of the cuts can be illustrated by a distribution of some cut variable after all cuts but this one are applied, for example, the distribution of $E_{vis}/\sqrt{s}$ after all cuts except the cuts on the visible energy itself. These distributions are presented in Figures 7.15-7.17 for various variables and various ΔM of the $\tilde{t}_1 \to c\tilde{\chi}_1^0$ and $\tilde{b}_1 \to b\tilde{\chi}_1^0$ signal channels (similar plots for the leptonic squark decays $\tilde{t}_1 \to bl\tilde{\nu}$ and $\tilde{t}_1 \to b\tau\tilde{\nu}$ are

Variable	Cut	very low ΔM	low ΔM	medium ΔM	high ΔM
$E_{vis}/\sqrt{s}$	$\geq$	0.038	0.018	0.196	0.302
$E_{vis}/\sqrt{s}$	$\leq$	0.103	0.174	0.329	0.473
E^{30}_{vis}/E_{vis}	$\leq$	0.078	0.034	0.053	0.072
$p_T/\sqrt{s}$	$\geq$	0.020	0.047	0.016	0.207
$\vert\cos\theta_{miss}\vert$	$\leq$	0.960	0.919	0.979	0.757
$\vert\cos\theta_{thrust}\vert$	$\leq$	0.612	0.875	0.785	0.918
copl., rad	$\leq$	3.120	3.124	2.868	1.367
E_{TTJ}/p_T	$\geq$	0.416	0.408	0.358	0.319
$y^{min}_{\perp} \times y^{max}_{\perp}$	$\geq$	0.016	0.006	0.004	0.001
D_{Btag}	-	-	-	-	-
$E^{max}_{lept}/\sqrt{s}$	-	-	-	-	-

Table 7.5: *Optimal selection cuts, obtained after the minimization of the sensitivity function (7.7) for four ΔM regions of the squark decay $\tilde{t}_1 \to c\tilde{\chi}^0_1$. The cuts on D_{Btag} and $E^{max}_{lept}/\sqrt{s}$ were not used in the optimization, because the signal does not contain leptons or b-quarks.*

Variable	Cut	very low ΔM	low ΔM	medium ΔM	high ΔM
$E_{vis}/\sqrt{s}$	$\geq$	0.060	0.079	0.043	0.002
$E_{vis}/\sqrt{s}$	$\leq$	0.192	0.240	0.384	0.537
E^{30}_{vis}/E_{vis}	$\leq$	0.158	0.145	0.126	0.072
$p_T/\sqrt{s}$	$\geq$	0.020	0.026	0.062	0.029
$\vert\cos\theta_{miss}\vert$	$\leq$	0.868	0.854	0.848	0.800
$\vert\cos\theta_{thrust}\vert$	$\leq$	0.948	0.971	0.880	0.986
copl., rad	$\leq$	3.077	3.102	3.141	3.141
E_{TTJ}/p_T	$\geq$	0.574	0.245	0.230	0.268
$y^{min}_{\perp} \times y^{max}_{\perp}$	$\geq$	0.072	0.052	0.009	0.003
D_{Btag}	$\geq$	0.862	0.801	0.835	2.826
$E^{max}_{lept}/\sqrt{s}$	-	-	-	-	-

Table 7.6: *Optimal selection cuts, obtained after the minimization of the sensitivity function (7.7) for four ΔM regions of the squark decay $\tilde{b}_1 \to b\tilde{\chi}^0_1$. The cut on D_{Btag} was used in the optimization because of the presence of the b-quark, while a cut on $E^{max}_{lept}/\sqrt{s}$ was not used because the signal does not contain leptons.*

	Variable	Cut	very low ΔM	low ΔM	medium ΔM	high ΔM
$l = e$	$E_{vis}/\sqrt{s}$	$\geq$	0.072	0.127	0.201	0.152
	$E_{vis}/\sqrt{s}$	$\leq$	0.369	0.366	0.386	0.433
	E^{30}_{vis}/E_{vis}	$\leq$	0.096	0.118	0.238	0.098
	$p_T/\sqrt{s}$	$\geq$	0.016	0.020	0.028	0.041
	$\|\cos\theta_{miss}\|$	$\leq$	0.905	0.923	0.858	0.934
	$\|\cos\theta_{thrust}\|$	$\leq$	0.886	0.870	0.904	0.950
	copl., rad	$\leq$	3.127	3.101	3.073	3.137
	E_{TTJ}/p_T	$\geq$	0.619	0.444	0.054	0.149
	$y^{min}_{\perp} \times y^{max}_{\perp}$	$\geq$	0.179	0.070	0.030	0.052
	D_{Btag}	$\geq$	0.127	0.305	0.224	0.670
	$E^{max}_{lept}/\sqrt{s}$	*	0.187	0.284	0.017	0.010
$l = \mu$	$E_{vis}/\sqrt{s}$	$\geq$	0.062	0.117	0.216	0.185
	$E_{vis}/\sqrt{s}$	$\leq$	0.183	0.353	0.431	0.458
	E^{30}_{vis}/E_{vis}	$\leq$	0.085	0.101	0.133	0.197
	$p_T/\sqrt{s}$	$\geq$	0.018	0.042	0.027	0.011
	$\|\cos\theta_{miss}\|$	$\leq$	0.910	0.926	0.977	0.939
	$\|\cos\theta_{thrust}\|$	$\leq$	0.836	0.948	0.909	0.991
	copl., rad	$\leq$	3.095	3.128	3.123	3.109
	E_{TTJ}/p_T	$\geq$	0.464	0.308	0.092	0.127
	$y^{min}_{\perp} \times y^{max}_{\perp}$	$\geq$	0.183	0.087	0.071	0.074
	D_{Btag}	$\geq$	0.224	0.009	0.414	0.358
	$E^{max}_{lept}/\sqrt{s}$	*	0.219	0.490	0.025	0.051
$l = \tau$	$E_{vis}/\sqrt{s}$	$\geq$	0.065	0.111	0.071	0.148
	$E_{vis}/\sqrt{s}$	$\leq$	0.190	0.300	0.414	0.488
	E^{30}_{vis}/E_{vis}	$\leq$	0.100	0.055	0.100	0.043
	$p_T/\sqrt{s}$	$\geq$	0.018	0.030	0.033	0.031
	$\|\cos\theta_{miss}\|$	$\leq$	0.933	0.938	0.916	0.774
	$\|\cos\theta_{thrust}\|$	$\leq$	0.923	0.885	0.913	0.816
	copl., rad	$\leq$	3.117	2.965	3.112	3.110
	E_{TTJ}/p_T	$\geq$	0.418	0.192	0.373	0.044
	$y^{min}_{\perp} \times y^{max}_{\perp}$	$\geq$	0.129	0.054	0.062	0.060
	D_{Btag}	$\geq$	0.479	0.574	0.634	0.965
	$E^{max}_{lept}/\sqrt{s}$	*	0.486	0.247	0.021	0.010

Table 7.7: *Optimal selection cuts, obtained after the minimization of the sensitivity function (7.7) for four ΔM regions of the squark decay $\tilde{t}_1 \rightarrow bl\tilde{\nu}$. Separate optimizations were performed for events where the most energetic lepton is e, μ or τ. For the very low and low ΔM regions the cut on $E^{max}_{lept}/\sqrt{s}$ is the lower one (so, "*" in the table means "$\geq$"), while for the medium and high ΔM regions it is the upper one (and "*" means "$\leq$").*

	Variable	Cut	very low ΔM	low ΔM	medium ΔM	high ΔM
$l = e$	$E_{vis}/\sqrt{s}$	$\geq$	0.066	0.121	0.177	0.172
	$E_{vis}/\sqrt{s}$	$\leq$	0.203	0.258	0.367	0.418
	E^{30}_{vis}/E_{vis}	$\leq$	0.103	0.103	0.041	0.202
	$p_T/\sqrt{s}$	$\geq$	0.017	0.021	0.024	0.028
	$\lvert\cos\theta_{miss}\rvert$	$\leq$	0.940	0.901	0.825	0.824
	$\lvert\cos\theta_{thrust}\rvert$	$\leq$	0.941	0.897	0.873	0.993
	$copl.$, rad	$\leq$	3.100	3.096	3.098	3.078
	E_{TTJ}/p_T	$\geq$	0.231	0.554	0.076	0.152
	$y^{min}_{\perp} \times y^{max}_{\perp}$	$\geq$	0.249	0.043	0.049	0.049
	D_{Btag}	$\geq$	0.080	0.665	0.222	0.790
	$E^{max}_{lept}/\sqrt{s}$	$*$	0.485	0.485	0.014	0.010
$l = \mu$	$E_{vis}/\sqrt{s}$	$\geq$	0.053	0.129	0.074	0.126
	$E_{vis}/\sqrt{s}$	$\leq$	0.094	0.264	0.373	0.485
	E^{30}_{vis}/E_{vis}	$\leq$	0.100	0.057	0.104	0.103
	$p_T/\sqrt{s}$	$\geq$	0.016	0.027	0.064	0.027
	$\lvert\cos\theta_{miss}\rvert$	$\leq$	0.919	0.962	0.842	0.876
	$\lvert\cos\theta_{thrust}\rvert$	$\leq$	0.916	0.957	0.898	0.896
	$copl.$, rad	$\leq$	3.109	3.111	3.099	3.118
	E_{TTJ}/p_T	$\geq$	0.625	0.329	0.035	0.318
	$y^{min}_{\perp} \times y^{max}_{\perp}$	$\geq$	0.064	0.110	0.021	0.089
	D_{Btag}	$\geq$	0.870	0.104	0.658	0.594
	$E^{max}_{lept}/\sqrt{s}$	$*$	0.488	0.307	0.013	0.015
$l = \tau$	$E_{vis}/\sqrt{s}$	$\geq$	0.072	0.013	0.165	0.117
	$E_{vis}/\sqrt{s}$	$\leq$	0.124	0.322	0.431	0.427
	E^{30}_{vis}/E_{vis}	$\leq$	0.070	0.028	0.130	0.222
	$p_T/\sqrt{s}$	$\geq$	0.010	0.036	0.015	0.033
	$\lvert\cos\theta_{miss}\rvert$	$\leq$	0.854	0.747	0.927	0.892
	$\lvert\cos\theta_{thrust}\rvert$	$\leq$	0.831	0.845	0.900	0.785
	$copl.$, rad	$\leq$	3.100	3.137	2.960	3.046
	E_{TTJ}/p_T	$\geq$	0.032	0.032	0.061	0.208
	$y^{min}_{\perp} \times y^{max}_{\perp}$	$\geq$	0.142	0.059	0.047	0.062
	D_{Btag}	$\geq$	0.870	0.815	0.598	0.411
	$E^{max}_{lept}/\sqrt{s}$	$*$	0.360	0.338	0.017	0.015

Table 7.8: *Optimal selection cuts, obtained after the minimization of the sensitivity function (7.7) for four ΔM regions of the squark decay $\tilde{t}_1 \rightarrow b\tau\tilde{\nu}$. Separate optimizations were performed for events where the most energetic lepton is e, μ or τ. For the very low and low ΔM regions the cut on $E^{max}_{lept}/\sqrt{s}$ is the lower one (so, "*" in the table means "$\geq$"), while for the medium and high ΔM regions it is the upper one (and "*" means "$\leq$").*

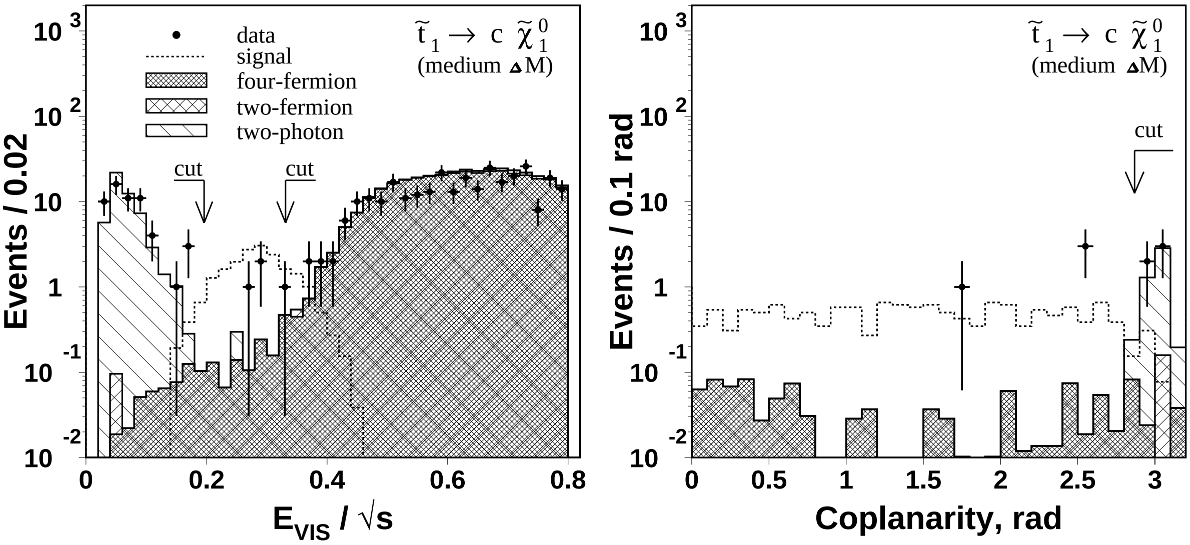

Figure 7.15: *Distributions of the $E_{vis}/\sqrt{s}$ and coplanarity variables after applying the optimal cuts except the cut on the displayed variable. Both plots are given for the squark decay $\tilde{t}_1 \to c\tilde{\chi}_1^0$ and medium ΔM.*

omitted because for these channels there are three sets of optimal cut values depending on the type of the most energetic lepton, e, μ or τ, in any particular event). The shown positions of the cut(s) on the displayed variable correspond to the numerical values listed in Tables 7.5-7.6. From these Figures (together with Figure 7.12) and the corresponding Tables it is seen, that the upper and lower cuts on the $E_{vis}/\sqrt{s}$ are the most important due to the strong dependency of the signal kinematics on $\Delta M \sim E_{vis}/\sqrt{s}$ and differ quite for different ΔM ranges. The cut on D_{Btag} is very important for squark decays with b-quarks. Other cuts are also very useful in separating signal from SM background, for example, cuts on E_{vis}^{30}/E_{vis} and on $p_T/\sqrt{s}$ are helpful in rejecting $e^+e^-q\ \bar{q}$ events.

The signal selection efficiencies and SM event numbers for the optimized selections, are shown for the available signal MC samples at $M_{squark} = 90$ GeV in Table 7.9.

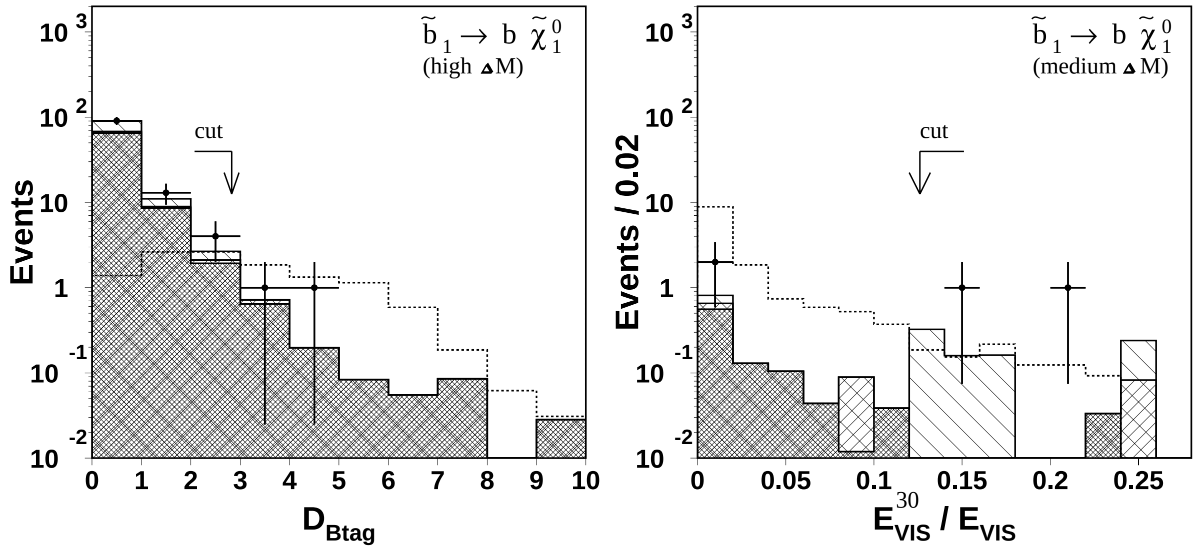

Figure 7.16: *Distributions of the* D_{Btag} *and* E^{30}_{vis}/E_{vis} *variables after applying the optimal cuts except the cut on the displayed variable. Both plots are given for the sbottom quark decay* $\tilde{b}_1 \to b\tilde{\chi}^0_1$*. The designations for the SM background types, data and the signal are the same as in Figure 7.15 (left).*

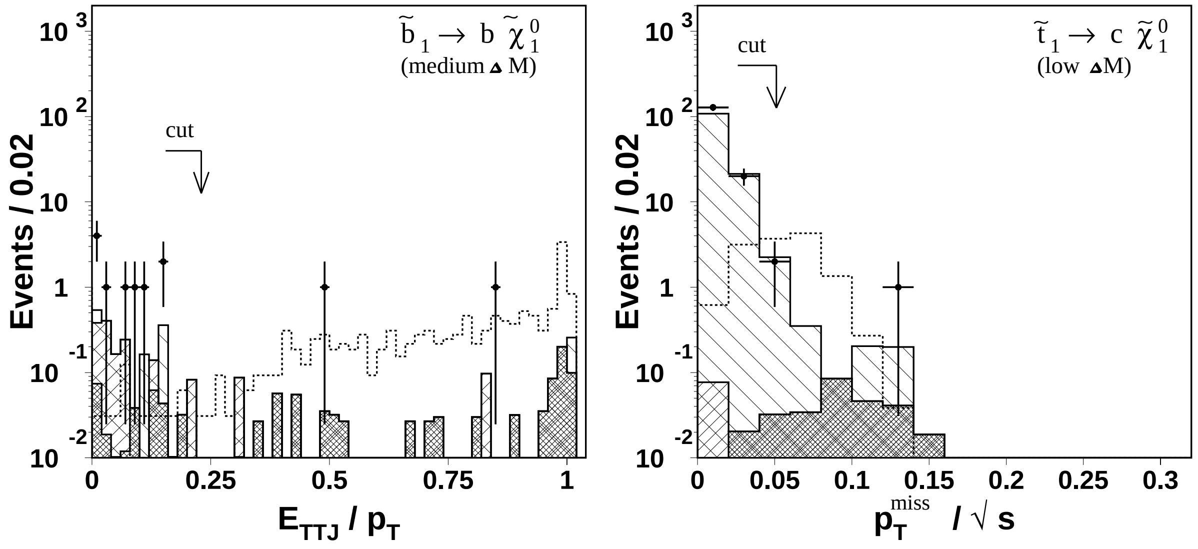

Figure 7.17: *Distributions of the* E_{TTJ}/p_T *and* $p_T^{miss}/\sqrt{s}$ *variables after applying the optimal cuts except the cut on the displayed variable. The left plot corresponds to medium* ΔM *of the* $\tilde{b}_1 \to b\tilde{\chi}^0_1$ *decay; the right one corresponds to low* ΔM *of the decay* $\tilde{t}_1 \to c\tilde{\chi}^0_1$*. The designations for the SM background types, for data and the signal are the same as in Figure 7.15 (left).*

ΔM region	ΔM value (GeV)	$\tilde{t}_1 \rightarrow c\tilde{\chi}_1^0$		$\tilde{t}_1 \rightarrow b\ell\tilde{\nu}$		$\tilde{t}_1 \rightarrow b\tau\tilde{\nu}$		$\tilde{b}_1 \rightarrow b\tilde{\chi}_1^0$	
		ϵ (%)	$N_{\rm SM}$	ϵ (%)	$N_{\rm SM}$	ϵ (%)	$N_{\rm SM}$	ϵ (%)	$N_{\rm SM}$
very low	3	4.6	21.6	-	-	-	-	-	-
	5	18.0	21.6	-	-	-	-	-	-
	7	-	-	-	-	-	-	13.4	3.8
	8	-	-	14.0	2.2	6.0	1.3	-	-
low	10	22.8	3.1	2.8	0.4	1.6	1.6	22.0	2.3
	20	-	-	25.8	0.4	15.8	1.6	-	-
medium	30	36.0	1.3	15.1	1.4	21.5	0.5	42.2	1.5
	40	-	-	30.4	1.4	23.4	0.5	-	-
high	47	-	-	25.4	0.7	24.6	0.7	-	-
	50	16.1	1.9	-	-	-	-	24.0	1.6
	70	17.4	1.9	-	-	-	-	17.4	1.6
	89	15.0	1.9	-	-	-	-	21.5	1.6

Table 7.9: *The signal selection efficiencies ϵ and SM event numbers $N_{\rm SM}$ in the selections optimized for the (main considered) stop and sbottom decay channels, preselected as a function of ΔM for the available signal MC samples with $M_{\tilde{t}_1}$ and $M_{\tilde{b}_1}$ equal to 90 GeV.*

Chapter 8

Search for Squark Events in the Experimental Data

8.1 The Experimental Data Sample

As it was described in chapter 6, starting from the year 1995 the LEP accelerator has entered into a new phase of operation at center-of-mass energies above the Z-peak, first, starting from $\sqrt{s} = 130\ GeV$ and then increasing the beam energy more and more. During the years 1995-1999, data from e^+e^- collisions were collected at center-of-mass energy values listed in Table 8.1. The year 2000 was the last year of the LEP accelerator operations. In that year the LEP machine was running at the center-of-mass energy range of $202 - 208$ GeV and the total luminosity collected by the L3 detector during that year amounts to 217.3 pb^{-1}. Like in the previous years, the luminosity is not uniformly distributed over the whole center-of-mass energy range as shown in the Figure 8.1. But as it was noted in the previous chapter, the present squark analysis deals with the whole data sample of $\sqrt{s}$ of $202 - 208$ GeV having all the energy-type kinematic variables normalized to the particular value of $\sqrt{s}$, which allows us to perform the optimization once for the whole energy sample and then to use the same optimal cuts for any particular energy subsamples.

Operation year	$\sqrt{s}$, GeV	$L_{int},\ pb^{-1}$	Operation year	$\sqrt{s}$, GeV	$L_{int},\ pb^{-1}$
1995, 1997	130	6.1	1998	189	176.8
1995, 1997	136	5.9	1999	192	29.7
1996	161	10.9	1999	196	83.7
1996	172	10.3	1999	200	81.7
1997	183	55.5	1999	202	37.0

Table 8.1: *The center-of-mass energies and corresponding integrated L3 luminosities of the LEP II operation phase during the years 1995-1999.*

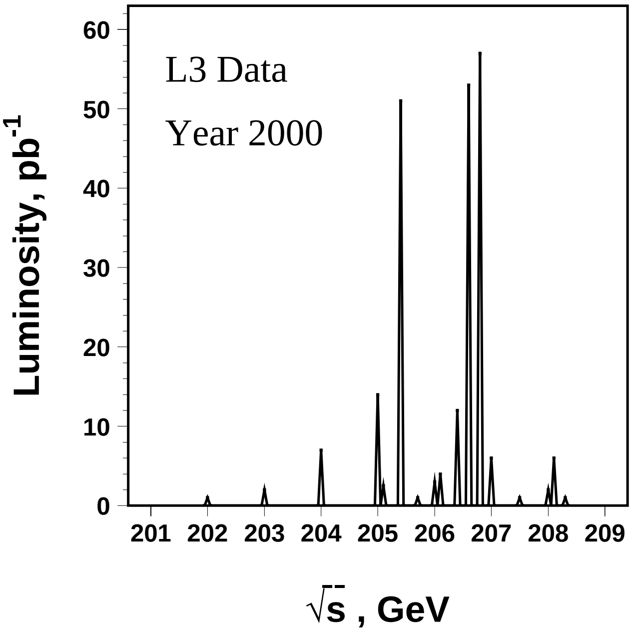

Figure 8.1: *Distribution of the luminosity of experimental data, collected by the L3 detector in the year 2000, over the center-of-mass energy.*

The search for the scalar quark events (i.e. selecting the squark candidate events in the experimental data and estimation of the statistical consistency between the numbers of the observed data events and those expected from the Standard Model Monte Carlo), described in this thesis, has been performed on the L3 experimental data, collected during the year 2000.

8.2 The Squark Selection Results

8.2.1 The Experimental Observations and SM Expectations

After the selection cuts are frozen as result of the optimization, they are applied to the second halves of the SM background and SUSY signal Monte Carlo samples and to the data. The numbers of the selected data events and corresponding expectations from the SM Monte Carlo, as well as the signal selection efficiencies are listed in Tables 8.2-8.5 for the four scalar quark decay channels and four ΔM ranges in each channel after the optimal cuts have been applied. The results of "OR" combination of the four ΔM selection cuts are presented (i.e. a particular event is required to satisfy at least one set of the cuts among the four cut sets corresponding to the four ΔM ranges) Here the data sample of total integrated luminosity 217.3 pb^{-1} with center-of-mass energies in the range $202 - 208$ GeV is used.

Totally, in the combinations over all four ΔM ranges, 29 data events are observed and 26.47 ± 2.74 are expected from the Standard Model processes for the $\tilde{t}_1 \rightarrow c\tilde{\chi}^0_1$ decay

	very low ΔM	low ΔM	medium ΔM	high ΔM	combined
ε_{signal}, %	18.0 ± 1.7	22.8 ± 1.9	36.0 ± 2.2	17.4 ± 1.7	-
$\mathrm{e^+e^-}$	-	-	-	-	-
$\mu^+\mu^-$	-	-	-	-	-
$\tau^+\tau^-$	-	-	-	-	-
$q\bar{q}$	-	-	-	-	-
W^+W^-	-	-	0.15 ± 0.09	0.50 ± 0.16	0.65 ± 0.18
$W^\pm e^\mp \nu$	0.09 ± 0.02	0.23 ± 0.03	0.63 ± 0.04	0.35 ± 0.03	1.19 ± 0.06
Z^0Z^0	-	0.06 ± 0.06	0.17 ± 0.10	1.02 ± 0.24	1.25 ± 0.27
$Z^0\mathrm{e^+e^-}$	-	-	-	-	-
$e^+e^-e^+e^-$	-	-	-	-	-
$e^+e^-\mu^+\mu^-$	-	-	-	-	-
$e^+e^-\tau^+\tau^-$	-	-	-	-	-
$e^+e^-q\,\bar{q}$	21.48 ± 2.61	2.84 ± 0.95	0.32 ± 0.32	-	23.38 ± 2.72
All bg.	21.57 ± 2.60	3.13 ± 0.95	1.27 ± 0.35	1.87 ± 0.29	26.47 ± 2.74
Data	23	1	4	1	29

Table 8.2: *Number of observed data events, the expectations from the Standard Model processes and the signal selection efficiencies as result of the application of the optimal cuts for the squark decay $\tilde{t}_1 \to c\tilde{\chi}_1^0$ onto the independent samples of the Monte Carlo events and to the whole data sample of center-of-mass energy $202-208$ GeV. The quoted errors are due to MC statistics only.*

channel. The same numbers for the decays $\tilde{t}_1 \to bl\tilde{\nu}$ and $\tilde{t}_1 \to b\tau\tilde{\nu}$ are 4 to 4.04 ± 1.00 and 5 to 3.90 ± 1.01, respectively. The observation from the data for the $\tilde{b}_1 \to b\tilde{\chi}_1^0$ decay is 6 events which again is in good agreement with 7.72 ± 1.34 events expected from the Standard Model Monte Carlo.

To summarize, a good statistical agreement between numbers of observed data events and expectations from the Standard Model processes is seen in all channels and ΔM ranges. The biggest difference between the observations and expectations from the Standard Model corresponds to medium ΔM of the $\tilde{t}_1 \to c\tilde{\chi}_1^0$ decay (4 data events comparing to 1.27 ± 0.35 from the backgrounds) and to high ΔM of the $\tilde{t}_1 \to b\tau\tilde{\nu}$ decay (3 data and 0.68 ± 0.34 background events). Taking into account the statistical errors, both of them are about 1.6 standard deviations.

In all squark channels, the $e^+e^-q\,\bar{q}$ process is the dominant background in the very low ΔM range, which makes the signal/background separation most difficult for the $\tilde{t}_1 \to c\tilde{\chi}_1^0$ channel. The reason is that one cannot use powerful cuts on D_{Btag} and on the energy of the most energetic lepton. For medium and high ΔM for all channels

	very low ΔM	low ΔM	medium ΔM	high ΔM	combined
ε_{signal}, %	14.0 ± 1.6	25.8 ± 1.9	30.4 ± 2.1	25.4 ± 1.9	-
$\mathrm{e}^+\mathrm{e}^-$	-	-	-	-	-
$\mu^+\mu^-$	-	-	-	-	-
$\tau^+\tau^-$	-	-	-	-	-
$q\bar{q}$	-	-	0.31 ± 0.22	0.31 ± 0.22	0.46 ± 0.27
W^+W^-	-	0.05 ± 0.05	0.40 ± 0.14	0.30 ± 0.12	0.60 ± 0.17
$W^\pm e^\mp \nu$	-	0.02 ± 0.01	0.05 ± 0.01	0.02 ± 0.01	0.08 ± 0.01
Z^0Z^0	-	-	-	0.06 ± 0.06	0.06 ± 0.06
$Z^0\mathrm{e}^+\mathrm{e}^-$	-	-	-	-	-
$e^+e^-e^+e^-$	-	-	-	-	-
$e^+e^-\mu^+\mu^-$	-	-	-	-	-
$e^+e^-\tau^+\tau^-$	-	-	-	-	-
$e^+e^-q\,\bar{q}$	2.21 ± 0.84	0.32 ± 0.32	0.63 ± 0.45	-	2.84 ± 0.95
All bg.	2.21 ± 0.84	0.39 ± 0.32	1.39 ± 0.52	0.69 ± 0.26	4.04 ± 1.00
Data	2	0	2	1	4

Table 8.3: *Number of observed data events, the expectations from the Standard Model processes and the signal selection efficiencies as result of the application of the optimal cuts for the squark decay $\tilde{t}_1 \to bl\tilde{\nu}$ onto the independent samples of the Monte Carlo events and to the whole data sample of center-of-mass energy $202-208$ GeV. The quoted errors are due to MC statistics only.*

the fraction of the $e^+e^-q\,\bar{q}$ background becomes already comparable with contributions from the four-fermion processes. This makes the cut optimization easier. Also note that the signal of all channels and all ΔM ranges becomes very well separated from $\mathrm{e}^+\mathrm{e}^-$, $\mu^+\mu^-$, $e^+e^-e^+e^-$, $e^+e^-\mu^+\mu^-$, $e^+e^-\tau^+\tau^-$ and $Z^0\mathrm{e}^+\mathrm{e}^-$ Standard Model processes. Of all 12 considered background processes only $e^+e^-q\,\bar{q}$ and W^+W^-, $W^\pm e\nu$ and Z^0Z^0 remain important in the optimized selection. The minimal value of the signal selection efficiency of 6.0 ± 1.1 % again corresponds to the very low ΔM range of the $\tilde{t}_1 \to b\tau\tilde{\nu}$ decay. This is the case when the hardest cuts have been used to provide optimal separation In the other cases the signal selection efficiency varies in the order of $20-30$ % with a maximum of 42.2 ± 2.2 % for the medium ΔM of the $\tilde{b}_1 \to b\tilde{\chi}_1^0$ channel.

The distributions of the kinematic variables after the optimal selection are identical to those shown in Figures 7.15-7.17 after removing events that are cut away. Therefore the plots are not duplicated here. Event numbers after applying the optimal cuts in Figures 7.15-7.17 can be also compared with the numbers of observed data and expected Standard Model events presented in the Tables 8.2-8.5.

	very low ΔM	low ΔM	medium ΔM	high ΔM	combined
ε_{signal}, %	6.0 ± 1.1	15.8 ± 1.6	23.4 ± 1.9	24.6 ± 1.9	-
e^+e^-	-	-	-	-	-
$\mu^+\mu^-$	-	-	-	-	-
$\tau^+\tau^-$	-	-	-	-	-
$q\bar{q}$	-	-	-	-	-
W^+W^-	-	-	0.30 ± 0.12	0.30 ± 0.12	0.50 ± 0.16
$W^\pm e^\mp \nu$	-	0.01 ± 0.01	0.09 ± 0.02	0.06 ± 0.01	0.13 ± 0.02
Z^0Z^0	-	-	0.11 ± 0.08	-	0.11 ± 0.08
$Z^0e^+e^-$	-	-	-	-	-
$e^+e^-e^+e^-$	-	-	-	-	-
$e^+e^-\mu^+\mu^-$	-	-	-	-	-
$e^+e^-\tau^+\tau^-$	-	-	-	-	-
$e^+e^-q\,\bar{q}$	1.26 ± 0.63	1.58 ± 0.71	-	0.32 ± 0.32	3.16 ± 1.00
All bg.	1.26 ± 0.63	1.59 ± 0.71	0.50 ± 0.15	0.68 ± 0.34	3.90 ± 1.01
Data	1	0	2	3	5

Table 8.4: *Number of observed data events, the expectations from the Standard Model processes and the signal selection efficiencies as result of the application of the optimal cuts for the squark decay $\tilde{t}_1 \to b\tau\tilde{\nu}$ onto the independent samples of the Monte Carlo events and to the whole data sample of center-of-mass energy $202-208$ GeV. The quoted errors are due to MC statistics only.*

The overall event numbers for data and SM background are shown in Table 8.6 combined for all ΔM regions and decay channels. Different background types are shown separately.

8.2.2 The Selected Squark Candidate Events

The number of the data events, selected by the optimized cuts in searches for each of the considered stop and sbottom decay channels are in statistical agreement with the corresponding expectations from the Standard Model processes, that's why *we conclude that signal events are not observed in the data.* On the other hand, the selected data events have similar topology and kinematic properties to the expected events of the corresponding squark decay channel. Therefore we consider them as *candidate events.* Having this in mind, Figures 8.2-8.3 present the transverse and longitudinal view of such a selected (candidate) event in the L3 detector setup. This data event was selected in the search for the scalar top quark decay $\tilde{t}_1 \to c\tilde{\chi}_1^0$ at medium ΔM region. The event

	very low ΔM	low ΔM	medium ΔM	high ΔM	combined
ε_{signal}, %	13.4 ± 1.5	22.0 ± 1.9	42.2 ± 2.2	17.4 ± 1.7	-
e^+e^-	-	-	-	-	-
$\mu^+\mu^-$	-	-	-	-	-
$\tau^+\tau^-$	-	-	0.19 ± 0.19	-	0.19 ± 0.19
$q\bar{q}$	-	-	0.15 ± 0.15	0.15 ± 0.15	0.31 ± 0.22
W^+W^-	-	-	0.15 ± 0.09	0.40 ± 0.14	0.55 ± 0.17
$W^\pm e^\mp \nu$	0.01 ± 0.01	0.04 ± 0.04	0.28 ± 0.03	0.03 ± 0.01	0.31 ± 0.03
Z^0Z^0	-	-	0.45 ± 0.16	0.97 ± 0.24	1.31 ± 0.27
$Z^0e^+e^-$	-	-	-	-	-
$e^+e^-e^+e^-$	-	-	-	-	-
$e^+e^-\mu^+\mu^-$	-	-	-	-	-
$e^+e^-\tau^+\tau^-$	-	-	-	-	-
$e^+e^-q\ \bar{q}$	3.79 ± 1.09	2.21 ± 0.84	0.32 ± 0.32	-	5.05 ± 1.26
All bg.	3.80 ± 1.09	2.25 ± 0.84	1.54 ± 0.44	1.55 ± 0.31	7.72 ± 1.34
Data	1	1	2	2	6

Table 8.5: *Number of observed data events, the expectations from the Standard Model processes and the signal selection efficiencies as result of the application of the optimal cuts for the squark decay $\tilde{b}_1 \to b\tilde{\chi}_1^0$ onto the independent samples of the Monte Carlo events and to the whole data sample of center-of-mass energy $202-208$ GeV. The quoted errors are due to MC statistics only.*

shows two jets and has significant missing energy, which is visible both from the space orientation of the jets (both jets point to the same side with respect to the XY plane) and from the amount of the total reconstructed visible energy, 53.63 GeV.

Other selected data events have the same features: two jets and high missing energy (small E_{vis}). In principle, these could be the squark events, but in this case their production cross section is so small, that we can not distinguish them from the Standard Model events in the collected amount of the experimental data. If the scalar quarks of the considered masses do not exist, then these are the Standard Model (mainly, the two-photon) events.

8.2.3 Selections in the Data Subsamples of Particular Energy

After the optimization has been performed and the optimal cuts for the four squark decay channels and four ΔM regions are fixed, we can check whether the search results (i.e. the consistency of the selected data events and predictions from the Standard Model)

Channel	N_{D}	$N_{\mathrm{two-fermion}}$	$N_{\mathrm{four-fermion}}$	$N_{\mathrm{two-photon}}$	N_{SM}
$\tilde{t}_1 \rightarrow \mathrm{c}\tilde{\chi}_1^0$	29	0.0 ± 0.0	3.1 ± 0.3	23.4 ± 2.7	26.5 ± 2.7
$\tilde{t}_1 \rightarrow \mathrm{b}\ell\tilde{\nu}$	4	0.5 ± 0.3	0.7 ± 0.2	2.8 ± 0.9	4.0 ± 1.0
$\tilde{t}_1 \rightarrow \mathrm{b}\tau\tilde{\nu}$	5	0.0 ± 0.0	0.7 ± 0.2	3.2 ± 1.0	3.9 ± 1.0
$\tilde{b}_1 \rightarrow \mathrm{b}\tilde{\chi}_1^0$	6	0.5 ± 0.3	2.1 ± 0.3	5.1 ± 1.3	7.7 ± 1.3
Combined	38	1.0 ± 0.4	5.8 ± 0.5	31.0 ± 3.1	37.8 ± 3.2

Table 8.6: *Number of observed events, N_{D}, and SM background expectations, N_{SM}, for the main stop and sbottom channels and for selection combined over all these channels. The contribution of two-fermion ($\mathrm{q\bar{q}}$, $\tau^+\tau^-$), four-fermion ($\mathrm{W^+W^-}$, $\mathrm{W^\pm e^\mp}\nu$, ZZ, $\mathrm{Ze^+e^-}$) and two-photon ($\mathrm{e^+e^-q\bar{q}}$, $\mathrm{e^+e^-}\tau^+\tau^-$) processes are given separately. The quoted errors are due to MC statistics only.*

do depend on the particular value of the center-of-mass energy in the analyzed $\sqrt{s}$-range of 202 – 208 GeV. We need to subdivide the whole data sample in subsamples with particular beam energy values according to the collected amount of luminosity per center-of-mass energy, Figure 8.1, which roughly gives us the subranges of 202 – 204, 204 – 206, 206 – 207 and 207 – 208 GeV. On each of these data subsamples we perform the event selection using the same (obtained for the value of the total luminosity over $\sqrt{s} = 202{-}208\ GeV$ range) selection cuts, which are energy-independent since all energy or momenta variables are normalized to $\sqrt{s}$) in each data subsample. To estimate the corresponding event numbers, expected from the Standard Model, we do not subdivide the used Monte Carlo event samples, but just re-weight according to the integrated luminosities of the data subsamples the "old" numbers, which were before weighted according to the total luminosity of the whole energy range data sample. The results of such selection in the *narrow* subsamples of the total year 2000 data are presented in Tables 8.7-8.10 for the four scalar quark decay channels. After studying the particular subsamples separately, one observes that the numbers of observed data events are still in agreement with the Standard Model expectation. This means, that even when looking for the energy subranges separately, no signal is observed. This confirms, that our treatment of the data with $\sqrt{s} = 202{-}208\ GeV$ as a whole is a safe procedure and does not influence the conclusions of the analysis.

Run # **878701** **Event #** **256** Total Energy : 53.63 GeV

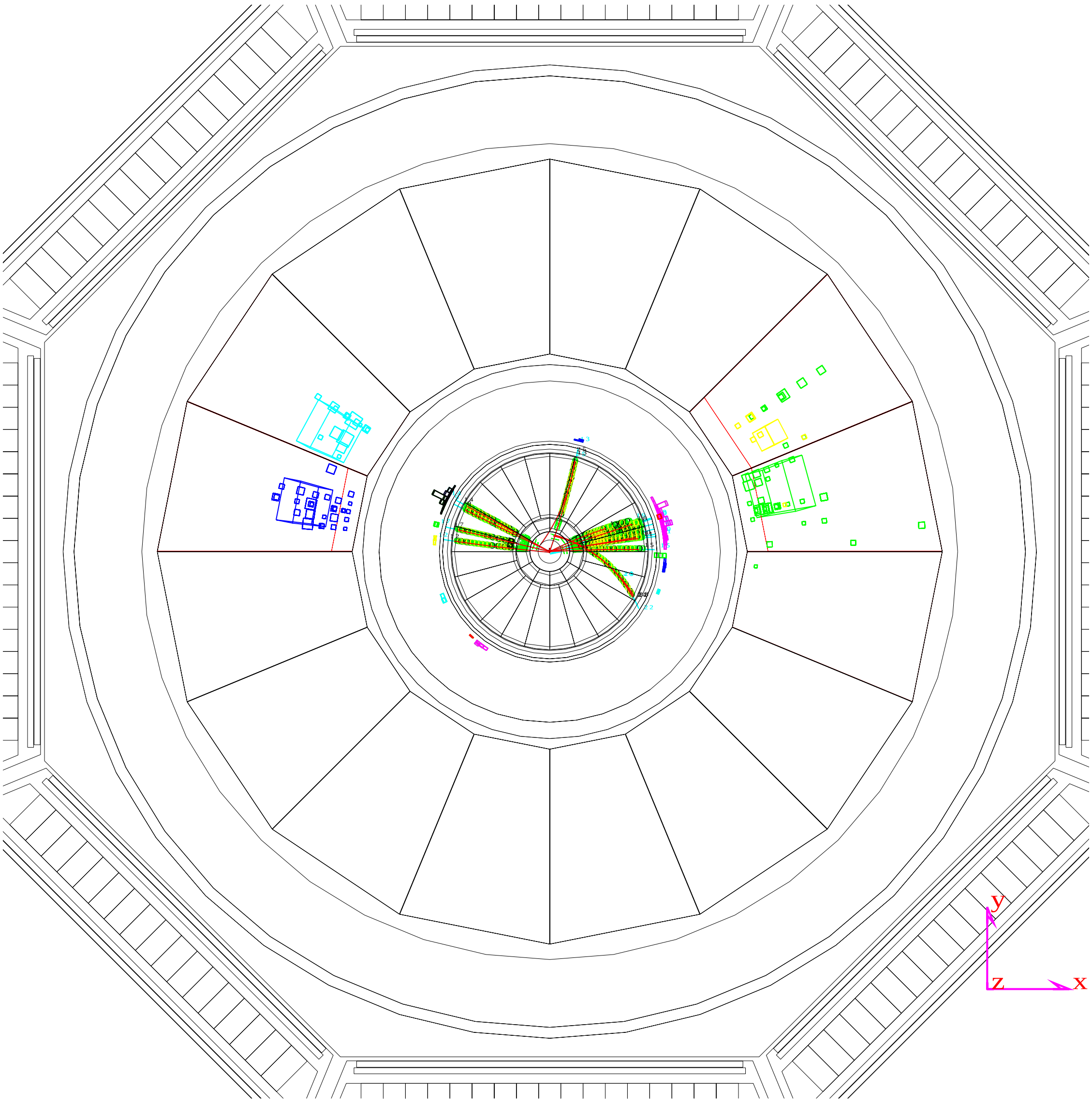

<table>
<tr><td colspan="3">Transverse Imbalance : .3083</td><td colspan="3">Longitudinal Imbalance : .3704</td></tr>
<tr><td colspan="2">Thrust : .8730</td><td colspan="2">Major : .4392</td><td colspan="2">Minor : .0814</td></tr>
<tr><td colspan="6">Event DAQ Time : <i>728 182043</i></td></tr>
</table>

Figure 8.2: *Example of the data event in the L3 detector setup, (run number 878701, event number 256, the xy-plane), selected as a candidate in the search for the scalar quark decay* $\tilde{t}_1 \rightarrow c\tilde{\chi}^0_1$ *at medium* ΔM.

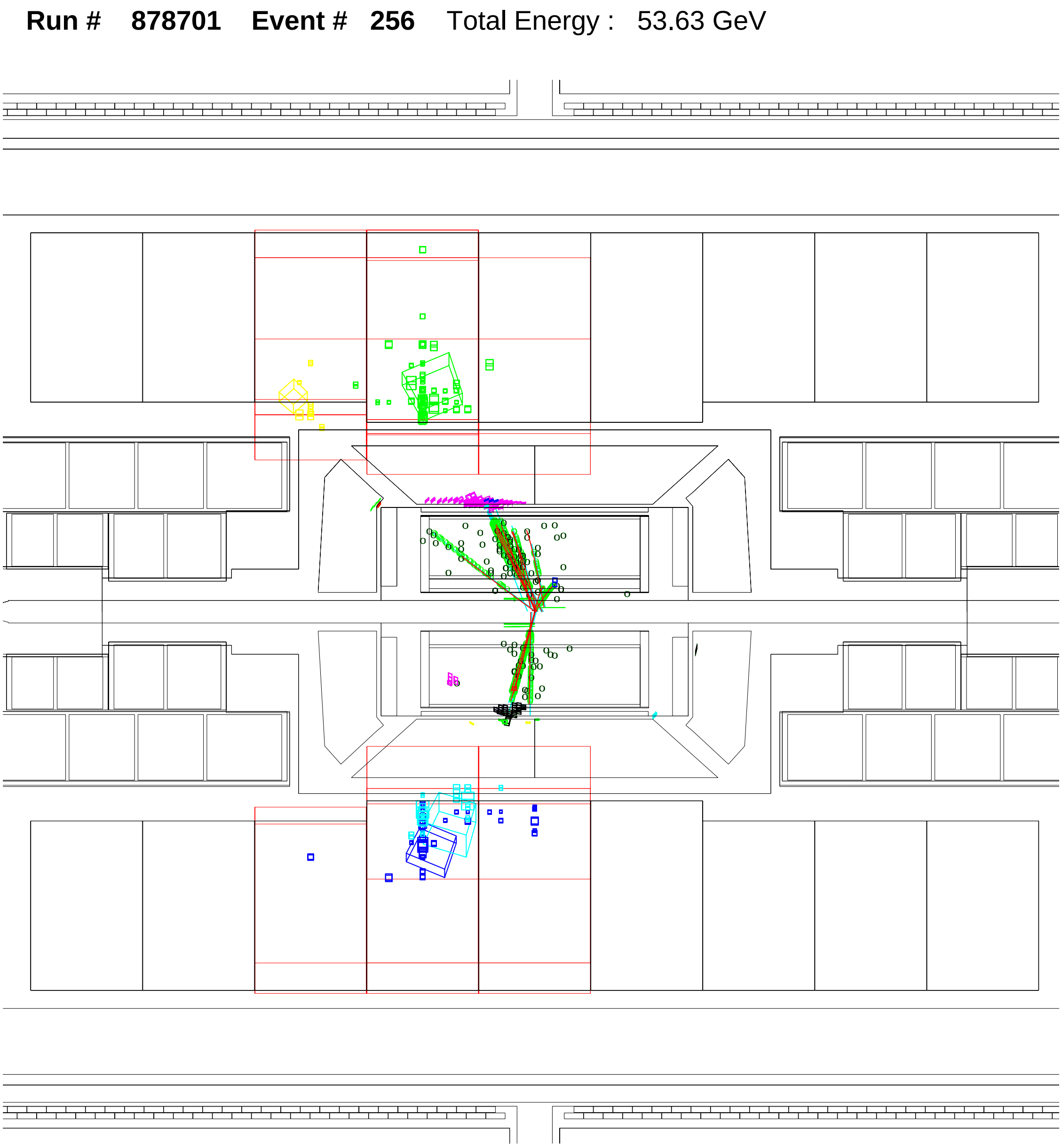

Transverse Imbalance :	.3083		**Longitudinal Imbalance :**	.3704	
Thrust :	.8730	**Major :**	.4392	**Minor :**	.0814
Event DAQ Time :	*728 182043*				

Figure 8.3: *Example of the data event in the L3 detector setup, (run number 878701, event number 256, the xz-plane), selected as a candidate in the search for the scalar quark decay* $\tilde{t}_1 \rightarrow c\tilde{\chi}_1^0$ *at medium* ΔM*.*

$\sqrt{s}$ range	very low ΔM		low ΔM		medium ΔM		high ΔM		"OR"	
GeV	N_D	N_{SM}	N_D	N_{SM}	N_D	N_{SM}	N_D	N_{SM}	N_D	N_{SM}
202 – 204	1	0.87 ± 0.10	0	0.13 ± 0.04	0	0.05 ± 0.01	1	0.07 ± 0.01	2	1.07 ± 0.11
204 – 206	8	6.99 ± 0.84	0	1.01 ± 0.31	1	0.41 ± 0.11	0	0.60 ± 0.09	9	8.59 ± 0.88
206 – 207	14	12.84 ± 1.54	1	1.86 ± 0.56	3	0.76 ± 0.20	0	1.13 ± 0.17	18	15.74 ± 1.62
207 – 208	0	0.87 ± 0.10	0	0.13 ± 0.04	0	0.05 ± 0.01	0	0.07 ± 0.01	0	1.07 ± 0.11
202 – 208	23	21.57 ± 2.60	1	3.13 ± 0.95	4	1.27 ± 0.35	1	1.87 ± 0.29	29	26.47 ± 2.74

Table8.7 : The four ΔM and "OR" combination selections for the $\tilde{t}_1 \rightarrow c\tilde{\chi}_1^0$ decay in the data subsamples of particular center-of-mass energy. The quoted errors are due to MC statistics only.

$\sqrt{s}$ range	very low ΔM		low ΔM		medium ΔM		high ΔM		"OR"	
GeV	N_D	N_{SM}	N_D	N_{SM}	N_D	N_{SM}	N_D	N_{SM}	N_D	N_{SM}
202 – 204	0	0.09 ± 0.03	0	0.02 ± 0.01	0	0.06 ± 0.02	0	0.03 ± 0.01	0	0.16 ± 0.04
204 – 206	1	0.72 ± 0.27	0	0.13 ± 0.10	2	0.45 ± 0.17	1	0.22 ± 0.08	2	1.31 ± 0.32
206 – 207	1	1.31 ± 0.50	0	0.22 ± 0.19	0	0.82 ± 0.31	0	0.41 ± 0.15	2	2.41 ± 0.59
207 – 208	0	0.09 ± 0.03	0	0.02 ± 0.01	0	0.06 ± 0.02	0	0.03 ± 0.01	0	0.16 ± 0.04
202 – 208	2	2.21 ± 0.84	0	0.39 ± 0.32	2	1.39 ± 0.52	1	0.69 ± 0.26	4	4.04 ± 1.00

Table8.8 : The four ΔM and "OR" combination selections for the $\tilde{t}_1 \rightarrow bl\tilde{\nu}$ decay in the data subsamples of particular center-of-mass energy. The quoted errors are due to MC statistics only.

$\sqrt{s}$ range	very low ΔM		low ΔM		medium ΔM		high ΔM		"OR"	
GeV	N_D	N_{SM}	N_D	N_{SM}	N_D	N_{SM}	N_D	N_{SM}	N_D	N_{SM}
$202-204$	0	0.05 ± 0.03	0	0.06 ± 0.03	0	0.02 ± 0.01	0	0.03 ± 0.01	0	0.16 ± 0.04
$204-206$	0	0.41 ± 0.20	0	0.51 ± 0.23	2	0.16 ± 0.05	2	0.22 ± 0.11	2	1.26 ± 0.33
$206-207$	0	0.75 ± 0.37	0	0.96 ± 0.42	0	0.30 ± 0.09	1	0.40 ± 0.20	2	2.32 ± 0.60
$207-208$	1	0.05 ± 0.03	0	0.06 ± 0.03	0	0.02 ± 0.01	0	0.03 ± 0.01	1	0.16 ± 0.04
$202-208$	1	1.26 ± 0.63	0	1.59 ± 0.71	2	0.50 ± 0.15	3	0.68 ± 0.34	5	3.90 ± 1.01

Table8.9 : The four ΔM and "OR" combination selections for the $\tilde{t}_1 \rightarrow b\tau\tilde{\nu}$ decay in the data subsamples of particular center-of-mass energy. The quoted errors are due to MC statistics only.

$\sqrt{s}$ range	very low ΔM		low ΔM		medium ΔM		high ΔM		"OR"	
GeV	N_D	N_{SM}	N_D	N_{SM}	N_D	N_{SM}	N_D	N_{SM}	N_D	N_{SM}
$202-204$	0	0.15 ± 0.04	0	0.09 ± 0.03	0	0.06 ± 0.02	0	0.06 ± 0.01	0	0.31 ± 0.05
$204-206$	0	1.23 ± 0.35	1	0.73 ± 0.27	1	0.50 ± 0.14	0	0.50 ± 0.10	2	2.51 ± 0.43
$206-207$	1	2.27 ± 0.65	0	1.34 ± 0.50	1	0.92 ± 0.26	2	0.93 ± 0.19	4	4.59 ± 0.79
$207-208$	0	0.15 ± 0.04	0	0.09 ± 0.03	0	0.06 ± 0.02	0	0.06 ± 0.01	0	0.31 ± 0.05
$202-208$	1	3.80 ± 1.09	1	2.25 ± 0.84	2	1.54 ± 0.44	2	1.55 ± 0.31	6	7.72 ± 1.34

Table8.10 : The four ΔM and "OR" combination selections for the $\tilde{b}_1 \rightarrow b\tilde{\chi}_1^0$ decay in the data subsamples of particular center-of-mass energy. The quoted errors are due to MC statistics only.

8.3 Systematic Uncertainties

The event numbers, expected from the Standard Model Monte Carlo and the signal selection efficiencies can be systematically biased due to several factors. The following sources of the systematic uncertainties have been investigated.

Monte Carlo Statistics

The uncertainties in the signal selection efficiencies arising from the signal MC statistics are about $\Delta\varepsilon \sim 1-2$ % both for the stop and for the sbottom quark decays depending on the particular channel and the ΔM selection. The statistical uncertainty in the SM background estimation depends significantly on the ΔM (E_{vis}) region for all squark decay channels and amounts to 12–82 % for the very low and low ΔM and to 16-50 % for the medium and high ΔM, respectively. The high uncertainty in the low ΔM regions is due to the fact, that the two photon background is large. Since this process has a very high rate, it is difficult to accumulate MC statistics for it in necessary excess over the rate expected from the available data luminosity.

The SM Processes Cross Section Uncertainty

Since the background rates are estimated by normalization of the Monte Carlo events to the experimental data luminosity (Formula (7.1)), the uncertainty in the SM processes cross section is a source of systematics. The cross section values for each particular process as well as their uncertainties have been calculated by the corresponding MC generator (see description of MC generators and references in the previous chapter). The used uncertainties on the cross sections of the SM processes are: 10 % for the two photon processes, 5 % for two fermion, 2 % for the WW and Weν production and 5 % for the ZZ and Zee processes. All these uncertainties together cause a systematic uncertainty in the background normalization of 2–10 % depending on the particular squark decay channel and the ΔM region.

The Luminosity Determination Uncertainty

The relative error on the integrated luminosity of the collected experimental data was estimated by the L3 Collaboration and amounts to $\sim$ 0.3%. This influences the background normalization and causes a systematic uncertainty in the SM rate estimation of 0.2–0.4 % for various squark decays.

The Energy Reconstruction

The uncertainty in the reconstructed energy was estimated by the L3 Collaboration by comparison between various calibration and reconstruction methods and amounts to 2 %. The influence of this uncertainty on the background rate and on the signal selection efficiency has been determined by varying all the energy related quantities by ± 2 %. This caused a systematic shift in the background rates of 1–18 % and 1–32 % in the signal selection efficiency depending on the particular squark decay and ΔM region.

The Squark Signal MC Simulation

The main contribution to the uncertainty of the squark signal selection efficiency comes from the uncertainties in the simulation of the squark production, hadronisation and decay in the GSQUARK generator program [66]. The following effects are taken into account here:

- The squark signal samples used in the analysis are generated for a fixed value of the mixing angle between left and right squark eigenstates, chosen as $\cos\theta_{LR} = 1$. However, since the sfermion coupling to the Z boson depends on $\cos\theta_{LR}$, the initial state radiation also depends on the mixing angle. The maximal difference occurs at the $\cos\theta_{LR}$ value, where the scalar quark decouples from the Z boson. The largest decrease in the selection efficiencies, 4% for stop and 6% for sbottom, is observed at low $\Delta M \sim$ 5–10 GeV. With increasing ΔM the selection efficiencies are less affected by this source of systematics. At $\Delta M \sim 70$ GeV the error is estimated to be negligible. Conservatively, for the limit calculation we use the efficiencies obtained at decoupling values of $\cos\theta_{\mathrm{LR}}$.

- As discussed in Chapter 5, the scalar top and the scalar bottom quarks in the considered theoretical framework hadronise before they decay. The invariant mass available for spectator quarks in the formed supersymmetric hadron has been assumed to be M_{eff}=0.5 GeV [67]. The hadronic energy and track multiplicity of the event depend on the value of this variable. A variation of M_{eff} from 0.25 GeV to 0.75 GeV [67] results in a $4-12\%$ relative change in the efficiency for stop and $6-8\%$ for sbottom.

- For the hadron containing a squark, the Peterson fragmentation scheme [69] is used with the parameter $\epsilon_{\tilde{\mathrm{q}}}$ propagated from ϵ_{b} such that $\epsilon_{\tilde{\mathrm{q}}} = \epsilon_{\mathrm{b}} m_{\mathrm{b}}^2/m_{\tilde{\mathrm{q}}}^2$ with $\epsilon_{\mathrm{b}} = 0.0035$ [70] and m_{b}=5 GeV. The value of ϵ_{b} is varied in the range from 0.002 to 0.006 [70]. This induces $5-12\%$ and $2-6\%$ relative changes in the selection efficiencies for $\tilde{t}_1$ and $\tilde{b}_1$, respectively.

- For the $\tilde{t}_1 \rightarrow \mathrm{c}\tilde{\chi}_1^0$ decay the variation of the c-quark fragmentation parameter ε_c from 0.02 to 0.06 (with central value chosen as 0.03) results in $1-4\%$ relative change in the selection efficiency [70].

- For the stop three-body decay mode $\tilde{t}_1 \rightarrow \mathrm{b}\ell\tilde{\nu}$, the weak structure of the decay matrix element [58] was taken into account. The related possible source of systematics has been evaluated by generating signal events with only a phase-space model. The selection efficiencies are slightly higher in this case. Therefore the efficiency values obtained with the matrix element are used.

The B-tag Discriminant Calculation

In the selections of the scalar bottom decays as well as the three-body stop decays, a cut on the event b-tagging variable, D_{Btag}, plays an important role and possible errors in this variable may be a source of uncertainties in the signal selection efficiency and the background rates estimation. An agreement or possible discrepancy between the experimental data and the Monte-Carlo events in the distribution of the D_{Btag} variable is chosen as a criterion of the corresponding uncertainty estimation. This was evaluated using a reference sample of radiative $q\bar{q}(\gamma)$ events. The sample was obtained applying cuts on the number of tracks and calorimetric clusters, $N_{trk} \geq 5$ and $N_{clust} \geq 15$ and requiring the normalized visible energy to be $0.3 < E_{vis}/\sqrt{s} < 0.8$. The two-photon contribution was suppressed by vetoing the energy depositions in the forward regions: $E^{30}_{vis}/E_{vis} < 0.5$ and $E_{LUMI} + E_{ALR} < 10$ GeV. A further reduction of the $e^+e^-q\ \bar{q}$ contribution was achieved by the requirement $|\cos\theta_{thrust}| < 0.95$. The W^+W^- events with one W decaying leptonically are rejected by an upper cut on the transverse energy imbalance $p_\perp/E_{vis}$, while hadronic W decays are removed by requirement $ln(y_{34}) < -6$ (see Chapter 7 for a description of the kinematic variables). After all these requirements, 1326 data events are left, which agrees with the number of Standard Model MC events, 1339.7 ± 8.2. The consistency between the data and SM Monte Carlo events was also analyzed at the D_{Btag} distribution, shown in Figure 8.4. In general, the data points are well reproduced by the Monte Carlo, except only the region very close to zero ($D_{Btag} < 0.3$). But the squark signal can be better selected in the region of $D_{Btag} \geq 0.5 - 1$ and, correspondingly, the selected events are located in this region. That's why we conclude that the systematic effects in the b-tagging calculations are small compared to the statistical uncertainty and therefore this source of systematics can be neglected.

The Lepton Identification

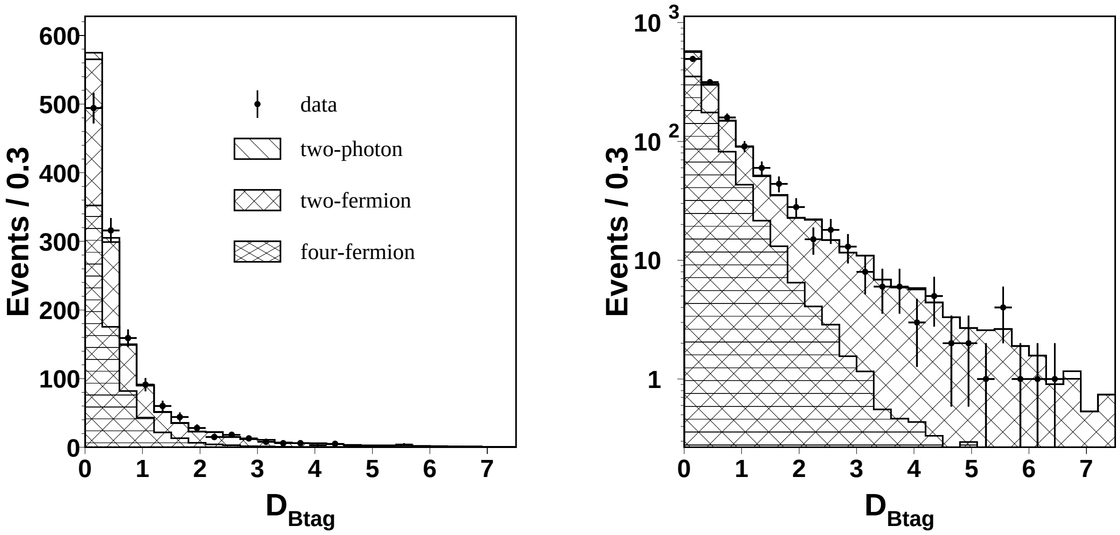

Figure 8.4: *The D_{Btag} distribution with selection of $q\bar{q}(\gamma)$ events for analysis of consistency between MC simulation and the L3 Detector response. The distributions are shown in linear (left) and logarithmic (right) scales.*

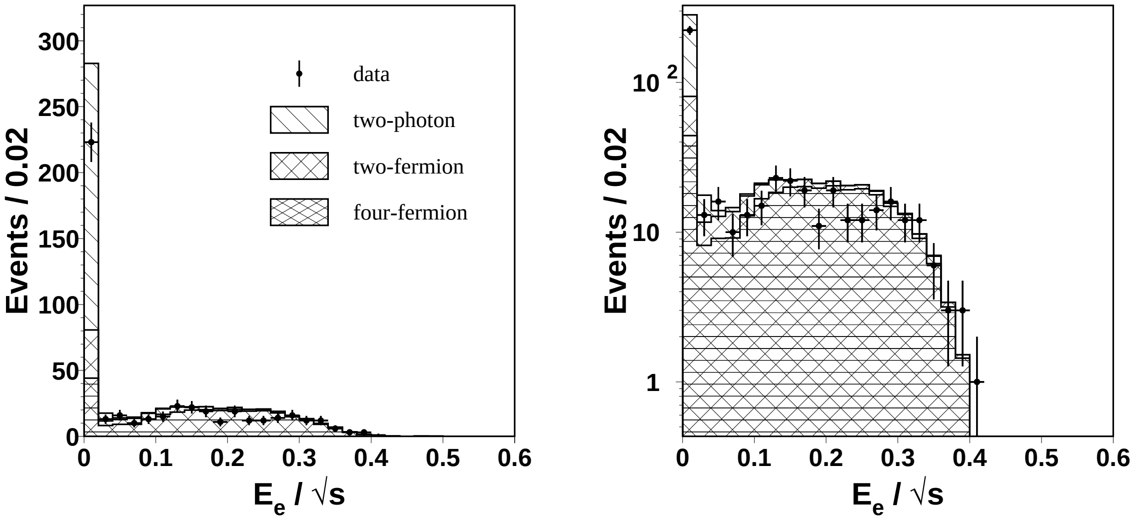

Figure 8.5: *The preselected energy distribution of the leading lepton being electron for analysis of consistency between MC simulation and the L3 Detector response. The distributions are shown in linear (left) and logarithmic (right) scales.*

Optimization of selections for the leptonic stop decays $\tilde{t}_1 \to bl\tilde{\nu}$ and $\tilde{t}_1 \to b\tau\tilde{\nu}$ is based on classification of events by type of the leading isolated lepton. Possible misidentification of the lepton type may lead to a systematic bias in the signal selection efficiency and SM background rate estimation. This possible lepton misidentification was investigated by comparison of preselected energy distributions of the leading lepton for possible discrepancy between the data and the Standard Model Monte Carlo for the three cases of the leading lepton type: electron, muon and tau lepton. These distributions are presented in Figures 8.5-8.7. The data points in the distributions for leading muon and leading tau-lepton are very well reproduced by the Monte Carlo. There is also overall consistency in the distribution for the leading electron, except the very first bin, where the uncertainty in simulation of the two photon process influences. Finally, we conclude that the identification of the leading lepton type is well simulated and we can neglect this source of systematics.

All the considered sources of the systematic uncertainties in the signal selection efficiency and the SM background rate estimation are summarized (with averaged values per each squark decay channel) in Table 8.11. The overall relative systematic uncertainty on the selection efficiencies ranges from 2% to 34% for the scalar top and from 4% to 15% for the scalar bottom quark decays; the error on the Standard Model background rate estimation varies from 10% to 83% for stop and from 20% to 39% for sbottom quarks respectively. These uncertainties have been incorporated in the final results [97].

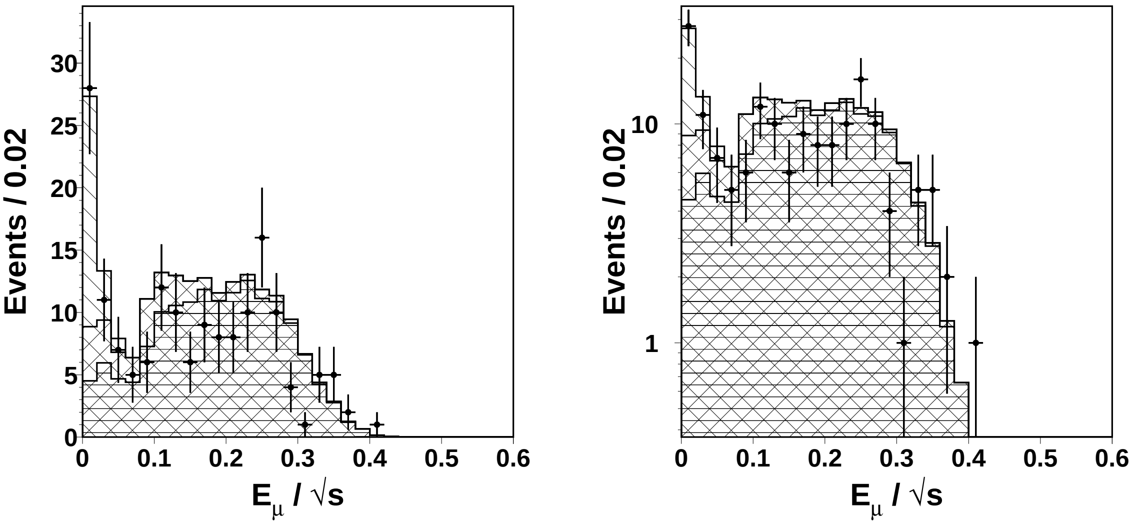

Figure 8.6: *The preselected energy distribution of the leading lepton being muon for analysis of consistency between MC simulation and the L3 Detector response. The distributions are shown in linear (left) and logarithmic (right) scales.*

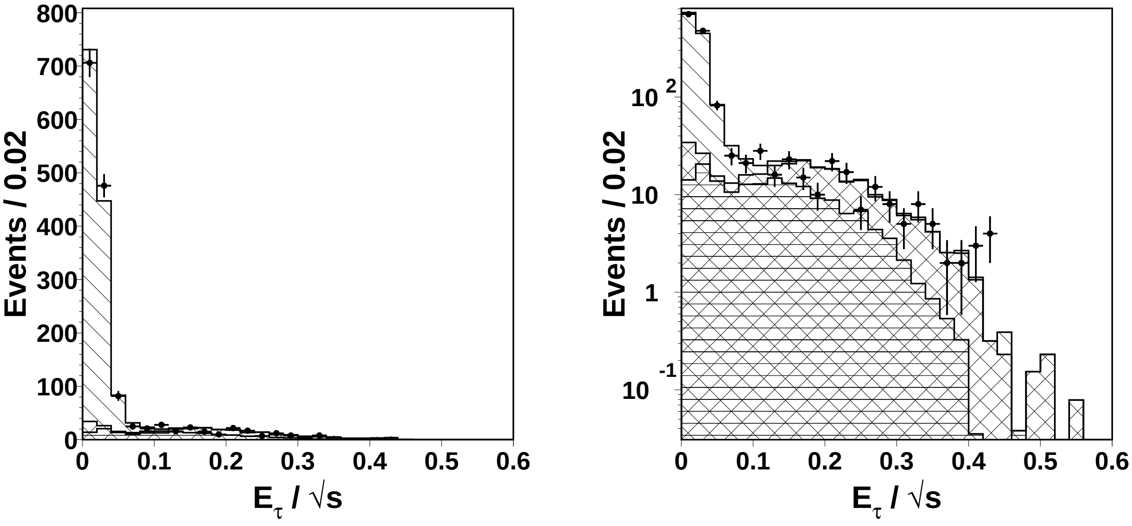

Figure 8.7: *The preselected energy distribution of the leading lepton being tau lepton for analysis of consistency between MC simulation and the L3 Detector response. The distributions are shown in linear (left) and logarithmic (right) scales.*

Source / Channel		$\tilde{t}_1 \to c\tilde{\chi}^0_1$	$\tilde{t}_1 \to b\ell\tilde{\nu}$	$\tilde{t}_1 \to b\tau\tilde{\nu}$	$\tilde{b}_1 \to b\tilde{\chi}^0_1$
Monte Carlo	$\Delta\varepsilon$	1.7–2.2	1.6–2.1	1.1–1.9	1.5–2.2
statistics	ΔN_{SM}	12–30	37–82	30–50	20–37
SM cross	$\Delta\varepsilon$	–	–	–	–
section	ΔN_{SM}	4–10	4–10	2–10	4–10
Luminosity	$\Delta\varepsilon$	–	–	–	–
uncertainty	ΔN_{SM}	0.2–0.4	0.2	0.3–0.4	0.2–0.3
Energy	$\Delta\varepsilon$	1–6	1–29	8–32	3–13
calibration	ΔN_{SM}	1–5	1–7	1–4	2–7
Squark signal	$\Delta\varepsilon$	1–12	4–12	4–12	2–8
simulation	ΔN_{SM}	–	–	–	–
Overall	$\Delta\varepsilon$	2–14	4–31	9–34	4–15
	ΔN_{SM}	13–32	37–83	30–51	20–39

Table 8.11: Relative systematic errors (in %) on the signal selection efficiency and the Standard Model background rate for various considered uncertainties sources per the investigated scalar top and scalar bottom quark decay channels.

Chapter 9

Interpretation of the Search Results

In our search for scalar quark decays in the year 2000 data we find a good statistical agreement between the selected data events and the expectation from the Standard Model processes, i.e. *absence* of an excess in the data with respect to the SM event rate. It means that the result of the search is negative: *no evidence for the MSSM squark signal is seen.* The negative results of the search for SUSY quarks can be interpreted as an exclusion of the signal at given conditions with a certain level of confidence.

First, from the relation between the observed number of data events and the Standard Model predictions we can derive an upper limit on the number of signal events, which allows us to calculate a *model independent* upper limit on the production cross section of the MSSM scalar quarks.

Then, having derived the model independent limits on the production cross section, we can interpret them further in the framework of the considered CMSSM model, convert them into the exclusion limits on the squark and the LSP (or the sneutrino) [1] masses and relate these limits to other model parameters.

9.1 Upper Limits on the Production Cross Section

To calculate the upper limit on the number of signal events we use the values of the selection efficiency of the simulated signal. Since the signal kinematics and, consequently, the selection efficiency is generally dependent on the masses of both the scalar quark and the LSP (or the sneutrino), we have to consider various combinations of these masses and deal with efficiency changes over a *mass plane*, where one axis is M_{squark} and another one is M_{LSP} (or $M_{\tilde{\nu}}$).

It is obviously time consuming and meaningless to simulate the squark signal samples for all possible combination of the squark and the LSP masses (to say, with mass steps of 1 GeV), because for close mass points ($M^A_{squark}; M^A_{LSP}$) and ($M^B_{squark}; M^B_{LSP}$) the behaviour of the signal and the selection efficiency are expected to change smoothly. Instead of this, it is better to simulate and analyze the signal samples with the squark and the LSP (or the sneutrino) mass values changing in steps of a few (5-20) GeV and then to *interpolate* the signal behaviour (the signal selection efficiency) in the whole mass

---

[1] See note about dependency on the LSP and the sneutrino masses in chapter 7.

plane between the simulated points. The points of the mass plane, corresponding to the simulated squark decay $\tilde{t}_1 \rightarrow c\tilde{\chi}_1^0$, are illustrated in Figure 9.1 by the black squares; the empty area between these points is to be interpolated. The grid step size near the boundaries of the allowed mass area is smaller than in the central area, because the interpolation in the center is easier. Signal samples of the other scalar quark decays were simulated with a similar grid on the mass parameter plane.

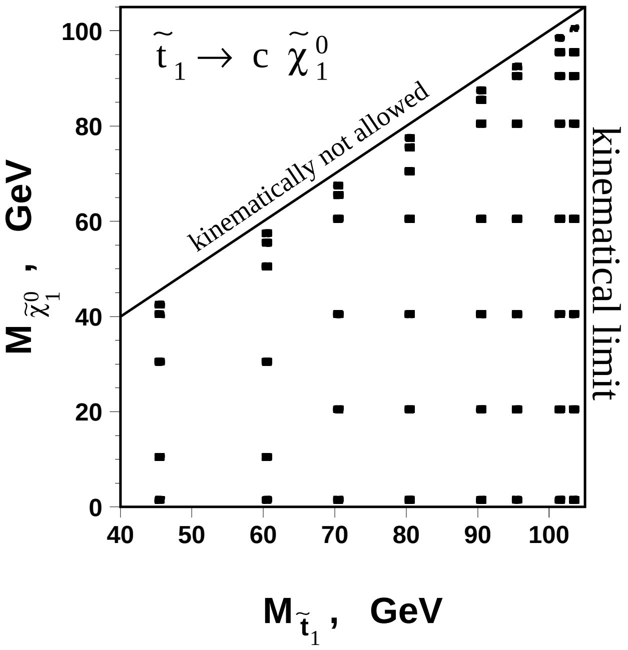

__Figure 9.1:__ Mass parameter points of the simulated stop quark signal ($\tilde{t}_1 \rightarrow c\tilde{\chi}_1^0$ decay). The grid steps near the parameter space boundaries are smaller than in the center area, which is easier to interpolate.

9.1.1 The Efficiency Interpolation over the Mass Plane

The interpolation of the signal selection efficiency between the simulated points is performed (within every particular optimized selection) by building a smooth surface (with efficiency values as z-coordinate) which covers the ”known” mass points. The interpolation procedure is iterative. First, efficiency values for each ”unknown” mass point are calculated by constructing a plane, built on the three closest ”known” mass points, that form a triangle (being not on the same line). The efficiency value for an “unknown” point is calculated by a linear interpolation from the efficiency values of “known” neighbour points. These points, which are already interpolated, are then added to the set of ”known” points. In the next iterations, the efficiency values of each non-simulated mass point are corrected by information from the closest points, including those, which were calculated in the previous iteration. This procedure is repeated until the efficiency values are calculated and corrected for all points on the mass plane and the efficiency surface becomes smooth.

One thing should be taken into account here: the selection cuts are optimized for the four ΔM ranges independently, so, on the boundaries between two adjacent selections the numbers of selected events and the efficiency values can be quite different, i.e. the efficiency surface can be far from a smooth shape. To avoid this problem, the efficiency interpolations were performed separately for each of the four ΔM selection types and for their combinations (very low ΔM (type 1), very low OR low (2), low ΔM (3), low OR medium (4), medium ΔM (5), medium OR high (6) and high ΔM (7)), applying the same selection for efficiency determination on the whole plane. An example of the simulated points with their efficiency values and the result of the efficiency interpolation for selection type 5 (medium ΔM) is shown in Figure 9.2. Note, that each particular ΔM selection gives a very small efficiency in the area far from the current ΔM (medium ΔM selection gives a very small efficiency in the area of very low and very high ΔM values, etc.).

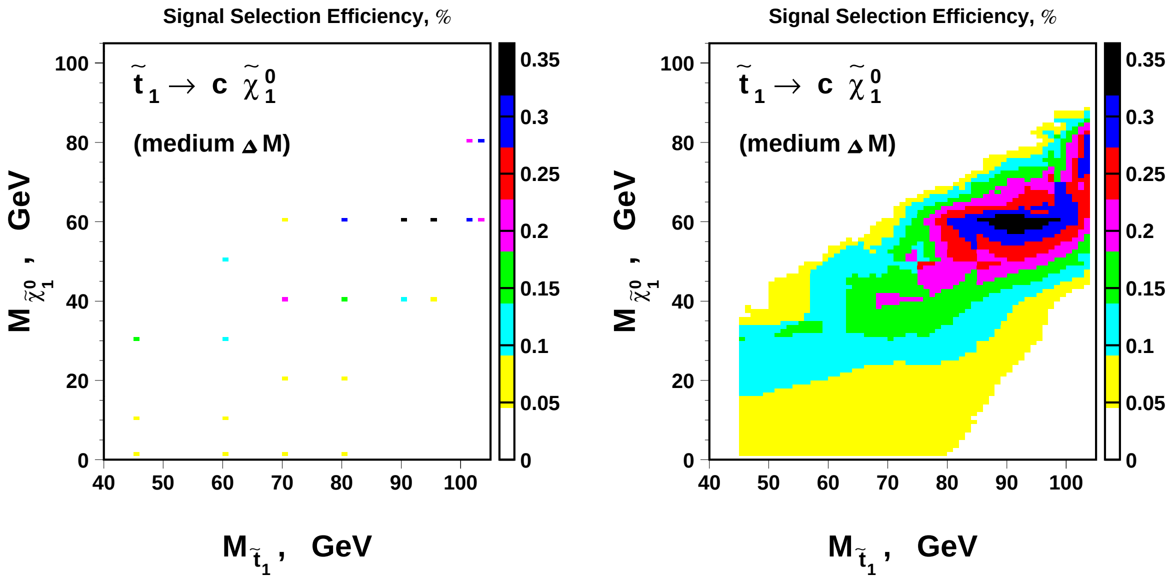

Figure 9.2: *Signal selection efficiencies versus the masses of squark and the LSP for the medium ΔM selection of the $\tilde{t}_1 \rightarrow c\tilde{\chi}^0_1$ decay channel before (left) and after (right) the efficiency interpolation over the mass plane.*

9.1.2 Combination of the ΔM Selections

After the efficiency interpolation, we have seven selections and seven *smooth* surfaces of the interpolated efficiencies and correspondingly seven surfaces of sensitivity, defined by the efficiency and by the number of expected events from the Standard Model according to Equation (7.7). The sensitivity surfaces for selections 1,3,5 and 7 (the $\tilde{t}_1$ channel) are

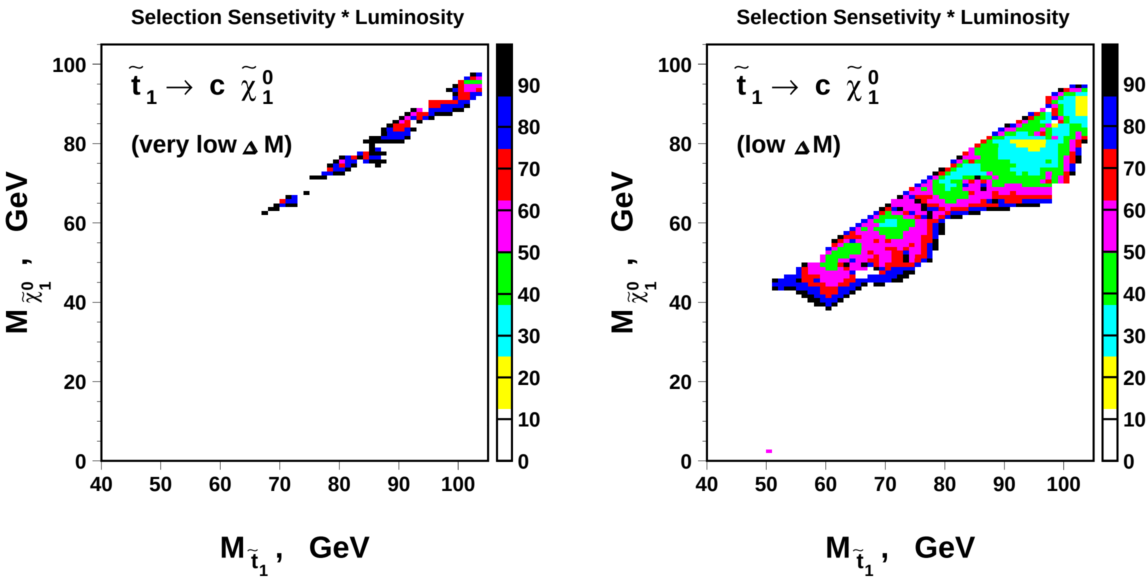

Figure 9.3: *Selection sensitivity after interpolation of the efficiency versus the masses of squark and the LSP for the* $\tilde{t}_1 \rightarrow c\tilde{\chi}^0_1$ *decay channel. Selections for very low (left) and low (right)* ΔM *regions. (The blank area corresponds to the kinematical limits or to the very bad sensitivity values, above 100)*

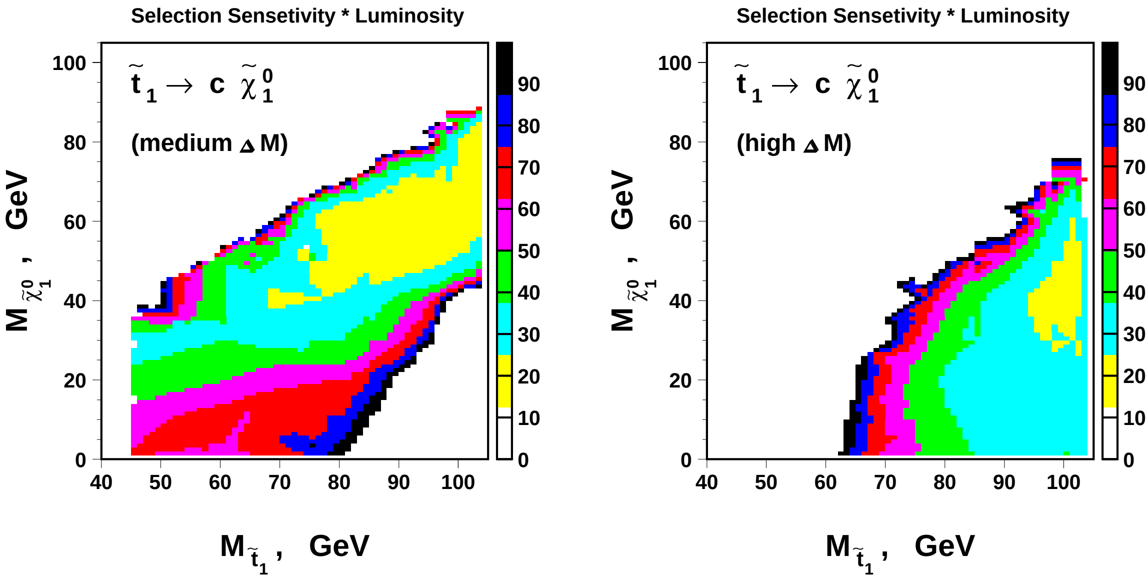

Figure 9.4: *Selection sensitivity after interpolation of the efficiency versus the masses of squark and the LSP for the* $\tilde{t}_1 \rightarrow c\tilde{\chi}^0_1$ *decay channel. Selections for medium (left) and high (right)* ΔM *regions. (The blank area corresponds to the kinematical limits or to the very bad sensitivity values, above 100)*

given in Figures 9.3-9.4, the dependency on the ΔM range is clearly visible from one plot to another.

Then, to finally choose the best selection for each point of the mass plane, we combine these seven selections in a way that leads to the best *selection sensitivity* (i.e. lowest values of the sensitivity function (7.7)) for any particular mass point. Since the criterion for this combination is not the efficiency, but the sensitivity, the final efficiency surface is not smooth, but the sensitivity surface is.

The indexes of chosen selection type for each mass point and the best chosen sensitivity over the mass plane are shown in Figure 9.5. The general dependency on ΔM is kept, while the boundaries between different selections are not straight as in the definitions of the ΔM regions.

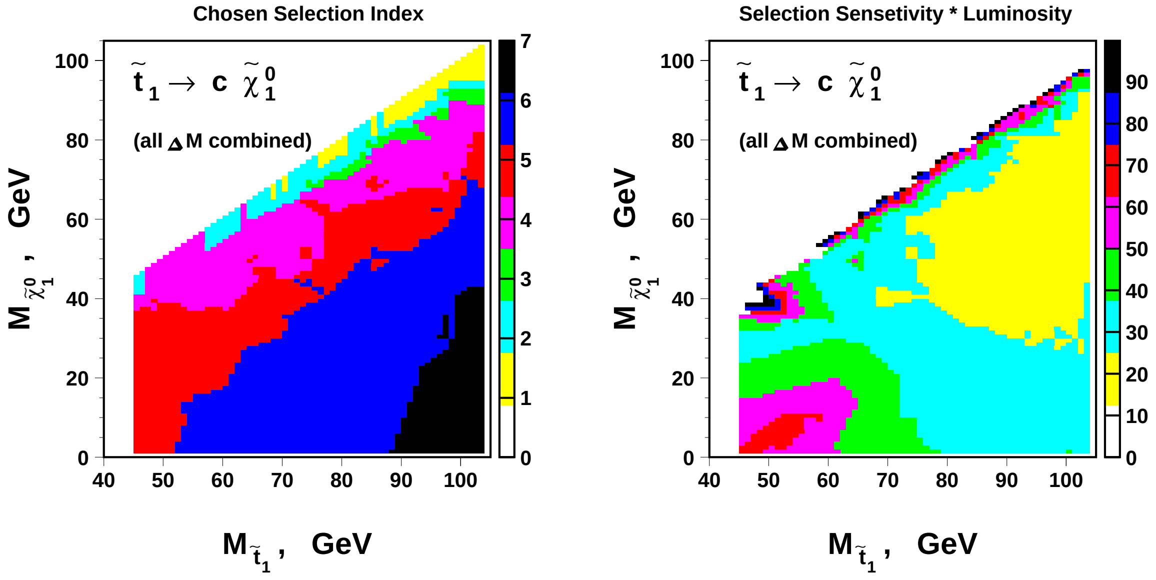

Figure 9.5: *Chosen selection types (left), provided the best (with lowest value) selection sensitivity over the mass plane (right). (The blank area corresponds to the kinematical limits or to the very bad sensitivity values, above 100)*

9.1.3 Calculation of Limits on the Production Cross Section

Now, having the best sensitivity and correspondingly the best selections for each mass point, we can calculate the 95 % C.L. upper limit on the number of signal events, and, consequently, the 95 % C.L. upper limit on the squark production cross section.

According to the Bayesian approach [98, 95] for N_D observations and N_{BG} expectations from the SM background processes, the 95 % confidence level upper limit on the number of signal events N_S^{95} can be calculated numerically from

$$C.L. = \frac{\int\limits_0^{N_S^{CL}} P(N_{BG} + N_S;\ N_D)\ dN_S}{\int\limits_0^{\infty} P(N_{BG} + N_S;\ N_D)\ dN_S}\ , \tag{9.1}$$

setting the C.L. equal to 0.95, where $P(\mu;\ n)$ is a probability density function (p.d.f.) of n observations with average expectation μ. If we deal with only one measurement (in each mass point) and the p.d.f. is the Poisson probability, as given in (7.8), then the formula (9.1) can be simplified to

$$1 - C.L. = \frac{\sum\limits_{n=0}^{N_D} P(N_{BG} + N_S^{CL};\ n)}{\sum\limits_{n=0}^{N_D} P(N_{BG};\ n)}\ . \tag{9.2}$$

After that, the 95 % C.L. upper limit on the squark production cross section is calculated as

$$\sigma^{95} = \frac{N_S^{95}}{\varepsilon\ L_{int}}\ , \tag{9.3}$$

where ε is the signal selection efficiency and L_{int} is the integrated luminosity of the data sample.

Except for the upper limit on the production cross section, which is derived from the L3 data sample on the basis of the statistical correspondence between the *observation* N_D and the *expectation* N_{BG} we can also calculate the *expected* upper limit on the production cross section, i.e. a limit, which we expect only from Monte Carlo studies without *experimental measurements* (and assuming “no signal” hypothesis). This is done by substituting the value of N_D in (9.2) by a random integer number K, which is a *hypothetic* number of *possible* observation. Since the number K can have any particular value with Poisson probability, we should take a sum of all possible values of K with the probability weight $P(N_{BG};\ K)$. Then

$$\sigma^{95}_{exp} = \sum_{K=0}^{\infty} P(N_{BG};\ K)\ \sigma^{95}(K) = \sum_{K=0}^{\infty} P(N_{BG};\ K)\ \frac{N_S^{95}(K)}{\epsilon\ L_{int}}\ , \tag{9.4}$$

where $N_S^{95}(n)$ is calculated numerically from formula (9.2), substituting N_D by K.

Now we see, that formulae (7.7) and (7.9) are the same as (9.4) and (9.2). It means that the sensitivity function, which was used in the optimization of the selections, is in fact the *expected* 95 % C.L. upper limit on the squark production cross section (in the absence of a signal). The smaller this limit is, the higher is the sensitivity to the new physics processes with very small cross sections.

The 95 % C.L. upper limits on the squark production cross section calculated in this way are presented in Figures 9.6-9.7. Note, that these cross section limits should be considered as intermediate, because they are calculated only for the year 2000 L3 data sample of $\sqrt{s} = 202 - 208$ GeV. For the calculation of the final limits the results of previous L3 squark searches should be also accounted for, because this improves the limits significantly due to using a larger data sample.

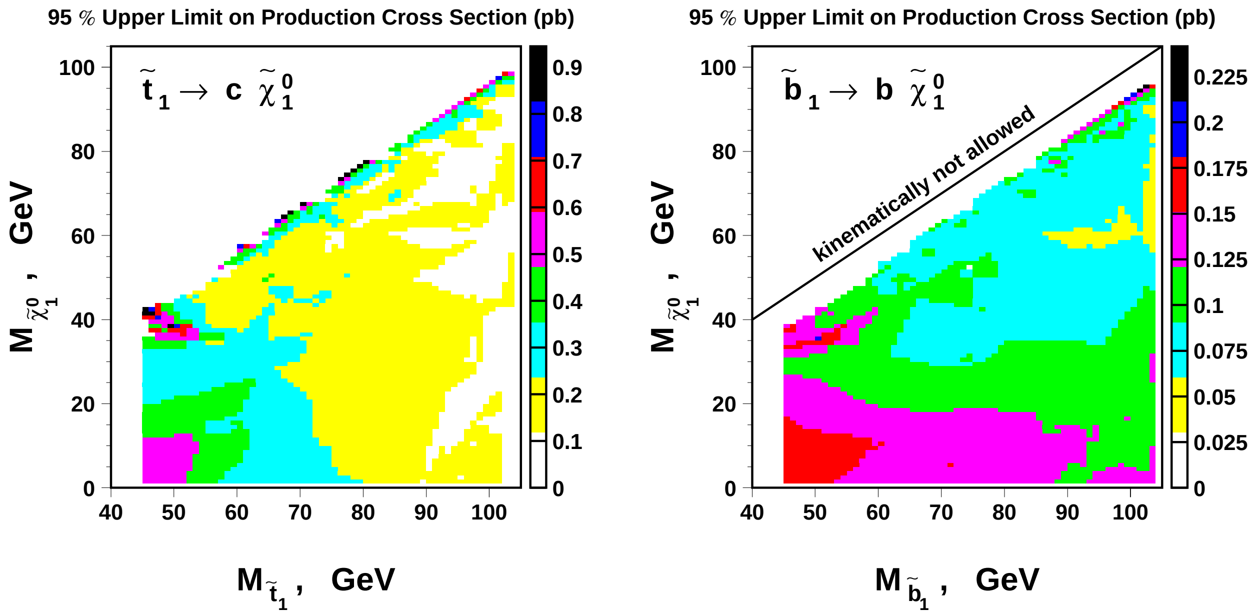

Figure 9.6: *The 95 % C.L. upper limit on the squark production cross section, calculated only for the year 2000 data sample of* $\sqrt{s} = 202 - 208$ *GeV.*

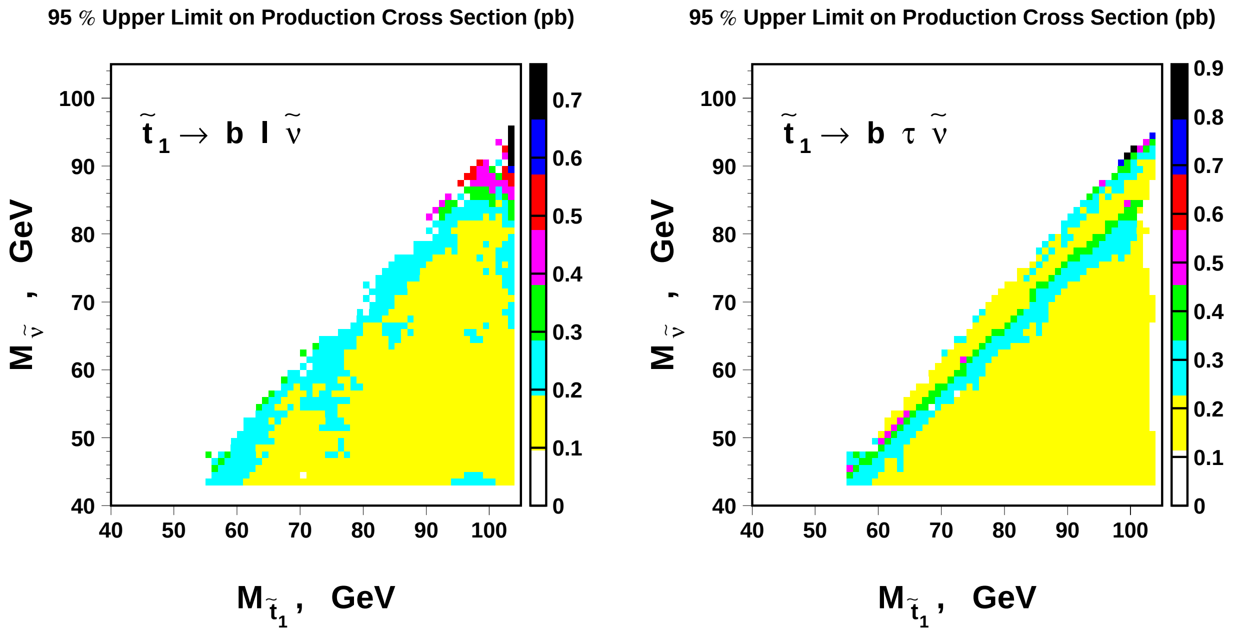

Figure 9.7: *The 95 % C.L. upper limit on the squark production cross section, calculated only for the year 2000 data sample of* $\sqrt{s} = 202 - 208$ *GeV.*

9.1.4 Combining Limits from the Year 2000 with Limits from Previous L3 Squark Searches

For each L3 squark search analysis performed in the previous years of LEP II operation (in the lower $\sqrt{s}$ L3 data samples), we know event numbers for data, N^i_D, the event numbers expected from Standard Model, N^i_{BG}, and the signal selection efficiencies, ε^i (interpolated over the squark and the LSP or the sneutrino mass plane with a procedure similar to the one described above).

To combine all these sets of measurements into single (final over the L3 experiment) 95 % C.L. limit on the squark production cross section, the Bayesian formula (9.1) should be generalized. Given N^i_D data, N^i_{BG} background and N^i_S signal events and treating all measurements independently, the combined probability can be calculated as a product of probabilities for each particular measurement:

$$Prob. = \prod_{i=1}^{n} P(N^i_{BG} + N^i_S;\ N^i_D)\ . \tag{9.5}$$

As illustrated in Figure 9.8, the stop and the sbottom production cross sections depend on the center-of-mass energy. According to the theoretical calculations, this change becomes significant over the considered $\sqrt{s}$ range of all the L3 squark search analyses (161–208 GeV). To account for this effect, we should deal with a cross section

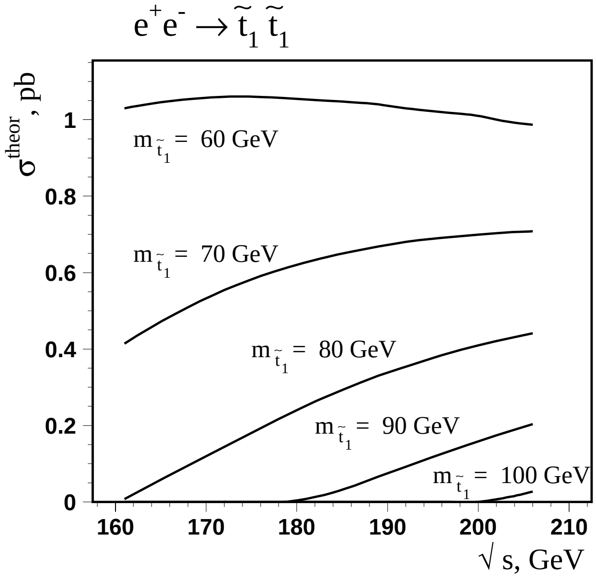

Figure 9.8: *The dependency of the theoretically predicted stop quark production cross section on the center-of-mass energy for various squark masses. The cross section change is significant near the kinematic limit, while this change can be neglected far away from it.*

σ_0 at a fixed center-of-mass energy and calculate the limit on the cross section at this particular $\sqrt{s}$ instead of a cross section averaged over the whole energy range. Therefore, instead of (upper limits on the) numbers of the signal events N_S^i in each L3 squark search, we operate with the (upper limits on the) production cross sections and normalize all the cross sections at different center-of-mass energies to the cross section of the chosen $\sqrt{s}$ of 206 GeV according to the theoretically predicted dependency of the cross section on the energy:

$$N_S^i \to \varepsilon_i \; L_{int}^i \; \sigma_i \qquad \sigma_i = f_i^{theor} \; \sigma_0 \qquad f_i^{theor} = \frac{\sigma_i^{theor}}{\sigma_0^{theor}} \; , \tag{9.6}$$

where L_{int}^i is an integrated luminosity of the i^{th} experimental data sample, ε_i and σ_i are the signal selection efficiency and the (upper limit on the) production cross section at i^{th} measurement (and, correspondingly, i^{th} center-of-mass energy), respectively.

Having all this in mind, we can generalize the Bayesian formula (9.1) for the calculation of the 95 % C.L. upper limit on the squark production cross section, *combined* over several *independent* measurements, *made at different center-of-mass energies*, in the following way:

$$C.L. = \frac{\int\limits_0^{\sigma^{CL}} \prod\limits_{i=1}^{n} P(N_{BG}^i + \epsilon_i L_i f_i^{theor} \sigma_0; \; N_D^i) \; d\sigma_0}{\int\limits_0^{\infty} \prod\limits_{i=1}^{n} P(N_{BG}^i + \epsilon_i L_i f_i^{theor} \sigma_0; \; N_D^i) \; d\sigma_0} \; . \tag{9.7}$$

In contrast to the case of only one measurement, this formula can not be simplified similar as (9.1) was simplified to (9.2); the calculation of the 95 % C.L. upper limit on the cross section here should be done numerically, setting $C.L. = 0.95$. Normalization of the cross sections of different center-of-mass energies to some fixed value allows us to perform the integration over the same variable σ_0 and in this sense to combine the results of different measurements into a single limit.

The 95 % C.L. upper limits on the cross section of the scalar top and scalar bottom quark pair production in e^+e^- collisions, combined over all available results of the squark searches in L3, are presented in Figures 9.9-9.12. The results of squark searches at center-of-mass energies 161, 172, 183, 189, 192, 196, 200, 202 (of previous years) and $202 - 208$ GeV (of the year 2000) are combined for the stop two-body ($\tilde{t}_1 \to c\tilde{\chi}_1^0$) and sbottom ($\tilde{t}_1 \to c\tilde{\chi}_1^0$) decay channels. For the leptonic stop decays ($\tilde{t}_1 \to bl\tilde{\nu}$ and $\tilde{t}_1 \to b\tau\tilde{\nu}$) the combined results correspond to the center-of-mass energies 189, 192, 196, 200, 202 and $202 - 208$ GeV (searches for these channels started only from 189 GeV).

These cross section limits are still not the final ones, because one should also take into account the systematic uncertainties on the signal selection efficiencies and on the Standard Model background rates estimation (which will be accounted for in the next section). Therefore the above mentioned plots are given for illustration of the combination of several measurements.

Comparing Figures 9.6-9.7 and 9.9-9.12 we see, that the combination of several measurements into one limit improves the limits significantly (by a factor about $2 - 5$ over the whole mass plane). Two factors contribute here. First, the more measurements we

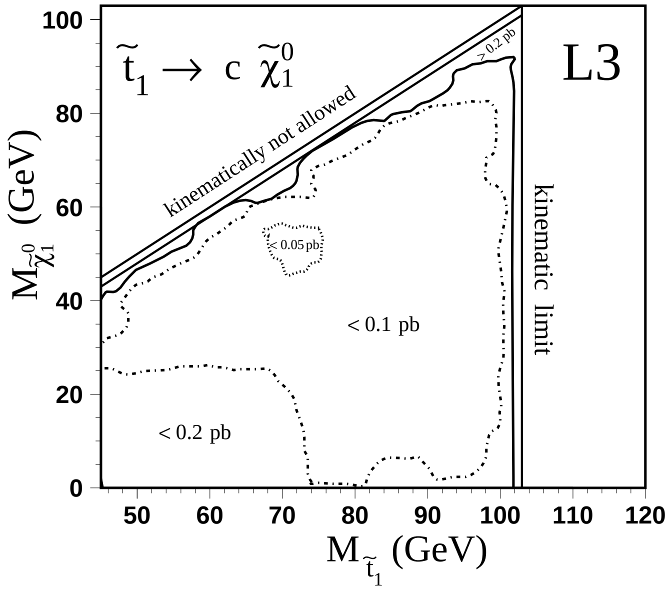

Figure 9.9: *The 95 % C.L. upper limit on the* $e^+e^- \to \tilde{t}_1\bar{\tilde{t}}_1 \to c\tilde{\chi}^0_1\bar{c}\tilde{\chi}^0_1$ *production cross section at* $\sqrt{s} = 206$ *GeV, combined over the L3 squark searches performed at the center-of-mass energies of* $161 - 208$ *GeV. Systematic uncertainties are not taken into account here.*

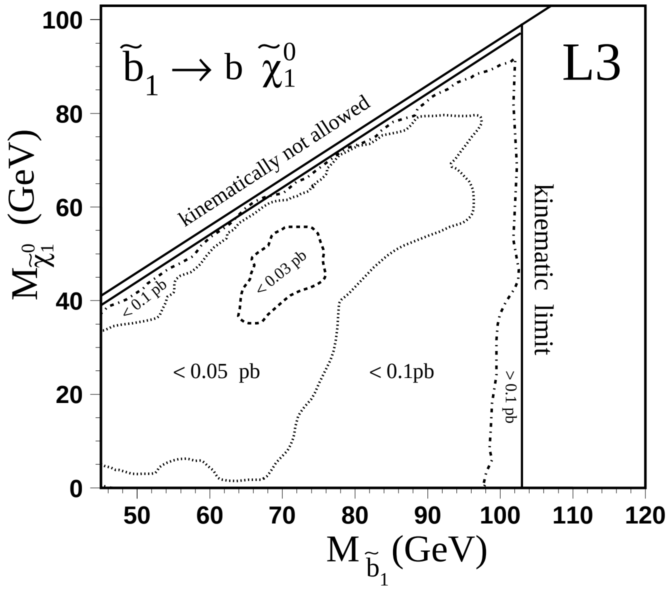

Figure 9.10: *The 95 % C.L. upper limit on the* $e^+e^- \to \tilde{b}_1\bar{\tilde{b}}_1 \to b\tilde{\chi}^0_1\bar{b}\tilde{\chi}^0_1$ *production cross section at* $\sqrt{s} = 206$ *GeV, combined over the L3 squark searches performed at the center-of-mass energies of* $161 - 208$ *GeV. Systematic uncertainties are not taken into account here.*

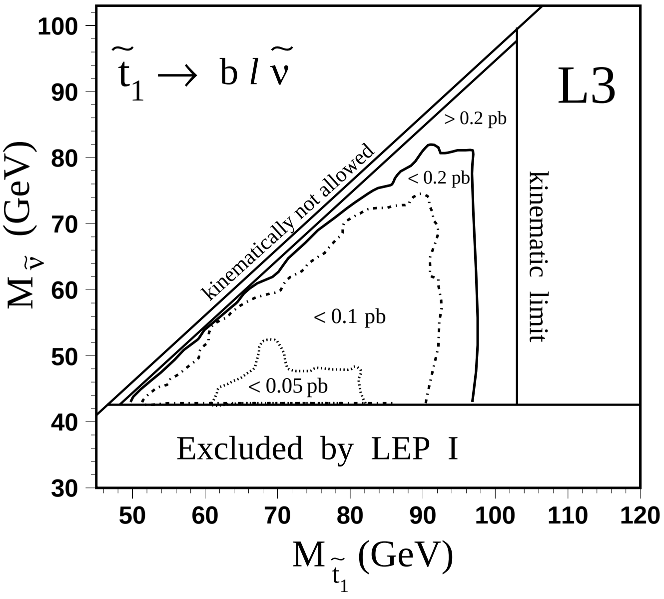

Figure 9.11: *The 95 % C.L. upper limit on the* $e^+e^- \rightarrow \tilde{t}_1 \bar{\tilde{t}}_1 \rightarrow bl^+\tilde{\nu}\bar{b}l^-\tilde{\nu}$ *(*$l = e, \mu, \tau$*) production cross section at* $\sqrt{s} = 206$ *GeV, combined over the L3 squark searches performed at the center-of-mass energies of* $189 - 208$ *GeV. Systematic uncertainties are not taken into account here.*

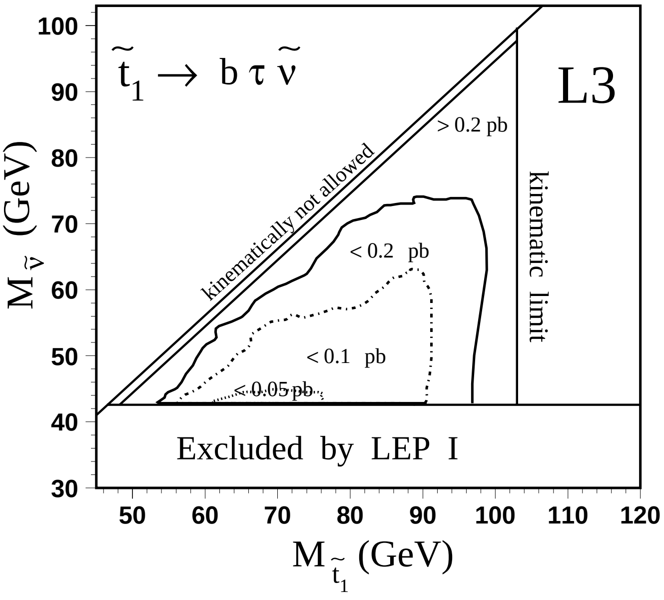

Figure 9.12: *The 95 % C.L. upper limit on the* $e^+e^- \rightarrow \tilde{t}_1 \bar{\tilde{t}}_1 \rightarrow b\tau^+\tilde{\nu}\bar{b}\tau^-\tilde{\nu}$ *production cross section at* $\sqrt{s} = 206$ *GeV, combined over the L3 squark searches performed at the center-of-mass energies of* $189 - 208$ *GeV. Systematic uncertainties are not taken into account here.*

take into account, the bigger the total integrated luminosity, which makes the cross section limit smaller (better) as can generally be seen from Equation (9.3). Another factor is that the combination of several independent measurements reduces the effect of statistical fluctuations. In general, an excess of N_D^i over N_{BG}^i leads to a smaller exclusion of cross sections, i.e. to a *higher* value of the upper limit. Correspondingly, a deficit-like deviation leads to a bigger exclusion, i.e. to *smaller* values of the upper limits. The combination of several independent measurements makes the cross section limits more adequate to the real situation: absence of excesses caused by the new physics processes. A detailed discussion about the effects of particular measurements and methods of their combination into obtained limits can be found in [95].

The calculation of the *combined* 95 % C.L. *expected* upper limit on the cross section is based on the same principle as for one measurement: the numbers of experimentally observed data events are represented by Poisson random numbers, which are taken with corresponding Poisson probability weights. But since we deal with several *independent* measurements, the random numbers K_i are also *independent* and we should sum over all their possible values separately for each measurement:

$$\sigma_{exp}^{95} = \sum_{K_1=0}^{\infty} P(N_1^{BG};\ K_1) \ldots \sum_{K_n=0}^{\infty} P(N_n^{BG};\ K_n)\ \sigma^{95}(K_1; \ldots; K_n)\ . \tag{9.8}$$

This obviously is a quite time-consuming calculation. That's why one has to use a Monte-Carlo method (to generate *not an infinite*, but a large set of K_i values). Alternatively, one can use the well known *Gamma function* $\Gamma(x)$ in order to replace the Poisson p.d.f. $P(\mu; n)$ (7.8) by a similar probability function $P_\Gamma(\mu; x)$ suitable for non-integer values of N_i^{BG}:

$$P_\Gamma(\mu; x) = e^{-\mu} \frac{\mu^x}{\Gamma(x+1)}\ . \tag{9.9}$$

Using this approximation, we can represent the set of numbers of the observed data events by the set of the corresponding expectations from the Standard Model: $N_D^i \to N_{BG}^i$ (since we concluded that there is no experimental evidence for the searched scalar quark signal). Then the expected cross section limits can be calculated faster in the following way:

$$C.L. = \frac{\int_0^{\sigma_{exp}^{CL}} \prod_{i=1}^{n} P_\Gamma(N_{BG}^i + \epsilon_i L_i f_i^{theor} \sigma_0\ ;\ N_{BG}^i)\ d\sigma_0}{\int_0^{\infty} \prod_{i=1}^{n} P_\Gamma(N_{BG}^i + \epsilon_i L_i f_i^{theor} \sigma_0\ ;\ N_{BG}^i)\ d\sigma_0}\ . \tag{9.10}$$

9.1.5 Including Systematic Uncertainties in the Limits

The upper limits on the squark production cross section are determined by the values of the signal selection efficiencies and by the numbers of the events expected from the Standard Model (in addition to the numbers of the observed data events and the integrated luminosity). These are subject to systematic uncertainties due to several factors, as discussed in section 8.3. Accounting for these uncertainties implies changes in the cross section limits. To obtain adequate limits, systematic uncertainties *must* be taken into account.

Several approaches of including systematic uncertainties into the limits calculation have been considered and compared:

1. a trivial decrease of the event numbers of the SM background and the signal selection efficiencies within their standard deviations:

$$N^i_{BG} \rightarrow N^i_{BG} - \Delta N^i_{BG},$$

$$\varepsilon^i \rightarrow \varepsilon^i - \Delta\varepsilon^i;$$

2. a Monte Carlo variation of the event numbers and efficiencies within one sigma deviation according to a uniform random number distribution:

$$N^i_{BG} \rightarrow \Big[N^i_{BG} - \Delta N^i_{BG} \times R_1(k)\Big],$$

$$\varepsilon^i \rightarrow \Big[\varepsilon^i - \Delta\varepsilon^i \times R_2(k)\Big],$$

$$\sigma(N^i_{BG};\varepsilon^i) \rightarrow \frac{1}{n}\sum_{k=1}^{n}\sigma(N^i_{BG};\varepsilon^i;k),$$

   where $R_1(k)$ and $R_2(k)$ are independent *positive* uniform random numbers varying from 0 to 1;

3. and a Monte Carlo smearing of the SM background rates and signal efficiencies around their mean values according to gaussian distribution:

$$N^i_{BG} \rightarrow \Big[N^i_{BG} + \Delta N^i_{BG} \times G_1(k)\Big],$$

$$\varepsilon^i \rightarrow \Big[\varepsilon^i + \Delta\varepsilon^i \times G_2(k)\Big],$$

$$\sigma(N^i_{BG};\varepsilon^i) \rightarrow \frac{1}{n}\sum_{k=1}^{n}\sigma(N^i_{BG};\varepsilon^i;k),$$

   where $G_1(k)$ and $G_2(k)$ are independent gaussian random numbers (with a mean of zero and a standard deviation of one).

Here the index i corresponds to one particular L3 squark search analysis over $\sqrt{s} = 161 - 208$ GeV, which has been included into the limits combination, and the error values ΔN^i_{BG} and $\Delta\varepsilon^i$ are within each $\sqrt{s}$ also dependent on the particular squark and the LSP (or the sneutrino) masses. The index $k = 1, n$ represents a Monte Carlo trial loop number and n should be some big number ($n = 100 - 300$ has been used).

All these approaches give a difference in the cross section limits (with respect to the limits calculation without systematics) of 0.05–0.1 pb for the considered stop and sbottom decay channels.

The first two cases are *conservative* approaches, leading to the most pessimistic numerical results, while the third one, the Monte Carlo approach of Gaussian random smearing around the mean values of the SM background rates and the signal efficiencies within the corresponding systematic errors has been chosen as the most correct as allowing for random variations in both positive and negative directions with treating the mean values of N^i_{BG} and ε^i as the most probable.

The 95 % C.L. upper limits on the squark production cross sections, which have been obtained this way (with both combination of all available L3 search results and with taking into account the systematic uncertainties), can be considered as the final cross section limits, and the corresponding plots are presented in Figures 9.13-9.16.

Comparison of Figures 9.13-9.16 and 9.9-9.12 shows that taking the systematic uncertainties into consideration slightly reduces the upper cross section limits (i.e. makes them slightly bigger).

To conclude, we set the 95 % confidence level upper limits on the scalar top production cross section at the level of 0.1 pb in the central area of the stop-LSP mass plane and of 0.2 pb in almost the whole remaining area in the analysis for the $\tilde{t}_1 \to c\tilde{\chi}^0_1$ decay channel. The scalar bottom quark production cross sections above 0.05 pb in the central area of the sbottom-LSP mass plane and above 0.1 pb in the remaining area are excluded at 95 % C.L for the $\tilde{b}_1 \to b\tilde{\chi}^0_1$ decay. The corresponding 95 % C.L. upper limits on the stop production cross section for the $\tilde{t}_1 \to bl\tilde{\nu}$ and for the $\tilde{t}_1 \to b\tau\tilde{\nu}$ decay channels are set at the level of 0.05-0.2 pb.

9.2 The CMSSM Interpretation

The upper limits on the squark production cross section can be considered as *model independent* limits, because they were calculated from the statistics of the observed data and expected SM events and the squark signal selection efficiency with general assumptions on the signal topology (two jets plus missing energy plus leptons in the stop three-body decays), but without fixing the CMSSM model parameters. (Strictly speaking, we used the information about change of the cross section with the center-of-mass energy when scaled all the cross sections to the one at $\sqrt{s} = 206$ GeV, but the CMSSM parameters were not used explicitly). If we constrain the parameters of the CMSSM and investigate their influence on the theoretically calculated scalar top and scalar bottom production cross sections in e^+e^- collisions at the considered center-of-mass energy, we can compare values of the theoretical cross section σ^{theor} with the experimentally obtained 95 % C.L. upper limit on this quantity, σ^{95}. If σ^{theor} turns out to be bigger than σ^{95}, then we can exclude the corresponding values of CMSSM parameters with a 95 % confidence level.

Similar to the above, we can obtain the *expected* exclusion of the theoretical model parameters comparing the theoretically calculated cross section with *expected* upper limits on it, σ^{95}_{exp}.

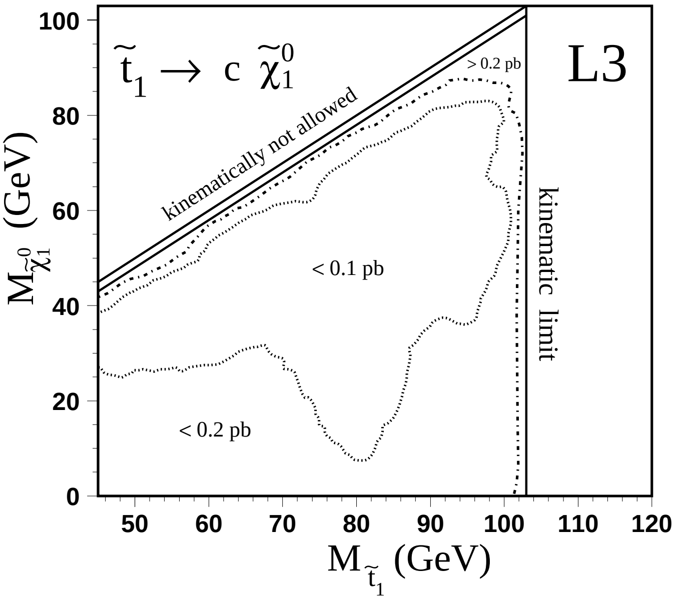

Figure 9.13: *The* 95 % *C.L. upper limit on the* $e^+e^- \rightarrow \tilde{t}_1\bar{\tilde{t}}_1 \rightarrow c\tilde{\chi}^0_1\bar{c}\tilde{\chi}^0_1$ *production cross section, combined over the L3 squark searches performed at the center-of-mass energies of* 161 − 208 *GeV with systematic uncertainties included into the calculation.*

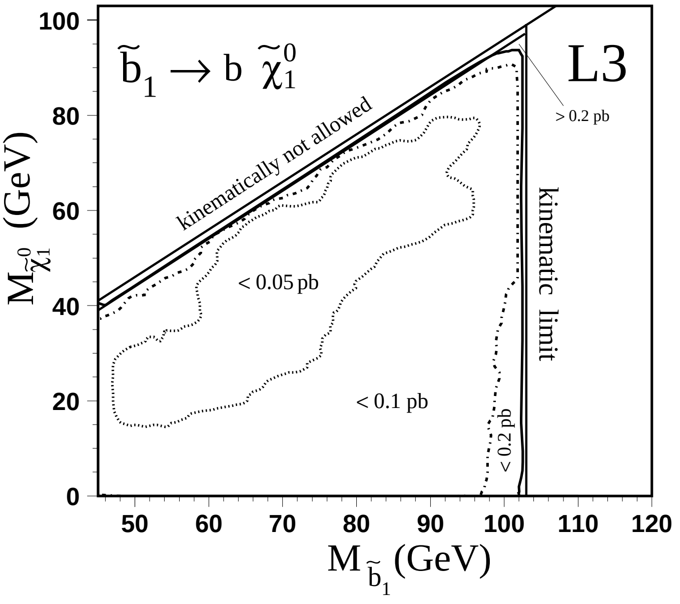

Figure 9.14: *The* 95 % *C.L. upper limit on the* $e^+e^- \rightarrow \tilde{b}_1\bar{\tilde{b}}_1 \rightarrow b\tilde{\chi}^0_1\bar{b}\tilde{\chi}^0_1$ *production cross section, combined over the L3 squark searches performed at the center-of-mass energies of* 161 − 208 *GeV with systematic uncertainties included into the calculation.*

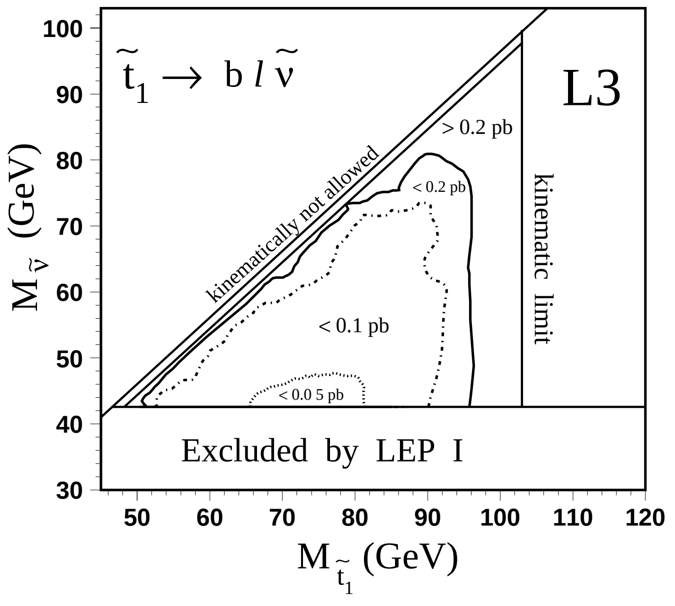

Figure 9.15: *The* 95 % *C.L. upper limit on the* $e^+e^- \to \tilde{t}_1\bar{\tilde{t}}_1 \to bl^+\tilde{\nu}\bar{b}l^-\tilde{\nu}$ *(*$l = e, \mu, \tau$*) production cross section, combined over the L3 squark searches performed at the center-of-mass energies of* $189 - 208$ *GeV with systematic uncertainties included into the calculation.*

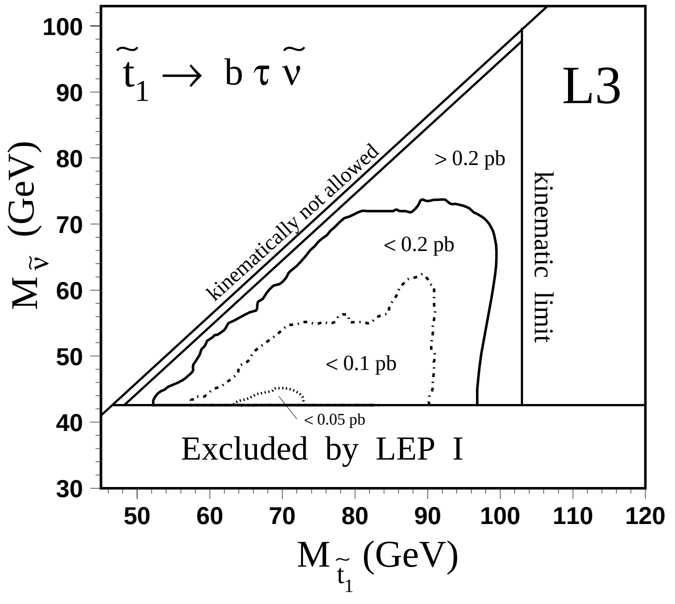

Figure 9.16: *The* 95 % *C.L. upper limit on the* $e^+e^- \to \tilde{t}_1\bar{\tilde{t}}_1 \to b\tau^+\tilde{\nu}\bar{b}\tau^-\tilde{\nu}$ *production cross section, combined over the L3 squark searches performed at the center-of-mass energies of* $189 - 208$ *GeV with systematic uncertainties included into the calculation.*

Using the 95 % C.L. upper limits on the cross section, *combined* over several L3 squark searches (and several center-of-mass energies), as described in the previous section, we obtain, correspondingly, the *combined* 95 % C.L. exclusion limits on the model parameters.

9.2.1 Limits on the Squark and the LSP Masses

The simplest dependency of the squark production cross section on the model parameters, which can be considered for the parameter exclusion, is the dependency of σ^{theor} on the scalar quark and the LSP (or the sneutrino) masses.

The theoretical cross section of the scalar top and scalar bottom quark production in e^+e^- collisions was calculated for the whole considered squark and LSP mass ranges with scan steps of 1 GeV. The calculations were performed using the CALVIN program, developed by the theoretical group of Prof. A. Bartl at Vienna University for the MSSM scalar quarks pair production at LEP II ([99]). The program takes into account standard QCD corrections as well as initial state radiation. Since the cross section also depends on the mixing angle between the left and right weak eigenstates of squarks (see Chapter 4 and [51], [100]), the cross sections were calculated for two values of θ_{LR}, corresponding to the maximal cross section value (at $\cos\theta_{LR} = 1$) and to the decoupling from the Z boson, where the cross section as a function of $\cos\theta_{LR}$ has a flat form and its value is approximately equal to the minimal one (at $\cos\theta_{LR} = 0.57$ for the stop and at $\cos\theta_{LR} = 0.39$ for the sbottom quarks). This allows us to determine the minimal and the maximal exclusion of particular masses of the scalar quarks and the LSP.

The 95 % C.L. exclusion limits obtained on the scalar top, scalar bottom and LSP (or the sneutrino) masses, combined over the same L3 squark searches (center-of-mass energies), as in the calculation of upper limits on the production cross section, are presented in Figures 9.17-9.20. For the considered decay channels, the scalar top and the scalar bottom quark masses were excluded at a 95% confidence level for the cases of maximum and minimum of the production cross section up to the following values (for not too small values of ΔM):

$$\begin{aligned}
\tilde{t}_1 \to c\tilde{\chi}^0_1 &: \quad M^{\sigma_{min}}_{\tilde{t}_1} < 90-93 \text{ GeV}, \quad M^{\sigma_{max}}_{\tilde{t}_1} < 95-96 \text{ GeV};\\
\tilde{t}_1 \to bl\tilde{\nu} &: \quad M^{\sigma_{min}}_{\tilde{t}_1} < 87-89 \text{ GeV}, \quad M^{\sigma_{max}}_{\tilde{t}_1} < 90-91 \text{ GeV};\\
\tilde{t}_1 \to b\tau\tilde{\nu} &: \quad M^{\sigma_{min}}_{\tilde{t}_1} < 83-88 \text{ GeV}, \quad M^{\sigma_{max}}_{\tilde{t}_1} < 88-91 \text{ GeV};\\
\tilde{b}_1 \to b\tilde{\chi}^0_1 &: \quad M^{\sigma_{min}}_{\tilde{b}_1} < 76-83 \text{ GeV}, \quad M^{\sigma_{max}}_{\tilde{b}_1} < 94-97 \text{ GeV}.
\end{aligned}$$

The contours of the expected mass exclusion are in general close to the experimental exclusion curves. A possible statistical excess-like fluctuation in the number of observed data events with respect to the Standard Model expectations (although, not significant enough to speak about any evidence for the signal observation) causes a situation, when we expect to exclude higher squark masses, than we really exclude by the experiment. For example, the higher *expected* exclusion of the stop mass in decay channel $\tilde{t}_1 \to c\tilde{\chi}^0_1$ at medium ΔM corresponds to a small deviation of the number of 4 observed data events from the Standard Model expectation of 1.3 ± 0.4 (*stat.*) ± 0.1 (*syst.*). Similarly, a small excess of 3 data events with respect to 0.7 ± 0.3 $(stat.)$ ± 0.2 $(syst.)$ expected from the Standard Model at high ΔM for the $\tilde{t}_1 \rightarrow b\tau\tilde{\nu}$ decay channel causes a higher *expected* exclusion compared to the experimental one.

Since systematic uncertainties on the signal selection efficiencies and on the SM background rates have been taken into account in the calculations of the upper limits on the production cross sections, they are also accounted for in the obtained 95 % C.L. mass inclusion limits.

The dependency of the scalar quark mass exclusion on the mixing angle θ_{LR} between the left and right weak eigenstates of squarks in the framework of the CMSSM is illustrated for a fixed value of $\Delta M = 15$ GeV in Figures 9.21-9.22. Actually, these curves reflect the dependency of the squark production cross section on θ_{LR}: at $\cos\theta_{LR} = 1$ the cross sections of $\tilde{t}_1$ and $\tilde{b}_1$ quark production are similar, while at lower values of $\cos\theta_{LR}$ the squark production proceeds mainly via γ exchange, which makes the sbottom quark production cross section smaller than the cross section of stop. The curves for $\tilde{t}_1 \rightarrow bl\tilde{\nu}$ and $\tilde{t}_1 \rightarrow b\tau\tilde{\nu}$ decay channels are quite close to each other and have a shape similar to the line for the $\tilde{t}_1 \rightarrow c\tilde{\chi}^0_1$ decay, although shifted a bit lower.

9.2.2 Extrapolation to the Squarks of the First Two Families

The interpretation of the squark search results can be extended to the scalar quarks of the first two generations, $\tilde{q} = \tilde{u}, \tilde{d}, \tilde{c}, \tilde{s}$, which are assumed within the MSSM framework as mass-degenerate. Since the dominant decay channel for these squarks in the e^+e^- collisions at LEP energies is $\tilde{q} \rightarrow q\tilde{\chi}^0_1$, the signal event topologies will be the same as for the $\tilde{t}_1 \rightarrow c\tilde{\chi}^0_1$ decay of the stop quark (but not as $\tilde{b}_1 \rightarrow b\tilde{\chi}^0_1$ because of the specific features of b-quark decays): two jets from the quark pair plus missing energy from two neutralinos. Therefore, for the mass degenerate squarks we can assume approximately the same selection efficiencies, as for the $\tilde{t}_1 \rightarrow c\tilde{\chi}^0_1$ signal.

If we make more assumptions on the production cross sections of the squarks, i.e. assume the (theoretical) cross section for *up-type* squarks being the same as for the scalar top ($\sigma^{theor}_{\tilde{u}} = \sigma^{theor}_{\tilde{c}} = \sigma^{theor}_{\tilde{t}}$) and cross section for *down-type* ones the same as for the scalar bottom ($\sigma^{theor}_{\tilde{d}} = \sigma^{theor}_{\tilde{s}} = \sigma^{theor}_{\tilde{b}}$), then we can exclude mass regions of the squarks of the first two generations in a similar way, as for stop and sbottom. Taking into account, that the total production cross section for the mass degenerate squarks $\tilde{q} = \tilde{u}, \tilde{d}, \tilde{c}, \tilde{s}$ is a sum of cross sections of particular squarks ($\tilde{u}, \tilde{d}, \tilde{c}$ and $\tilde{s}$), we get the total theoretical cross section in this case approximately four times bigger, than for stop or sbottom alone. Thus, the 95 % C.L. mass exclusion contour here comes closer to the kinematic limit, i.e. we exclude more. Also, we can consider either the case of purely *right* squark eigenstates $\tilde{q_R}$ or the case of presence of both *left* $\tilde{q_L}$ and *right* $\tilde{q_R}$ squarks, calculating the theoretical cross section with appropriate values of the mixing angle θ_{LR} (as $\cos\theta_{LR} = 1$ for the left and $\cos\theta_{LR} = 0$ for the right eigenstates). Furthermore, if the sbottom left-right mixing can be assumed as negligible, then we can consider the case, when the five squarks, $\tilde{u}, \tilde{d}, \tilde{c}, \tilde{s}$ and also $\tilde{b}$, are mass degenerate (as it was discussed in Chapter 4, the mixing for stop is much bigger because it is proportional to the SM top quark mass).

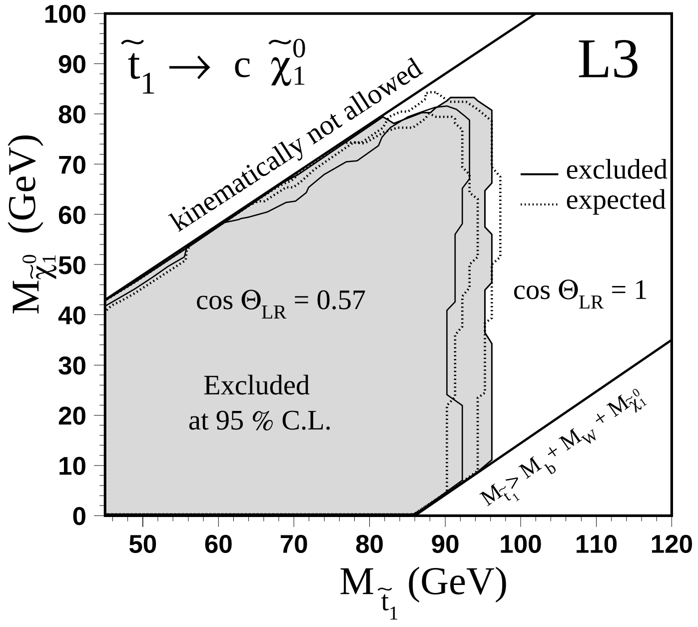

Figure 9.17: *The 95 % C.L. experimental and expected exclusion limits on the* $M_{\tilde{t}_1}$ *and* $M_{\tilde{\chi}_1^0}$ *masses within the framework of CMSSM for the* $\tilde{t}_1 \to c\tilde{\chi}_1^0$ *decay. The exclusions are given for maximal and minimal cross section assumptions.*

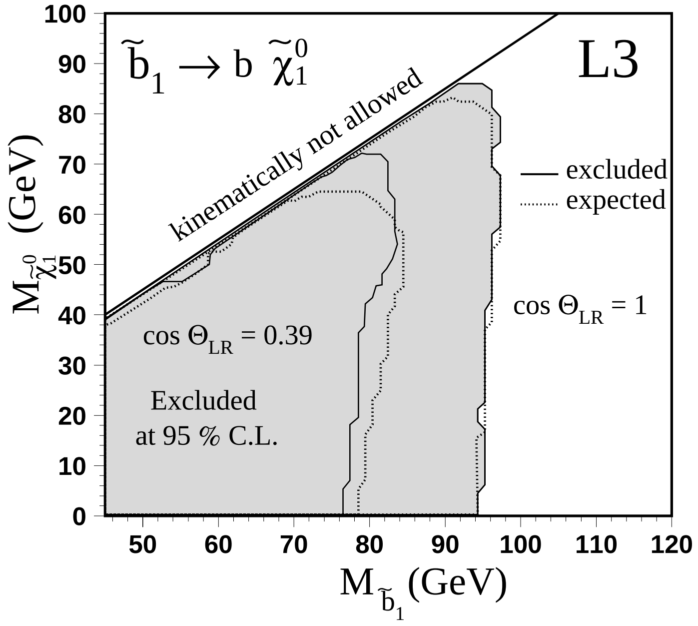

Figure 9.18: *The 95 % C.L. experimental and expected exclusion limits on the* $M_{\tilde{b}_1}$ *and* $M_{\tilde{\chi}_1^0}$ *masses within the framework of CMSSM for the* $\tilde{b}_1 \to b\tilde{\chi}_1^0$ *decay. The exclusions are given for maximal and minimal cross section assumptions.*

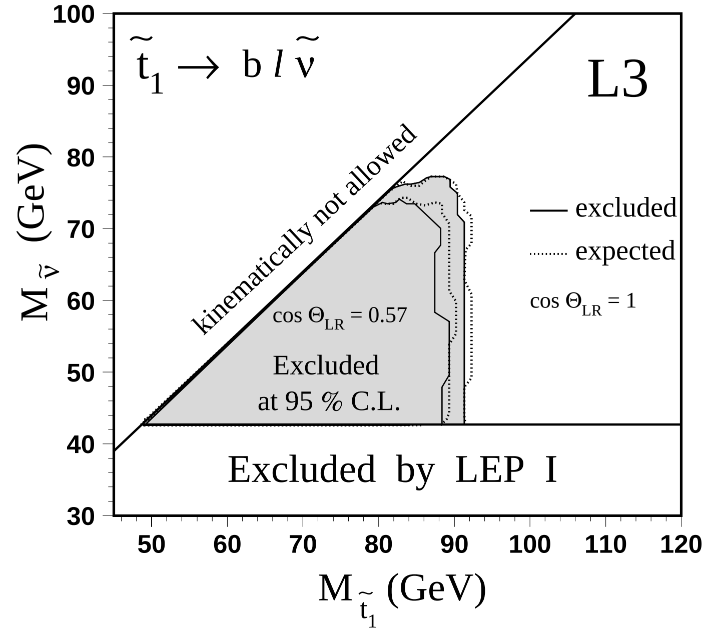

Figure 9.19: *The 95 % C.L. experimental and expected exclusion limits on the* $M_{\tilde{t}_1}$ *and* $M_{\tilde{\nu}}$ *masses within the framework of CMSSM for the* $\tilde{t}_1 \to bl\tilde{\nu}$ *decay. The exclusions are given for maximal and minimal cross section assumptions.*

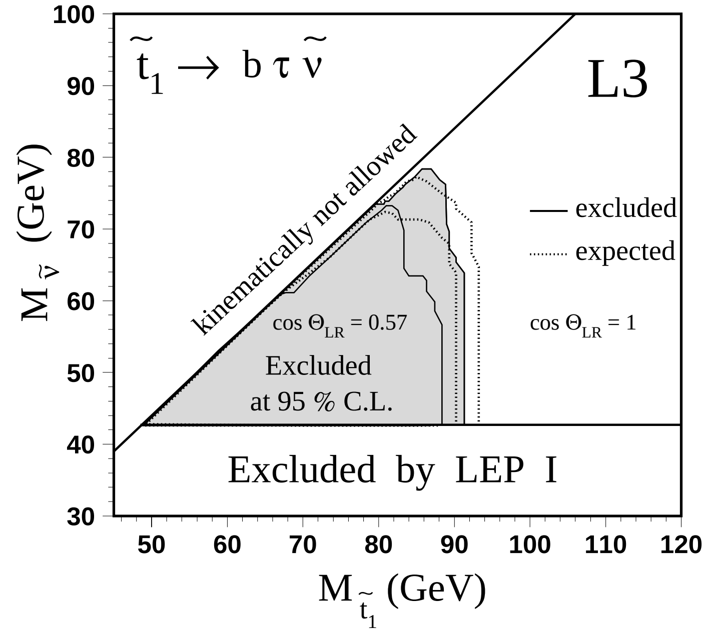

Figure 9.20: *The 95 % C.L. experimental and expected exclusion limits on the* $M_{\tilde{t}_1}$ *and* $M_{\tilde{\nu}}$ *masses within the framework of CMSSM for the* $\tilde{t}_1 \to b\tau\tilde{\nu}$ *decay. The exclusions are given for maximal and minimal cross section assumptions.*

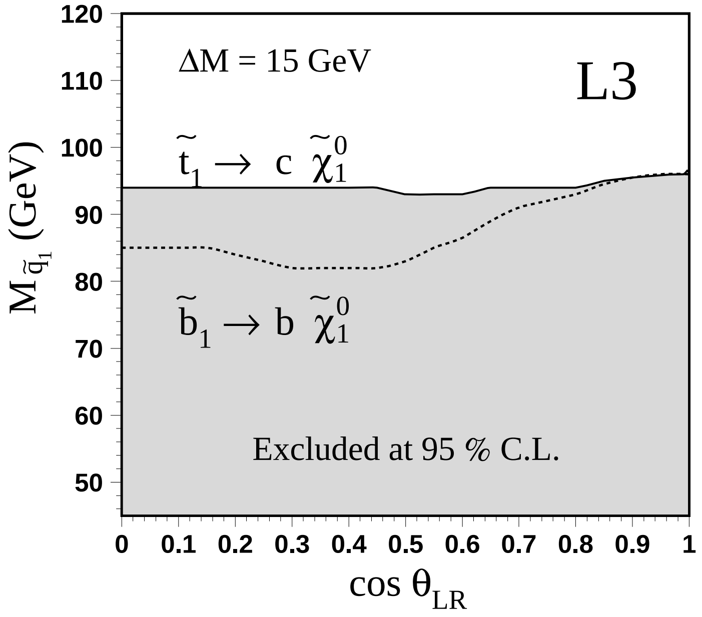

Figure 9.21: *The dependency of the* 95 % *C.L. exclusion of the scalar top (solid line) and scalar bottom (dashed one) quark masses on the mixing angle* θ_{LR} *for* $\tilde{t}_1 \rightarrow c\tilde{\chi}_1^0$ *and* $\tilde{b}_1 \rightarrow b\tilde{\chi}_1^0$ *decay channels at fixed* $\Delta M = 15$ *GeV.*

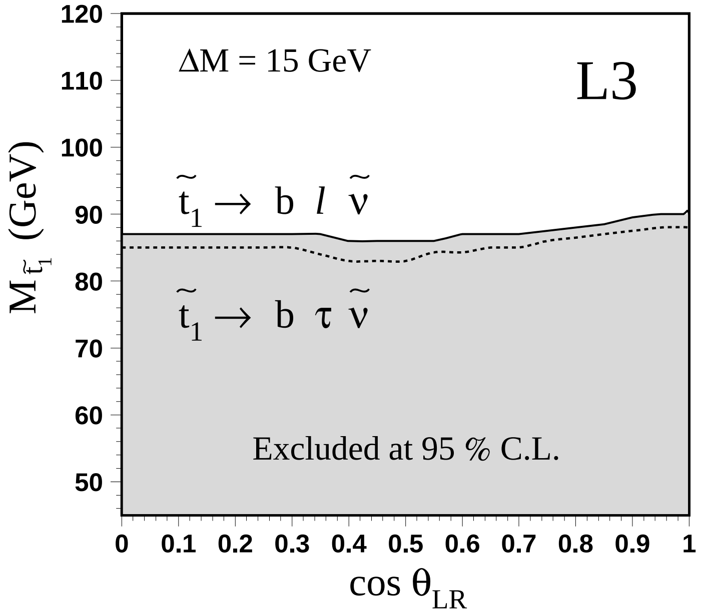

Figure 9.22: *The dependency of the* 95 % *C.L. exclusion of the scalar top quark mass on the mixing angle* θ_{LR} *for* $\tilde{t}_1 \rightarrow bl\tilde{\nu}$ *(solid line) and* $\tilde{b}_1 \rightarrow b\tilde{\chi}_1^0$ *(dashed one) decay channels at fixed* $\Delta M = 15$ *GeV.*

Figure 9.23 shows the 95 % C.L. mass exclusion contours for the cases of the mass degeneracy between the four and five scalar quarks, both for the right-only and for the left-and-right eigenstates hypotheses. For these cases the squark masses are excluded (for the region $\Delta M > 10\ GeV$) up to the following values:

$$\tilde{q} = \tilde{u}\ \tilde{d}\ \tilde{c}\ \tilde{s}: \qquad M_{\tilde{q_R}} < 95 - 96\ \mathrm{GeV}, \quad M_{\tilde{q_{LR}}} < \ 99 - 100\ \mathrm{GeV};$$

$$\tilde{q} = \tilde{u}\ \tilde{d}\ \tilde{c}\ \tilde{s}\ \tilde{b}: \qquad M_{\tilde{q_R}} < 96 - 97\ \mathrm{GeV}, \quad M_{\tilde{q_{LR}}} < \ 99 - 101\ \mathrm{GeV}.$$

9.2.3 Interpretation in the Squark-Gluino Mass Plane

As it was mentioned in Chapter 4, in the Minimal Supergravity (mSUGRA) scenario of the Supersymmetry Breaking, masses of all the scalar particles (Higgs, sleptons and squarks) are assumed to unify at the GUT scale to m_0 and all masses of gauginos (Bino, Wino and gluino) are also unified to $m_{1/2}$ [60], [61]. Using the renormalization group equations (the RGEs), the soft SUSY Breaking parameters, specified at the GUT scale, can be related to the Electroweak scale ($M_{EW} \sim M_Z$) and, fixing the values of parameters m_0, $m_{1/2}$, A_0, $\tan\beta$ and μ, we can define the particle mass spectrum at M_{EW}. In particular, for $|\mu| > M_1, M_2$ and small $\tan\beta$ values (when $\tilde{\chi}_1^0$ is the LSP) we have:

$$M_{\tilde{\chi}_2^0} \simeq 2M_{\tilde{\chi}_1^0} \simeq M_{\tilde{\chi}_1^\pm} \simeq 1/3\ M_{\tilde{g}} \simeq 0.8\ m_{1/2}\ , \tag{9.11}$$

This allows us to relate the gluino and the LSP masses:

$$M_{\tilde{g}} \simeq 6\ M_{\tilde{\chi}_1^0}\ , \tag{9.12}$$

and so, to reinterpret the obtained 95 % C.L. squark-LSP mass limits (for the mass degenerate squarks) in the ($M_{\tilde{g}}$, $M_{\tilde{q}}$) plane.

From the other side, the limits on the neutralino or gaugino masses, obtained (for a certain value $\tan\beta = 4$) from the chargino, neutralino and slepton searches, can be also related to the gluino and squark masses (although, as indirect limits). This can be realized with help of the ISAJET/ISASUGRA program [101], fixing the parameters A_0, $\tan\beta$ and μ, using the limit value for M_1 (M_2 or $m_{1/2}$) and varying m_0 and $M_{\tilde{g}}$.

In the sense of these reinterpretations of the L3 squark (and also sleptons, chargino and neutralino) search results the masses of gluino and degenerated squarks are excluded at 95 % C.L. at the level of:

$$M_{\tilde{\mathrm{g}}} > 267 - 314\ \mathrm{GeV},$$

$$M_{\tilde{\mathrm{q}}} > 98 - 100\ \mathrm{GeV}.$$

Moreover, these reinterpretations give us the complete picture of the strongly-interacting SUSY sector at LEP II and allow to directly compare our results with those of the other High Energy Physics experiments - D0 and CDF at the Tevatron $p\bar{p}$-collider at Fermilab [102, 103] and the UA1/UA2 experiments at CERN [104], as shown in Figure 9.24.

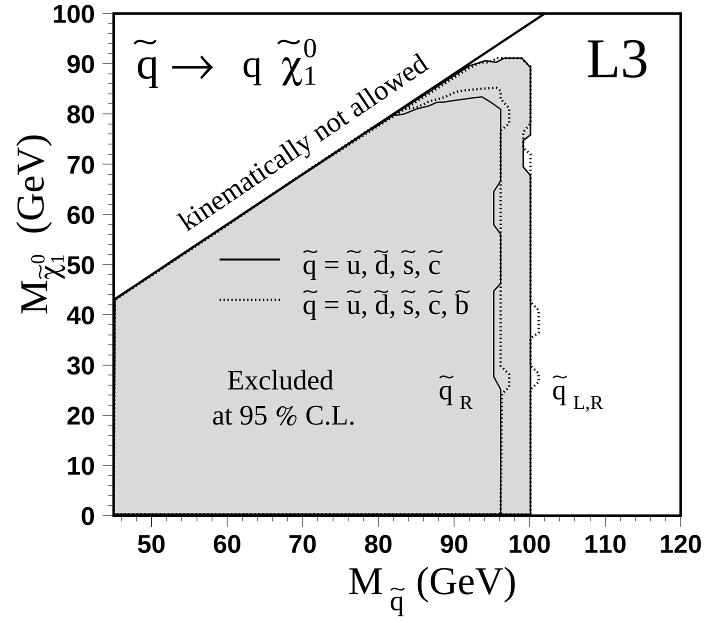

Figure 9.23: *The 95 % C.L. mass exclusions for the cases of the mass degeneration between four ($\tilde{u}, \tilde{d}, \tilde{c}, \tilde{s}$) and five ($\tilde{u}, \tilde{d}, \tilde{c}, \tilde{s}$ and $\tilde{b}$) squarks with assumption of presence of either right-only or left-and-right squark eigenstates.*

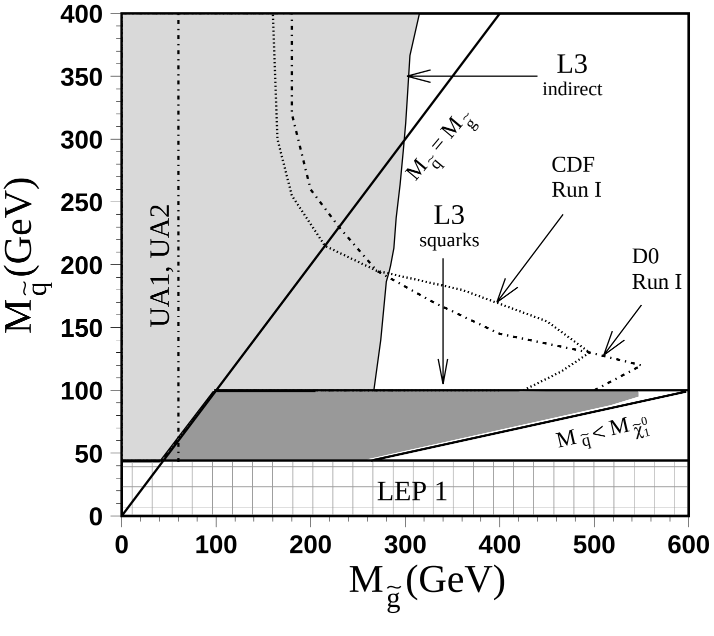

Figure 9.24: *The LEP squark, slepton, chargino and neutralino search results interpretation on the ($M_{\tilde{q}}$, $M_{\tilde{g}}$) plane, where LEP results can be compared with results of various HEP experiments: UA1/UA2 and CDF/D0. Values of $\tan\beta = 4$ and $\mu = -400$ GeV were used here.*

Chapter 10

Search for the Decay $\tilde{t}_1 \to bW\tilde{\chi}_1^0$

As discussed before, the decay mode of type $\tilde{q} \to q\tilde{\chi}_1^0$, which is the most preferable for all scalar quarks, is not possible for the stop quark pairs produced at the LEP II energies ($\sqrt{s} \leq 208$ GeV) because of the high mass of the SM top quark ($m_t \simeq 175$ GeV). That's why, the decay mode $\tilde{t}_1 \to c\tilde{\chi}_1^0$ was considered instead. But since it is the flavour changing weak process, the three-body decays $\tilde{t}_1 \to b\ell\tilde{\nu}_\ell$ and $\tilde{t}_1 \to \mathrm{b}W\tilde{\chi}_1^0$ can dominate over this channel when kinematically allowed.

The stop decay $\tilde{t}_1 \to b\ell\tilde{\nu}_\ell$ is allowed in the whole considered range of the scalar top and the sneutrino masses (from those excluded by LEP I up to the kinematic limit). On the contrary, due to the high mass of the W boson, the $\tilde{t}_1 \to \mathrm{b}W\tilde{\chi}_1^0$ decay is kinematically allowed only in the relatively small region of the stop-LSP mass plane $M_{\tilde{t}_1} > M_\mathrm{b} + M_W + M_{\tilde{\chi}_1^0} \geq 86$ GeV.

Moreover, the stop decays $\tilde{t}_1 \to c\tilde{\chi}_1^0$ and $\tilde{t}_1 \to b\ell\tilde{\nu}_\ell$ have very similar topology: two jets plus missing energy (plus two leptons in the case of the leptonic decay). On the other side, the topology of the $\tilde{t}_1 \to \mathrm{b}W\tilde{\chi}_1^0$ mode is determined by the subsequent decay of the W boson and additional jets may be present in the event, when one or both (from the *pair* of the stop quarks produced in e^+e^- collision) W bosons decay to a quark-antiquark pair.

For these reasons, the leptonic three-body stop decay $\tilde{t}_1 \to b\ell\tilde{\nu}_\ell$ was considered as a standalone possible stop decay and was analyzed in a similar manner and in parallel to the other stop and sbottom decays ($\tilde{t}_1 \to c\tilde{\chi}_1^0$ and $\tilde{b}_1 \to b\tilde{\chi}_1^0$); this group of the squark decays is for distinction referred to as *the main considered* squark decay channels. The analysis of the $\tilde{t}_1 \to \mathrm{b}W\tilde{\chi}_1^0$ decay has certain differences from this group and is considered separately, as *additional* (and *complementary* to the $\tilde{t}_1 \to c\tilde{\chi}_1^0$ decay), although, we tried to keep the general strategy of the analysis and the kinematic variables and cuts the same (when possible) as for the main squark decays, but some cut variables, specific to the $\tilde{t}_1 \to \mathrm{b}W\tilde{\chi}_1^0$ decay, were modified in an appropriate way.

10.1 The Signal and the SM Background

The process considered here, $\tilde{t}_1 \to \mathrm{b}W\tilde{\chi}_1^0$, may occur via the following three decay schemes (for a detailed description see [105]):

- via $\tilde{t}_1 \to W^+ \tilde{b}_1$ with further decay $\tilde{b}_1 \to \mathrm{b}\tilde{\chi}_1^0$;
- via $\tilde{t}_1 \to \mathrm{b}\tilde{\chi}_1^+$ with $\tilde{\chi}_1^+ \to W^+ \tilde{\chi}_1^0$;
- or, for higher $\tilde{t}_1$ masses or a virtual t, via $\tilde{t}_1 \to \mathrm{t}\tilde{\chi}_1^0$ with $\mathrm{t} \to \mathrm{b}W^+$.

The Feynman graphs for these processes are shown in Figure 10.1. For the generation of this signal events, the Monte Carlo program GSQUARK [66] has been modified taking into account the kinematics of the three-body decay and the matrix elements for this process [105]. For various combinations of the stop quark and the LSP masses, $M_{\tilde{t}_1} = 88 - 103.5$ GeV and $M_{\tilde{\chi}_1^0} = 2 - 16$ GeV (within the allowed area of the mass corner of $M_{\tilde{t}_1} > M_\mathrm{b} + M_W + M_{\tilde{\chi}_1^0} \geq 86$ GeV), 15 MC samples of 1000 events each were generated.

Since the signal topology has the common features with the main considered squark decays (two or more jets plus missing energy), the same Standard Model processes serve as the background here and the same Monte Carlo samples of the SM background have been used.

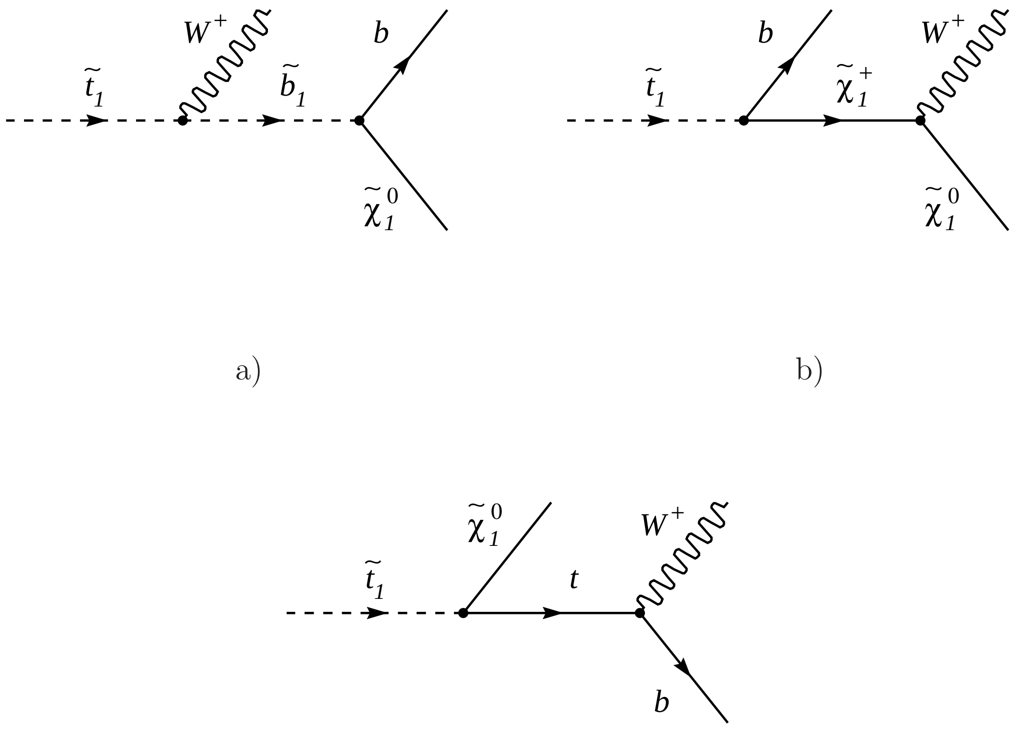

a) b)

c)

Figure 10.1: *Feynman graphs for the considered three-body decay of the scalar top quark* $\tilde{t}_1 \to \mathrm{b}W\tilde{\chi}_1^0$.

10.2 Preselection of the Event Samples

The preselection of the squark signal and the SM background Monte Carlo event samples was kept in general similar to the one used for the main stop and sbottom decays as described in section 7.4.1, while there were certain changes specific to the considered three-body stop decay $\tilde{t}_1 \to \mathrm{b}W\tilde{\chi}_1^0$.

As already mentioned, for this decay, the event topology depends on the decay mode of the W boson: either $W \to \bar{q}q$ with about 67% branching fraction or $W \to \ell\nu_\ell$ with branching of 33% (where ℓ can be e, μ or τ with approximately equal probabilities). Thus, the signal topology for this decay mode of the produced stop quark pair can be:

- either 2 b-jets + E_{miss} (from $\tilde{\chi}_1^0$) + 2 × 2 jets (from $W \to \bar{q}q$),
- or 2 b-jets + E_{miss} (from $\tilde{\chi}_1^0$ and ν) + 2 leptons (from $W \to \ell\nu_\ell$),
- or 2 b-jets + E_{miss} + 2 jets + 1 lepton (when one W goes to a $q\bar{q}$ pair and another one to $\ell\nu_\ell$).

So, the specific features of the $\tilde{t}_1 \to bW\tilde{\chi}_1^0$ decay are: the possible presence of additional jets from $W \to \bar{q}q$ and a relatively bigger $E_{vis} \simeq \Delta M = M_{\tilde{t}_1} - M_{\tilde{\chi}_1^0}$ (and smaller E_{miss}) in the allowed mass parameter region, compared to the $\tilde{t}_1 \to c\tilde{\chi}_1^0$ decay, as illustrated in Figure 10.2. As a result, the $\tilde{t}_1 \to bW\tilde{\chi}_1^0$ signal sample contains a significant fraction of high multiplicity hadronic events (Fig. 10.2), and, correspondingly, at the preselection level the upper cuts on the numbers of tracks and number of calorimeter clusters were loosened compared to the main analyzed squark channels.

Since the number of jets differs from one event to another, all the $\tilde{t}_1 \to bW\tilde{\chi}_1^0$ signal events have been analyzed in terms of kinematic variables after clustering of the event into two jets by the DURHAM jet reconstruction algorithm. So, except for the upper cuts on the event multiplicity, the other preselection cuts and the cut variables themselves were kept the same as for the main analyzed squark channels.

The change of the preselection cuts in the analysis for the $\tilde{t}_1 \to bW\tilde{\chi}_1^0$ channel affects both the numbers of the preselected data and the SM background events, which amount for this channel to 4446 experimental data events and 4659.1 ± 23.4 (stat.) events of the expected Standard Model processes, while the signal efficiency is kept at the level of 63 – 75%.

10.3 Optimization of Selection

Because of the above mentioned dependency of the $\tilde{t}_1 \to bW\tilde{\chi}_1^0$ decay topology on the subsequent decay mode of the W boson, the optimizations for each type of the W decay were performed separately. It means, that the signal events were classified for the optimization according to the presence or absence of the lepton from the W decay and according to the flavour of this lepton: events with hadronic W decays, with decays to $e\bar{\nu}_e$, to $\mu\bar{\nu}_\mu$ and to $\tau\bar{\nu}_\tau$. For this classification, the presence of a lepton with energy above 10 GeV was used as a signature of the leptonic W decay, as illustrated in Figure 10.2, d). Taking into account the possibility of mis-identification or loss of a lepton in

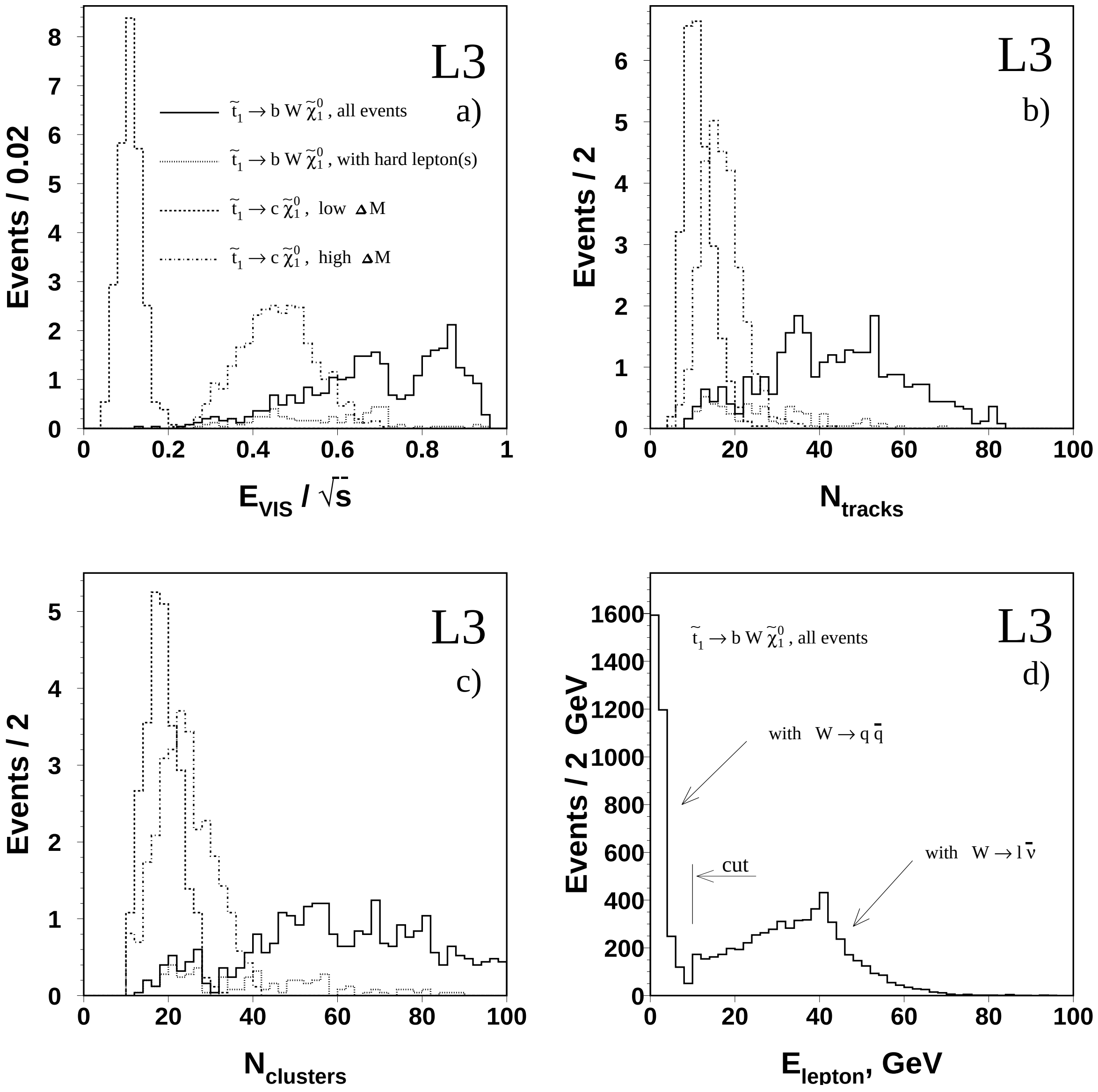

Figure 10.2: *Distributions of a) $E_{vis}/\sqrt{s}$; b) number of tracks and c) number of calorimeter clusters after the preselection in the analysis for the $\tilde{t}_1 \rightarrow bW\tilde{\chi}^0_1$ decays in comparison to the $\tilde{t}_1 \rightarrow c\tilde{\chi}^0_1$ channel. The $\tilde{t}_1 \rightarrow bW\tilde{\chi}^0_1$ decay sample has a significant fraction of events with bigger E_{vis} and higher track and cluster multiplicities (see text). The distribution of energy of identified leptons (d) helps to separate the events with $W \rightarrow \ell\tilde{\nu}_\ell$ from those with $W \rightarrow q\bar{q}$. Signal curves are weighted according to the cross sections of the squark generator program (with $\cos\theta_{LR} = 1$) and the luminosity of the data sample.*

the detector, and also because of the relatively small fraction of simultaneous leptonic decays of two W bosons from the stop quark pair, only (at least) one lepton was required for classifying an event as event with leptonic W decay.

Moreover, the $\tilde{t}_1 \to bW\tilde{\chi}_1^0$ signal events with non-leptonic decays of the W (i.e. without identified lepton above 10 GeV) have the smallest missing energy and are more similar to the fully-hadronic events than to the SUSY events with large E_{miss} as a signature. So, their separation from the hadronic SM background events is more difficult. Thus, it was found more rational to fully exclude such kind of events from the optimal selection. This of course leads to a certain loss of the signal selection efficiency, but, on the other side, it makes the signal/background separation and the optimization procedure itself much more easy and it results in a more sensitive selection due to the bigger suppression of the hadronic SM background.

To follow the same two-jet analysis scheme as for the main stop and sbottom decay channels, the same cut variables (as described in section 7.4.2) have been used for the selection optimization for the $\tilde{t}_1 \to bW\tilde{\chi}_1^0$ decay. Since the masses of the scalar top quark and the neutralino are varied in a relatively small corner of the mass plane ($M_{\tilde{t}_1} > M_{\rm b}+M_W+M_{\tilde{\chi}_1^0} \geq 86$ GeV), the mass difference ΔM varies not so much compared to the other stop and sbottom channels and the analysis can be considered as corresponding to one (high) ΔM region. Nevertheless, to achieve the most sensitive selection over the considered mass corner, three independent selection optimizations have been performed (for the 'edge' points of the allowed mass triangle).

The signal selection efficiencies and the Standard Model background rates for the optimal selections found for these three stop-neutralino mass plane points are presented in Table 10.1 together with the corresponding stop quark and the neutralino mass values.

$M_{\tilde{t}_1}$ (GeV)	$M_{\tilde{\chi}_1^0}$ (GeV)	ΔM (GeV)	ε (%)	N_{SM}
103.5	16	87.5	10.6	26.9
103.5	2	101.5	11.2	68.3
88.0	2	86.0	12.8	135.6

Table 10.1: *Signal selection efficiencies, ϵ, number of events expected from the SM processes, $N_{\rm SM}$, in the selections optimized for the $\tilde{t}_1 \to bW\tilde{\chi}_1^0$ decay channel and corresponding stop quark and the neutralino masses. Typical statistical errors on the signal selection efficiency are about 1–2 % and those on the SM background rate are about 2–5 %.*

10.4 The Search Results and the Interpretation

The results of the optimal selections (numbers of the observed data events and numbers of events, expected from the SM background) for the considered $\tilde{t}_1 \to bW\tilde{\chi}_1^0$ stop decay are presented in Table 10.2 for the three used values of the stop and the neutralino masses and for the "OR"-combination of these three selection (see section 8.2.1 about the "OR"-combination of selections).

$M_{\tilde{t}_1}$ (GeV)	$M_{\tilde{\chi}^0_1}$ (GeV)	ΔM (GeV)	N_D	N_{SM}
103.5	16	87.5	30	26.9 ± 1.2
103.5	2	101.5	68	68.3 ± 1.9
88.0	2	86.0	144	135.6 ± 2.6
Combined			184	181.6 ± 3.0

Table 10.2: *Number of observed data events, N_{D}, the SM background expectations, N_{SM}, and corresponding stop quark and the neutralino masses for selections, optimized for the $\tilde{t}_1 \to bW\tilde{\chi}^0_1$ decay channel. The quoted errors are due to MC statistics only.*

In the combined optimal selection, 184 data candidate events are observed, which agrees with the SM expectation of 181.6 ± 3.0 (stat.) ± 23.4 (syst.) events. Comparing to the other investigated squark decay channels, the contribution from the hadronic SM processes (WW, $We\nu$, ZZ) is as significant as the contribution from the $eeq\bar{q}$ process. A similar (as in searches for the main considered stop and sbottom quark decays) conclusion about the non-observation of any signal evidence has been obtained also for the $\tilde{t}_1 \to bW\tilde{\chi}^0_1$ channel.

The sources of the systematical errors in estimation of the signal selection efficiency and the Standard Model background rate are obviously the same, as considered for the other scalar top and scalar bottom quark decays, as described in detail in section 8.3. The relative systematic errors on the signal selection efficiency and on the number of the SM Monte Carlo events calculated for the $\tilde{t}_1 \to bW\tilde{\chi}^0_1$ decay are presented in Table 10.3.

The interpolation of the signal selection efficiencies over the stop-neutralino mass plane and the choice of the best (the most sensitive) selection for each particular mass point have been done exactly in the same way, as for the other considered stop and sbottom decays (as described in details in Chapter 9). Then, the 95 % C.L. upper limits on the stop quark production cross section have been derived also in the same way, as described in detail above. The systematical errors have been taken into account with the MC approach of the gaussian smearing of the ε and N_{BG} around their mean values, but, since there were no searches for the $\tilde{t}_1 \to bW\tilde{\chi}^0_1$ stop decay performed in the L3 Collaboration before (for the previous years of the LEP operation and for the smaller $\sqrt{s}$ energies), there was no combination with any other searches for this stop decay.

The obtained 95 % C.L. upper limits on the stop production cross section for the case of the considered $\tilde{t}_1 \to bW\tilde{\chi}^0_1$ decay are presented in Figure 10.3. The production cross sections above 0.7–0.9 pb are excluded at 95 % C.L. almost everywhere in the allowed mass corner. These limits are quite big compared to the main investigated stop and sbottom channels due to several factors: first, the above mentioned higher multiplicity

Syst. Error Source		$\tilde{t}_1 \rightarrow \mathrm{b}W\tilde{\chi}^0_1$
Monte Carlo statistics	$\Delta\varepsilon$	1.4–1.7
	ΔN_{SM}	2–5
SM cross section	$\Delta\varepsilon$	–
	ΔN_{SM}	2
Luminosity uncertainty	$\Delta\varepsilon$	–
	ΔN_{SM}	0.3
Energy calibration	$\Delta\varepsilon$	2–6
	ΔN_{SM}	10–18
Squark signal simulation	$\Delta\varepsilon$	4–12
	ΔN_{SM}	–
Overall	$\Delta\varepsilon$	5–14
	ΔN_{SM}	10–19

Table 10.3: *Relative systematic errors (in %) on the signal selection efficiency and the Standard Model background rate for various considered uncertainties sources for the* $\tilde{t}_1 \rightarrow bW\tilde{\chi}^0_1$ *stop quark decay.*

and higher visible energy, specific for this channel, make the separation of the hadronic background events more difficult; second, the restriction to only events with at least one identified lepton above 10 GeV (i.e. requirement of at least one leptonic decay of produced W) results in efficiency losses and thus, also does not allow to reach smaller limit values; moreover, the absence of results of the other searches for this stop decay does not allow us to combine more measurements and more data luminosity in the limits calculation.

Since the 95 % C.L. upper limits on the production cross section in the scenario of the $\tilde{t}_1 \rightarrow bW\tilde{\chi}^0_1$ decay do not reach the level of the theoretical cross section values, no 95 % C.L. exclusion limits on the stop and neutralino masses under the assumption of this three-body decay could be set.

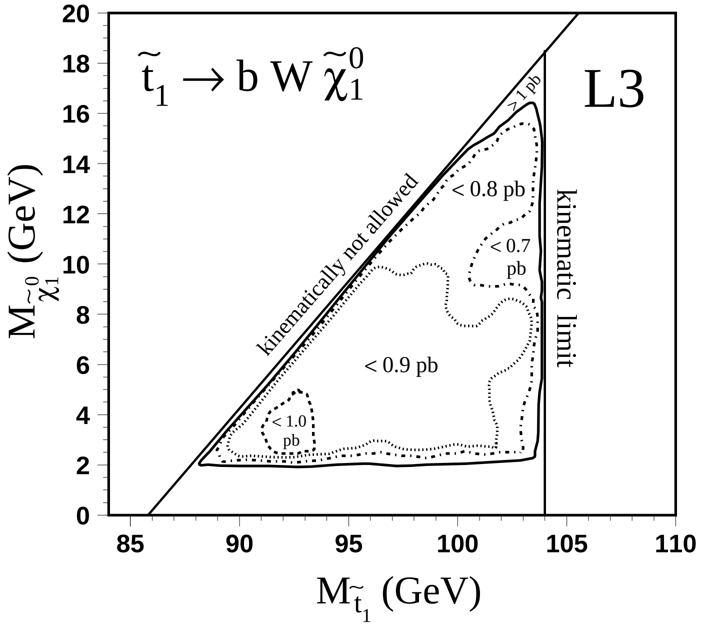

Figure 10.3: *95% upper limits on* $e^+e^- \to \tilde{t}_1\bar{\tilde{t}}_1 \to bW^+\tilde{\chi}_1^0\ \bar{b}W^-\tilde{\chi}_1^0$ *production cross section times branching ratio of the considered stop decay. Since this stop decay channel has not been searched for by the L3 experiment in the past years, the limits correspond to only the year 2000 L3 data. The statistical and systematical errors on the signal selection efficiency and on the numbers of expected SM events have been taken into account.*

Chapter 11

Comparison to Other Experiments and Future Prospects

As mentioned in Chapter 6, there were four particle detectors installed at the LEP Accelerator Ring and correspondingly, four experiments operating in parallel: ALEPH, DELPHI, L3 and OPAL [70]. All of these detectors are of the general purpose type and have been used for studies of similar e^+e^- reactions at the same center-of-mass energy: the Standard Model measurements (especially, Z and W physics) as well as searches for new physics (search for the Higgs boson, SUSY particles and other model beyond the Standard Model). Thus, the results obtained independently by each of the LEP Experiments can be directly compared to (and cross checked with) the corresponding results of the other LEP Collaborations.

In particular, searches for the MSSM scalar top and scalar bottom quarks have been performed by each of the LEP Collaborations and the L3 results presented and described in this thesis can be directly compared to those obtained by the ALEPH, DELPHI and OPAL Collaborations. All of the LEP Experiments confirm each other with the conclusion of absence of any evidence for the MSSM scalar quark signal. As the most general results of the squark searches, the 95 % C.L. exclusion limits on the squark and the LSP masses obtained by the ALEPH, DELPHI and OPAL Experiments for the two body decays $\tilde{t}_1 \to c\tilde{\chi}_1^0$ and $\tilde{b}_1 \to b\tilde{\chi}_1^0$ are presented in Figures 11.1-11.3 [106]. The corresponding limit plots, representing the L3 Collaboration results, are shown in Chapter 9 (Figures 9.17 and 9.18).

For a better numerical comparison between these plots, the squark masses excluded at 95 % C.L. for the $\tilde{t}_1 \to c\tilde{\chi}_1^0$ and $\tilde{b}_1 \to b\tilde{\chi}_1^0$ decays with ΔM between 15 and 65 GeV are summarized in Table 11.1 for all four LEP experiments, together with results of the L3 squark analysis presented here. Both from visual and numerical comparisons we see, that the limits on the scalar top and the scalar bottom masses are in good accordance with results of similar analyses performed by the other LEP Experiments. This agreement was expected because of the same physics processes being under investigation (the same theoretical framework for the MC simulation of the squark signal and the Standard Model processes), because of the similarity of the ALEPH, DELPHI, L3 and OPAL detectors (all of them have central tracking systems, surrounded by electromagnetic and hadron calorimeters and by outer muon spectrometers) and because of similar cut-based

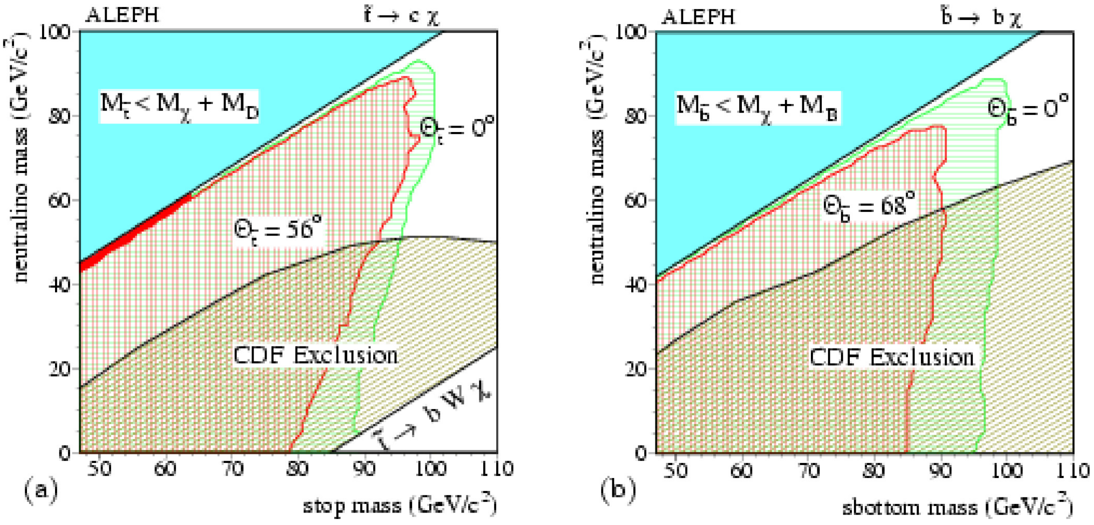

Figure 11.1: *95 % C.L. exclusion limits on the scalar top and the scalar bottom quark masses obtained for* $\tilde{t}_1 \to c\tilde{\chi}_1^0$ *(left) and* $\tilde{b}_1 \to b\tilde{\chi}_1^0$ *(right) decay channels by the ALEPH experiment [106].*

analyses. The small differences are obviously defined by differences in systematics from the performance of the detectors, MC simulations and numerical calculations, which all are independent in each LEP Experiment. The cross section limits obtained by ALEPH, DELPHI and OPAL for the $\tilde{t}_1 \to bl\tilde{\nu}$ and $\tilde{t}_1 \to b\tau\tilde{\nu}$ squark decay channels can be found in [106]; results for these channels are also close to each other.

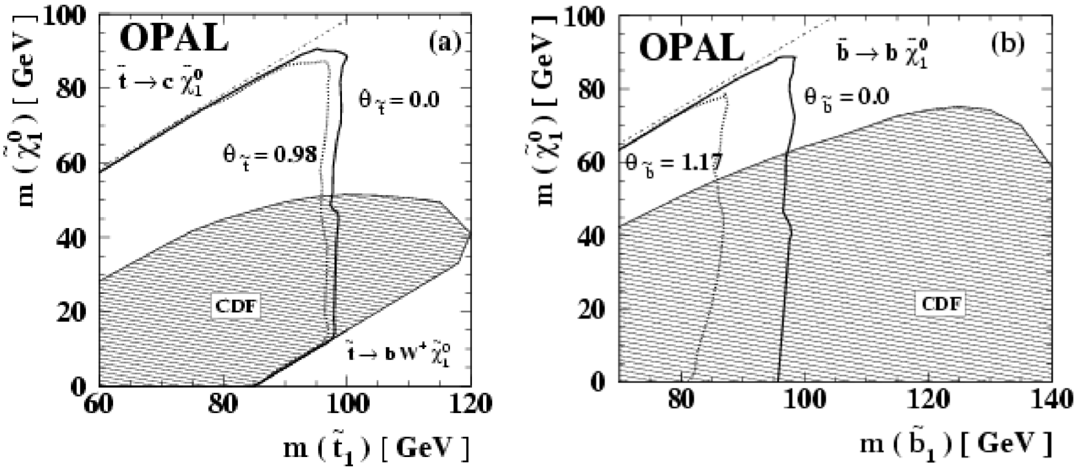

Figure 11.2: *95 % C.L. exclusion limits on the scalar top and the scalar bottom quark masses obtained for* $\tilde{t}_1 \to c\tilde{\chi}_1^0$ *(left) and* $\tilde{b}_1 \to b\tilde{\chi}_1^0$ *(right) decay channels by the OPAL experiment [106].*

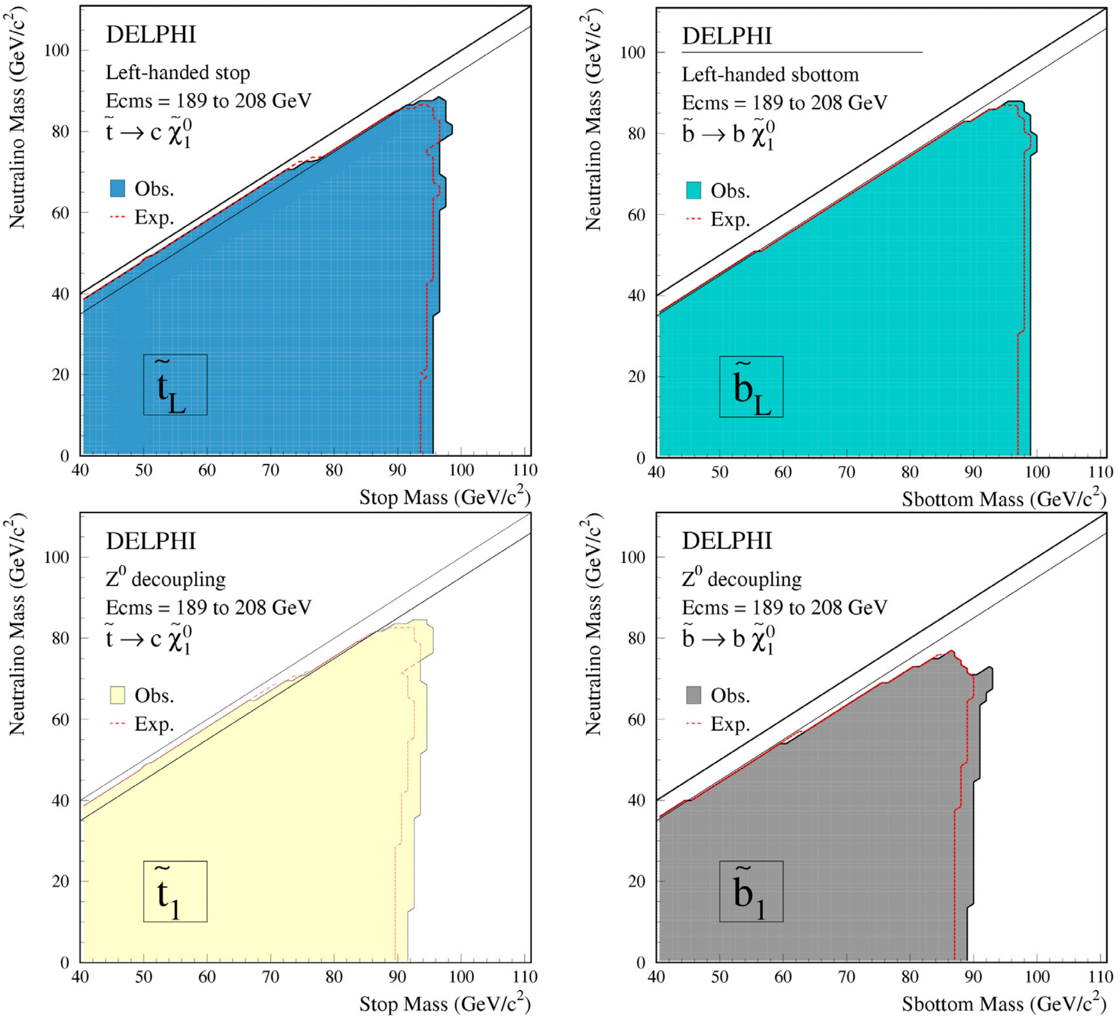

Figure 11.3: *95 % C.L. exclusion limits on the scalar top and the scalar bottom quark masses obtained for $\tilde{t}_1 \to c\tilde{\chi}^0_1$ (left) and $\tilde{b}_1 \to b\tilde{\chi}^0_1$ (right) decay channels by the DELPHI experiment [106].*

The results of the analysis presented in this thesis can be also compared to those obtained by the CDF and D0 Experiments [102, 103] during the Run I operation period of the Tevatron Collider, when data of $p\bar{p}$ interactions at center-of-mass energy 1.8 TeV were collected with a total integrated luminosity of about 0.1 fb^{-1}. But since the $p\bar{p}$ physics differs significantly from the e^+e^- processes, the comparison between the L3 (LEP) and the CDF/D0 (Tevatron) squark results can be done either after the MSSM interpretation of the LEP results into the squark-gluino mass plane, as it was described in Chapter 9, Figure 9.24, or after representation of the Tevatron squark and the LSP mass limits on the squark-neutralino mass plane, as shown in Figures 11.1-11.2. The comparison between the LEP and the Tevatron results reflects the difference in the center-of-mass energy between them ($\sqrt{s}$ is much bigger at Tevatron) On the

LEP Experiment	$\tilde{t}_1 \to c\tilde{\chi}^0_1$		$\tilde{b}_1 \to b\tilde{\chi}^0_1$	
	$M^{95\%}_{excl}$ for σ_{min}	$M^{95\%}_{excl}$ for σ_{max}	$M^{95\%}_{excl}$ for σ_{min}	$M^{95\%}_{excl}$ for σ_{max}
ALEPH	85	92	85	95
DELPHI	92	96	90	99
OPAL	91	95	85	96
L3 (this analysis)	90	95	78	94

Table 11.1: *Comparison of the 95 % C.L. exclusion limits on the scalar top and the scalar bottom masses for the two body decays $\tilde{t}_1 \to c\tilde{\chi}^0_1$ and $\tilde{b}_1 \to b\tilde{\chi}^0_1$ between the four LEP Experiments. The presented numbers correspond to the ΔM range between 15 and 65 GeV.*

other side, there is a difference in the experimental sensitivities, especially at the small $M_{squark} - M_{LSP}$ regions corresponding to the high missing energy (where Tevatron is less sensitive due to the high hadronic backgrounds). That's why, the Tevatron Experiments exclude more squark masses than LEP at high values of $M_{squark} - M_{LSP}$, but less in the region of high E_{miss} (small ΔM).

The difference between the $p\bar{p}$ and the e^+e^- physics implies the significant difference in SUSY phenomenology and consequently, in strategy of SUSY searches [107, 108]. Firstly, at LEP (or, at lepton colliders in general), sfermions are expected to appear as sfermion-antisfermion pairs (with assumed R-parity conservation scenario), mainly via the Z/γ exchange. Secondly, the direct decays to the LSP (the neutralino $\tilde{\chi}^0_1$), e.g. $\tilde{q} \to q\tilde{\chi}^0_1$, $\tilde{\ell} \to \ell\tilde{\chi}^0_1$ should dominate. Therefore, the sfermion topology at lepton colliders is relatively simple: two acoplanar objects (leptons or jets) plus missing energy. On the other hand, at Tevatron (or, at hadron colliders), the production of $\tilde{q}\tilde{q}$, $\tilde{g}\tilde{g}$ and $\tilde{q}\tilde{g}$, which is mediated by strong interactions, well dominates over the electroweak production channels. Moreover, due to the higher Tevatron energy, additional gluon and gluinos appear in the squark/gluino decays, which proceed through multi-step cascades, like for example, $\tilde{q} \to q\tilde{g}$ and $\tilde{g} \to q\tilde{q} \to qq\tilde{\chi}^0_2 \to qqZ\tilde{\chi}^0_1$. Such decays give rise to high multiplicity final states with many high-p_T jets and leptons and large missing *transverse* energy E_T^{miss}, and the QCD background is more difficult to suppress. Also, additional channels appear as kinematically open in SUSY searches at Tevatron, for example, $\tilde{t}_1 \to b\tilde{\chi}^+_1$ and $\tilde{t}_1 \to bW\tilde{\chi}^0_1$.

The Run II Tevatron operation period has started in March 2001. Due to the new Main Injector the beam intensity has been increased and CDF and D0 detectors expect to accumulate about 15 fb^{-1} integrated luminosity at $\sqrt{s} = 2$ TeV by year 2007. So, the scalar top and the scalar bottom quarks can be probed in Run II up to masses of about 200-260 GeV depending on the particular decay channel [108].

The *Large Hadron Collider* (LHC, [109,110]) is being currently constructed at CERN in the LEP tunnel and is planned to start in 2007. It will produce proton-proton collisions at a center-of-mass energy of 14 TeV. Four interaction points are foreseen and correspondingly, four experimental detectors are being constructed now, namely ATLAS, CMS, ALICE and LHCb. First two, ATLAS and CMS [109, 110], are general purpose particle detectors. During the initial phase of operation, the integrated luminosity accumulated per experiment and per year is expected to be about $L_{int} = 10 fb^{-1}$. Over the following years, the increase of luminosity up to $L = 10^{34}\ cm^{-2}s^{-1}$ will allow to collect $L_{int} \sim 100 fb^{-1}$ per experiment and per year. In pp collisions at such high center-of-mass energy, all squarks and gluinos are expected to be copiously produced and squark decay patterns in the relevant mass ranges can be quite complicated. All of the possible decays $\tilde{t}_1 \to t\tilde{\chi}^0_{1,2}$, $\tilde{t}_1 \to b\tilde{\chi}^+_{1,2,3,4}$, $\tilde{t}_1 \to t\tilde{g}$, $\tilde{b}_1 \to b\tilde{\chi}^0_{1,2}$, $\tilde{b}_1 \to t\tilde{\chi}^-_{1,2,3,4}$ and $\tilde{b}_1 \to b\tilde{g}$ may occur with the corresponding branchings defined by SUSY parameter values. Depending on the particular decay, a number of jets and leptons accompanied by *transverse* missing energy E_T^{miss} are expected in the final state and the QCD background rates will be high and difficult to separate. According to theoretical and Monte Carlo predictions within the various MSSM scenarios [111], the production of $\tilde{t}_1\bar{\tilde{t}}_1$ can be observed with 3σ statistical significance for a stop mass range from 250 GeV up to 700 GeV. However, a high integrated luminosity of about 100 fb^{-1} is required for this. Moreover, production of numerous squarks of the first two families and gluinos, which also result to jets, leptons and missing E_T in the final state, could make it very difficult to separate clean $\tilde{t}_1\bar{\tilde{t}}_1$ or $\tilde{b}_1\bar{\tilde{b}}_1$ patterns from the overall SUSY particle production. Thus, since $\tilde{t}_1$ and $\tilde{b}_1$ decays involve heavy flavors more frequently than decays of the other squarks, efficient b-tagging will be very important for squark identification at LHC.

Another famous future collider proposed for further investigation of the Higgs mechanism and physics beyond the Standard Model is *TESLA* Linear e$^+$e$^-$ Collider at DESY equipped with a general purpose detector [112]. This experiment is also being currently under an active preparation and start of its operation is planned to the end of the decade. This superconducting collider is being designed to produce e^+e^- collisions at center-of-mass energy of 500 GeV in the first 1-2 years, when the accumulated integrated luminosity is expected to be about 50 fb^{-1}; then the $\sqrt{s}$ is planned to increase to 800 GeV for the second operation period. In its physics potential, TESLA is considered as a facility for deeper and more precise investigations of properties of Higgs and SUSY particles with respect to the Tevatron Run II and the LHC Experiments, which can discover Higgs and SUSY before TESLA.

The phenomenology of the SUSY scalar quarks at TESLA should be similar to that at LEP e^+e^- Collider. However, higher energies and an option of polarized electron beam introduces new possibilities [113]. According to Monte Carlo studies, the stop pair production at TESLA at $\sqrt{s} = 500$ GeV and with $L_{int} \sim 10 fb^{-1}$ can be discovered with 3σ statistical significance up to the stop mass value of about 200 GeV in both $\tilde{t}_1 \to \tilde{\chi}^0_1$ and $\tilde{t}_1 \to b\tilde{\chi}^+_1$ channels and independently of the mixing angle. An increase of center-of-mass energy up to 800 GeV and integrated luminosity up to $L_{int} = 200\ fb^{-1}$ would push the discovery potential up to 350 GeV in the stop mass value. Moreover, even if squarks are already discovered at Tevatron Run II or at LHC, the TESLA Linear Collider will still remain the best facility for the precision measurements of the stop and the sbottom masses and the squark mixing angle through the measurement of the stop pair production cross section, which is sensitive to the electron beam polarization [113].

Chapter 12

Summary and Conclusions

Searches for SUSY quarks in e^+e^- interactions at LEP II have been performed with the L3 detector. In the year 2000 experimental data, signals for one of the most attractive theoretical scenarios, the Minimal Supersymmetric Standard Model [28, 29, 30], have been looked for. The pair produced scalar top $\tilde{t}_1$ and the scalar bottom $\tilde{b}_1$ quarks have been searched for as the possible lightest SUSY particles available at LEP II energies, $\sqrt{s}$ up to 208 GeV, under the assumption of R-parity conservation and taking into account experimental exclusion limits on the masses of other SUSY particles.

The following scalar top and scalar bottom decays have been considered: $\tilde{t}_1 \to c\tilde{\chi}^0_1$, $\tilde{t}_1 \to b\ell\tilde{\nu}$ (with two possibilities: ℓ being either e, μ or τ with equal probabilities or only the τ-lepton) and $\tilde{b}_1 \to b\tilde{\chi}^0_1$ (with the assumption of the LSP to be the lightest neutralino $\tilde{\chi}^0_1$ and the sneutrino decaying as $\tilde{\nu} \to \nu\tilde{\chi}^0_1$). For the allowed mass parameter space $M_{\tilde{t}_1} > M_b + M_W + M_{\tilde{\chi}^0_1} \geq 86$ GeV, the three body stop decay $\tilde{t}_1 \to bW\tilde{\chi}^0_1$ have been considered as complementary to the decay $\tilde{t}_1 \to c\tilde{\chi}^0_1$.

Due to the very small predicted values of the stop and the sbottom production cross sections with respect to the Standard Model processes, the smallest 95 % C.L. expected upper limit on the squarks production cross section have been used as a criterion for the event selection optimisation. The numbers of the selected experimental data events are found to be in a good statistical agreement with expectations from the Standard Model processes and no evidence for a new physics signal is found.

The model-independent 95 % C.L. upper limits on the scalar top and the scalar bottom quark production cross sections have been derived and set typically at the level of:

0.1-0.2 pb	for $\tilde{t}_1 \to c\tilde{\chi}^0_1$ decay,
0.05-0.2 pb	for $\tilde{t}_1 \to b\ell\tilde{\nu}$ and $\tilde{t}_1 \to b\tau\tilde{\nu}$ decays,
0.05-0.1 pb	for $\tilde{b}_1 \to b\tilde{\chi}^0_1$ decay and
0.7-1.0 pb	for $\tilde{t}_1 \to bW\tilde{\chi}^0_1$ decay.

In calculation of these limits, the results of the year 2000 L3 data analysis have been combined with results of the corresponding L3 squark searches performed at center-of-mass energies from 161 up to 202 GeV.

The cross section limits have been interpreted within the CMSSM theoretical framework as the 95 % C.L. exclusion limits on the squark and the LSP (or the sneutrino) masses. The squark masses for each particular decay channel are excluded for the cases of maximum and minimum of the production cross section (which correspond to the maximal mixing at $\cos\theta = 1$ and $\cos\theta$ of the Z-decoupling) at the 95% confidence level up to the following values (depending on particular values of the LSP or the sneutrino masses):

$$\tilde{t}_1 \rightarrow c\tilde{\chi}^0_1 \ : \qquad M^{\sigma_{min}}_{\tilde{t}_1} < 90 - 93 \text{ GeV}, \quad M^{\sigma_{max}}_{\tilde{t}_1} < 95 - 96 \text{ GeV};$$

$$\tilde{t}_1 \rightarrow bl\tilde{\nu} \ : \qquad M^{\sigma_{min}}_{\tilde{t}_1} < 87 - 89 \text{ GeV}, \quad M^{\sigma_{max}}_{\tilde{t}_1} < 90 - 91 \text{ GeV};$$

$$\tilde{t}_1 \rightarrow b\tau\tilde{\nu} \ : \qquad M^{\sigma_{min}}_{\tilde{t}_1} < 83 - 88 \text{ GeV}, \quad M^{\sigma_{max}}_{\tilde{t}_1} < 88 - 91 \text{ GeV};$$

$$\tilde{b}_1 \rightarrow b\tilde{\chi}^0_1 \ : \qquad M^{\sigma_{min}}_{\tilde{b}_1} < 76 - 83 \text{ GeV}, \quad M^{\sigma_{max}}_{\tilde{b}_1} < 94 - 97 \text{ GeV}.$$

The limits on the stop quark production cross section for the $\tilde{t}_1 \rightarrow bW\tilde{\chi}^0_1$ decay channel do not allow us to set any mass exclusion limits in the considered area of the stop and the LSP masses.

The results of scalar top two body decay searches have been used for the calculation of the exclusion limits of the mass degenerate squarks. The 95% C.L. exclusion limits on the mass degenerate scalar quarks for the cases of four and five squarks and for the cases of right-only or left and right eigenstates are the following:

$$\tilde{q} = \tilde{u}\ \tilde{d}\ \tilde{c}\ \tilde{s} : \qquad M_{\tilde{q_R}} < 95 - 96 \text{ GeV}, \quad M_{\tilde{q_{LR}}} < \ 99 - 100 \text{ GeV};$$

$$\tilde{q} = \tilde{u}\ \tilde{d}\ \tilde{c}\ \tilde{s}\ \tilde{b} : \qquad M_{\tilde{q_R}} < 96 - 97 \text{ GeV}, \quad M_{\tilde{q_{LR}}} < \ 99 - 101 \text{ GeV}.$$

Using the MSSM assumption about gaugino unification at the GUT scale, the results on the four mass degenerate squarks are reinterpreted on the $m_{\tilde{\mathrm{g}}}$, $m_{\tilde{\mathrm{q}}}$ plane. Moreover, the absolute limit on the M_2 MSSM parameter, obtained for $\tan\beta = 4$ from other L3 SUSY searches (for chargino, neutralino and scalar leptons), is translated into a limit on the gluino mass. The 95% C.L. exclusions on the $m_{\tilde{\mathrm{g}}}$, $m_{\tilde{\mathrm{q}}}$ mass plane are the following:

$$M_{\tilde{\mathrm{g}}} > 267 - 314 \text{ GeV},$$

$$M_{\tilde{\mathrm{q}}} > 99 - 100 \text{ GeV}.$$

Bibliography

[1] D. H. Perkins, *"Introduction to High Energy Physics"*, 4th Ed., Cambridge Univ. Press, 2000

[2] V. Novikov, *"Field Theory and the Standard Model"*, Proc. of European School of High Energy Physics, Ed. N. Ellis and J. March-Russel, CERN, 1998, CERN 99-04

[3] F. Zwirner, *"Beyond the Standard Model"*, Proc. of European School of High Energy Physics, CERN, 1997

[4] K. Hagiwara et al., *"Review of Particle Physics"*, Phys. Rev. D 66, 010001 (2002)

[5] M. Kobayashi and T. Maskawa, *Prog. Theor. Phys.* 49 (1973) 652;
N. Cabibbo, *Phys. Rev. Lett.* 10 (1963) 531

[6] M. Herrero, *"The Standard Model"*, Proc. of the NATO ASI 98 School, "Techniques and Concepts of High Energy Physics", St. Croix, Virgin Islands, USA, 1998, hep-ph/9812242

[7] S. L. Glashow, *Nucl. Phys.* 22 (1961) 579;
S. Weinberg, *Phys. Rev. Lett.* 19 (1967) 1264;
A. Salam, Proc. 8th Nobel Symposium, Stockholm 1968, ed. N. Svartholm (Almqvist and Wiksells, Stockholm, 1968), p. 367

[8] P. W. Higgs, *Phys. Lett.* 12 (1964) 132;
G. S. Guralnik, C. R. Hagen and T. W. B. Kibble, *Phys. Rev. Lett.* 13 (1964) 585;
P. W. Higgs, *Phys. Rev.* 145 (1966) 1156;
T. W. B. Kibble, *Phys. Rev.* 155 (1967) 1554

[9] F. J. Hasert, *Phys. Lett.* B46 (1973) 138

[10] UA1 Collaboration, G. Arnison et al., *Phys. Lett.* B122 (1983) 103;
UA2 Collaboration, M. Banner et al., *Phys. Lett.* B122 (1983) 476

[11] MARK J Collaboration, D. P. Barber et al., *Phys. Rev. Lett.* 43 (1979) 830;
TASSO Collaboration, R. Brandelik et al., *Phys. Lett.* B86 (1979) 243;
PLUTO Collaboration, C. Berger et al., *Phys. Lett.* B86 (1979) 418;
JADE Collaboration, W. Bartel et al., *Phys. Lett.* B91 (1980) 142

[12] M. L. Perl et al., *Phys. Rev. Lett.* 35 (1975) 1489;
M. L. Perl et al., *Phys. Lett.* B70 (1977) 487

[13] J. J. Aubert et al., *Phys. Rev. Lett.* 33 (1974) 1404;
J. E. Augustin et al., *Phys. Rev. Lett.* 33 (1974) 1406

[14] S. W. Herbq et al., *Phys. Rev. Lett.* 39 (1977) 252;
L. M. Lederman, Proc. 19th Int. Conf. on High Energy Phys., Tokyo, 1978, Ed. G. Takeda, Physical Society of Japan, Tokyo

[15] CDF Collaboration, F. Abe et al., *Phys. Rev. Lett.* 73 (1994) 225;
CDF Collaboration, F. Abe et al., *Phys. Rev.* D50 (1994) 2966;
CDF Collaboration, F. Abe et al., *Phys. Rev. Lett.* 74 (1995) 2626;
D0 Collaboration, S. Abachi et al., *Phys. Rev. Lett.* 74 (1995) 2632

[16] L3 Collaboration, M. Acciarri et al., *"Search for Higgs Boson in* e^+e^- *Interactions at* $\sqrt{s}$ *up to 208 GeV"*, L3 Note 2766, 2002

[17] H. Georgi and S. L. Glashow, *Phys. Rev. Lett.* 32 (1974) 438;
H. Georgi, H. R. Quinn and S. Weinberg, *Phys. Rev. Lett.* 33 (1974) 451;
P. Langacker, *Phys. Rev.* 72 (1981) 185

[18] L. Susskind, *Phys. Rev.* D20 (1979) 2619

[19] G. F. Giudice, *"Beyond the Standard Model"*, Proc. of European School of High Energy Physics, CERN, 1997

[20] R. Kaul, *Rev. Mod. Phys.* 55 (1981) 449;
E. Fahri and L. Susskind, *Phys. Rev.* 74 (1981) 277

[21] M. Peskin, Proc. Int. Symposium on Lepton and Photon Interactions at High Energy (Bonn, 1981), Ed. W. Pfiel, pq. 880

[22] Yu. A. Golfand and E. P. Likhtman, *ZhETF Pis. Red.* 13 (1971) 452;
JETP Lett. 13 (1971) 323;
D. V. Volkov and V. P. Akulov, *Phys. Lett.* B46 (1973) 109;
J. Wess and B. Zumino, *Nucl. Phys.* B70 (1974) 39;
Supersymmetry and Supergravity, Preprint Volume of Phys. Reports,
Ed. M. Jacob (North Holland / World Scientific, 1986)

[23] M. E. Peskin, *"Beyond the Standard Model"*, Proc. of European School of High Energy Physics, CERN, 2000

[24] R. Haag, J. Lopuszanski and M. Sohnius, *Nucl. Phys.* B88 (1975) 257

[25] E. Witten, *Nucl. Phys.* B188 (1981) 513;
N. Sakai, *Z Phys.* C11 (1981) 153;
S. Dimopoulos and H. Georgi, *Nucl. Phys.* B193 (1981) 150;
R. K. Kaul and P. Majumdar, *Nucl. Phys.* B199 (1982) 36

[26] S. Dimopoulos and H. Georgi, *Nucl. Phys.* B193 (1981) 150;
N. Sakai, *Z Phys.* C11 (1981) 153

[27] J. Wess and J. Bagger, *Supersymmetry and Supergravity*
Princton Univ. Press, 2nd edition, 1991

[28] P. Fayet, *Phys. Lett.* B64 (1976) 159

[29] P. Fayet, *Phys. Lett.* B69 (1977) 489; *Phys. Lett.* B84 (1979) 416

[30] G. R. Farrar and P. Fayet, *Phys. Lett.* B76 (1978) 575

[31] M. Dine, A. Nelson, Y. Shirman, *Phys. Rev.* D48 (1993) 1277;
Phys. Rev. D51 (1995) 1362;
M. Dine et al., *Phys. Rev.* D53 (1996) 2658

[32] A. Raspereza, *"Search for Neutral Higgs Bosons in e^+e^- Collisions"*,
Ph. D. Thesis, DESY-Zeuthen, 2002

[33] I. Iashvili, *"Search for SUSY Partners of Fermions at LEP and Prospects for SUSY at LHC"*, Ph. D. Thesis, Phys. Inst. of Humboldt Univ., Berlin, 2000

[34] S. P. Martin, *Perspectives of Supersymmetry*, Ed. G. L. Kane,
World Scientific, Singapore, 1997; hep-ph/9709356

[35] F. Zwirner, *Phys. Lett.* B132 (1983) 103;
L. Hall and M. Suzuki, *Nucl. Phys.* B231 (1984) 419;
J. Ellis, G. Gelmini, C. Jarlskog, G. Ross and J. Valle,
Phys. Lett. B150 (1985) 142;
G. Ross and J. Valle, *Phys. Lett.* B151 (1985) 375;
S. Dawson, *Nucl. Phys.* B261 (1985) 297;
S. Dimopoulos and L. Hall, *Phys. Lett.* B207 (1988) 210

[36] P. F. Smith et al., *Nucl. Phys.* B149 (1979) 525; *Nucl. Phys.* B206 (1982) 333;
E. Norman et al., *Phys. Rev. Lett.* 58 (1987) 1403;
T. K. Hemmick et al., *Phys. Rev.* D41 (1990) 2074

[37] Th. Hebbeker, *Phys. Lett.* B470 (1999) 259

[38] H. P. Nilles, *Phys. Rev.* 110 (1984) 1

[39] H. E. Haber and G. L. Kane, *Phys. Rev.* 117 (1985) 75;
R. Barbieri, *Riv. Nuov. Cim.* 11 (1988) 1

[40] R. Arnowitt, P. Nath, *Particles and Fields*, Proc. of the VII J. A. Swieca Summer School, Sao Paolo, Brasil, 1993, Ed. O. Eboli, V. Rivelles,
World Scientific, Singapore, 1993;
V. Barger, R. J. N. Phillips, *Recent Advances in the Superworld*, Proc. of the Int. Workshop, Woodlands, Texas, 1993, Ed. J. Lopez, D. Nanopoulos,

World Scientific, Singapore, 1994;
Properties of SUSY Particles, Ed. L. Ciffarelli, V. Khoze,
World Scientific, Singapore, 1993;
X. Tata, Lectures presented at TASI95, Univ. of Colorado, Boulder 1995,
hep-ph/9510287

[41] A. H. Chamseddine, R. Arnowitt and P. Nath, *Phys. Rev. Lett.* 49 (1982) 970

[42] L. J. Hall, J. Lykken and S. Weinberg, *Phys. Rev.* D27 (1983) 2359

[43] L. Girardello and M. Grisaru, *Nucl. Phys.* B194 (1982) 65;
K. Harada and N. Sakai, *Prog. Theor. Phys.* 67 (1982) 67

[44] S. Dimopoulos and D. Sutter, *Nucl. Phys.* B452 (1995) 496

[45] P. Chankowski, S. Pokorski and J. Rosiek, *Phys. Lett.* B274 (1992) 191;
Phys. Lett. B281 (1992) 100;
Y. Okada, M. Yamaguchi and T. Yanagida, *Phys. Lett.* B262 (1991) 54;
J. Espinosa and M. Quiros, *Phys. Lett.* B267 (1991) 27;
Phys. Lett. B266 (1991) 389;
H. Haber and R. Hemptling, *Phys. Rev.* D48 (1993) 4280;
Phys. Rev. Lett. 66 (1991) 1815;
J. Gunion and A. Turski, *Phys. Rev.* D39 (1989) 2701;
Phys. Rev. D40 (1990) 2333;
M. Berger, *Phys. Rev.* D41 (1990) 225;
K. Sasaki, M. Carena and C. Wagner, *Nucl. Phys.* B381 (1992) 66;
R. Barbieri and M. Frigeni, *Phys. Lett.* B258 (1991) 395;
J. Ellis, G. Ridolfi and F. Zwirner, *Phys. Lett.* B257 (1991) 83;
Phys. Lett. B262 (1991) 477;
R. Hemptling and A. Hoang, *Phys. Lett.* B331 (1994) 99;
R. Barbieri, F. Caravaglios and M. Frigeni, *Phys. Lett.* B258 (1991) 167;
H. Haber, R. Hemptling and H. Hoang, hep-ph/9609331, 1996;
M. Carena, M. Qquiros and C. Wagner, *Nucl. Phys.* B461 (1996) 407;
M. Carena, J. Espinosa, M. Quiros and C. Wagner, *Phys. Lett.* B355 (1995) 209

[46] L. Ibáñez and G. G. Ross, *Phys. Lett.* B110 (1982) 215

[47] K. Inoue et al., *Prog. Theor. Phys.* 68 (1982) 927;
Prog. Theor. Phys. 71 (1984) 413

[48] F. Gabbiani, E. Gabbrielo, A. Masiero and L. Silvestrini,
Nucl. Phys. B477 (1996) 321;
J. Ellis, D. V. Nanopoulos, *Phys. Lett.* B110 (1982) 44

[49] L. Ibáñez, *Phys. Lett.* B118 (1982) 73;
J. Ellis, D. V. Nanopoulos and K. Tamvakis, *Phys. Lett.* B121 (1983) 123;
J. Ellis, J. Hagelin, D. V. Nanopoulos and K. Tamvakis,
Phys. Lett. B125 (1983) 275;

L. Alvarez-Gaumé, J. Polchinski and M. Wise, *Nucl. Phys.* B221 (1983) 495;
G. Kane, C. Kolda, L. Roszkowski, J. Wells, *Phys. Rev.* D49 (1994) 6173

[50] P. Nath, R. Arnowitt and A. H. Chamseddine, *Applied N=1 Supergravity*, World Scientific, Singapore, 1984

[51] J. Ellis, S. Rudaz, *Phys. Lett.* B128 (1983) 248;
J. F. Gunion, H. E. Haber, *Nucl. Phys.* B272 (1986) 1;
A. Bartl, W. Majerotto and W. Porod, *Z Phys.* C64 (1994) 499;
Z Phys. C68 (1995) 518

[52] V. Barger, M. S. Berger and P. Ohmann, *Phys. Rev.* D49 (1994) 4908;
D. J. Castaño, E. J. Oiard and P. Ramond, *Phys. Rev.* D49 (1994) 4882

[53] M. Drees, S. P. Martin, Wisconsin preprint MADPH-95-879, hep-ph/9504324

[54] B. Pendleton and G. Ross, *Phys. Lett.* B98 (1981) 291;
V. Barger et al., *Phys. Lett.* B314 (1993) 351;
S. Kelley, J. Lopez and D. Nanopoulos, *Phys. Lett.* B274 (1992) 387;
M. Carena et al., *Nucl. Phys.* B426 (1994) 269

[55] A. Bartl, H. Fraas, W. Majerotto and B. Moesslacher, *Z Phys.* C55 (1992) 257

[56] J. Ellis, J. S. Hagelin, D. V. Nanopoulos, K. A. Olive and M. Srednicki, *Nucl. Phys.* B238 (1984) 453

[57] D. Pierce and A. Papadopoulos, *Nucl. Phys.* B430 (1994) 278

[58] K. I. Hikasa and M. Kobayashi, *Phys. Rev.* D36 (1987) 724

[59] H. Eberl, A. Bartl and W. Majerotto, *Nucl. Phys.* B472 (1996) 481

[60] A. Bartl, H. Eberl, S. Kraml, W. Majerotto and W. Porod, *Z Phys.* C73 (1997) 469

[61] A. Bartl, H. Eberl, S. Kraml, W. Majerotto and W. Porod, *Z Phys.* C76 (1997) 549

[62] M. Dress, K. Hikassa, *Phys. Lett.* B252 (1995) 463

[63] W. Beenaker, R. Hoepker and P. M. Zerwas, *Phys. Lett.* B349 (1995) 463

[64] H. Eberl, A. Bartl, W. Majerotto, UWThPh-1996-6, HEPHY-PUB 640/96

[65] L3 Collaboration, B. Adeva et al., *Phys. Lett.* B472 (2000) 420

[66] S. Asai et al., Preprint UT-ICEPP 95-10 (1995)

[67] T. Sjoestrand, *"PYTHIA 5.7 and JETSET 7.4 Physics and Manual"*, CERN-TH/7112/93 (1993), revised Aug. 1995;
T. Sjoestrand, *Comp. Phys. Comm.* 82 (1994) 74

[68] G. Altarelli et al., *Physics at LEP 2*, vol. 2, CERN 96-01

[69] C. Peterson et al., *Phys. Rev.* D27 (1983) 105

[70] The LEP Experiments: ALEPH, DELPHI, L3, OPAL, *Nucl. Inst. and Meth.* A378 (1996) 101

[71] D0 Collaboration, S. Abachi et al., FERMILAB-CONF-97/357-E

[72] M. Acciarri et al., *Nucl. Inst. and Meth.* A351 (1994) 300;
M. Acciarri et al., *Nucl. Inst. and Meth.* A360 (1995) 103

[73] A. Adam et al., *Nucl. Inst. and Meth.* A344 (1994) 521

[74] F. Beissel et al., *Nucl. Inst. and Meth.* A332 (1993) 33

[75] B. Adeva et al., *Nucl. Inst. and Meth.* A265 (1988) 252

[76] Y. Karyotakis, *The L3 Electromagnetic Calorimeter*, Proc. of Beijing Calorimetry Symposium, Beijing, China, 1995, Ed. H. S. Chen, p. 27-35

[77] G. Basti et al., *Nucl. Inst. and Meth.* A374 (1996) 293

[78] B. Adeva et al., *Nucl. Inst. and Meth.* A323 (1992) 109;
A. Adam et al., *Nucl. Ins. and Meth.* A282 (1996) 342

[79] I. C. Brock et al., Preprint CERN-PPE/96-89 (1996)

[80] BHWIDE, version 1.01;
S. Jadach et al., *Phys. Lett.* B390 (1997) 298

[81] KORALZ, version 4.03;
S. Jadach, B. F. L. Ward and Z. Was, *Comp. Phys. Comm.* 79 (1994) 503

[82] KORALW, version 1.33;
M. Skrzypek et al., *Comp. Phys. Comm.* 94 (1996) 216;
M. Skrzypek et al., *Phys. Lett.* B372 (1996) 289

[83] PHOJET, version 1.10;
R. Engel, *Z Phys.* C66 (1995) 203;
R. Engel and J. Ranft, *Phys. Rev.* D54 (1996) 4244

[84] EXCALIBUR, versoin 1.11;
F. A. Berends, R. Kleiss and R. Pittau, *Nucl. Phys.* B424 (1994) 308;
Nucl. Phys. B426 (1994) 344; *Nucl. Phys.* B37 (1994) 163;
Phys. Lett. B335 (1994) 490; *Comp. Phys. Comm.* 83 (1994) 141

[85] F. A. Berends, P. H. Daverfeld and R. Kleiss, *Nucl. Phys.* B253 (1985) 441

[86] SUSYGEN, version 2.2;
S. Katsanevas and P. Morawitz, *Comp. Phys. Comm.* 112 (1998) 227

[87] S. Banerjee, *"Monte Carlo Tuning in L3"*, L3 Note 2662, 2001

[88] W. van Rossum, *"Comparison of the two-photon Monte-Carlo event generators TWOGEN, TWOGAM, TWOGAMMA and PYTHIA"*, L3 Note 1917, 1996

[89] R. Brun et al., CERN DD/EE/84-1 (Revised 1987), Version 3.15

[90] H. Fesefeldt, *RWTH Aachen Report PITHA 85/2* (1985)

[91] S. Catani et al., *Phys. Lett.* B269 (1991) 432;
S. Bethke et al., *Nucl. Phys.* B370 (1992) 310

[92] J. Branson, A. Dominiquez, I. Fisk and G. Raven, *"The UCSD B Tag for 1996"*, L3 Int. Note 2018, 1997

[93] A. Dominiquez, *"Search for Neutral Higgs Boson in* e^+e^- *Interactions at Center-of-Mass Energies between 130 GeV and 183 GeV"*, Ph. D. Thesis, UCSD, 1998, *http://hep.ucsd.edu/thesis/aaron.html*

[94] L. Montanet et al., *Phys. Rev.* D30 (1994) 1173

[95] Th. Hebbeker, *"Calculating Upper Limits with Poisson Statistics"*, L3 Note 2633, 2001;
S. Sushkov, *"Combining Limits with Poisson Statistics: Comparison of Practical Implementations"*, L3 Note 2795, 2003

[96] F. James and M. Goossens, *"MINUIT: Function Minimizationq and Error Analysis"*, CERN Program Library D506, 1992

[97] S. Sushkov and Th. Hebbeker, *"Searches for Scalar Quarks in* e^+e^- *Interactions at* $\sqrt{s} = 202 - 208$ *GeV"*, L3 Note 2796, 2003;
L3 Collaboration, M. Acciarri et al., *"Search for Sleptons and Squarks in* e^+e^- *Collisions at* $\sqrt{s} = 192 - 208$ *GeV"*, *Submitted to Phys. Lett. B*

[98] L3 Collaboration, M. Acciarri et al., *Phys. Lett.* B456 (1999) 283

[99] S. Kraml, *CALVIN, Program for Calculation the Stop, Sbottom, Stau Pair Production Cross Section in* e^+e^- *Collisions*

[100] T. Plehn, *"Production of Supersymmetric Particles at High Energy Colliders"*, Ph. D. Thesis, hep-ph/9809319

[101] ISAJET, version 7.58, H. Baer et al., Preprint BNL-HET-99/43

[102] CDF Collaboration, B. Abe et al., *Phys. Rev.* D56 (1997) 1357

[103] D0 Collaboration, S. Abachi et al., *Phys. Rev. Lett.* 75 (1995) 618

[104] UA1 Collaboration, C. Albajar et al., *Phys. Lett.* B198 (1987) 261;
UA2 Collaboration, J. Alitti et al., *Phys. Lett.* B235 (1990) 363

[105] K. Hikasa and M. Kobayashi, *"Light Scalar Top Quark at e^+e^- Colliders"*, *Phys. Rev.* D36 (1987) 724;
C. Boehm, A. Djouadi and Y. Mambrini, *"Decays of the Lightest Top Squark"*, Preprint hep-ph/9907428;
W. Porod and T. Woehrmann, *"Higher Order Top Squark Decays"*, Preprint UWThPh-1996-45;
W. Porod, *"More on Higher Order Decays of the Lighter Top Squark"*, Preprint hep-ph/9812230

[106] ALEPH Collaboration, D. Buskulich et al., *"Search for Scalar Quarks in e^+e^- Collisions at $\sqrt{s}$ up to 209 GeV"*, Preprint CERN-EP/2002-026, *Submitted to Phys. Lett. B*;
DELPHI Collaboration, J. Abdallah et al., *"Searches for Supersymmetric Particles in e^+e^- Collisions up to 208 GeV, and Interpretation of the Results wqithin the MSSM"*, DEPLHI 2002-027 CONF 561;
OPAL Collaboration, G. Abbiendi et al., *"Search for Scalar Top and Scalar Bottom Quarks at LEP"*, Preprint CERN-EP/2002-050, *Submitted to Phys. Lett. B*

[107] F. Gianotti, *"Searches for Supersymmetry at High Energy Colliders: the Past, the Present and the Future"*, *New J. of Phys.* 4 (2002) 63.1

[108] R. Demina et al., hep-ph/9910275, 1999; FERMILAB-PUB-99/259-T

[109] CMS Collaboration, *"Technical Proposal"*, CERN/LHCC 94-38, LHCC/P1, December 1994

[110] ATLAS Collaboration, *"Technical Proposal"*, CERN/LHCC 94-43, LHCC/P2, December 1994

[111] U. Dydak, *"Search for the Stop Quark with CMS at the LHC"*, CMS TN/96-022

[112] R. Brinkmann et al., *"Conceptual Design Report of a 500 GeV e^+e^- Liner Collider with Integrated X-Ray Laser Facility"*, DESY 1997-048

[113] A. Bartl et al., *Z Phys.* C76 (1997) 549.

Acknowledgments

A thesis in experimental high energy physics is not possible without the combined effort of many people. I am grateful to the numerous technicians, engineers and physicists who have built and maintained LEP and the L3 detector.

I acknowledge the effort of all shift takers and experts on call who ensured data taking and I thank all those people who have made these data usable by calibrating the detector, writing reconstruction code, producing Monte Carlos and providing the collaboration with software and computer environment...

I enjoyed the work in the SUSY group of the L3 collaboration and thank very much to all colleagues, who helped me with numerous advices and discussions during my work: Dr. Alvise Favara, Dr. Sylvie Rosier-Lies, Dr. Salvatore Mele in CERN, Dr. Hannelies Novak and Dr. Sabina Rieman in DESY-Zeuthen, and, of course, Dr. Martin Gruenewald, Dr. Ia Iashvili, Dr. Alexei Raspereza, Dr. Valeri Andreev and many-many other colleagues.

I wish to thank especially my supervisor Prof. Thomas Hebbeker, who provided me the possibility to work in this interesting field of physics within the framework of the Graduate College of Berlin Humboldt University, and who patiently teached me a lot during these three years, both in physics and in life.

I am also very thankful to the staff of the Institutes of Physics in the Humboldt University in Berlin and RWTH University in Aachen, who helped me a lot to organize my work. My special thanks also to Dr. Martin Weber for his kind suggestions and corrections to the text of this thesis.

Last but not least, I remember deep in my heart those people, who teached me through all years of my studies: my school teacher L. V. Krivopusk from Chelyabinsk, my university supervisor Prof. N. Maksimenko from Gomel, also Prof. Ju. Budagov and Dr. A. Kurilin from Dubna, and of course, my Mother.

Selbständigkeitserklärung

Ich erkläre eidesstattlich, dass ich die Dissertation selbstständig verfasst und alle in Anspruch genommenen Hilfen in der Dissertation angegeben habe.

Aachen, 22.05.2003

Serge Sushkov